

Multiphysics modelling and experimental validation of microelectromechanical resonator dynamics

Citation for published version (APA):

Mestrom, R. M. C. (2009). *Multiphysics modelling and experimental validation of microelectromechanical resonator dynamics*. [Phd Thesis 1 (Research TU/e / Graduation TU/e), Mechanical Engineering]. Technische Universiteit Eindhoven. <https://doi.org/10.6100/IR652849>

DOI:

[10.6100/IR652849](https://doi.org/10.6100/IR652849)

Document status and date:

Published: 01/01/2009

Document Version:

Publisher's PDF, also known as Version of Record (includes final page, issue and volume numbers)

Please check the document version of this publication:

- A submitted manuscript is the version of the article upon submission and before peer-review. There can be important differences between the submitted version and the official published version of record. People interested in the research are advised to contact the author for the final version of the publication, or visit the DOI to the publisher's website.
- The final author version and the galley proof are versions of the publication after peer review.
- The final published version features the final layout of the paper including the volume, issue and page numbers.

[Link to publication](#)

General rights

Copyright and moral rights for the publications made accessible in the public portal are retained by the authors and/or other copyright owners and it is a condition of accessing publications that users recognise and abide by the legal requirements associated with these rights.

- Users may download and print one copy of any publication from the public portal for the purpose of private study or research.
- You may not further distribute the material or use it for any profit-making activity or commercial gain
- You may freely distribute the URL identifying the publication in the public portal.

If the publication is distributed under the terms of Article 25fa of the Dutch Copyright Act, indicated by the "Taverne" license above, please follow below link for the End User Agreement:

www.tue.nl/taverne

Take down policy

If you believe that this document breaches copyright please contact us at:

openaccess@tue.nl

providing details and we will investigate your claim.

**Multiphysics modelling and experimental
validation of microelectromechanical
resonator dynamics**

Multiphysics modelling and experimental validation of microelectromechanical resonator dynamics / by Robertus M.C. Mestrom – Eindhoven : Technische Universiteit Eindhoven, 2009 – Proefschrift

A catalogue record is available from the Eindhoven University of Technology Library

ISBN: 978-90-386-2034-3

NUR: 978

This thesis was prepared with the \LaTeX 2_ε documentation system

Reproduction: Ipskamp Drukkers B.V., Enschede, The Netherlands

Cover design: Rob Mestrom

Copyright ©2009 by R.M.C. Mestrom. All rights reserved.

Multiphysics modelling and experimental validation of microelectromechanical resonator dynamics

PROEFSCHRIFT

ter verkrijging van de graad van doctor aan de
Technische Universiteit Eindhoven, op gezag van de
rector magnificus, prof.dr.ir. C.J. van Duijn, voor een
commissie aangewezen door het College voor
Promoties in het openbaar te verdedigen
op donderdag 12 november 2009 om 16.00 uur

door

Robertus Matheus Catharina Mestrom

geboren te Weert

Dit proefschrift is goedgekeurd door de promotor:

prof.dr. H. Nijmeijer

Copromotor:

dr.ir. R.H.B. Fey

Contents

Summary	ix
Samenvatting	xi
Nomenclature	xiii
I Introduction	I
I.1 General introduction	I
I.2 Modelling of MEMS	3
I.2.1 Multiphysics modelling	3
I.2.2 Modelling levels	4
I.2.3 Modelling for dynamics	7
I.2.4 Model requirements	8
I.3 Research objectives and outline	9
2 Background information	I3
2.1 Introduction	I3
2.2 MEMS resonators	I4
2.2.1 Research overview	I5
2.2.2 Actuation and detection	20
2.2.3 Resonator types	2I
2.3 Oscillators	23
2.3.1 Working principle	24
2.3.2 Key properties	25
2.4 Steady-state behaviour of nonlinear dynamical systems	29
2.4.1 Nonlinear dynamical system	29
2.4.2 Equilibrium points, local stability and bifurcations	3I
2.4.3 Periodic solutions, local stability and bifurcations	33
2.4.4 Numerical continuation	35

3	Heuristic modelling of MEMS resonators	37
3.1	Introduction	37
3.2	Case study I: clamped-clamped beam MEMS resonator	38
3.2.1	Experiments using a clamped-clamped beam resonator	38
3.2.2	Modelling approach	41
3.2.3	Numerical and experimental results	45
3.2.4	Discussion	53
3.3	Case study II: dog-bone MEMS resonator	54
3.3.1	Experiments using a dog-bone resonator	54
3.3.2	Modelling approach	59
3.3.3	Numerical results	67
3.3.4	Discussion	68
3.4	Conclusions	69
4	Multiphysics modelling framework	71
4.1	Introduction	71
4.2	Modelling philosophy	73
4.3	Relevant physical effects	74
4.3.1	Structural dynamics	75
4.3.2	Material behaviour	76
4.3.3	Loss mechanisms	78
4.3.4	Anchor loss	79
4.3.5	Thermoelastic damping	79
4.3.6	Electrostatic actuation and fringing fields	82
4.3.7	Capacitive or piezoresistive detection	83
4.3.8	Thermal noise	85
4.4	Modelling framework	85
4.4.1	Construction of reduced-order models	86
4.4.2	Framework overview	87
5	Modelling of a clamped-clamped beam MEMS resonator	91
5.1	Introduction	91
5.2	Models of the clamped-clamped beam MEMS resonator	92
5.2.1	Assumptions	93
5.2.2	Physical level models	94
5.2.3	Models in non-dimensional form	98
5.2.4	Galerkin discretisation	100
5.2.5	Reduced-order models	103
5.2.6	Modelling of anchor loss	106
5.2.7	Numerical implementation	108
5.3	Validation with finite element solutions	109

5.3.1	Natural frequencies and mode shapes	110
5.3.2	Thermoelastic modeshapes and damping	111
5.3.3	Fringing field effects	114
5.4	Simulation results and model comparison	116
5.4.1	Equilibrium points and stability	117
5.4.2	Periodic solutions and stability	122
5.5	Conclusions	130
6	Experiments on a clamped-clamped beam MEMS resonator	133
6.1	Introduction	133
6.2	Clamped-clamped beam MEMS resonator	134
6.3	Measurement set-up and techniques	136
6.3.1	Set-up overview	136
6.3.2	Measurement techniques	137
6.3.3	Network analyzer measurements	138
6.3.4	Labview measurements	139
6.4	Electrical circuit representation and parameter estimation	140
6.4.1	Electrical equivalent circuit	141
6.4.2	Y-parameters calculation	143
6.4.3	Parasitic and motional parameters	144
6.4.4	Measurement circuit	145
6.5	Experimental results and model validation	146
6.5.1	Validation approach	146
6.5.2	Results for the thick beam	148
6.5.3	Results for the thin beam	155
6.6	Conclusions	164
7	Phase feedback for nonlinear MEMS resonators in oscillator circuits	165
7.1	Introduction	165
7.2	Open-loop response of the Duffing resonator	166
7.3	Phase feedback	169
7.3.1	Principle of phase feedback	169
7.3.2	Application to a MEMS resonator	170
7.4	Results	172
7.4.1	Open-loop response of the MEMS resonator	172
7.4.2	Oscillator response using phase feedback	173
7.4.3	Influence of saturation level	177
7.4.4	Influence of amplifier gain	179
7.4.5	Response up to dynamic pull-in	179
7.5	Conclusion	181

8	Conclusions and recommendations	183
8.1	Conclusions	183
8.2	Recommendations	186
A	Silicon as an engineering material	189
A.1	Structural and mechanical properties	189
A.1.1	Crystal structure	189
A.1.2	Elastic properties	190
A.1.3	Intrinsic losses	194
A.1.4	Effect of impurities	194
A.1.5	Measurement techniques	195
A.2	Thermal properties	197
A.2.1	Specific heat	197
A.2.2	Thermal expansion coefficient	197
A.2.3	Thermal conductivity	197
A.2.4	Temperature influence on elastic constants	198
A.3	Manufacturing techniques	198
A.4	Effect of third-order elastic constants	199
A.4.1	Linear elasticity	199
A.4.2	Nonlinear elasticity	199
A.4.3	Nonlinear Young's modulus for homogeneous uni-axial loading	202
B	Some aspects of the clamped-clamped beam MEMS resonator models	205
B.1	Beam theory	205
B.2	Models for the clamped-clamped beam MEMS resonator	206
B.2.1	Strain-displacement relations	207
B.2.2	Hamilton's principle	207
B.2.3	Inclusion of the constitutive equations	209
B.2.4	The heat equation	212
B.2.5	Distributed electrostatic load	213
B.3	Basis functions for Galerkin discretisation	214
B.3.1	Basis functions for Euler-Bernoulli beam	214
B.3.2	Basis functions for the Timoshenko beam	215
B.3.3	Basis functions for the heat equation	218
B.4	Multi-mode Galerkin discretisations	220
	Bibliography	225
	Dankwoord / Acknowledgements	237
	Curriculum Vitae	239

Summary

Multiphysics modelling and experimental validation of microelectromechanical resonator dynamics

The modelling of microelectromechanical systems provides a very challenging task in microsystems engineering. This field of research is inherently multiphysics of nature, since different physical phenomena are tightly intertwined at microscale. Typically, up to four different physical domains are usually considered in the analysis of microsystems: mechanical, electrical, thermal and fluidic. For each of these separate domains, well-established modelling and analysis techniques are available. However, one of the main challenges in the field of microsystems engineering is to connect models for the behavior of the device in each of these domains to equivalent lumped or reduced-order models without making unacceptably inaccurate assumptions and simplifications and to couple these domains correctly and efficiently. Such a so-called multiphysics modelling framework is very important for simulation of microdevices, since fast and accurate computational prototyping may greatly shorten the design cycle and thus the time-to-market of new products.

This research will focus on a specific class of microsystems: microelectromechanical resonators. MEMS resonators provide a promising alternative for quartz crystals in time reference oscillators, due to their small size and on-chip integrability. However, because of their small size, they have to be driven into nonlinear regimes in order to store enough energy for obtaining an acceptable signal-to-noise ratio in the oscillator. Since these resonators are to be used as a frequency reference in the oscillator circuits, their steady-state (nonlinear) dynamic vibration behaviour is of special interest.

A heuristic modelling approach is investigated for two different MEMS resonators, a clamped-clamped beam resonator and a dog-bone resonator. For the clamped-clamped beam resonator, the simulations with the proposed model shows a good agreement with experimental results, but the model is limited in its predictive capabilities. For the dog-bone resonator, the proposed heuristic modelling approach does not lead to a match be-

tween simulations and experiments. Shortcomings of the heuristic modelling approach serve as a motivation for a first-principles based approach.

The main objective of this research is to derive a multiphysics modelling framework for MEMS resonators that is based on first-principles formulations. The framework is intended for fast and accurate simulation of the steady-state nonlinear dynamic behaviour of MEMS resonators. Moreover, the proposed approach is validated by means of experiments. Although the multiphysics modelling framework is proposed for MEMS resonators, it is not restricted to this application field within microsystems engineering. Other fields, such as (resonant) sensors, switches and variable capacitors, allow for a similar modelling approach.

In the proposed framework, the mechanical, electrical and thermal domains are included. Since the resonators considered are operated in vacuum, the fluidic domain (squeeze film damping) is not included. Starting from a first-principles description, founded on partial differential equations (PDEs), characteristic nonlinear effects from each of the included domains are incorporated. Both flexural and bulk resonators can be considered. Next, Galerkin discretization of the coupled PDEs takes place, to construct reduced-order models while retaining the nonlinear effects. The multiphysics model consists of the combined reduced-order models from the different domains. Designated numerical tools are used to solve for the steady-state nonlinear dynamic behaviour of the combined model.

The proposed semi-analytical (i.e. analytical-numerical) multiphysics modeling framework is illustrated for a full case study of an electrostatically actuated single-crystal silicon clamped-clamped beam MEMS resonator. By means of the modelling framework, multiphysics models of varying complexity have been derived for this resonator, including effects like electrostatic actuation, fringing fields, shear deformation, rotary inertia, thermoelastic damping and nonlinear material behaviour. The first-principles based approach allows for addressing the relevance of individual effects in a straightforward way, such that the models can be used as a (pre-)design tool for dynamic response analysis. The method can be considered complementary to conventional finite element simulations.

The multiphysics model for the clamped-clamped beam resonator is validated by means of experiments. A good match between the simulations and experiments is obtained, thereby giving confidence in the proposed modelling framework.

Finally, next to the modelling approach for MEMS resonators, a technique for using these nonlinear resonators in an oscillator circuit setting is presented. This approach, called phase feedback, allows for operation of the resonator in its nonlinear regime. The closed-loop technique enables control of both the frequency of oscillation and the output power of the signal. Additionally, optimal operation points for oscillator circuits incorporating a nonlinear resonator can be defined.

Samenvatting

Het modelleren van micro-elektro-mechanische systemen vormt een grote uitdaging in de microsysteemtechnologie. Dit onderzoeksgebied is intrinsiek multifysisch van aard, omdat verschillende fysische effecten nauw met elkaar verweven zijn op microschaal. Typisch worden er tot vier verschillende domeinen beschouwd bij de analyse van microsystemen: mechanisch, elektrisch, thermisch en fluïdisch. Voor elk van deze afzonderlijke domeinen zijn er goed bekende analysetechnieken voorhanden. Een van de belangrijkste uitdagingen in het gebied van de microsysteemtechnologie is het koppelen van modellen voor het gedrag van het systeem in elk van deze domeinen aan equivalente of verlaagde-orde modellen, zonder daarbij onacceptabele aannames en vereenvoudigingen te doen, en om de domeinen efficiënt te koppelen. Een zogenoemde multifysische modelleeraanpak is erg belangrijk voor het simuleren van microsystemen, omdat snel en nauwkeurig prototype-ontwerp de ontwerpcyclus en daarmee de tijd die nodig is om een product op de markt te brengen flink kan verkorten.

Dit onderzoek richt zich op een specifieke klasse van microsystemen: micro-elektro-mechanische resonatoren. MEMS resonatoren vormen een veelbelovend alternatief voor kwartskristallen in oscillatoren voor tijd-referentie, omdat ze klein en op de chip integreerbaar zijn. Vanwege hun kleine afmetingen, moeten ze echter in niet-lineaire bereiken bedreven worden, om genoeg energie op te slaan voor een acceptabele signaal-ruis-verhouding in de oscillator. Omdat deze resonatoren gebruikt gaan worden als frequentie-referentie in oscillator circuits, is hun lange termijn (niet-lineair) dynamisch trillingsgedrag van belang.

Een heuristische modelleeraanpak is onderzocht voor twee verschillende MEMS resonatoren: een dubbelzijdig ingeklemde balk en een 'dog-bone' resonator. Voor de balk resonator laten simulaties met het voorgestelde model een goede overeenkomst zien met experimenten. De voorspellende aard van het model is echter beperkt. Voor de 'dog-bone' resonator leidt het voorgestelde heuristische model niet tot een overeenkomst tussen simulaties en experimenten. Tekortkomingen van de heuristische modelleeraanpak motiveren een op grondbeginselen gebaseerde aanpak.

Het hoofddoel van dit onderzoek is om een op grondbeginsel-formuleringen gebaseerd multifysisch modelleerkader af te leiden voor MEMS resonatoren. Dit kader is bedoeld voor het snel en nauwkeurig simuleren van lange termijn niet-lineair dynamisch gedrag van MEMS resonatoren. Bovendien wordt de voorgestelde aanpak gevalideerd met experimenten. Hoewel het modelleerkader wordt gepresenteerd voor MEMS resonatoren, is de toepassing niet beperkt tot dit veld in de microsysteemtechnologie. De aanpak kan ook gebruikt worden voor andere toepassingen, zoals (resonante) sensoren, schakelaars en variabele condensatoren.

In het modelleerkader zijn het mechanische, het elektrische en het thermische domein inbegrepen. Omdat de beschouwde resonatoren in vacuum opereren wordt het fluïdische domein (samengeperste-film damping) niet meegenomen. Startend vanuit een beschrijving van de grondbeginselen die gestaafd is op partiële differentiaalvergelijkingen (PDVs), worden karakteristieke niet-lineaire effecten van elk van de beschouwde domeinen meegenomen. Zowel buigings- als bulkresonatoren kunnen beschreven worden. Vervolgens wordt Galerkin discretisatie toegepast op de gekoppelde PDVs om verlaagde-orde modellen te construeren met behoud van niet-lineaire effecten. Het multifysisch model wordt gevormd door een combinatie van de verlaagde-orde modellen uit elk van de verschillende domeinen. Vervolgens worden specifieke numerieke gereedschappen gebruikt om het lange-termijn niet-lineair dynamisch gedrag van dit model te bepalen.

Het voorgestelde semi-analytische (i.e. analytisch-numeriek) multifysische modelleerkader wordt geïllustreerd aan de hand van volledige gevalsstudie van een elektrostatisch geactueerde dubbelzijdig ingeklemde balk MEMS resonator van monokristallijn silicium. Met behulp van het modelleerkader zijn voor deze resonator modellen van verschillende complexiteit afgeleid, waarbij effecten als elektrostatische actuatie, strooivelden, afschuiving, rotatie-traagheid, thermoelastische damping en niet-lineair materiaalgedrag zijn meegenomen. De op grondbeginselen gebaseerde aanpak maakt het mogelijk om de relevantie van individuele effecten op een eenduidige manier te bepalen, waardoor de modellen gebruikt kunnen worden als een (voor-)ontwerp gereedschap voor dynamische respons analyse. Deze methode kan beschouwd worden als complementair aan conventionele eindige elementen simulaties.

Het multifysisch model voor de dubbelzijdig ingeklemde balk resonator is gevalideerd via experimenten. Een goede overeenkomst tussen simulaties en experimenten is verkregen, hetgeen vertrouwen geeft in het voorgestelde modelleerkader.

Tenslotte is, naast de modelleeraanpak voor MEMS resonatoren, een techniek beschreven om deze niet-lineaire resonatoren in een oscillator circuit te gebruiken. Deze aanpak, fase terugkoppeling genaamd, maakt het mogelijk om de resonator in zijn niet-lineaire bereik aan te sturen. Met deze gesloten-lus techniek kan zowel de oscillatiefrequentie als het uitgangsvermogen van het signaal geregeld worden. Bovendien kunnen optimale werkpunten bepaald worden voor oscillator circuits met niet-lineaire resonator.

Nomenclature

General notation

a, A	scalar
\mathbf{a}	column, vector
\mathbf{A}	matrix, tensor
\dot{a}	time derivative
$\frac{\partial}{\partial a}$	partial derivative with respect to a
\bar{a}	non-dimensional scalar
δ	variational operator
∇	gradient operator

Roman symbols

Symbol	Description	Unit
\mathcal{A}	area	m^2
\mathcal{B}	body	
\mathcal{B}	column of operators for boundary conditions	
\mathcal{F}	free energy	
$\mathcal{L}(\Delta\omega)$	phase noise at frequency offset $\Delta\omega$	dBc Hz^{-1}
\mathcal{L}	column of differential operators	
\mathcal{R}	Rayleigh dissipation function	J
\mathcal{S}	surface	m^2
\mathcal{T}	kinetic energy	J
\mathcal{V}	volume	m^3
\mathcal{U}_{in}	internal (or strain) energy	J
\mathcal{W}_{ex}	external work	J
A	surface	m^2
\mathbf{A}	complex amplifier gain	
C_0	nominal capacitance	F
C_{11}, C_{12}, C_{44}	stiffness coefficients	Pa

Symbol (continued)	Description	Unit
C_{dec}	decoupling capacitance	F
C_{ijk}	third-order stiffness coefficients	Pa
E	Young's modulus	Pa
\mathbf{E}	Green-Lagrange strain tensor	
F	force	N
F_0	forcing amplitude	N
G	shear modulus	Pa
G_A	amplifier gain	
G_R	resonator gain	
I	second moment of area	m^4
J	dilatation factor	
L	inductance	H
\mathbf{K}	stiffness matrix	
\mathbf{M}	mass matrix	
M	moment	N m
M_T	thermoelastic moment	N m
M_{xx}	bending moment	N m
N_0	initial axial force	N
N_{xx}	axial force	N
N_T	thermoelastic axial force	N
P	power	W
Q	Q-factor	–
Q_x	shear force	N
R	resistance	Ω
\mathbf{R}	complex resonator gain	
S	S-parameters	
S	entropy	J K^{-1}
S_{11}, S_{12}, S_{44}	compliance coefficients	Pa^{-1}
T	absolute temperature	K
	time function	s
T_e	excitation period	s
\mathbf{T}	matrix with thermal time constants	
	surface force vector	N m^{-2}
V_0	voltage amplitude	V
V_{ac}	ac excitation amplitude	V
V_{dc}	dc bias voltage	V
V_{out}	output voltage	V
V_{pi}	pull-in voltage	V
W	basis function for transverse displacement field	
Y	admittance	S
Z	impedance	Ω

Symbol (continued)	Description	Unit
a	amplitude	m
a_1, a_2, b_1, b_2	complex voltage waves	V
a_i, b_i	roots of the Timoshenko frequency equation	
b	beam thickness	m
	(lumped) damping	N s m ⁻¹
c	coefficient, model parameter	
c_p	heat capacity per unit volume at constant pressure	J kg ⁻¹ K ⁻¹
c_L	longitudinal wave propagation velocity	m s ⁻¹
d_0, d_1, d_2	electrode gaps	m
e	dilatation	–
f	frequency	Hz
f_0	nominal or natural frequency	Hz
f_e	excitation frequency	Hz
\mathbf{f}	force column or vector	
\mathbf{g}	column of forcing functions	
h	beam width	m
i	current	A
k	(lumped) stiffness	N m ⁻¹
	thermal conductivity	W m ⁻¹ K ⁻¹
k_B	Boltzmann's constant	J K ⁻¹
k_s	shear correction factor	–
l	beam length	m
n_T	number of periods	
\mathbf{n}	outward normal vector	
p	pressure	Pa
p_i, q_i, r_i	generalised coordinates	
q	forcing parameter	N kg ⁻¹
q_e	electric charge	C
\mathbf{q}	column with mechanical degrees of freedom	
\mathbf{r}	column with thermal degrees of freedom	
t	time	s
t_{ij}	thermodynamic tension	Pa
u, v, w	displacements	m
\mathbf{u}	displacement vector	m
v	voltage	V
\mathbf{v}	column of state variables	
w	width	m
w_0	transverse deflection	m
w_{mid}	midpoint displacement	m
x	state	
x, y	oscillator states	
x, y, z	cartesian coordinates	m
\mathbf{x}	state column	

Symbol (continued)	Description	Unit
\mathbf{x}_e	equilibrium point	
\mathbf{x}_p	periodic solution	

Greek symbols

Symbol	Description	Unit
Θ	basis function for thermal field	
Φ	basis function for shear deformation field	
Φ_T	monodromy matrix	
α	thermal expansion coefficient	K^{-1}
α_i, β_i	roots of the Timoshenko frequency equation	
β	thermal modulus	$Pa K^{-1}$
γ	nonlinearity parameter for cubic stiffness	$m^4 s^{-2}$
γ_{ij}	Green-Lagrange shear strain component ($i \neq j$)	–
ϵ_0	permittivity of vacuum	$F m^{-1}$
ϵ_{ij}	infinitesimal linear strain component	–
η	electromechanical coupling coefficient	$V F m^{-1}$
η_{ij}	Green-Lagrange normal strain component ($i = j$)	–
θ	temperature difference	K
λ	eigenvalue	$rad s^{-1}$
	floquet multiplier	
λ_c	critical floquet multiplier	
λ_i	roots of the Euler-Bernoulli beam frequency equation	
	principal stretch	–
μ	bifurcation parameter	
ν	Poisson's ratio	–
ξ	non-dimensional damping coefficient	–
π_1	longitudinal piezoresistive coefficient	Pa^{-1}
ρ	density	$kg m^{-3}$
ρ_0	resistivity	Ωm
σ	stress tensor	Pa
σ	frequency detuning	Hz
σ_0	initial axial stress	Pa
σ_e	surface charge density	$C m^{-2}$
σ_{ij}	normal stress component ($i = j$)	Pa
τ	thermal relaxation time	s
τ_{ij}	shear stress component ($i \neq j$)	Pa
ϕ	eigencolumn	
ϕ	phase	rad

Symbol (continued)	Description	Unit
φ	shear deformation	—
$\boldsymbol{\varphi}, \boldsymbol{\psi}$	basis functions	
ψ	rotation	rad
ψ_A	amplifier phase	rad
ψ_R	resonator phase	rad
ω	angular frequency	rad s^{-1}
ω_0	nominal or natural angular frequency	rads^{-1}

Indices

Symbol	Description
0	nominal, natural, initial
E	Euler-Bernoulli
S	adiabatic
T	Timoshenko
	isothermal
a	anchor
ex	external
ij	stress/strain directions
in	internal
m	motional
max	maximum
nc	non-conservative
p	parasitic
s	parasitic
th	thermal, thermoelastic
tot	total
x	x -direction
y	y -direction
z	z -direction

Acronyms

BAW	bulk acoustic wave
BEM	boundary element method
CAD	computer-aided design
CF	cyclic fold
CFD	computational fluid dynamics
CMOS	complementary metal oxide semiconductor
DRIE	deep reactive ion etching
DOF	degree-of-freedom
FCC	face centered cubic
FD	finite difference
FE	finite element
FEM	finite element method
FET	field effect transistor
IC	integrated circuit
LP	limit point
MEMS	microelectromechanical system
MST	microsystems technology
ODE	ordinary differential equation
PCB	printed circuit board
PD	period doubling
PDE	partial differential equation
PLL	phase-locked loop
RHS	right-hand side
SAW	surface acoustic wave
SOI	silicon-on-insulator
SOLT	short-open-load-trans
TCAD	technology computer-aided design
VCO	voltage controlled oscillator

CHAPTER ONE

Introduction

Abstract / In this chapter, a general introduction for the thesis is presented. An overview of important demands and requirements for multiphysics modelling of dynamics in MEMS or microsystems serves as the motivation for the work in this thesis and will lead to the research objectives. Furthermore, an outline of the thesis is given.

1.1 General introduction

During the past 25 years, miniaturisation of mechanical parts has seen an increasing number of applications in industrial and medical fields. This has already been envisioned – “There’s plenty of room at the bottom” – by Feynman (1960) (reprinted in Feynman (1992) and Feynman (1993)) and it has opened the door for a new engineering discipline called *microsystems technology (MST)* or *microelectromechanical systems (MEMS)*¹. This discipline has emerged from a combination of IC-processing (Integrated Circuit) and conventional miniaturised fabrication technologies. A characteristic feature of MEMS is that they form a field in engineering in which multiple physical domains (mechanical, electrical, thermal, fluidic, optical, magnetic and chemical) meet each other. The term MEMS refers to devices that have a characteristic length of less than 1 mm but more than 1 μm , that combine electrical and mechanical components and that are fabricated using integrated circuit batch-processing technologies.

The trend of miniaturisation has been initiated by the following two facts. Firstly, on a small scale, systems and components perform differently, simply because of their small size. For instance, this is due to low weight and/or different energy efficiency. The multiphysics interaction between the physical domains is a direct result of the scaling of the systems (see Gad-el Hak, 2002; Allen, 2005). Moreover, these systems explicitly make use of physical effects at small scale, such as negligible influence of gravity or more effi-

¹The discipline is called *microsystems technology* in Europe, and *microelectromechanical systems* in the United States, but nowadays, mostly the term MEMS is used.

cient chemical reactions. Secondly, the manufacturing process of MEMS provides unique possibilities. Due to the small size, material costs are very low, and materials can be used that would otherwise result in prohibitive costs. Technology from IC-fabrication processes can be used to allow production of miniature components in large volumes for low prices. In this way, distributed systems with numerous components can be realised.

Unlike IC-technology and their explosive growth rate, the field of MEMS has shown a higher diversity and a slower learning curve (Senturia, 2003). This is explained by the fact that technology is progressing at a very high rate, whereas on the other hand, the MEMS field features a huge technological diversity. The state of MEMS around 1980 was such that most of the activity was either in basic research (materials, sensing/actuation methods and phenomena at micron scale) or the engineering science associated with the technology and devices themselves (materials, process technology, integration methodologies and system design). Relatively little effort was devoted to actual products (Senturia, 2003). More than 20 years later, products now dominate the field of MEMS, supported by continuing and expanding efforts in the engineering science domain. However, the basic research has not grown to keep pace. Rather than having reached maturity, the MEMS field has not yet evolved from the initial trial and error approach. The ratio of commercially successful MEMS to the total of prototype devices created as part of research and development efforts also reflects this (Bell et al., 2005).

Furthermore, as design complexity increases and reliability becomes a more important issue, increasingly detailed knowledge about coupled-physics phenomena is necessary. A solid foundation of the underlying multiphysics fundamentals is needed in the MEMS field. Fabrication technology enables the designer to integrate many physical and chemical functions into a compact system. However, due to the small details in the miniaturised systems, one cannot assemble a microsystem from components off the shelf, in contrast to macrosystems. In microsystems, all components have to be designed during the design process of the whole system. Component design is an integral part of the complete system design and can, therefore, not be separated from system design. Although the basis for the production techniques of MEMS has been developed over the last decades, the full technological potential of MEMS is far from understood.

Principal reasons for this are that MEMS are not only characterised by the small size of the systems, but also by the requirement of a multidisciplinary design approach, by the integration of many functions in a single system and by the potential of mass fabrication. As a result, microsystems design is an integral process, which requires knowledge of system aspects ranging from mechanics and fluidics to thermodynamics and electronics (Senturia, 2001; Kaajakari, 2009). Microsystem designers must have a large number of skills and a broad experience. Furthermore, microsystems design requires knowledge of fabrication technology to meet knowledge of the particular application of the system.

This poses a very demanding task on the designers, requiring intimate knowledge of the whole system, but it also means that for each particular application, the design process has to be started all over again. Currently, microsystems design is mainly rooted in electronics. However, for both their applications and design, it is necessary that their design scope is broadened and that all relevant disciplines are included throughout the

design process. Although the physical basics and phenomena of the separate disciplines in MEMS have been investigated for a long time, understanding, experimenting with and modelling of all these aspects interacting at micro-scale is a very demanding challenge for science and engineering disciplines in the 21st century.

Research on MEMS can be categorised in two main groups. Firstly, production techniques and manufacturing principles are investigated. Secondly, multiphysics analysis and behavioural modelling is performed. The first category will not be discussed in this thesis. The interested reader is referred to, for instance, Senturia (2001), Gad-el Hak (2002) and Maluf and Williams (2004). This thesis deals on the latter category and will address the fundamentals, modelling and design of MEMS. The work will concentrate on the modelling of dynamics in MEMS in a multiphysics context, see also Section 1.2.3.

1.2 Modelling of MEMS

As has become clear from the previous section, the modelling of MEMS provides a very challenging task in microsystems engineering. Two important aspects related to this task are the multiphysics nature of MEMS and the abstraction levels at which models are developed. These topics will be described in the next two sections. In a subsequent section, modelling with respect to dynamics in MEMS will be addressed. The modelling considerations will lead to a list of model requirements that will provide the motivation for the work presented in this thesis.

1.2.1 Multiphysics modelling

The field of research is inherently multiphysical of nature, since different physical phenomena are tightly intertwined at microscale. Typically, up to four different physical domains are usually considered in the analysis of microsystems: the mechanical, the electrical, the thermal and the fluidic domain (Senturia, 2001; Gad-el Hak, 2002). For each of these separate domains, well-established modelling and analysis techniques are available. However, due to tight coupling between the domains at microscale, they should not be considered separately. This greatly increases the complexity of microsystem design problems because all disciplines involved have to be incorporated in simulation models.

Of the important challenges in micromechanical modelling, two appear to be most significant (Senturia, 1998). The first is the critical step of connecting the behaviour of the continuum, as expressed in, for instance, highly meshed simulations, to equivalent lumped or reduced-order models that can be used efficiently for system-level design and modelling. Secondly, non-steady-state dissipative behaviour has to be incorporated into a modelling environment, without making unacceptable inaccurate assumptions or simplifications. The reason why modelling and simulation for microsystems is important, is obvious: computational prototyping, when sufficiently precise and fast, is far more economical than physical prototyping, as it can shorten the design cycle and reduce the time-to-market.

Due to scaling in microelectromechanical devices, effects that normally remain hidden in the macro-world can show up or even become dominant in microscale devices. Effects that are negligible at macroscopic level may be important at microscopic level and vice versa. For instance, for systems with smaller dimensions, the effect of gravity decreases, while, simultaneously, the importance of surface effects increases. Therefore, common reasoning, based on experience at macroscopic level is no longer valid; rules of thinking may have to be modified. However, the boundary between the macroscopic and microscopic levels is not sharp, but depends on the effects to be considered (Wautelet, 2001).

Additionally, there is a large difference between energy domains in which energy is strictly conserved (like ideal elasticity, electromagnetic fields in linear, lossless media, and ideal hydraulics) and those that have intrinsic dissipation mechanisms (fluidic viscosity, friction, heat flow, viscoelasticity and hysteresis). It is important to discern between these energy domains because there is a major difference in their modelling. For instance, in order to describe dynamical behaviour in conservative domains, forces can be expressed as gradients of suitable (potential) energy functions. In the dissipative energy domains, however, time-dependency is important as the dissipation depends explicitly on the motion of the device considered. As a result, this poses much higher demands on the complexity of the modelling and simulation tools.

According to Lin and Wang (2006), two groups of studies can be identified for the research in the field of microsystems modelling. The first group focuses on the introduction of new designs or on the demonstration of new ideas. This group uses simple analytical models (lumped or distributed) or generic finite element software to predict behaviour of microdevices and compares this with experiments. Most of the analysis and prediction methods are directly borrowed from the individual disciplines involved, such as linearisation, perturbation, energy methods and direct numerical integration. The second group, on the other hand, mainly pays attention to the modelling of devices and to predicting their dynamic behaviour. The modelling is considered the goal of the research in this area, whereas the actual realisation of devices is considered to be less important.

The work presented in this thesis will mainly be rooted in the second group. However, the modelling will not be considered as the goal per se. Experimental verification will form an important and integral aspect of the work.

1.2.2 Modelling levels

The modelling and analysis of MEMS may take place on various levels of abstraction, see Senturia (2001). In Figure 1.1, a simplified overview of these levels is depicted. Note that this representation is specific for modelling and analysis. Other representations, containing different (or more) dimensions of abstraction, such as the size of the (sub)system, are also possible.

Four modelling levels can be identified in Figure 1.1: System, Device, Physical and Process level. A movement to the right in the figure corresponds to a decrease in abstraction level. Iterative exchange of information takes place between the various modelling levels.

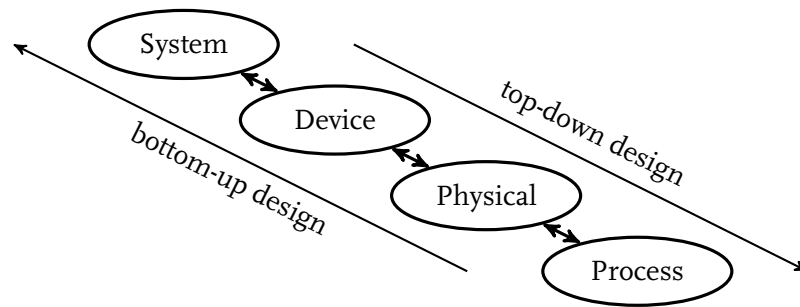


Figure 1.1 / Different modelling levels for MEMS (based on Senturia (2001)).

Furthermore, both at and across the modelling levels, simulation and (experimental) verification takes place. Finally, a top-down or bottom-up design approach is possible. The different modelling levels and the flow across them will be treated in the next sections.

Process level

On the process level, the process sequence and the lithography masks for device manufacture are created. This is a highly numerical activity (Senturia, 2001) for which several commercial tools have been developed, generally referred to as technology CAD (TCAD). These tools can predict device geometry from the masks and process sequence. In this work, the process level is the only level which will not be considered.

Physical level

The second level in microsystem design is the physical level, which describes the full behavior of the three-dimensional continuum. Governing equations here are typically partial differential equations (PDEs). Analytical methods can be used to find closed-form solutions for ideal geometries, but the modelling of more realistic microstructures is often only possible with help of highly meshed 3D simulations. These models tend to have a large number of degrees of freedom (DOFs) and consist of a combination of process (see the process level), material and structural modelling. Due to the number of disciplines interacting with each other, analytical analysis is either impossible or very cumbersome. As a result, simulations in this modelling level are certainly necessary, but are impractical for rigorously analysing (dynamic) behaviour of complete microstructures and their dependency on physical parameters. Typical methods applied here are three-dimensional, for instance, finite element (FEM), boundary element (BEM), computational fluid dynamics (CFD) and finite difference (FD) methods. For each of these fields, special optimised packages are available but coupling between them can still be difficult. However, nowadays, software packages with multiphysics capabilities appear².

²For instance, finite element packages COMSOL Multiphysics (www.comsol.com) and ANSYS (www.ansys.com).

Device or component level

The device level is the third abstraction level in Figure 1.1 and corresponds to the domain of, for instance, circuit and ODE (ordinary differential equations) simulators. Due to limitations in computer resources, it is impractical to use highly detailed device level models for simulating a complete microelectromechanical device. Instead, low(er)-order behavioural models of the various components or disciplines involved in the device are required. Typically, these consists of systems of ODEs, describing the dynamic behaviour. This is often referred to as macromodelling or reduced-order modelling. In general, three different methods can be applied to create reduced-order models (see Lishchynska et al., 2004). Going from an analytical to a more numerical approach, these are:

- analytical derivation by applying model reduction or approximation techniques, starting from PDEs and first principles;
- descriptive (heuristic) modelling by means of simplified models with an a priori defined complexity;
- model extraction from dedicated and well-chosen numerical simulations (for instance, FEM).

Depending on the type of modelling applied, models are generated that are still near to physics, since they capture the essential physical behaviour of the component, while, at the same time, they are compatible with the system level model at the highest abstraction level. Reduced-order modelling allows the designer to determine parameter values and load and boundary conditions for individual components or subsystems. It is used to represent both static and dynamic behaviour to an acceptable level of fidelity.

System level

System level modelling is the highest, and most abstract level of modelling. This level requires linking of various device (or component) level models – both electronic and micromechanical – into a microelectromechanical system. Typically, block-diagram descriptions and lumped-element circuit models for components are connected into a full system. Mostly, this description is used for functional analysis of a design concept.

Top-down or bottom-up design approach

In general, two different design approaches are possible for designing and creating new devices (see Figure 1.1). Within these approaches, some iteration usually takes place, but this will not be elaborated further.

In the top-down approach, first at system level, critical design parameters in the design space are determined. This can be done without giving much thought to which technology will be used and how implementation will take place. This is more or less a

conceptual design phase. Once critical design parameters have been determined, focus is shifted to examining implementation options and specific technologies through the use of device or component level models. In this step, the system is decomposed into components which are analysed by reduced-order models or even physical models. After some iterations between the last two steps, prototyping (process level) and testing of the new device can start.

In the bottom-up approach, a designer has a new idea for a microelectromechanical application and starts with performing the necessary process and physical simulations to determine device characteristics and to generate data necessary to create a reduced-order model. Next, reduced-order modelling of the device is performed, together with the necessary control and sensing circuitry to see how the component functions at device level. Finally, system level modelling is conducted to determine the potential impact the device will have on the whole system.

1.2.3 Modelling for dynamics

As stated in Section 1.1, the research presented in this thesis will address multiphysics analysis and behavioural modelling in MEMS. The modelling approach will be developed from a mechanical point of view with a strong focus on dynamics. The dynamic effects in MEMS, that is, their spatio-temporal behaviour, is intrinsically nonlinear due to the small size of the microstructures and due to multiphysics coupling between the physical fields. For instance, nonlinear systems typically do not satisfy the superposition principle in terms of input-output. The nonlinear dynamical effects in MEMS will be investigated by means of modelling and simulation, together with experimental validation. Ultimately, this will lead to a predictive modelling approach for addressing these effects. A graphical representation of the focus of the research in this thesis is depicted in Figure 1.2.

On the left-hand side of Figure 1.2, the MEMS research field is depicted. As already described in Section 1.1, two main research topics can be distinguished here: investigation of production and manufacturing techniques and multiphysics modelling. On the right-

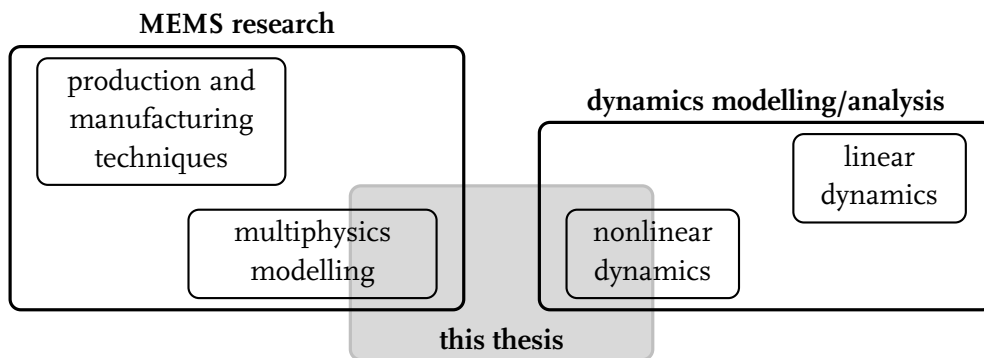


Figure 1.2 / Research focus of the thesis: nonlinear dynamics modelling for MEMS in multiphysics context.

hand side of Figure 1.2, the dynamics modelling/analysis field is depicted. Both linear and nonlinear dynamics topics are shown here. Actually, the topic of linear dynamics may result from linearisation of the nonlinear dynamics of a system under investigation around a certain operating point. As will become clear from Section 2.4, typical phenomena that are considered in the nonlinear dynamics field are equilibrium points, periodic solutions and their bifurcations.

The focus of the work in this thesis is depicted in the grey box in Figure 1.2: the work will combine modelling and analysis for nonlinear dynamics with multiphysics modelling for MEMS. This line of approach will be applied at and across the various modelling levels depicted in Figure 1.1.

1.2.4 Model requirements

The technologies for fabricating a wide variety of MEMS devices have developed rapidly during the past ten years (Senturia et al., 1997; Senturia, 2003), but computational tools that allow engineers to design and optimise MEMS have not kept pace. This forces MEMS designers to resort to expensive physical prototyping, which might result in an unacceptably long product development cycle or unnecessarily conservative designs.

Therefore, in the MEMS field, there is a need for computational analysis and design tools, which are efficient, accurate, versatile and applicable to practical design problems. Especially for the modelling with respect to (nonlinear) dynamics at the device or component level, where reduced-order models are extracted from the physical level (see Figure 1.1), mathematical expressions and functional relations for the description of the device are needed. Important requirements for these models are the following (Senturia, 1998, 2001). The models should:

- be in an analytical or functional representation, such that reasoning about the effects of design changes is possible, without resorting to (FEM) simulations at the physical level again;
- capture all the essential device behaviour in, preferably, only a few degrees of freedom;
- permit rapid calculation and insertion into system level simulation models;
- obey the laws of thermodynamics where appropriate, conserving energy in accordance with the first law and dissipating energy in accordance with the second law;
- exhibit correct dependencies on device dimensions and material properties;
- represent quasistatic and dynamic behaviour for both small- and large-amplitude excitations;
- be sufficiently accurate, when compared with experiments on suitable test devices and with fully meshed 3D simulations, to permit the designer to proceed with confidence that the final design will behave as expected.

These requirements relate to the two main goals of models that are used as analysis and design tool. They can be used for gaining insight in physical aspects that play a role for MEMS devices and they can be used as a predictive modelling tool. Once the model requirements are met, MEMS design can come to its full potential by combining both simulations and experiments in the most effective way.

1.3 Research objectives and outline

Based on the insights from Section 1.2, the research objective for this thesis can be formulated. It has become clear that one of the main challenges in the multiphysics field of microsystems engineering is to connect models for describing the nonlinear dynamical behaviour of the devices or components in each of the involved physical domains to equivalent lumped or reduced-order models without making unacceptably inaccurate assumptions and simplifications (which are often application dependent). This requires correct and efficient coupling between the involved physical domains.

The main research objective of the work in this thesis is to address the model requirements of Section 1.2.4 by means of modelling approaches on the various levels in the design of MEMS, see Figure 1.1. The approach is aimed at multiphysics modelling for nonlinear dynamics in MEMS, see Section 1.2.3.

Furthermore, the research will focus on the dynamical behaviour of a specific class of microsystems: microelectromechanical resonators, or MEMS resonators³. These resonators provide a promising alternative for quartz crystals in time reference oscillators, due to their small size and on-chip integrability, see Nguyen (2005) and Nguyen (2007). However, because of their small size, they have to be driven into nonlinear regimes in order to store enough energy for obtaining an acceptable signal-to-noise ratio in the oscillator (Kaajakari et al., 2004a). Since these resonators are to be used as a frequency reference in oscillator circuits, their steady-state (nonlinear) dynamic vibration behaviour is of special interest, see the research focus depicted in Figure 1.2.

A heuristic modelling approach is investigated for two different MEMS resonators, a clamped-clamped beam resonator and a dog-bone resonator. For the clamped-clamped beam resonator, the simulations with the proposed model shows a good agreement with experimental results, but the model is limited in its predictive capabilities. For the dog-bone resonator, the proposed heuristic modelling approach does not lead to a match between simulations and experiments. Shortcomings of the heuristic modelling approach serve as a motivation for a first-principles based approach.

A multiphysics modelling framework for nonlinear dynamics of MEMS resonators will be derived that mainly takes place on the physical and device level in microsystem design, see Figure 1.1. The modelling philosophy and the essence of first-principles based modelling that underlie the framework will be explained. Also, the differences with heuristic

³Although the term MEM resonator would be grammatically correct, the term MEMS resonator is commonly used.

modelling will be addressed. The framework is intended for fast and accurate simulation of the steady-state nonlinear dynamic behaviour of MEMS resonators. Moreover, the multiphysics model is validated by means of experiments. Although the multiphysics modelling framework is proposed for MEMS resonators, it is not restricted to this application field within microsystems engineering. Other fields, such as (resonant) sensors, switches and variable capacitors, allow for a similar modelling approach.

The proposed semi-analytical (i.e. analytical-numerical) modeling framework is illustrated for a full case study of an electrostatically actuated single-crystal silicon clamped-clamped beam MEMS resonator. The first-principles based approach allows for addressing the relevance of individual multiphysical effects in a straightforward way, such that the models can be used as a (pre-)design tool for dynamic response analysis. The semi-analytic approach can be considered to be complementary to conventional finite element simulations. It is suitable for fast (preliminary) analysis of microdevices in order to determine influences of various multiphysical effects. Therefore, the approach is relevant and important for simulation of MEMS, since fast and accurate computational prototyping may greatly shorten the design cycle and thus the time-to-market of new products.

The work presented in this thesis can be categorised into the modelling levels described in Section 1.2.2. Figure 1.3 shows a schematic overview of these modelling levels and shows the positioning of most of the remaining chapters of the thesis. The outline is as follows.

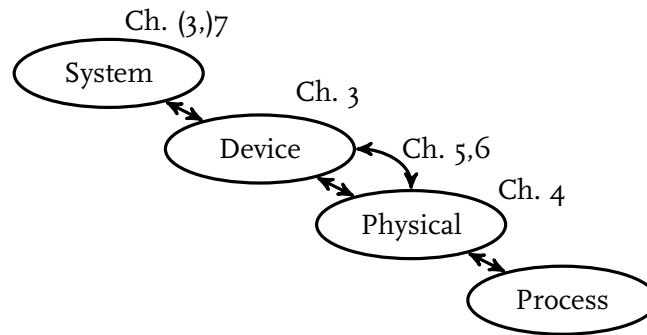


Figure 1.3 / Outline and positioning of the work within the different modelling levels.

First, in Chapter 2, relevant background information on MEMS resonators and oscillator circuits will be given. Furthermore, since a nonlinear dynamics point of view is used in the modelling approach, some important aspects of the steady-state behaviour of nonlinear dynamic systems will be described.

Next, in Chapter 3, (partly) heuristic device level models will be proposed for two case studies: a clamped-clamped beam MEMS resonator and a dog-bone MEMS resonator. The models will be verified by experiments. Shortcomings and limitations of heuristic modelling will serve as the motivation for the next chapters.

In Chapter 4, the general multiphysics modelling framework for dynamics in MEMS will

be proposed (this will take place on the physical modelling level). The philosophy behind first-principles based modelling will be described. Next, relevant disciplines and physical phenomena, some of which are specific for MEMS, will be discussed and the general approach for deriving the reduced-order models will be described.

Next, the modelling framework will be applied to a case study of a clamped-clamped beam MEMS resonator in Chapter 5. The resonator is similar to the one investigated in the first case study in Chapter 3. Model assumptions will be elaborated and a detailed derivation of models of varying complexity will be given. In this way, device level models are constructed from physical level models. Furthermore, a simulation study will be presented, in which the influence of individual nonlinear effects is investigated.

Chapter 6 contains the description of the experimental set-up. Furthermore, the measurement techniques and the model parameter identification will be described which will be used for a thorough experimental validation of the model(s) of Chapter 5.

In Chapter 7, the heuristic device level model for the clamped-clamped beam MEMS resonator, the first case study in Chapter 3, will be included in a system level simulation model that uses the nonlinear MEMS resonator in an oscillator circuit. A technique, called phase feedback, will be proposed, which allows for using the nonlinear MEMS resonator in a feedback circuit while the resonator operates in its nonlinear regime. Various aspects of phase feedback will be investigated.

Finally, in Chapter 8, the main conclusions will be summarised and recommendations for future work will be given.

CHAPTER TWO

Background information

Abstract / Some background information on various subjects is presented in this chapter. It gives an overview of oscillator circuits and their key properties. A historical overview of developments in the field of micromechanical resonators is presented together with a description of their application fields. The chapter ends with some concepts and tools for investigating the steady-state behaviour of nonlinear dynamic systems.

2.1 Introduction

The research presented in this thesis focuses on microelectromechanical resonators that are used as a frequency reference in the oscillator circuits. Conventionally used mechanical quartz crystals provide high stability and exceptional precision as resonators. Over the years, they have obtained a well-established position in, for instance, communications and sensing applications, ranging from aerospace and industrial to consumer and automotive field. However, the ongoing trend of miniaturisation in industry demands for resonators and oscillators with ever decreasing dimensions. The major drawback of quartz crystals is that they are rather bulky in size and have poor integrability with IC-technology. Their millimeter to centimeter size makes them only available as separate packages which have to be matched to other IC components on a PCB.

Silicon micromechanical resonators provide an interesting miniature alternative for quartz crystals in time reference oscillators. Due to their small size and on-chip integrability, they have a very promising application potential that may ultimately lead to the design of a single-chip radio. With respect to oscillator applications, micromechanical resonators and quartz crystals mainly differ in their power handling capabilities (see Lin et al., 2004). The larger quartz crystals are capable of handling much higher power than their tiny micromechanical counterparts. As a result, micromechanical resonators may be driven into nonlinear operation regimes more easily. For oscillator applications, their steady-state (nonlinear) dynamic vibration behaviour is of interest, being one of the main properties that determines oscillator performance.

In the following sections, background information on several subjects will be provided. First, in Section 2.2, an introduction to MEMS resonators and their application possibilities will be presented. Additionally, a historical overview of developments in this field will be given. Section 2.3 will provide background on one of the application fields of MEMS resonators: oscillator circuits. Both the working principle and the key properties of oscillator circuits will be described. Finally, since a nonlinear dynamics point of view (see Figure 1.2) will be utilised for the multiphysics modelling approach in the following chapters, relevant concepts for analysis of the steady-state behaviour of (nonlinear) dynamical systems will be introduced in Section 2.4.

2.2 MEMS resonators

Silicon integrated circuits have been used extensively in the field of digital circuitry since their discovery in the early 1960s. Since the 1970s, further progress in this field has been self-sustaining as already predicted in Nathanson et al. (1967). In other areas, one could similarly benefit from the capabilities of integrated circuitry, but the application of IC-technology has not progressed as rapidly.

Another area that has had a large benefit from integrated circuitry is the field of non-digital circuits. In order to use silicon integrated circuits in non-digital systems, a compatible tuning element – oscillator or resonator – is needed to couple the non-digital and the digital part (background on oscillators will follow in Section 2.3). Such a tuning device has to satisfy various constraints and properties, such as small size, capability of high Q -factor¹ and the possibility of batch fabrication conform the current IC-technology. The use of a mechanical resonator seems to offer a promising solution that can satisfy these constraints.

The first micromechanical resonant tuning device, compatible with silicon integrated circuits and able to solve the aforementioned tuning problem, has been documented by Nathanson et al. (1967). The authors describe a resonant gate transistor, which essentially contains three elements that are always present in (micro)electromechanical resonators:

1. an input transducer which converts an electric signal into a mechanical force;
2. a mechanical resonator, sufficiently isolated from the surroundings in order to obtain a high Q -factor;
3. an output transducer to sense the motion of the resonator and to convert this motion into a corresponding electrical signal.

The resonant gate transistor, described in Nathanson et al. (1967), consists of a metal (cantilever) beam electrode, clamped on one side to an insulating oxide and suspended

¹The Q -factor is a measure for energy loss in a system. It can be defined as the ratio of the total energy stored in a system to the sum of the energy losses per cycle.

over a silicon slice. The input transducer is an insulated plate at the end of the beam, which exerts an electrostatic force on the beam. At the mechanical resonance frequency of the beam, appreciable vibration occurs. The motion of the beam is detected as a variation in the field-effect induced charge in the channel region of a MOS-type (Metal Oxide Semiconductor) detector under the middle of the beam. Output is extracted as the 'drain' of this FET-like (Field Effect Transistor) element. The cantilever beam has a characteristic length of around 0.5 mm, a thickness ranging from 3 to 8 μm and electrode gaps in the order of 10 μm , yielding a mechanical resonance frequency in the range from kHz to MHz.

The project on the resonant gate transistor was abandoned due to low Q -factors, high temperature coefficients of frequency and aging of the metal films (Lin et al., 1992).

2.2.1 Research overview

After the first introduction of micromechanical resonators, described above, interest in micromechanical resonators was renewed in the mid 1980s and, since then, the applications of micromechanical resonant elements have been ever increasing and they have been of great interest for an ever expanding range of applications. The research history in the field of microelectromechanical resonators can conveniently be represented in a graphical overview, see Figure 2.1. This figure gives a partial overview of the research that has followed after the paper of Nathanson et al. (1967). The vertical direction corresponds to the time line. In the columns, the research contributions have been grouped into three main application fields for microelectromechanical resonators: sensors, filters and resonators for oscillators. These three fields will briefly be discussed next, based on a number of selected publications. Several important contributions will be listed and key papers have been indicated by boxes in Figure 2.1.

Resonant sensors

Research in the field of microelectromechanical resonators has started at the sensor side, which is the biggest field of application. Resonant sensors, configured to have a mechanical resonance frequency or relative phase with respect to the measurand, have an advantage over conventional analogue sensors, see Langdon (1985) and Gast (1985). Namely, their output can be measured directly in digital systems by pulse counting. For this reason, resonator sensors are often referred to as being semi-digital in nature. The frequency output of the resonator can easily be transmitted over large distances without any error. Moreover, such a signal is much less susceptible to noise and interference than non-periodic signals, and can be recovered using filtering or phase-locked-loop techniques (Middelhoek et al., 1988).

The frequency change of resonant sensors can be caused by various effects (Langdon, 1985). For instance, variable stress or tension in a resonator structure may change the resonance frequency. In this way, a stress dependent output signal is obtained. This stress can be produced by a diaphragm (pressure sensor) or a bending beam to make a

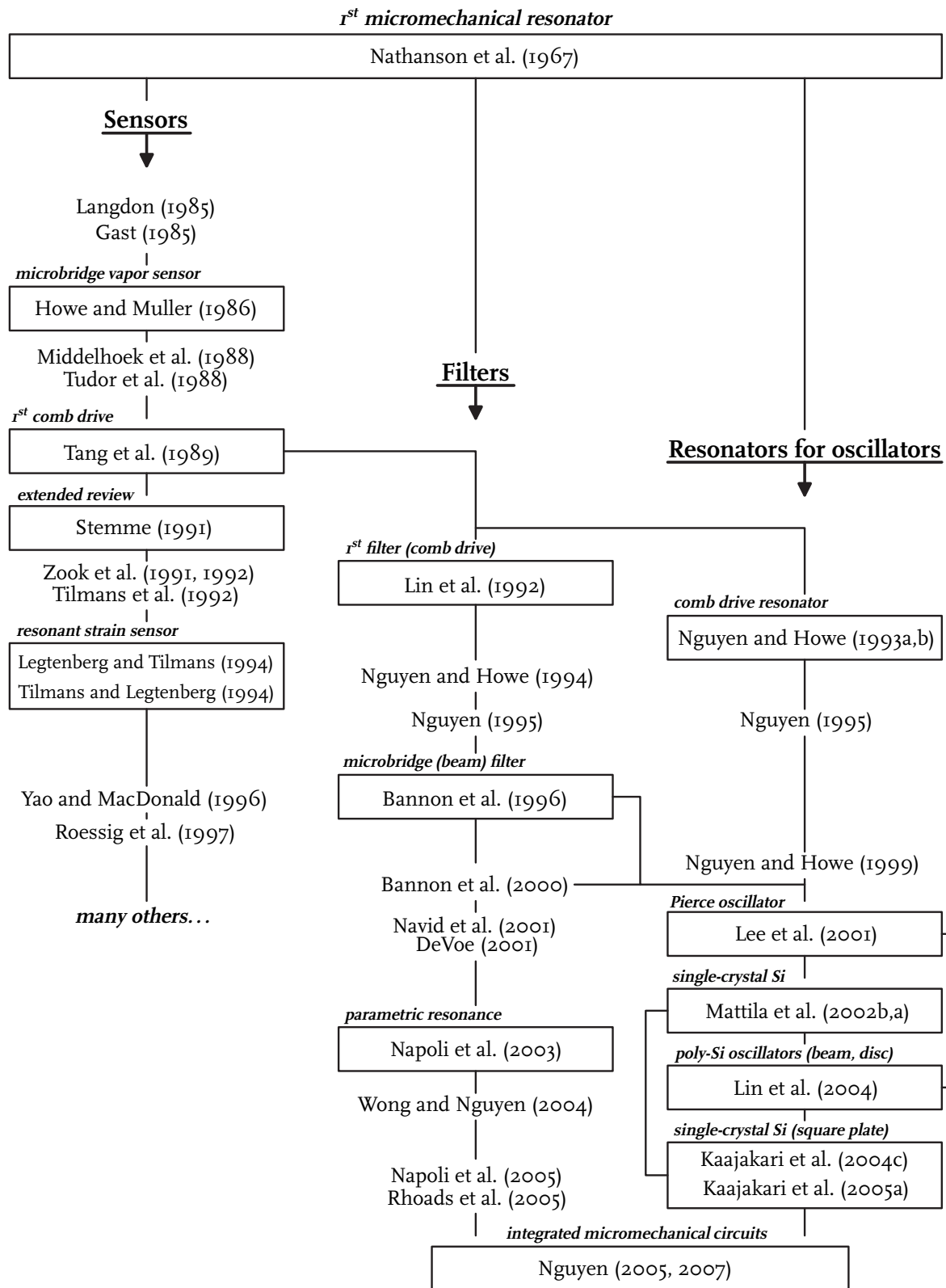


Figure 2.1 / Overview of the research in the field of micromechanical resonators.

load cell. Additionally, other parameters associated with mechanical resonance, like mass and damping, can be used to make measurements. For instance, the decay time of the transient mechanical vibration of a resonator in a liquid depends on the viscosity of the surrounding medium. Added mass effects due to the liquid can also be measured from frequency changes, yielding information on the fluid density. Fluid velocity or surface acoustic waves can be measured from phase differences between two sensing elements placed close to each other. Finally, since both the elastic parameters and the density of a resonator are temperature dependent, the frequency of a resonator is intrinsically a function of temperature.

The first micromechanical sensor, a microbridge vapor sensor, was documented in Howe and Muller (1986). The resonant element of this sensor is a polymer-coated polycrystalline silicon microbridge.

The mechanical performance of resonators can be described by several key parameters (Tudor et al., 1988). These include, but are not limited to, the mode shape, nonlinearity, mode coupling, the quality factor Q , the intrinsic sensitivity to temperature and the sensitivity to the measurand. A more extensive list of undesirable parameters is included in Middelhoek et al. (1988) and contains drift, offset, time dependence, non-repeatability, cross-sensitivity to temperature and strain, hysteresis, low resolution, low sensitivity, unsuitable output impedance, self-heating and unsuitable frequency response. The nature of these properties shows that resonator sensor design requires engineers to have an intimate knowledge of several closely related disciplines.

Three years after Howe and Muller (1986), the first comb drive resonator was described in Tang et al. (1989). They described a polysilicon resonator, consisting of an interdigitated finger (or comb) structure that is driven electrostatically, for a virtually linear actuation. This device has served as the basis for the two other fields of application of micromechanical resonators. Both the first micromechanical filter (Lin et al., 1992) and the first oscillator (Nguyen and Howe, 1993a,b) have been based on Tang et al. (1989), see Figure 2.1.

From the early 1990s, interest in resonant sensors has been growing rapidly. Many researchers have acknowledged the potential of resonant sensors having semi-digital output signals (Hauptmann, 1991; Stemme, 1991; Zook et al., 1991, 1992), especially for the rapidly developing IC technology. Stemme (1991) has presented an extended review on the various aspects that play a role in resonant silicon sensors.

The paper of Stemme (1991) also served as a basis for the resonant clamped-clamped beam strain sensor, described in Tilmans et al. (1992), Legtenberg and Tilmans (1994) and Tilmans and Legtenberg (1994), a few years later. These authors treat flexural polysilicon resonators that are encapsulated in vacuum. From then, numerous different resonator layouts have been proposed (see for instance Yao and MacDonald, 1996; Roessig et al., 1997) and many publications have followed.

Electromechanical filters

A second field of application for microresonators is to serve as a filtering element in circuits. Micromechanical resonators typically can be used for electromechanical filtering, HF (high-frequency) signal processing and mixing. Already in Lin et al. (1992), a microelectromechanical filter has been demonstrated, based on coupled, lateral microresonators (Tang et al., 1989). This topology can be used to create band-pass filters. Other examples of a similar topology have been described in Nguyen and Howe (1994) and Nguyen (1995).

Device layouts other than comb drives have been used from 1996 onwards. For instance, in Bannon et al. (1996) and Bannon et al. (2000), coupled microbridges are used. Furthermore, in bandpass filtering applications, nonlinear effects may play an important role. In Navid et al. (2001), a third-order intermodulation distortion in a single capacitively-driven clamped-clamped beam micromechanical resonator is discussed. In DeVoe (2001), piezoelectric micromechanical resonators have been investigated for filtering purposes.

The latest developments include filters based on parametric resonance. In Napoli et al. (2003), it is suggested, based on numerical and experimental investigations, to use parametric resonance in a microcantilever beam for filtering and sensor purposes. Investigation of this effect is continued in Napoli et al. (2005), where coupled microcantilever beams are considered, in order to create a bandpass filter and in Rhoads et al. (2005), where a similar structure using comb drives is proposed.

Another example of filtering by means of microresonators is described in Wong and Nguyen (2004). In communication receivers, often both highly selective filtering and low-loss, low-noise mixing has to take place. Instead of having two separate or distinct components for this, these two functions can also be integrated into one single device. For this mixer-filter, or 'mixler', a similar design as in Bannon et al. (1996, 2000) is used.

Resonators for oscillators

The application field of resonators for oscillators has started from comb drive resonators in 1993. Practically, Nguyen (Nguyen and Howe, 1993a,b) has started this field of application and has continued this ever since (Nguyen, 1995; Nguyen and Howe, 1999). In Nguyen and Howe (1993a), a completely monolithic high- Q oscillator is described, which is fabricated via a combined CMOS (complementary metal-oxide-semiconductor) and surface micromachining techniques. The resonator itself is made of polysilicon and is both driven and sensed capacitively. In Nguyen and Howe (1993b), a similar oscillator design is proposed, with an additional possibility for stabilisation against temperature variations. A micro-oven technique is proposed for controlling and stabilising the center frequency of a microresonator. The design consists of a microresonator, suspended above a platform, whose temperature can be changed by on-platform heating resistors.

Since Nguyen (1995), more interest has been directed towards integration of mi-

micromechanical resonators into oscillator circuits. The high Q -factor of micromechanical resonators contributes to improved oscillator stability, but limited power handling capability might prevent the oscillators from achieving the required short-term stability, or may cause nonlinear dynamic effects in resonators (Kaajakari et al., 2004a). In Nguyen and Howe (1999), an extensive equivalent circuit analysis of a micromechanical resonator based oscillator is presented.

Up to 1999, the work on resonators for oscillators has mainly concentrated on comb-drive resonators having interdigitated or non-interdigitated combs ('overlapping' or 'non-overlapping' fingers, respectively). However, since then, research interest has also been directed towards other types of resonators. These other resonator layouts have been available from the sensors and filters application fields.

In Lee et al. (2001) a Pierce oscillator circuit has been proposed based on microbridge resonators from Bannon et al. (1996) and Bannon et al. (2000). This work on oscillator circuits has also continued for beam and disk resonators in Lin et al. (2004). All of these devices are based on poly-Si, the isotropic variant of silicon.

In Mattila et al. (2002a) and Mattila et al. (2002b), single-crystal Si resonator devices have been investigated. Both flexural and longitudinal resonators have been implemented in oscillator circuits whose closed-loop response has been analysed and measured. The phase noise response of these oscillators is found to be nearly as good as the one from conventional quartz crystal based oscillators.

Their research has been continued towards oscillators based on different type of resonators (square plate) in Kaajakari et al. (2004c) and Kaajakari et al. (2005a).

Integrated circuits

Finally, the developments in the application fields of filters and resonators have led to integration of micromechanical components into electronic circuits. From the three application fields described above, it has become clear that the benefits of resonators and vibrating microelectromechanical components go far beyond mere component replacement, whether this is a sensor, filter or resonator for an oscillator. In fact, resonators are increasingly becoming on-chip building blocks instead of discrete stand-alone devices (Nguyen, 2005, 2007). By connecting vibrating micromechanical structures into more general networks, so-called integrated micromechanical circuits, they will eventually be capable of implementing virtually any signal processing function, which is presently realised using transistors. Reviews of the integration possibilities and demands are documented in Nguyen (2005) and Nguyen (2007). Nowadays, a lot of research is directed towards resonators for oscillator purposes, which is also the topic of the research presented in this work. Background information on oscillator circuits will be given in Section 2.3.

2.2.2 Actuation and detection

The three different fields of application for microresonators (see Section 2.2.1) all require some resonator structure that is excited into vibration and subsequent detection of this vibration. As described in Stemme (1991) and Tilmans et al. (1992), six main types of excitation techniques can be distinguished, each with a corresponding vibration detection method. These are:

1. electrostatic excitation and capacitive detection;
2. dielectric excitation and capacitive detection;
3. piezoelectric excitation and detection;
4. resistive heating excitation and piezoresistive detection;
5. optical heating excitation and optical detection;
6. magnetic excitation and detection.

In contrary to macroscopic mechanical world, mechanical actuation and detection (displacement measurement) is not applied, since the structures under consideration are too small.

The research in this work will mainly be confined to the first actuation/detection principle. Electrostatic excitation combined with capacitive detection is an attractive approach for silicon microstructures because of simplicity and compatibility with micromachining technology (Tang et al., 1989; Tilmans et al., 1992). This actuation/detection principle has been used since the first micromechanical resonators (see also Nathanson et al., 1967). Therefore, it is used in the majority of the current research on microelectromechanical resonators. Additional background on the other methods can be found in Stemme (1991), Tilmans et al. (1992), Beeby (2004) and Kaajakari (2009).

For electrostatic actuation as well as for capacitive detection, two electrodes are used, which are located in close proximity to each other. One electrode is formed by (a part of) the vibrating structure and the other by a stationary surface. The driving load, an ac voltage across the electrodes, will result in an alternating force between the two plates, causing resonator vibration. From an electrical point of view, the pair of electrodes constitutes a capacitor, whose capacitance varies with the distance between the two electrodes. As a result, capacitive detection is based on the ac current that will be induced by the resonator vibration. For proper operation in terms of signal conditioning, it is required that the capacitor is dc-biased (Tilmans et al., 1992). Larger bias voltages may result in higher ac-currents, but may also change the (nonlinear) dynamic behaviour of a resonator significantly.

Capacitive excitation and detection is a very effective principle when resonators are operated in vacuum, avoiding air damping between the plates. However, the use of capacitive excitation and detection requires relatively large electrode plates and small electrode

gaps in order to achieve usable signal amplitudes for reasonably low excitation levels. A solution to this problem may be found in comb-drive resonators. Here, movement or vibration of the (non-)interdigitated combs results in change in the effective electrode area, rather than the electrode distance.

2.2.3 Resonator types

All MEMS resonators consist of some vibrating mechanical part, whose vibration results in deformation of (part of) the structure. Based on their layout and the type of structural deformation, resonators can roughly be grouped into three different categories (Stemme, 1991), which are schematically depicted in Figure 2.2 for a cantilever beam resonator: flexural resonators, torsional resonators and bulk or longitudinal resonators. These three categories will be described next.

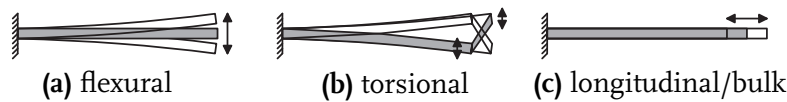


Figure 2.2 / Three different types of vibration for a cantilever beam.

Flexural resonators

A large group of resonators consists of flexural resonators. Also the first micromechanical resonator (Nathanson et al., 1967) was a flexural resonator. Structural deformation for these resonators is out-of-plane, like a transverse vibration of a beam or diaphragm. Basic flexural resonator shapes are cantilever beams, clamped-clamped beams (bridges) and diaphragms or rings. For the basic flexural resonator shape in Figure 2.2(a), flexural structural deformation takes place in almost the whole resonator. Therefore, the vibration frequency of these resonators is highly sensitive to initial stress or strain present in the material. Based on a doubly-clamped beam, a resonant strain gauge has been proposed in Tilmans et al. (1992), Legtenberg and Tilmans (1994) and Tilmans and Legtenberg (1994). The sensing principle is based on the fact that the resonant frequency changes as a function of axial forces on the ends of the bridge, resulting in axial stress in the resonator.

The basic resonator shapes can also be used for micromechanical filtering purposes. For instance, in Bannon et al. (2000) and Napoli et al. (2005), two coupled bridge and cantilever resonators have been used for filtering purposes, respectively. Cantilever and doubly-clamped beam structures have been proposed as resonators for oscillator purposes in Mattila et al. (2002a), Kaajakari et al. (2004a) and Lin et al. (2004).

Furthermore, vibration of a flexural resonator can take place in several different forms. Namely, depending on the frequency at which a resonator is driven, vibration can take place in fundamental vibration modes or higher (overtone) modes. Excitation of a specific

vibration mode is achieved by electrode placement around the resonator.

Based on combinations of the basic flexural resonator shapes, a large variety of other resonators has been designed, in which these basic shapes are used as building blocks. For instance, some resonators resemble tuning forks (Stemme, 1991; Beeby and Tudor, 1995) and consist of at least two cantilever or doubly clamped beams. These designs have been claimed to perform better than single-beam resonators in terms of balancing vibration. Namely, due to anti-phase vibration of two different parts of the resonator, losses through the suspension are supposed to be lower.

Comb drive resonators are a group of flexural resonators that make use of localised deformation. Almost all comb drive resonators consist of a large moving mass with combs, suspended via thin, flexible beams, in which the structural deformation takes place. A recent example of a comb drive that is used for investigation of pull-in behaviour has been described in Rocha (2005).

Often, in comb drive resonators, two groups of combs are present, one of which is used for driving the resonator into resonance and the other for detecting the motion by means of a capacitance change. A limitation of comb drive resonators is that their resonance frequencies are in the kHz range, due to their large moving mass.

Torsional resonators

Next to the resonators which feature transverse structural deformation as described above, also resonators based on torsional deformation can be used of, see Figure 2.2(b). One of the first torsional resonators has been described in Buser and Rooij (1990) and consists of a vane and two torsional bars. For this resonator, structural deformation is localised in the two torsional bars on either side of the beam. The advantage is that, for small torsional deformations, only moments and no forces are transmitted at the clamping parts of the resonator. Therefore, only pure shearing will be present in weak torsion (Buser and Rooij, 1990), which is accompanied by no volume change in the material during deformation. As a result, very little internal damping is expected.

In Turner et al. (1998), a comb-drive actuated torsional resonator is described, which is intended for scanning probe microscopy. Similar to Buser and Rooij (1990), torsional deformation is localised in two torsional bars. The resonator is excited parametrically, in order to separate the drive and sense side.

Another example of a torsional resonator is found in Ataman and Urey (2006), who describe a two-axis resonant microscanner. Such devices can produce a well-controlled 2D scan pattern, which is needed in various imaging applications. Typical oscillation frequencies of torsional resonators are limited to several tens of kHz, due to the high inertia of the resonators. This forms a limitation of torsional resonators for oscillator purposes, since they cannot reach the high oscillation frequencies of conventional quartz crystals.

Longitudinal/bulk resonators

A third group of resonators is based on bulk material deformation. The vibration pattern in these so-called bulk resonators, consists of either surface acoustic waves (SAW) or bulk acoustic waves (BAW), which travel along on the surface of the resonator or through the resonator body itself, respectively. In this way, a large part of the resonator participates in bulk vibration. Therefore, the resonators can store more energy and their damping is approximately equal to the intrinsic material damping present in the material.

One of the first bulk acoustic resonators has been reported in Ruby and Merchant (1994). The device consists of a thin layer of piezoelectric material (AlN), sandwiched between two electrodes. The bulk acoustic deformation consists of a transverse bulk wave in the piezoelectric material between the two electrodes.

Since 2002, interest has been renewed for bulk acoustic resonators. In Mattila et al. (2002b), a single-crystal silicon beam resonator has been described, in which the vibration shape consists of a longitudinal wave in the beam. Actuation and detection of the motion takes place electrostatically.

A two-dimensional bulk acoustic resonator has been investigated in Kaajakari et al. (2003b, 2004c). The described square plate resonator features a bi-directional in-plane structural deformation, in which the plate extends or contracts in both directions. Actuation is realised electrostatically, using four electrodes on the sides of the plate.

Next to basic beam or plate-like structures for bulk resonators, single-crystal silicon disk resonators have also been investigated, see for instance Pourkamali and Ayazi (2003), Hao et al. (2004), Pourkamali et al. (2004) and Lin et al. (2004). These electrostatically actuated resonators vibrate in elliptic bulk modes and are supported by one or more beams on their perimeter. The support beams (or anchors) are placed at nodal points of the elliptic mode and the electrodes are also placed at optimal locations around the perimeter of the disk.

2.3 Oscillators

An oscillator is a system, most often an electrical circuit, that produces a stable periodic output signal. In general, its output is sinusoidal, although the periodic output waveform can have sawtooth or square wave shapes, or any other periodic shape. Output frequencies may typically range from tens of kHz to hundreds of MHz (and even GHz). A schematic representation of an oscillator is depicted in Figure 2.3.

Virtually all oscillators consist of three essential components (Gerber and Ballato, 1985; Vig and Ballato, 1999): an amplifier (or gain circuit), a resonator, which acts as a frequency selective element and an amplitude control/limitation mechanism. The amplifier usually consists of one or more active devices (needing power supply) and the necessary biasing networks. It may also contain other elements for band limiting, impedance matching and gain control. The amplifier design and technology, together with the res-

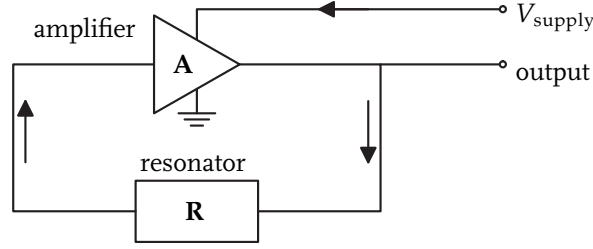


Figure 2.3 / Basic oscillator circuit, containing amplifier **A** and resonator **R**.

onator, determine the oscillator (noise) performance. In addition, the resonator determines the frequency and stability (in terms of phase noise, for instance) of the generated signal. It can be an *LC* circuit, a quartz crystal, a transmission line, a dielectric resonator, a cavity resonator, or a MEMS resonator, which is able to vibrate at a specific angular frequency Ω . Next to the resonator, some other components might be present, like variable capacitors for tuning or frequency trimming.

2.3.1 Working principle

The working principle of the oscillator circuit in Figure 2.3 can be understood by observing that the output of the resonator is fed back to the amplifier. If this happens with the correct amplitude and phase, sustained oscillations may occur, see Salt (1987). Suppose the amplifier has a voltage gain **A** and the resonator has a voltage ratio **R**. Consider for the moment that a signal **e** exists at the input of the amplifier. The signal appearing at the output terminal of the amplifier will be **Ae**. When this signal is transferred through the resonator, the ‘new’ amplifier input reads **e' = RAe**. If **e'** has the same angular frequency and phase as **e** and if $|\mathbf{e}'| \geq |\mathbf{e}|$, the circuit will oscillate. In general, both **A** and **R** are complex functions of the angular oscillation frequency Ω . By writing their complex gains as $\mathbf{R} = G_R(\Omega) \exp(j\psi_R(\Omega))$ and $\mathbf{A} = G_A(\Omega) \exp(j\psi_A(\Omega))$, respectively, the total gain of the oscillator circuit becomes:

$$\mathbf{RA} = G_R(\Omega)G_A(\Omega) \exp(j(\psi_R(\Omega) + \psi_A(\Omega))). \quad (2.1)$$

Here, $G_R(\Omega)$ and $G_A(\Omega)$ are the magnitudes of the resonator and amplifier gain, respectively and $\psi_R(\Omega)$ and $\psi_A(\Omega)$ represent the corresponding phase shifts. The requirements for oscillation can now be formulated as follows:

$$\psi_R(\Omega) + \psi_A(\Omega) = 2n\pi, \quad n \in \mathbb{Z} \quad (2.2)$$

$$G_R(\Omega)G_A(\Omega) \geq 1. \quad (2.3)$$

The first condition (2.2) states that the total phase shift around the oscillator must be an integer multiple of 2π radians. The oscillation frequency is determined by this condition. At this frequency, the second condition (2.3) states that the magnitude of the amplifier gain must be sufficient to compensate for the resonator losses. In other words, the loop gain must be greater than unity in order for oscillations to build up. As a result,

the signal level in the loop will continue to increase until the amplifier gain is reduced, either by nonlinearities in the active elements or by some automatic level-control method. Eventually, in steady-state, (2.3) becomes an equality.

When the oscillator is initially turned on, the only signal present in the circuit is ('white' or thermal) electrical noise associated with the components (mainly the active ones) in the circuit. The frequency component of the noise that satisfies the phase and gain requirement for oscillation is propagated around the loop with increasing amplitude, until the steady-state situation with sustained oscillation is reached. The rate of increase of the signal amplitude depends on the excess gain of the loop. Both the phase requirement (2.2) and the gain requirement (2.3) make that the resonator acts as a very selective band-pass filter in the oscillator circuit.

2.3.2 Key properties

A number of key properties of oscillators can be listed, see Vig and Ballato (1999). The overview, presented next, lists some of the most important properties. Depending on the specific application of the oscillator, relevance and importance of the properties may vary.

Accuracy, stability and precision

The terms accuracy, stability and precision are the main terms used for describing oscillator's quality with respect to various influences (see Vig and Ballato, 1999). Typically, these quantities are measured over time, and are expressed in units of ppm (parts per million). Depending on the length of the time interval considered, indications on aging, drift and phase noise can be obtained. In general, oscillators are designed to operate on a certain target frequency, often called center frequency f_c or nominal frequency f_{nom} .

Accuracy is the extent to which a given measurement, or the average of a set of measurements, agrees with the intended nominal frequency. The ability of a single oscillator to produce the same frequency, without adjustment, each time it is put into operation, is called reproducibility. Therefore, from the point of view of the user of an oscillator, reproducibility has a similar meaning as accuracy.

Stability is a measure to describe the change in frequency of an oscillator, under influence of various parameters like time, temperature and shock. Similar to accuracy, stability is also expressed in ppm.

Finally, *precision* expresses how well a given set of measurements of one sample agrees with the mean of the set (measure for process spread). This is not necessarily the same as accuracy, as a frequency source could be inaccurate but precise.

Aging

Aging (long-term stability) is the systematic cumulative change in oscillator frequency, due to electrical, thermal, physical and chemical internal changes in the oscillator, over a long time period (typically > 100 hours) (Vanier et al., 1992). At a constant temperature, aging usually has an approximately logarithmic dependence on time, see also Figure 2.4. The aging rate of an oscillator is expressed as a frequency stability in ppm per year and

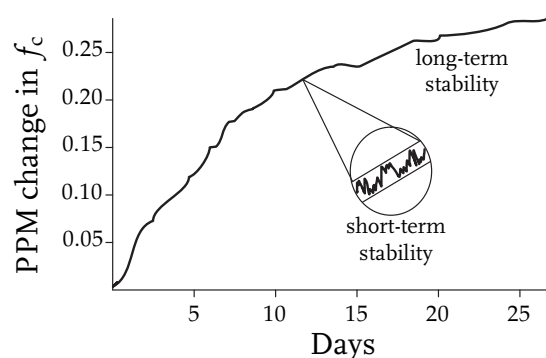


Figure 2.4 / Long-term (aging) and short-term stability of an oscillator output.

is highest when it is first turned on. Primary causes for this long-term effect are stress relief in the oscillator material and the mounting structure, mass transfer to or from the resonator's surfaces (for instance due to contamination) and changes in the oscillator circuitry. Therefore, to achieve low aging, oscillators must be fabricated and hermetically sealed in an ultra-clean high-vacuum environment.

In order to maintain an accurate oscillation frequency, periodic oscillator adjustments have to be made (calibration) to remove the effects of aging. In general, this can be done in the amplifier by a slight change in the phase of the feedback signal (see Figure 2.3).

Phase noise

As the time interval during which the oscillator output is considered gets shorter, random frequency fluctuations are resolved, see Figure 2.4. Oscillator phase noise is a measure for short-term frequency variations or time-domain stability. Therefore, phase noise determines the frequency domain uncertainty of an oscillator.

Frequency fluctuations are caused by noise in the amplifier and circuit components and, in addition, by naturally occurring thermal noise generated in resistive elements and by other dissipative effects, like mechanical loss, see for instance Kaajakari (2009). The noise can have numerous adverse effects on system stability and performance, see Vig and Ballato (1999).

To illustrate the concept of phase noise (see for instance Hajimiri and Lee, 1999; Lee and Hajimiri, 2000; Ham et al., 2004), consider an ideal oscillator circuit that gen-

erates a periodic signal $V_{\text{out}}(t)$ with constant amplitude V_0 and phase ϕ_0 :

$$V_{\text{out}}(t) = V_0 \cos(\omega_0 t + \phi_0). \quad (2.4)$$

In practice, however, circuit and device noise is present, which causes the output of the oscillator to be no longer ideal but to have the form:

$$V_{\text{out}}(t) = V_0[1 + A(t)] f(\omega_0 t + \phi(t)). \quad (2.5)$$

Here, the excess amplitude $A(t)$ and phase $\phi(t)$ are functions of time and $f(\cdot)$ is a periodic function, representing the shape of the steady-state waveform output. As a result, the output power spectrum will show sidebands close to the frequency of oscillation ω_0 (and its higher harmonics if the periodic waveform $f(\cdot)$ is not sinusoidal). These sidebands are generally referred to as *phase noise* sidebands.

From a frequency domain point of view, the short-term frequency variations of an oscillator are usually characterised in terms of single sideband noise spectral density (Hajimiri and Lee, 1999). This is conventionally expressed in units of decibels below the carrier per Hertz (dBc/Hz) and is given by:

$$\mathcal{L}(\Delta\omega) = 10 \log \left(\frac{P_{\text{sideband}}(\omega_0 + \Delta\omega, 1 \text{ Hz})}{P_{\text{carrier}}} \right), \quad (2.6)$$

where $P_{\text{sideband}}(\omega_0 + \Delta\omega, 1 \text{ Hz})$ represents the single sideband power at a frequency offset $\Delta\omega$ from the carrier in a measurement bandwidth of 1 Hz. Both amplitude $A(t)$ and phase $\phi(t)$ fluctuations (see (2.5)), may result in phase noise. In practice, however, all stable oscillators have some kind of amplitude restoring mechanism, which restores the oscillator output to the stable periodic solution. Therefore, amplitude fluctuations $A(t)$ will decay over time, whereas phase fluctuations $\phi(t)$ will not. Therefore, the latter are the dominant factor for close-in phase noise.

A well-known and widely accepted model for oscillator phase noise has been proposed by Leeson (1966). The model is based on thermal noise considerations for a linear time-invariant LC-oscillator and predicts the following behaviour for $\mathcal{L}(\Delta\omega)$ (see Leeson, 1966; Hajimiri and Lee, 1999; Lee and Hajimiri, 2000, for details):

$$\mathcal{L}(\Delta\omega) = 10 \log \left\{ \frac{2Fk_B T}{P_{\text{sig}}} \left[1 + \left(\frac{\omega_0}{2Q\Delta\omega} \right)^2 \right] \left(1 + \frac{\omega_{1/f^3}}{|\Delta\omega|} \right) \right\}. \quad (2.7)$$

Here, F is an empirical fitting parameter, k_B is Boltzmann's constant, T is the absolute temperature, P_{sig} is the average power dissipated in the resistive part of the oscillator, ω_0 is the oscillation frequency, Q is the effective quality factor of the oscillator, $\Delta\omega$ is the frequency offset from the carrier and ω_{1/f^3} is the corner frequency between the $\frac{1}{f^3}$ and $\frac{1}{f^2}$ regions. A schematic plot of the phase noise according to (2.7) is depicted in Figure 2.5. Regions with different slopes may be identified in $\mathcal{L}(\Delta\omega)$. At very large offset frequencies, a flat noise floor is present, at smaller frequency offsets, regions with slopes proportional to $\frac{1}{f^2}$ and $\frac{1}{f^3}$ are present. The corner between these two regions is at ω_{1/f^3} . Details on the precise shape of the spectrum can be found in Hajimiri and Lee (1999).

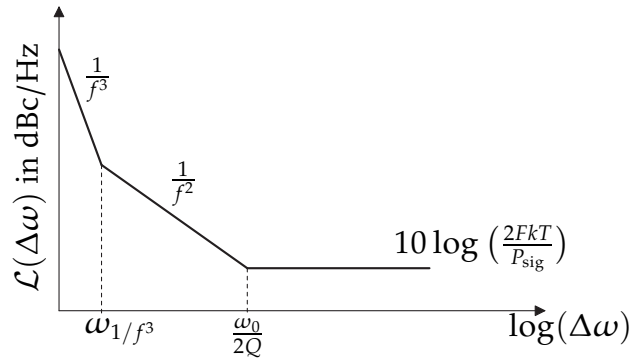


Figure 2.5 / Spectrum of the phase noise according to equation (2.7) (Leeson, 1966).

Temperature effects

In general, the frequency at which an oscillator operates, depends on the physical properties of both the resonator and the amplifier circuit. As these properties may change with temperature, also the oscillation frequency may change, resulting in so-called temperature drift and oscillators having a certain finite warm-up time.

Temperature drift requirements are often specified in terms of frequency stability over a relevant temperature range. Temperature and rate of temperature changes result in thermal gradient-induced stresses and the accompanying thermal(-transient) frequency changes. This could even result in thermal hysteresis for the oscillation frequency. This means that an oscillator, whose temperature is raised by a few tens of degrees and then lowered, may not return to the same frequency.

Furthermore, when power is applied to an oscillator or frequency standard, it takes a finite amount of time before the equilibrium frequency stability is reached. Warm-up time is the time taken by an oscillator, after turn on, to reach a steady state in which the quoted specifications are met (Vanier et al., 1992). The warm-up time of an oscillator generally is a function of the thermal properties of the resonator, the oscillator and input power and the temperature prior to turn-on. It takes for simple crystal oscillators typically a few seconds to warm up. Namely, in a high- Q circuit, it takes a finite amount of time for the signal to build up. During this build-up, the few tens of milliwatts of power dissipated in the oscillators change the temperature and, as a result, it takes some time for an oscillator to reach steady-state.

Power requirement and dissipation

The resonator in an oscillator is analogous to a mechanical clock. This clock relies upon permanent exchange between kinetic and potential energy in the resonator. Due to several energy dissipation mechanisms, an oscillator requires energy to sustain the vibration in the resonator. Typical values for the power dissipation range from 1 μ W to 5 mW, and usually a maximum allowable value is specified. Furthermore, excessive drive levels may cause damaging mechanical vibration in the resonator (for both quartz crystals and

MEMS resonators). Therefore, usually the operating point is chosen at a low-amplitude drive level, in order to avoid damaging mechanical vibrations. By this requirement, an oscillator is designed to operate at a nominal supply voltage and current. Their values depend on the specific application. For certain applications like frequency standards, ample power is available, but for mobile communication purposes, for instance, the oscillator has to operate from batteries, with a typical value of $V_{\text{supply}} = 2.4$ V. Oscillator manufacturers have to indicate a certain supply voltage, needed for the oscillator to operate within specification. Changes in supply voltage cause changes in the oscillation frequency. This sensitivity is expressed as frequency stability in ppm versus change in supply voltage.

2.4 Steady-state behaviour of nonlinear dynamical systems

In oscillator circuits, the steady-state dynamic behaviour of the resonator determines oscillator performance. Often, nonlinear behaviour is introduced in MEMS resonators for oscillator circuits, for example due to electrostatic actuation, nonlinear strain-displacement relations or nonlinear constitutive equations. Therefore, in this section, some concepts and tools for addressing the steady-state behaviour of nonlinear dynamical systems will be introduced. These will be used in the following chapters, in accordance with the research focus on multiphysics modelling for nonlinear dynamics, see Section 1.2.3. For a more detailed introduction in nonlinear dynamics, see, for instance, Guckenheimer and Holmes (1983), Parker and Chua (1989), Seydel (1994), Strogatz (2000), Thompson and Stewart (2002) and Thomsen (2003).

2.4.1 Nonlinear dynamical system

In general, the equations of motion for a dynamical system as considered in this work consist of both first-order and second-order ODEs in time and can be written as

$$\mathbf{M}\ddot{\mathbf{q}} + \mathbf{f}_{\text{in}}(\mathbf{q}, \dot{\mathbf{q}}, \mathbf{r}) = \mathbf{f}_{\text{ex}}(\mathbf{q}, t), \quad (2.8a)$$

$$\mathbf{T}\dot{\mathbf{r}} = \mathbf{f}_{\text{th}}(\mathbf{r}, \dot{\mathbf{q}}), \quad (2.8b)$$

where $\mathbf{q} \in \mathbb{R}^n$ represents the column with the n system DOFs related to the second-order variables (position) and \mathbf{r} is the column with n system DOFs related to first-order variables (temperature). Furthermore, $t \in \mathbb{R}$ denotes time, \mathbf{M} denotes the constant $n \times n$ mass matrix, $\mathbf{f}_{\text{in}}(\mathbf{q}, \dot{\mathbf{q}}, \mathbf{r}) \in \mathbb{R}^n$ denotes the column with internal nonlinear spring, damper and thermal forces, \mathbf{T} denotes the constant $n \times n$ matrix with thermal time constants, $\mathbf{f}_{\text{th}}(\mathbf{r}, \dot{\mathbf{q}}) \in \mathbb{R}^n$ denotes the column with heat-generating terms. Coupling between the thermal and position variables stems from thermoelastic damping. This will become clear in Chapter 4. Finally, $\mathbf{f}_{\text{ex}}(\mathbf{q}, t) \in \mathbb{R}^n$ in (2.8a) denotes the external forces depending on position and time. If $\mathbf{f}_{\text{ex}}(\mathbf{q}, t)$ is not explicitly dependent on time, system (2.8) is called autonomous, otherwise, it is called non-autonomous. The systems considered in this work are non-autonomous. Their external forces are either constant in time (static)

or they are periodic with a certain fundamental excitation frequency f_e . In that case, the (minimal) period time equals $T_e = 1/f_e$, such that:

$$\mathbf{f}_{\text{ex}}(\mathbf{q}, t + T_e) = \mathbf{f}_{\text{ex}}(\mathbf{q}, t). \quad (2.9)$$

System (2.8) can be rewritten to a set of first-order ODE by introducing the state $\mathbf{x}_1 = [\mathbf{q}^T \quad \dot{\mathbf{q}}^T \quad \mathbf{r}^T]^T$, $\mathbf{x}_1 \in \mathbb{R}^{3n}$. In this way, (2.8) becomes

$$\dot{\mathbf{x}}_1 = \mathbf{f}_1(\mathbf{x}_1, t), \quad (2.10)$$

where the vector field $\mathbf{f}_1 : \mathbb{R}^{3n} \rightarrow \mathbb{R}^{3n}$ is given by (see also (2.8)):

$$\mathbf{f}_1(\mathbf{x}_1, t) = \begin{bmatrix} \dot{\mathbf{q}} \\ \mathbf{M}^{-1}[\mathbf{f}_{\text{ex}}(\mathbf{q}, t) - \mathbf{f}_{\text{in}}(\mathbf{q}, \dot{\mathbf{q}}, \mathbf{r})] \\ \mathbf{T}^{-1}\mathbf{f}_{\text{th}}(\mathbf{r}, \dot{\mathbf{q}}) \end{bmatrix}. \quad (2.11)$$

When the system (2.10) is periodically forced with a single frequency f_e , that is, the time-dependency in $\mathbf{f}_{\text{ex}}(\mathbf{q}, t)$ consists of $\sin(2\pi f_e t)$ and $\cos(2\pi f_e t)$ terms, it can be rewritten to an autonomous system by extending its state \mathbf{x}_1 with two equations for a nonlinear oscillator:

$$\begin{aligned} \dot{x} &= x + 2\pi f_e y - y(x^2 + y^2), \\ \dot{y} &= -2\pi f_e x + y - y(x^2 + y^2). \end{aligned} \quad (2.12)$$

Oscillator (2.12) has the asymptotically stable solution $(x, y) = (\sin(2\pi f_e t), \cos(2\pi f_e t))$ and can be inserted into the external forcing function instead of the explicit time-dependency. The forcing then becomes $\mathbf{f}_{\text{ex}}(\mathbf{q}, x, y)$. The extended state can be defined as $\mathbf{x} = [\mathbf{x}_1^T \quad x \quad y]^T$, $\mathbf{x} \in \mathbb{R}^{3n+2}$ such that the autonomous form of (2.10) becomes

$$\dot{\mathbf{x}} = \mathbf{f}(\mathbf{x}), \quad (2.13)$$

where the vector field $\mathbf{f} : \mathbb{R}^{3n+2} \rightarrow \mathbb{R}^{3n+2}$ is given by:

$$\mathbf{f}(\mathbf{x}) = \begin{bmatrix} \dot{\mathbf{q}} \\ \mathbf{M}^{-1}[\mathbf{f}_{\text{ex}}(\mathbf{q}, x, y) - \mathbf{f}_{\text{in}}(\mathbf{q}, \dot{\mathbf{q}}, \mathbf{r})] \\ \mathbf{T}^{-1}\mathbf{f}_{\text{th}}(\mathbf{r}, \dot{\mathbf{q}}) \\ x + 2\pi f_e y - y(x^2 + y^2) \\ -2\pi f_e x + y - y(x^2 + y^2) \end{bmatrix}. \quad (2.14)$$

The long-term response of equivalent systems (2.8) and (2.13) consists of a transient response, after which the system settles into a steady state solution for $t \rightarrow \infty$, which may be a static equilibrium, a periodic solution, a quasi-periodic solution or a chaotic solution (Thompson and Stewart, 2002; Thomsen, 2003). Moreover, steady-state solutions may coexist and which solution will be reached depends on the initial condition $\mathbf{x}(t_0) = \mathbf{x}_0$ of the system. For this work, quasi-periodic and chaotic solutions are not relevant, therefore, no further information will be given on these types of solutions.

Often, it is of interest how the dynamic behaviour of a system changes under variation of one (or more) of the system parameters, for instance, a static load value, a dynamic load amplitude or the excitation frequency. Therefore, consider a parameterised version of (2.13)

$$\dot{\mathbf{x}} = \mathbf{f}(\mathbf{x}, \mu), \quad (2.15)$$

where μ denotes a system parameter of interest. Typically, small changes in the system parameter μ may result in small quantitative changes of the long-term system response. However, a small change in μ may also cause a qualitative change in system behaviour. So-called bifurcations mark these qualitative changes in system behaviour. The parameter value of μ at which this change occurs is called a bifurcation point. For instance, the number and/or the stability of the long-term solutions may change. A general classification of bifurcations can be found in Guckenheimer and Holmes (1983), Thompson and Stewart (2002) and Thomsen (2003).

A dynamical system is considered structurally stable (Guckenheimer and Holmes, 1983; Thomsen, 2003) if there exists no infinitesimal perturbation in the parameters of the system that results in a qualitative change of its long-term behaviour. A bifurcation can occur when a system is structurally unstable. A system that is structurally unstable does not retain its qualitative properties for small parameter changes. The qualitative behaviour of the system for parameter values μ around a bifurcation point can be graphically represented in a so-called bifurcation diagram, in which a response measure is depicted versus the system parameter μ .

The codimension of a bifurcation is the smallest dimension of a parameter space that contains the bifurcation in a persistent way (Thomsen, 2003). Bifurcations that will be studied in this work are typically co-dimension one bifurcations, which means that they need only a single system parameter to unfold them.

In the next two sections, static equilibria and periodic solutions of the system (2.8) or (2.13) will be discussed. The reason why these topics are relevant for MEMS will also be given. Furthermore, stability analysis and bifurcations for static equilibria and periodic solutions will be described.

2.4.2 Equilibrium points, local stability and bifurcations

As stated in Section 2.2.2, mainly electrostatically actuated MEMS are considered in this thesis. In general, two electrodes, which are separated by a gap, are present in such a device. Upon increasing the voltage over the electrode gap, a phenomenon called pull-in may occur, see for instance Senturia (2001). At a certain voltage, the electrostatic force may overcome the mechanical force (related to the stiffness) of the structure and the electrode gap suddenly closes (pulls in). The reason for studying equilibrium points and their stability for MEMS is because, from a static point of view, pull-in is associated with a static equilibrium point losing its stability.

For static equilibria, consider system (2.8), in which all time-dependency is removed. The solution to part related to the thermal variables (2.8b) will yield $\mathbf{r} = \mathbf{0}$, since $\dot{\mathbf{r}} = \mathbf{0}$ and

$\dot{\mathbf{q}} = \mathbf{0}$. When a constant, or static, external force $\mathbf{f}_{\text{ex}}(\mathbf{q})$ acts on the system (2.8a), it will settle in an equilibrium, or a fixed point, \mathbf{q}_e of (2.8), characterised by $\dot{\mathbf{q}} = \ddot{\mathbf{q}} = \mathbf{0}$, giving:

$$\mathbf{f}_{\text{in}}(\mathbf{q}_e) = \mathbf{f}_{\text{ex}}(\mathbf{q}_e). \quad (2.16)$$

By defining $\mathbf{f}_{\text{st}}(\mathbf{q}) = \mathbf{f}_{\text{in}}(\mathbf{q}) - \mathbf{f}_{\text{ex}}(\mathbf{q})$, where $\mathbf{f}_{\text{st}} : \mathbb{R}^n \rightarrow \mathbb{R}^n$, (2.16) can be rewritten to

$$\mathbf{f}_{\text{st}}(\mathbf{q}_e) = \mathbf{0}. \quad (2.17)$$

The equilibrium point(s) can be determined by solving the system of algebraic equations (2.17). This can be done numerically, by a zero-finding algorithm based on, for example, (damped) Newton-Raphson iteration (Heath, 2002).

Local stability of an equilibrium point \mathbf{q}_e follows from the eigenvalues of the Jacobian of (2.17) at an equilibrium point. The Jacobian is given by

$$\mathbf{J}(\mathbf{q}_e) = \frac{\partial \mathbf{f}_{\text{st}}}{\partial \mathbf{q}}(\mathbf{q}_e). \quad (2.18)$$

It has n real eigenvalues, since it is symmetric. Let λ_i denote the i^{th} eigenvalue of $\mathbf{J}(\mathbf{q}_e)$. An equilibrium point \mathbf{q}_e is said to be

1. locally stable if all eigenvalues λ_i are positive,
2. locally unstable if one or more λ_i are negative,
3. at a bifurcation point if one or more $\lambda_i = 0$.

With respect to the type of (codimension one) bifurcations that will be encountered in this work, only limit-points (also called saddle-node bifurcations, turning-points or fold bifurcations, see Thomsen (2003)) are of relevance, see Figure 2.6.

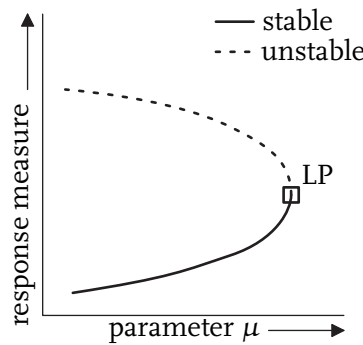


Figure 2.6 / Bifurcation diagram of an equilibrium, containing a limit-point (LP).

This type of bifurcation occurs where a branch of stable equilibrium points and a branch of unstable equilibrium points merge. Consider Figure 2.6 where, for large parameter values, locally no equilibrium exists. Upon decreasing the parameter, a stable and an unstable equilibrium point are created. The name limit point (turning point) arises from the fact that the tangent to the branch of equilibria is vertical in the bifurcation point.

2.4.3 Periodic solutions, local stability and bifurcations

When the system (2.8) is subject to periodic forcing (2.9), it may show a periodic response. In the MEMS field, microstructures may be excited periodically, such as vibrating sensors, filters, and resonators for oscillators. Periodic solution analysis is relevant for these structures, since one may be interested in what response these structures have at a certain excitation frequency. Stationary oscillations that may occur in these microstructures are denoted by the term steady-state periodic solutions. In contrast to linear systems, the steady-state periodic response does not have to have the same period as the excitation and it does not need to be unique. In general, the response obeys

$$\begin{bmatrix} \mathbf{q}(t) \\ \dot{\mathbf{q}}(t) \\ \mathbf{r}(t) \end{bmatrix} = \begin{bmatrix} \mathbf{q}(t + n_T T_e) \\ \dot{\mathbf{q}}(t + n_T T_e) \\ \mathbf{r}(t + n_T T_e) \end{bmatrix}, \quad (2.19)$$

where $n_T \geq 1$, $n_T \in \mathbb{N}$ and T_e denotes the (minimal) excitation period. If $n_T = 1$, the response is called harmonic, while for $n_T \geq 2$, the response is called a $1/n_T$ subharmonic of order $1/n_T$ or a period- n_T solution. In general, for an excitation with a base frequency f_e , the system response contains higher harmonic frequencies which are integer multiples of f_e . If one of these higher frequencies, say $m f_e$ causes a resonance, the system is said to exhibit an m^{th} superharmonic resonance (see also Fey, 1992; Fey et al., 1996; van de Vorst, 1996). Additionally, quasi-periodic or chaotic responses may occur, see Thompson and Stewart (2002) or Thomsen (2003), but these will not be discussed here.

In general (autonomous) form, a periodic solution $\mathbf{x}_p(t)$ for system (2.13) satisfies

$$\mathbf{x}_p(t) = \mathbf{x}_p(t + n_T T_e). \quad (2.20)$$

Periodic solutions can be calculated numerically by solving an initial value problem as discussed in Section 2.4.1. However, certainly for lightly-damped systems, which have long transient responses before the steady-state solution is reached, it is much more efficient to solve a two-point boundary value problem that satisfies (2.19) or (2.20). Various numerical algorithms exist for this purpose, for instance the (multiple) shooting method (Seydel, 1994; Nayfeh and Balachandran, 1995), the incremental harmonic balance method (Lau and Cheung, 1981; Lau et al., 1982; Pierre and Dowell, 1985), the finite difference method (Parker and Chua, 1989; Fey, 1992) and the orthogonal collocation method (Doedel et al., 1998). The last one will be applied extensively in this work.

Local stability of periodic solutions can be addressed using techniques that are based on Floquet theory, see for instance Guckenheimer and Holmes (1983) and Seydel (1994). Stability conditions follow from the linearisation of (2.13) around $\mathbf{x}_p(t)$. A perturbed solution $\mathbf{x}(t) = \mathbf{x}_p(t) + \Delta\mathbf{x}(t)$ must also satisfy (2.13). Stability of the periodic solution is determined by investigating how an initial perturbation $\Delta\mathbf{x}(t_0)$ around the periodic solution evolves in time. The mapping of an initial perturbation $\Delta\mathbf{x}(t_0)$ to the perturbation $\Delta\mathbf{x}(t_0 + n_T T_e)$ one period time later is determined by the so-called monodromy-matrix Φ_T (Guckenheimer and Holmes, 1983; Seydel, 1994). The eigenvalues of the

monodromy matrix Φ_T are called Floquet multipliers. Similar to the eigenvalues of the Jacobian around an equilibrium point (see Section 2.4.2), the Floquet multipliers determine the local stability of periodic solutions. They indicate the exponential growth or decay of the perturbations $\Delta \mathbf{x}$ in the directions of the eigenvectors of the monodromy matrix Φ_T and hence the stability of the periodic solution.

For system (2.13), the monodromy matrix will have $2n + 2$ (complex) Floquet multipliers $\lambda_1, \dots, \lambda_{2n+2}$. For autonomous systems, there will always be a Floquet multiplier $\lambda_1 = 1$ due to the freedom of phase in the system, see Seydel (1994). The remaining Floquet multipliers determine the stability of the periodic solution. Let λ_i ($i = 2, 3, \dots, 2n + 2$) denote the i^{th} Floquet multiplier of Φ_T for \mathbf{x}_p . The periodic solution $\mathbf{x}_p(t)$ is said to be

1. locally stable if all $|\lambda_i| < 1$,
2. locally unstable if one or more $|\lambda_i| > 1$,
3. at a bifurcation point if one or more $|\lambda_i| = 1$.

The loss (or gain) of stability when a critical Floquet multiplier exits (enters) the unit circle is accompanied with a bifurcation that depends on the point(s) where the unit circle is crossed. Three codimension one bifurcations may commonly be encountered for periodic solutions. These are the cyclic fold, period doubling and the Neimark-Sacker bifurcation (Fey, 1992; Seydel, 1994; Thompson and Stewart, 2002). The third type is not relevant for the work in this thesis and will, therefore, not be discussed.

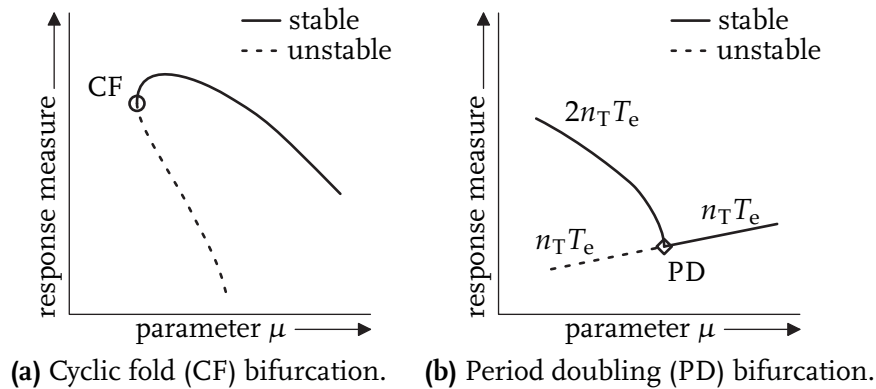


Figure 2.7 / Bifurcations of periodic solutions.

For the cyclic fold and period doubling bifurcation, consider Figure 2.7, where a response measure of the periodic solution (amplitude, for instance) is depicted versus a system parameter μ . The cyclic fold bifurcation is encountered when one of the critical Floquet multipliers exits (enters) the unit circle at $\lambda_c = 1$. This bifurcation is the periodic solution analogy of the limit point bifurcation for equilibrium points (Section 2.4.2). At a cyclic fold, or turning point, bifurcation limit cycles are created or destroyed, see Figure 2.7(a). At the period doubling (PD) bifurcation point, the unstable and stable branches of periodic so-

lutions connect. For parameter values below the CF point in Figure 2.7(a), locally no periodic solution exists.

In Figure 2.7(b), the period doubling bifurcation is indicated. This bifurcation (also called the flip or subharmonic bifurcation) occurs when the critical Floquet multiplier exits (enters) the unit circle at $\lambda_c = -1$. At the period doubling bifurcation point (PD), a continuous branch of periodic solutions (with period $n_T T_e$) changes stability. Additionally, a secondary branch of periodic solutions with double period ($2n_T T_e$) branches off the primary branch. The period doubling bifurcation is called super-critical if the secondary branch is stable, whereas it is called sub-critical if the secondary branch is unstable.

2.4.4 Numerical continuation

The change of an equilibrium point \mathbf{q}_e or a periodic solution $\mathbf{x}_p(t)$ with a change in a system parameter μ , see (2.15) can be investigated by combining an equilibrium or periodic solution solver with numerical continuation, or so-called path-following, techniques. By applying numerical continuation, bifurcation diagrams can be calculated. Starting from an initial guess, a zero finding algorithm (for equilibrium points) or a periodic solution solver (for periodic solutions) can be applied for obtaining \mathbf{q}_e or $\mathbf{x}_p(t)$, respectively, at a certain system parameter value μ . Next, the solution for $\mu + \Delta\mu$ is calculated by using the solution at μ as an initial guess. The solver is likely to converge for small $\Delta\mu$. This method is called sequential continuation (see Nayfeh and Balachandran, 1995).

At bifurcation points, problems may arise when a branch of solutions reaches a turning point (see Figures 2.6 and 2.7(a)). For small $\Delta\mu$, the solver may not converge. Therefore, the method can be improved by implementing so-called arclength continuation. This method is able to round corners in bifurcation diagrams, such as at the LP and CF points in Figures 2.6 and 2.7(a), respectively.

In this work, bifurcation diagrams for equilibrium points are calculated by applying damped Newton-Raphson iteration to find the zeros of the parameterised version of the static equilibrium equation (2.17): $\mathbf{f}_{st}(\mathbf{q}, \mu) = \mathbf{0}$. Next, path-following with arclength continuation (Parker and Chua, 1989) is used for calculating the bifurcation diagram.

Path-following for periodic solutions can also be used for calculating bifurcation diagrams for periodic solutions (Parker and Chua, 1989; Fey et al., 1996), but in this work, these bifurcation diagrams are calculated using the numerical package AUTO97 (Doedel et al., 1998). This package is dedicated for continuation calculations. The method of orthogonal collocation with automatic meshing is used for the discretisation of the two-point boundary value problem represented by (2.15) together with (2.20). One parameter continuation can be applied for constructing the bifurcation diagram. Local stability analysis, based on Floquet theory, is applied and includes the detection and classification of the bifurcation points. Furthermore, the package supports automatic branch switching and two parameter continuation of bifurcation points. The latter can be used to investigate how the occurrence of certain bifurcation points can be influenced in a two parameter subspace.

Heuristic modelling of MEMS resonators¹

Abstract / In this chapter, a heuristic modelling approach will be applied to two case studies: a clamped clamped beam MEMS resonator and a dog-bone MEMS resonator. Based on experimental results for these resonators, heuristic device level models are proposed to arrive at nonlinear dynamic models that potentially capture the experimentally observed behaviour. For the clamped-clamped beam resonator, a good quantitative match between the simulation and experimental results is established. However, for the dog-bone resonator, the (partly) heuristic model does not capture the observed behaviour. The chapter is ended with conclusions on the limited capabilities a heuristic modelling serving as the motivation for a first-principles based approach.

3.1 Introduction

Microelectromechanical silicon resonators provide an interesting alternative for quartz crystals as accurate timing devices in oscillators for modern data and communication applications (see Chapter 2). Their compact size, feasibility of integration with IC technology and low cost are major advantages. However, as the resonators are small in size, they have to be driven close to or even into nonlinear regimes in order to store enough energy for a sufficiently good signal to noise ratio (Kaajakari et al., 2004a). Nonlinearities in MEMS silicon resonators are caused by different effects. Depending on the resonator layout, different nonlinearities may be dominant in the dynamic behaviour of the resonator. The presence of the nonlinearities is relevant for oscillator performance and has to be incorporated in future resonator and oscillator design optimisation. However, in order to determine the influence of resonator nonlinearities on the performance of oscillators, first the dynamic behaviour of resonators has to be understood. The steady-state dynamic behaviour of the resonator can be described by a dynamic characteristic called an amplitude-frequency curve.

In this chapter, a heuristic modelling approach for the nonlinear dynamic behaviour of

¹Results from Section 3.2 are based on Mestrom et al. (2006) and Mestrom et al. (2008a).

MEMS resonators will be applied to two case studies. For both a clamped-clamped beam and a dog-bone MEMS resonator, models with a pre-defined complexity will be proposed, which potentially capture the nonlinear dynamic behaviour. From the (mis)match between the numerical results and experimental results for the two case studies, limitations and shortcomings of the heuristic modelling approach will become clear.

In Sections 3.2 and 3.3, two case studies for heuristic modelling will be presented. In Section 3.2, a clamped-clamped beam MEMS resonator will be described, for which the heuristic modelling approach leads to a good quantitative match between simulations and experiments. In Section 3.3, a so-called dog-bone MEMS resonator will be considered, for which the proposed partly heuristic model fails to capture experimentally observed behaviour. Finally, in Section 3.4, the chapter will end with a conclusion on the limitations and shortcomings of heuristic modelling. This serves as the motivation for the first-principles based multiphysics modelling framework, to be presented in Chapter 4.

3.2 Case study I: clamped-clamped beam MEMS resonator

The first case study is a flexural clamped-clamped beam MEMS resonator. Such resonators have been realised and measured by various research groups, see for instance Mattila et al. (2002b) and Kaajakari et al. (2004a). However, a combined numerical and experimental analysis of the nonlinear behaviour has only been limitedly addressed (Shao et al., 2008a).

In this section, a heuristic modelling approach is used that will yield a quantitative match between the simulation and experimental results. The outline for case study I is as follows. First, in Section 3.2.1, experimental results of a clamped-clamped beam resonator will be discussed. Next, in Section 3.2.2, a modelling approach will be proposed to describe the dynamic effects observed in the measurements. Additionally, the numerical analysis will be described briefly. Experimental and numerical results will be compared in Section 3.2.3. In Section 3.2.4, case I ends with some conclusions and a discussion on the model results.

3.2.1 Experiments using a clamped-clamped beam resonator

An example of a clamped-clamped beam resonator is depicted in Figure 3.1. Its characteristic vibration shape is also depicted (the dashed lines). Due to out-of-plane vibration, the resonator is often called a flexural resonator (see Section 2.2.3). The actuation of the resonator is realised by means of a dc (V_{dc}) and an ac (V_{ac}) voltage component, which are applied to the electrodes of the resonator by means of bias tees, see Figure 3.1. During measurements, the resonator output voltage V_{out} is measured. This quantity is related to the beam motion, as will become clear from Section 3.2.2.

Resonators are fabricated using Silicon-On-Insulator (SOI) wafers. The fabrication of the resonator is schematically depicted in Figure 3.2. First, aluminum bondpads are defined

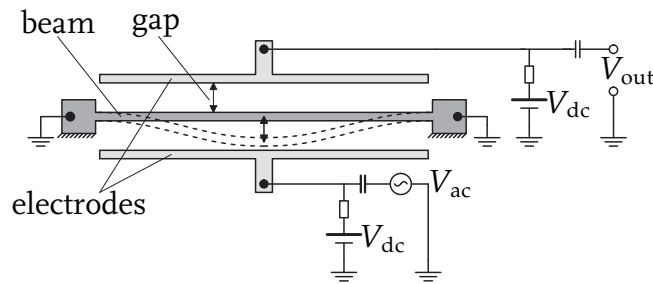


Figure 3.1 / Schematic layout of the clamped-clamped beam resonator.

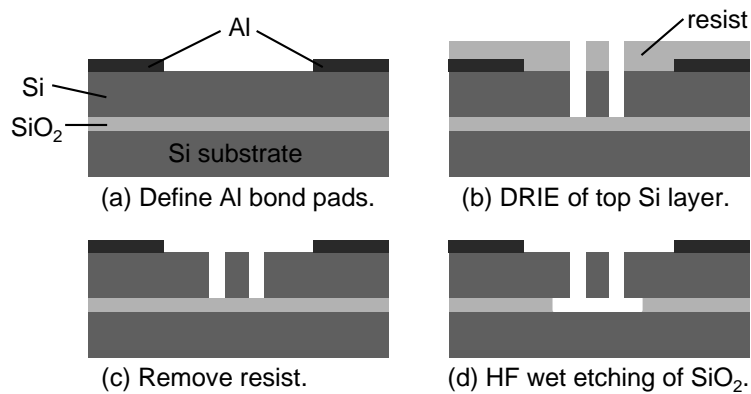


Figure 3.2 / Fabrication of the resonator: (a) define Al bond pads, (b) DRIE of top Si layer, (c) remove resist and (d) HF wet etch of SiO_2

on the wafer surface, see Figure 3.2(a). A layer of resist is deposited on top of the wafer and the resonator layout is defined by means of lithography. Next, the resonator layout is etched into the $1.4 \mu\text{m}$ thick SOI layer down to the buried oxide layer by means of deep reactive ion etching (DRIE) (Figure 3.2(b)). The resist is removed (Figure 3.2(c)) and, finally, the resonator is released from the substrate through isotropic etching of the buried oxide layer using an HF wet etch solution (Figure 3.2(d)).

A microscope image of the clamped-clamped beam resonator can be seen in Figure 3.3. Here, the dark grey material is silicon (Si), thin black lines are lithography etch gaps and the light grey, grainy material corresponds to the aluminum (Al) bond pads and electrical lines. Six aluminum bond pads can be distinguished. These are designed in such a way that they fit the ground-signal-ground probes that are used during the measurements. The outer four bond pads are connected to ‘ground’, such that the beam itself is grounded. The middle two bond pads are used for actuation and measurement purposes. Further information about the experimental setup can be found in Chapter 6.

During the experiments, performed on a custom-built set-up that is available at the NXP-TSMC Research Center², the MEMS resonator is located in a vacuum chamber (pressure $p = 4.6 \times 10^{-4}$ mbar). A more detailed description of the experimental set-up can be

²NXP Semiconductors, Eindhoven, the Netherlands.

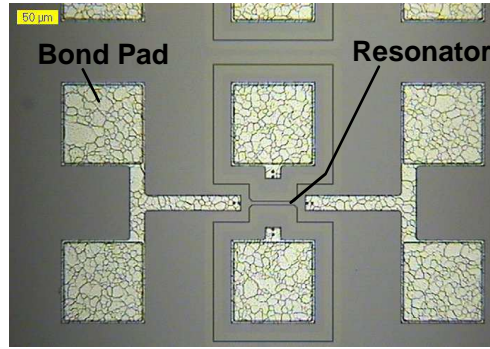


Figure 3.3 / Clamped-clamped beam resonator (beam dimensions: length: $44\ \mu\text{m}$, width: $4\ \mu\text{m}$ and thickness: $1.4\ \mu\text{m}$).

found in Section 6.3. The steady-state dynamic behaviour of the resonator is investigated experimentally by constructing a so-called amplitude-frequency plot. For this purpose, the ac excitation frequency f is slowly increased (sweep up) and decreased (sweep down) in steps of 250 Hz around the first harmonic resonance frequency of the resonator. At each frequency, after 2 seconds (to let the transient damp out), the output voltage V_{out} is measured, which is a measure for the steady-state beam motion (see also Section 3.2.2).

An example of a typical amplitude-frequency curve for the clamped-clamped beam considered is depicted in Figure 3.4. The excitation is given by a dc bias voltage of $V_{\text{dc}} = 70\ \text{V}$ and an ac excitation amplitude of $V_{\text{ac}} = 139\ \text{mV}$. From this figure, it can be seen that the first harmonic resonance frequency of the resonator is approximately 12.875 MHz. However, due to nonlinearities, the resonance peak is bent to the left (lower frequencies). As a result, in the frequency range near the resonance peak, the steady-state dynamic behaviour of the resonator is found to depend on the sweep direction. Sudden jumps

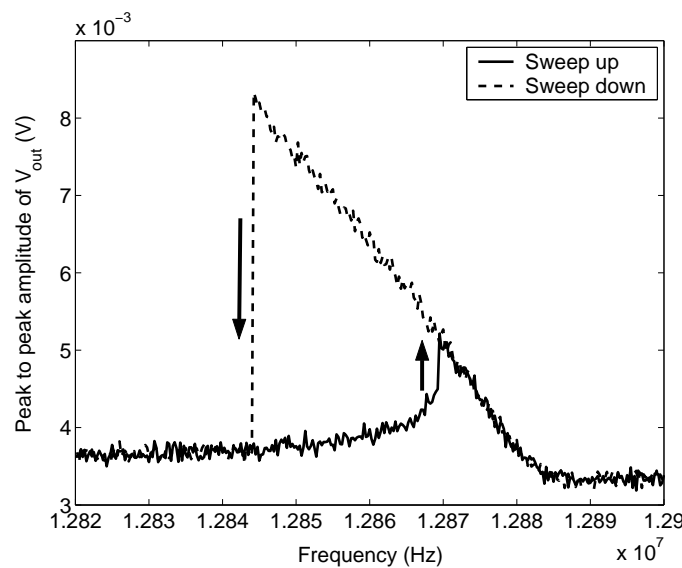


Figure 3.4 / Example of an amplitude-frequency curve.

in the response, indicated by black arrows, occur at different frequencies. This is called frequency hysteresis and has also been reported in Kaajakari et al. (2004b). However, in Kaajakari et al. (2004b), a longitudinal/bulk mode beam resonator was investigated, see also Figure 2.2(c). Frequency hysteresis is a typical nonlinear effect, which may be caused by hardening, or, in this case, softening nonlinear behaviour. This will be explained in section 3.2.2.

3.2.2 Modelling approach

Mechanical model

The nonlinear phenomena observed in the measurement (Figure 3.4) demand for a nonlinear dynamical model. A single degree-of-freedom (1DOF) model, in line with Kaajakari et al. (2004a,b), that may capture these phenomena is a Duffing-like model. The Duffing equation is a classical nonlinear dynamic equation which can be used to describe the response of a periodically excited mass–spring–damper system with linear viscous damping force and a spring force containing both a linear and a cubic term. From literature, it is well-known that a Duffing model may describe nonlinear effects like softening and hardening behaviour and sub- and superharmonic resonances (Weaver et al., 1990; Fey et al., 1990; Thomsen, 2003). Therefore, a Duffing-like model structure will be proposed. In contrast to a first principles-based approach, as for instance found in Younis and Nayfeh (2003), Abdel-Rahman and Nayfeh (2003) and Nayfeh and Younis (2005), a heuristic approach is utilised here. The single degree-of-freedom model for the mechanical part will form a suitable starting point for gaining insight in the nonlinear dynamics of the MEMS resonator, without the need for extensive distributed modelling. It can be considered as a device level model, see Section 1.2.2. On the one hand, essential nonlinear dynamics are believed to be captured by a 1DOF model (see also Kaajakari et al., 2004a,b) and it will allow for a more straightforward nonlinear dynamic analysis. On the other hand, results are likely to be less accurate than the ones based on a distributed modelling approach. Namely, included physical effects are described in a lumped sense (see (3.1)), instead of using a first-principles based description, and the lumped model parameter values are determined from estimation instead of from the physical quantities related to first-principles based modelling.

The following 1DOF model is proposed, which describes the dynamic behaviour of a measure for the flexural displacement x of the beam resonator:

$$m\ddot{x} + b\dot{x} + k(x)x = F_e(x, t), \quad (3.1)$$

where m , b and $k(x)$ are the lumped mass, the linear viscous damping constant and the nonlinear stiffness of the system, respectively. Since the beam is excited over the total beam length (see Figure 3.1), x is some characteristic displacement measure for the beam, vibrating in the first mode. x is defined positive in downward direction in Figure 3.1. Furthermore, \dot{x} and \ddot{x} denote the first and second time derivative of x , respectively. The

parametric excitation by the electrostatic force $F_e(x, t)$ is modelled by:

$$F_e(x, t) = \frac{1}{2} \frac{C_0 d_0}{(d_0 - x)^2} V_1^2(t) - \frac{1}{2} \frac{C_0 d_0}{(d_0 + x)^2} V_2^2, \quad (3.2)$$

where C_0 is the capacitance over the gap when $x = 0$ and d_0 is the corresponding initial gap width. $V_1(t)$ and V_2 denote the applied voltages on the electrodes and are written as:

$$V_1(t) = V_{dc} + V_{ac} \sin(2\pi f t), \quad V_2 = V_{dc}, \quad (3.3)$$

where V_{dc} is the so-called bias voltage, and V_{ac} and f are the amplitude and frequency of the ac voltage, respectively. The capacitance on the readout side for arbitrary x is given by $C(x) = C_0 d_0 / (d_0 + x)$.

Taylor expansion of the electrostatic force about $x = 0$,

$$F_e(x, t) = \frac{1}{2} \frac{C_0}{d_0} V_{dc}^2 \left(4 \frac{x}{d_0} + 8 \frac{x^3}{d_0^3} + \text{h.o.t.} \right) + \frac{1}{2} \frac{C_0}{d_0} (2 V_{dc} V_{ac} \sin(2\pi f t) + V_{ac}^2 \sin^2(2\pi f t)) \left(1 + 2 \frac{x}{d_0} + 3 \frac{x^2}{d_0^2} + 4 \frac{x^3}{d_0^3} + \text{h.o.t.} \right), \quad (3.4)$$

reveals that this force introduces softening nonlinear behaviour. In (3.4), h.o.t. denotes higher-order terms. This fourth-order Taylor expansion is only valid for small displacements, i.e. $x \in [-d_0/4, d_0/4]$. The nonlinearity in the mechanical spring stiffness results from hardening silicon material nonlinearities (higher-order elastic effects, see Appendix A.4.2, which is in line with Kim and Sachse (2000) and Kaajakari et al. (2004a)) and hardening geometric nonlinearities (mid-plane stretching of a clamped-clamped beam, see for instance Weaver et al. (1990) and Thomsen (2003)). A starting point for the nonlinear mechanical stiffness function, including terms up to fourth order reads:

$$k(x) = k_1 + k_2 x + k_3 x^2 + k_4 x^3 + k_5 x^4, \quad (3.5)$$

where k_1 is the stiffness parameter in the linear part of the spring force and k_2 , k_3 , k_4 and k_5 denote the stiffness parameters in the nonlinear part of the spring force. This approach allows for extension of the mechanical stiffness function to arbitrary order.

Depending on the specific layout of the clamped-clamped silicon beam resonator, k_2 to k_5 each may become positive or negative, resulting in hardening or softening behaviour, respectively. In Kaajakari et al. (2004b), a softening spring stiffness was observed (only terms k_2 and k_3 for a longitudinal bulk-mode beam resonator). The higher-order stiffness parameters k_4 and k_5 have not yet been found in literature related to MEMS resonators. However, as will become clear from Section 3.2.3, where the match between simulations and experiments will be established, these terms have to be included, at least in the current model.

Measurement circuit

An electrical circuit is used for the actuation and detection of the beam motion. The electrical circuit representation of Figure 3.1 is shown in Figure 3.5(a). In order to be able

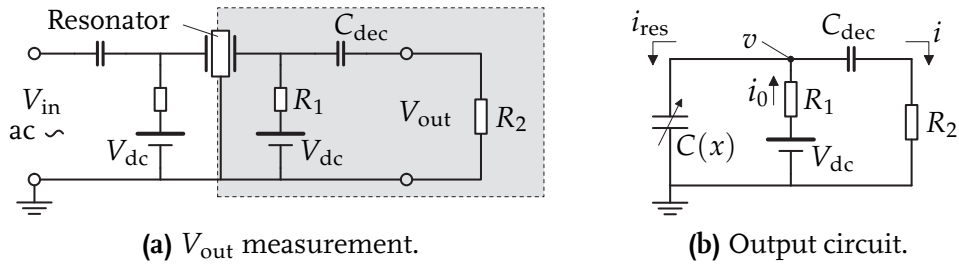


Figure 3.5 / Measurement configuration for the clamped-clamped beam resonator.

to measure the ac component of V_{out} , dc decoupling is present by means of an additional decoupling capacitor C_{dec} . This is also depicted in Figure 3.5(a). The resonator output voltage is measured on a $50\ \Omega$ resistor (R_2).

In order to relate the output voltage V_{out} , measured on R_2 , to the beam motion, consider Figure 3.5(b), which contains only the output part of the electrical circuit (grey part in Figure 3.5(a)). $C(x)$ denotes the variable resonator capacitance on the measurement side of the resonator. The differential equations with the two unknowns v and i for this electrical circuit are determined from node analysis. By using $V_{\text{out}} = iR_2$, two coupled differential equations for current i and voltage v are obtained:

$$C(x) \frac{dv}{dt} = - \left(\frac{1}{R_1} + \frac{\partial C(x)}{\partial x} \dot{x} \right) v - i + \frac{V_{\text{dc}}}{R_1}, \quad (3.6a)$$

$$C_{\text{dec}} \left(\frac{dv}{dt} - R_2 \frac{di}{dt} \right) = i, \quad (3.6b)$$

where, in (3.6a), the time derivative of the resonator capacitance $C(x)$ is elaborated as $\frac{dC(x)}{dt} = \frac{\partial C(x)}{\partial x} \dot{x}$. Note that (3.6) is heuristic in nature, since the displacement x is some measure for the beam deformation.

Thermal noise

In every electrical system, thermal agitation of the electrons inside electrical conductors forms a source of noise. This noise is called Johnson-Nyquist or thermal noise (Johnson, 1928; Nyquist, 1928). In Nyquist (1928), the expression for the root mean square (rms) of the noise voltage v_n generated in a resistor is given as

$$v_n = \sqrt{4k_B T R \Delta f}, \quad (3.7)$$

where k_B denotes Boltzmann's constant, T denotes absolute temperature, R is the resistor value and Δf is the bandwidth in which the noise is measured. An estimate for the thermal noise can be found by using the resonator motional resistance R_m for the resistor value R in (3.7). An expression for R_m will be derived next. Due to presence of other resistors in the measurement circuit, the estimate for v_n can be considered to be conservative.

In order to determine the noise generated in the circuit with the clamped-clamped beam resonator, the resistance value of its equivalent circuit representation can be used in (3.7). For this purpose, a *linear* ($k_i = 0$, $i = 2, \dots, 5$) mechanical model is considered, in which the electrostatic force is expanded in a Taylor series around $x = 0$, see (3.4). Furthermore, it is assumed that the ac voltage is much smaller than the bias voltage ($V_{ac} \ll V_{dc}$) and that small beam motions occur ($x \ll d_0$). Therefore, terms in (3.4) with V_{ac}^2 , $V_{dc}V_{ac}\frac{x}{d_0}$ (and higher) and $V_{dc}^2\frac{x^3}{d_0^3}$ are neglected, which gives

$$m\ddot{x} + b\dot{x} + \left(k_1 - 2\frac{C_0}{d_0^2}V_{dc}^2\right)x = \frac{C_0}{d_0}V_{dc}V_{ac}\sin(2\pi ft). \quad (3.8)$$

Next, the modified stiffness $k_{1,e} = k_1 - 2\frac{C_0}{d_0^2}V_{dc}^2$ and the electromechanical coupling coefficient (Mattila et al., 2002a) $\eta = \frac{C_0}{d_0}V_{dc}$ are defined. In this way, (3.8) can be rewritten as:

$$m\ddot{x} + b\dot{x} + k_{1,e}x = \eta V_{ac}\sin(2\pi ft). \quad (3.9)$$

By using the electromechanical coupling coefficient, a relation between the electrical current and the mechanical velocity can be established as $i_m = \eta\dot{x}$ (Mattila et al., 2002a). Substitution of this relation into (3.9) followed by division by η results in:

$$\frac{m}{\eta^2}\frac{di_m}{dt} + \frac{b}{\eta^2}i_m + \frac{k_{1,e}}{\eta^2}\int i_m dt = V_{ac}\sin(2\pi ft). \quad (3.10)$$

Equation (3.10) can be rewritten as a harmonically excited RLC circuit:

$$L_m\frac{di_m}{dt} + R_mi_m + \frac{1}{C_m}\int i_m dt = V_{ac}\sin(2\pi ft). \quad (3.11)$$

in which the motional inductance, motional resistance and motional capacitance (see Mattila et al., 2002a) are defined as:

$$L_m = \frac{m}{\eta^2}, \quad R_m = \frac{b}{\eta^2} = \frac{\sqrt{k_{1,e}m}}{\eta^2 Q}, \quad \text{and} \quad C_m = \frac{\eta^2}{k_{1,e}}, \quad (3.12)$$

respectively. Note that the quality factor Q is defined in a linear sense: $Q = \sqrt{k_{1,e}m}/b$. By (3.12), the mechanical parameters of the resonator are related to RLC-parameters of the equivalent circuit. The motional resistance R_m can be used to obtain a conservative estimate for the thermal noise using (3.7). Other noise sources or effects might also be present in the system, both in the actuation/sensing of the resonator and in the measurement equipment. However, within the scope of the current modelling approach, individual noise effects cannot be distinguished properly and, therefore, the discussion will be limited to thermal noise.

Numerical approach

The total simulation model for the clamped-clamped beam resonator and the measurement circuit consists of a state-space description of the 1DOF resonator model (3.1) (using (3.2), (3.3) and (3.5)), together with the equations for the measurement circuit (3.6a)–(3.6b). Therefore, the state column is defined as $\mathbf{x} = [x \ \dot{x} \ v \ i]^T = [x_1 \ x_2 \ x_3 \ x_4]^T$.

In this way, the total model can be written in a form that is more suitable for numerical implementation, as $\dot{\mathbf{x}} = \mathbf{f}(\mathbf{x}, t)$, where

$$\mathbf{f}(\mathbf{x}, t) = \begin{bmatrix} x_2 \\ \frac{1}{m} \left(-bx_2 - k(x_1) + \frac{1}{2} \frac{C_0 d_0}{(d_0 - x_1)^2} V_1^2(t) - \frac{1}{2} \frac{C_0 d_0}{(d_0 + x)^2} V_2^2 \right) \\ -\frac{d_0 + x_1}{C_0 d_0} \left\{ \left(\frac{1}{R_1} - \frac{C_0 d_0}{(d_0 + x_1)^2} x_2 \right) x_3 + x_4 - \frac{V_{dc}}{R_1} \right\} \\ -\frac{d_0 + x_1}{C_0 d_0 R_2} \left\{ \left(\frac{1}{R_1} - \frac{C_0 d_0}{(d_0 + x_1)^2} x_2 \right) x_3 + \left(1 + \frac{C_0 d_0}{(d_0 + x_1) C_{dec}} \right) x_4 - \frac{V_{dc}}{R_1} \right\} \end{bmatrix}. \quad (3.13)$$

In the numerical simulations, this representation of the total model allows for the mechanical part to be calculated first and the electrical (measurement) part to be calculated afterwards, since the states x_3 and x_4 do not appear in the first two elements (rows) of (3.13).

The steady-state nonlinear dynamic behaviour of the total model is investigated. Hereto, numerical collocation and continuation techniques, available in the numerical package AUTO (Doedel et al., 1998), are applied to the mechanical model for determining periodic solutions (resonator vibrations) for varying excitation frequency f , see also Section 2.4.4. Next, the results from the mechanical model are used as input for the measurement circuit part and time integration is applied to calculate the response of the measurement circuit in order to obtain V_{out} . Results will be discussed in Section 3.2.3.

3.2.3 Numerical and experimental results

For parameter estimation and later comparison of numerical and experimental results, a series of measurements has been performed on the clamped-clamped beam resonator. The bias voltage during all measurements has been kept constant to $V_{dc} = 70$ V and the ac amplitude V_{ac} has been varied between 20 and 279 mV.

First, the measurement of the (almost) linear response at the lowest excitation value will be used to estimate the motional resistance R_m and, thus, the thermal noise in the measurements. The result of the measurement and the numerical fit is depicted in Figure 3.6. In this figure, the black curves (both solid and dashed) denote experimentally determined peak to peak values of periodic solutions. These curves are rather noisy, since, for low ac excitation values, the peak to peak value of V_{out} is dominated by noise. The solid grey line denotes simulation results. Here, the response of the numerical model is shifted vertically 3.25 mV resulting in similar peak to peak amplitudes as in the measurement. This shift value can be justified to a large extent by the presence of thermal noise, which will be explained below. In Figure 3.7, a part of the time history at point A in Figure 3.6 can be seen. In this figure, the solid black line denotes the measured time history and the dashed line denotes the (scaled) ac excitation signal. The simulated time history (without the effect of thermal noise) is depicted as a solid grey curve.

Initial estimates for the linear parameters values in the numerical model have been obtained from the physical dimensions and the mass of the resonator. After some fine-tuning, the linear parameters for the numerical model have been collected in Table 3.1.

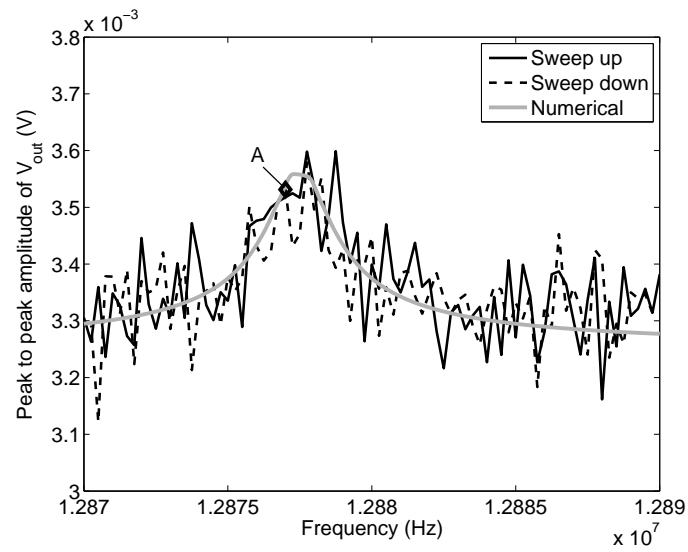


Figure 3.6 / Amplitude-frequency curve, $V_{dc} = 70$ V, $V_{ac} = 20$ mV.

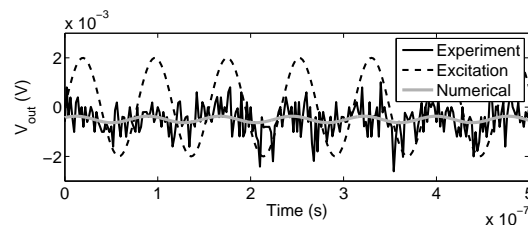


Figure 3.7 / Part of time history at point A in Figure 3.6 at $f = 12.877$ MHz.

Table 3.1 / Numerical values for the linear parameters in the total model for $V_{dc} = 70$ V and $V_{ac} = 20$ mV.

Parameter	Value	Unit
m	0.2273	ng
k_1	1.505	kN m ⁻¹
b	$3.083 \cdot 10^{-9}$	N s m ⁻¹
Q	6000	—
f_0	12.949	MHz
$f_{0,e}$	12.878	MHz
d_0	330	nm
C_0	0.185	fF
R_1	1.0	MΩ
R_2	50	Ω
C_{dec}	82	nF
ρ	2329	kg m ⁻³

Here, the mechanical linear natural frequency is defined as $f_0 = \frac{1}{2\pi} \sqrt{\frac{k_1}{m}}$. The actual natural frequency of the resonator is slightly different, due to the effect of the bias voltage: $f_{0,e} = \frac{1}{2\pi} \sqrt{\frac{k_{1,e}}{m}}$, where $k_{1,e}$ is defined as $k_{1,e} = k_1 - 2\frac{C_0}{d_0^2} V_{dc}^2$, see (3.8). The value $f_{0,e}$ matches very well with the measured value of 12.875 MHz, see Figure 3.4.

With these values, the motional resistance R_m can be estimated using (3.12): $R_m = 1.998 \text{ M}\Omega$. The rms thermal noise voltage results from (3.7). Measurements are performed using a bandwidth of 250 MHz and the temperature of the resonator is estimated to be 300 K. This yields an rms noise voltage of $v_n = 2.88 \text{ mV}$. This value corresponds very well to the vertical shift of 3.25 mV applied to the numerical result in Fig. 3.6 and, therefore, thermal noise is considered to be a plausible explanation for the observed effect. In the time history of the experimental result (Figure 3.7), the effect of the noise can clearly be observed.

Next, measurements for higher V_{ac} values are considered. Some parameters in the numerical model are adjusted such that the simulated amplitude-frequency curves match the measured ones. Parameters that are allowed to change are damping parameter b , the mass m and the nonlinear stiffness parameters k_2 to k_5 . The resonator lumped mass m is allowed to change because for higher excitation values, a slightly different beam vibration shape may take place, such that, effectively, more mass of the beam is moving, resulting in a (very) small increase in lumped mass.

Results for ac excitation values of $V_{ac} = 87 \text{ mV}$ and $V_{ac} = 279 \text{ mV}$ are depicted in Figures 3.8–3.9 and 3.10–3.11, respectively. In Figures 3.8 and 3.10, the measured responses are denoted by black curves (solid for sweep up and dashed for sweep down). Furthermore, stable and unstable parts of the numerical amplitude-frequency curves (in grey) are indicated. Solid grey curves correspond to stable periodic solutions, whereas dashed grey curves correspond to unstable ones (not seen in measurements). The tran-

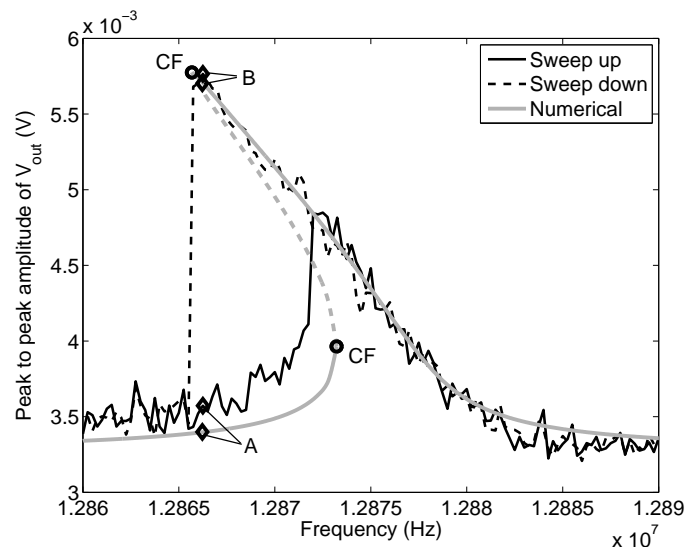


Figure 3.8 / Amplitude-frequency curve, $V_{dc} = 70 \text{ V}$, $V_{ac} = 87 \text{ mV}$.

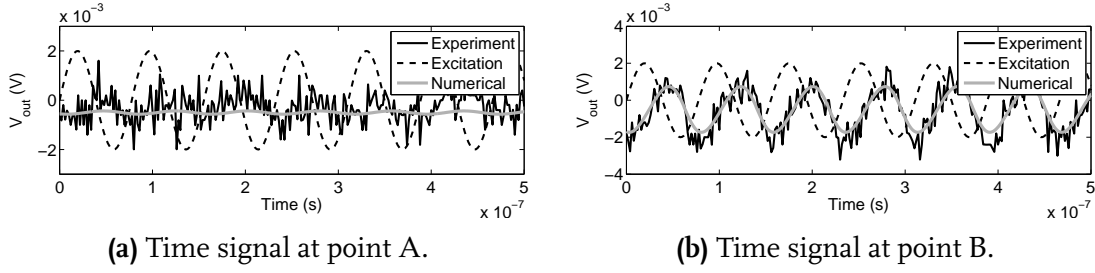


Figure 3.9 / Parts of time histories at selected points in Figure 3.8 at $f = 12.86625$ MHz.

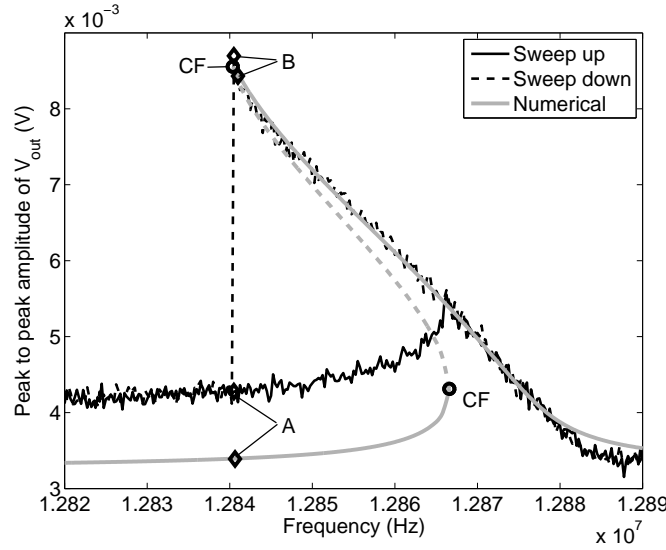


Figure 3.10 / Amplitude-frequency curve, $V_{dc} = 70$ V, $V_{ac} = 279$ mV.

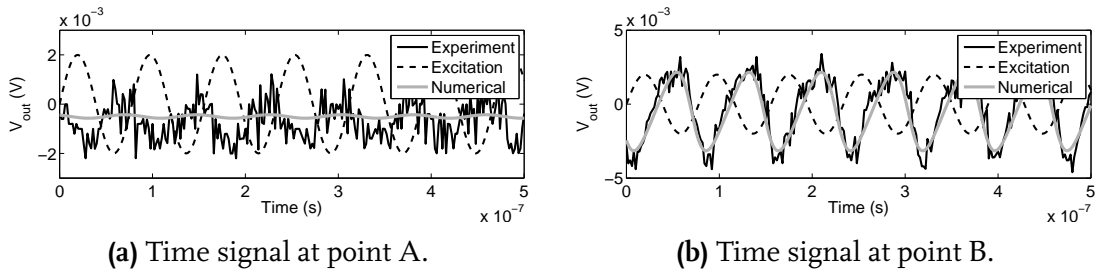


Figure 3.11 / Parts of time histories at selected points in Figure 3.10 at $f = 12.8405$ MHz.

sition between stable and unstable periodic solutions is characterised by cyclic fold (CF) bifurcations, see Section 2.4.3. The cyclic fold bifurcations in Figures 3.8 and 3.10 are responsible for sudden jumps in the measured amplitude-frequency behaviour during frequency sweeps (see also Figure 3.4). This can be understood by considering the numerical amplitude-frequency curves. Starting from a frequency below the fundamental resonance, the system's response follows the stable low amplitude branch if the excita-

tion frequency is increased until the lower CF point. From there, an increase in frequency makes the system ‘jump’ to the upper branch of stable solutions. This jump is clearly observed in the experimental curves. An analogous explanation holds for the sweep down behaviour by considering the upper CF bifurcation point.

A good quantitative match is obtained between the numerical and experimental results. The shape of the softening resonance peak can be predicted accurately, as well as the frequencies at which sudden jumps occur. Additionally, the time histories for points B on the stable high-amplitude branches match very well (Figures 3.9(b) and 3.11(b)). A clear distinction is present between the time histories at points A (Figs. 3.9(a) and 3.11(a)), in which thermal noise dominates, and the time histories at points B in which the noise is of significantly lower order than the periodic signal itself.

Furthermore, a discrepancy is present between the measured and simulated peak to peak values for excitation frequencies lower than the fundamental resonance, most clearly seen in Figure 3.10. Apart from the thermal noise considerations used for the linear response, other effects are also present, resulting in an additional offset between the numerical and experimental curves. In Chapter 6, the mismatch between the numerical and experimental curves at a frequency just above the resonance frequency is found to originate from an anti-resonance effect that can be captured using an improved description of the measurement circuit, see Section 6.4.4. However, in the heuristic modelling approach Chapter 3, this effect has not been included. Some discussion on this effect will follow in Section 3.2.4.

Parameters k_2 and k_4 of the nonlinear stiffness function (3.5) are not needed to match the peak to peak amplitudes of the simulation model to the experimental values. They are set to zero. This indicates that the mechanical stiffness function is symmetric around $x = 0$. This is expected, because the bias voltage V_{dc} is applied to both sides of the beam. In this way, the only parameters that vary between successive measurements are b , m , k_3 and k_5 , since they can be considered as ‘effective’ (lumped) parameters. The remaining parameters in (3.13) are assumed to be constant over changes in V_{ac} . Parameter variations as a function of the ac excitation amplitude V_{ac} are depicted in Figure 3.12. Parameters k_3 and k_5 remain relatively constant after a certain V_{ac} value. Due to limitations in the experimental setup, steps in V_{ac} are not uniform.

From this figure, it can be seen that the nonlinear stiffness terms have to be included from a certain V_{ac} value. Due to the very small characteristic flexural beam displacement x , the nonlinear stiffness parameters terms have large magnitudes: $k_3 = \mathcal{O}(10^{15}) \text{ N/m}^3$ and $k_5 = \mathcal{O}(10^{30}) \text{ N/m}^5$. Furthermore, k_3 and k_5 have different signs. The negative sign of k_3 indicates softening nonlinear behaviour, which is observed in Figure 3.8. This is not in line with analytical derivations of this coefficient as reported in Lifshitz and Cross (2008). Namely, both midplane stretching and the nonlinear material behaviour would result in hardening nonlinear behaviour. Instead, the additional softening that has to be included in the model has to be caused by the lumped description of the electrostatic forcing function $F_e(x, t)$, see (3.2), which is not accurate enough. This will also become clear in Chapters 5 and 6, where a first-principles description of the electrostatic forcing is derived that predicts the softening nonlinear behaviour better.

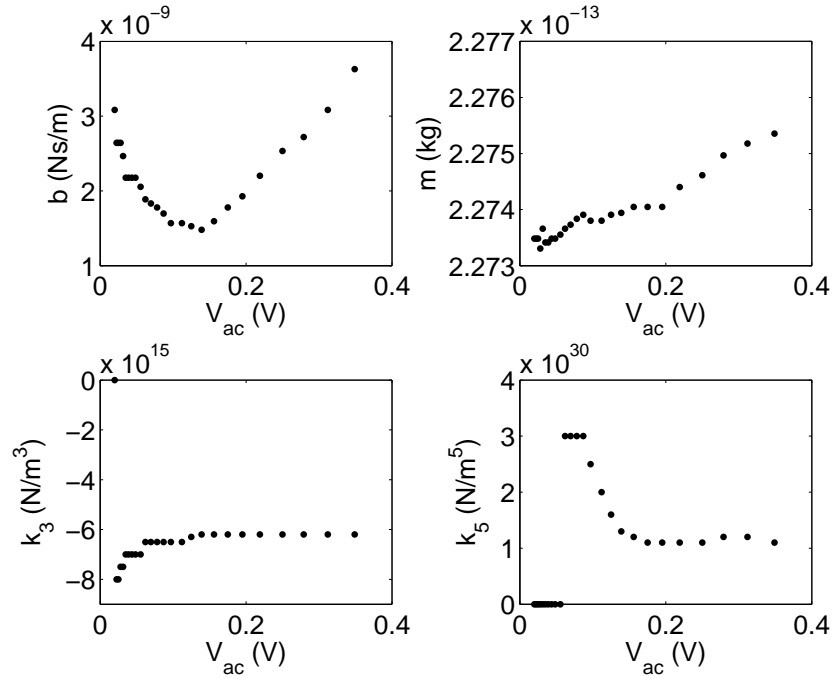


Figure 3.12 / Parameter variation as a function of the ac excitation voltage.

Furthermore, for large vibration amplitudes, the positive sign of k_5 (hardening) partly compensates for the softening effect of k_3 , since, near 12.845 MHz, the resonance peak slightly curves upwards, see Figure 3.10. In this way, it follows that both k_3 and k_5 have to be used in the model, which justifies the inclusion of higher order stiffness terms (3.5) in the modelling approach. The damping parameter b is used for fine-tuning the location of the cyclic fold bifurcation points such that they match the frequencies at which jumps in the experiment occur. Finally, it can be seen that the effective lumped mass of the resonator is hardly influenced by V_{ac} ; only it has to be slightly increased for large excitation values.

The parameter changes with the excitation parameter V_{ac} , although they are relatively small, emphasise/confirm that the modelling approach applied here is of heuristic nature. The Duffing-like modelling approach does not give analytical insight in how parameters will change with excitation parameters. A more fundamental modelling based on first principles will be necessary for this. This will be described in chapter 5.

In order to address the predictive value of the proposed modelling approach, amplitude-frequency curves have been calculated for a range of V_{ac} values using averaged values for the fitting parameters b , m , k_3 and k_5 . This is depicted in Figure 3.13, where, for three V_{ac} values, both the experimental and numerical response are depicted. For higher V_{ac} values, the response can be seen to become increasingly nonlinear. The calculated responses for the averaged parameter values qualitatively represent the dynamic behaviour of the resonator for a certain V_{ac} value. However, as indicated before, for the lumped modelling approach, the quantitative predictive nature of the model is limited.

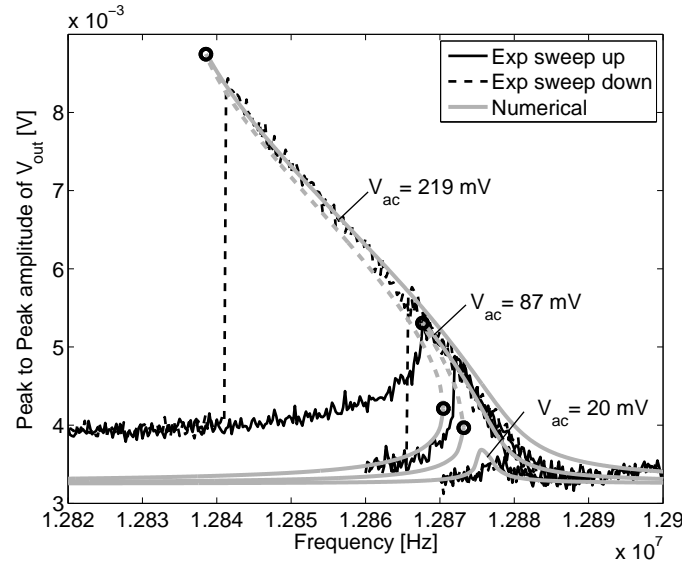


Figure 3.13 / Amplitude-frequency curves for various V_{ac} values, based on averaged values for the fitted parameters.

In order to investigate the influence of the ac excitation voltage on the size of the frequency hysteresis interval, the frequencies where the cyclic fold bifurcations occur are depicted versus V_{ac} in Figure 3.14. From this figure, it is observed that frequency hysteresis occurs for $V_{ac} > 28$ mV and that, for increasing V_{ac} , the hysteresis interval first increases but then decreases again for high V_{ac} values (≥ 200 mV).

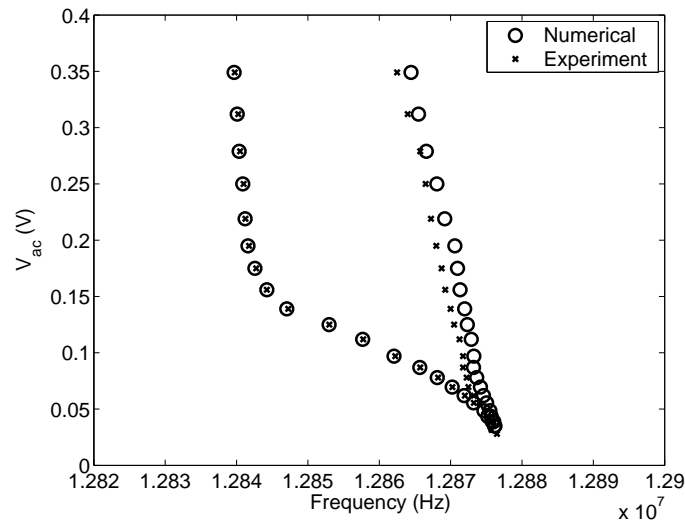


Figure 3.14 / Locus of cyclic fold bifurcations near the fundamental resonance.

Another phenomenon that has been observed in the experiments is the presence of a $1/2$ subharmonic resonance, which occurs at twice the first harmonic resonance frequency, near 25.753 MHz. For a $1/2$ subharmonic resonance, the fundamental frequency in the system response is half the excitation frequency (see also Figure 2.7(b) in Section 2.4.3). For excitation settings $V_{dc} = 70$ V and $V_{ac} = 350$ mV, the measured subharmonic resonance is depicted in Figure 3.15. The subharmonic resonance peak is initiated by two so-called period doubling (PD) bifurcations near $f = 25.753$ MHz, see the inset in Figure 3.15. In the $1/2$ subharmonic resonance peak (the upper branch of solutions), the resonator vibrates with a fundamental frequency (around 12.875 MHz) that is half the frequency of the excitation signal (around 25.75 MHz). This can also be seen from the time histories at point A, see Figure 3.16, in which the period time of the response (black solid line, labeled ‘experiment’) is twice that of the excitation (black dashed line). The numerical model is also capable of predicting these period doubling bifurcations and

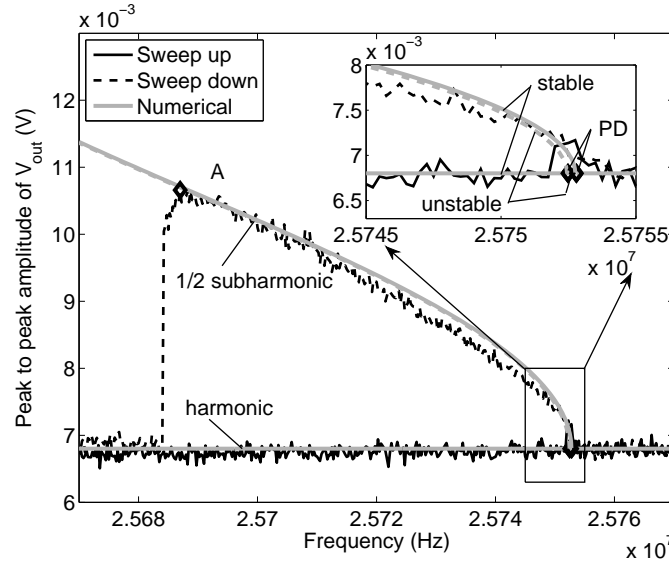


Figure 3.15 / Experimental $1/2$ subharmonic resonance, $V_{dc} = 70$ V, $V_{ac} = 350$ mV.

$1/2$ subharmonic solution branches for parameter values of $b = 4.625 \times 10^{-10}$ Ns/m, $k_3 = -8.0 \times 10^{15}$ N/m³ and $k_5 = 1.1 \times 10^{30}$ N/m⁵. The simulated amplitude-frequency plot is also depicted in Figure 3.15, together with the measured one. A vertical shift is applied in the numerical results in order to match the amplitudes of the harmonic branch. A good correspondence is present. However, using these parameter values, the match around the first harmonic resonance frequency of the resonator deteriorates, since too much softening behaviour is predicted. From the time history at point A in Figure 3.15, depicted in Figure 3.16, it is observed that both the experiment and the simulation show a periodic response with half the excitation frequency. However, the difference in shape between the experimental and numerical time history is significant. An explanation for this has not yet been found.

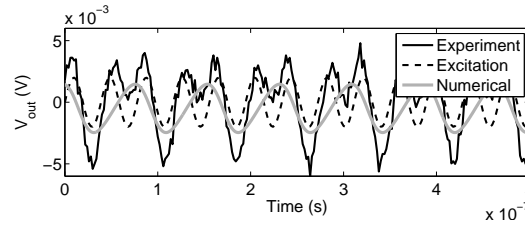


Figure 3.16 / Part of time history at point A in Figure 3.15 at $f = 25.687$ MHz. The system response has a base frequency of 12.844 MHz.

3.2.4 Discussion

The relatively simple dynamic model of the clamped-clamped beam resonator utilised here, is able to predict the measured resonator response for various parameter settings qualitatively and in many cases even quantitatively. The model is a typical example of a descriptive (heuristic) device level model (see, Section 1.2.2). Namely, the Duffing-based model has an a priori defined complexity and is able to predict characteristic nonlinear dynamic steady-state behaviour very well for the parameter settings used. Therefore, it represents a good first step in the modelling process and a suitable starting point for understanding and predicting the dynamic behaviour of MEMS resonators.

However, because of the heuristic nature of the proposed model, it is not capable of predicting the dynamic behaviour for a full range of excitation parameters. At each excitation setting, a best fit has been made in order to obtain an optimal match between simulation and experiment. At the bias voltage of $V_{dc} = 70$ V, already small parameter variations for changing ac excitation voltage are required for obtaining this best fit between the simulations and experiments. Therefore, the predictive nature of the heuristic model is rather limited. This suggests that a more fundamental, or first principles-based, modelling approach is required, which captures the subtle effects that have been observed under excitation parameter changes. In Chapter 5, the heuristic model of Section 3.2.2 will be extended to a first-principles based model for a similar resonator, based on the multiphysics modelling framework that will be derived in Chapter 4. Issues with respect to the lumped model for the clamped-clamped beam MEMS resonator that have become clear in this Section 3.2 will be treated in depth in the following chapters. These are the following:

- Different nonlinear effects that play a role have now been modelled in a descriptive way using a nonlinear stiffness function (3.5). In Chapters 4 and 5, individual contributions will be distinguished;
- Damping in the clamped-clamped beam resonator is now included using a single equivalent (overall) damping parameter b . Individual effects that contribute to the damping will be described and included in the first-principles based approach;
- The offset between the simulated and measured response in Figure 3.10 will be clarified. It is found to originate from an anti-resonance caused by the electrical

circuit of the resonator. This effect will be included in an improved description of the measurement circuit of the resonator, see Section 6.4.4. This will also have implications for the thermal noise considerations used for the lumped model (see Section 3.2.2).

3.3 Case study II: dog-bone MEMS resonator

The second case study concerns a bulk or longitudinal so-called dog-bone MEMS resonator. This type of resonator is based on piezoresistive readout (see Section 4.3.7) and has been designed and fabricated at the NXP-TSMC Research Center, see for instance van Beek et al. (2006), van Beek et al. (2007) and Phan et al. (2009). A more detailed description of the approach applied in this section can be found in van den Hoven (2008).

Similar to the approach used for case study I, in this section, modelling efforts for the dog-bone MEMS resonator are presented. Based on experimentally observed nonlinear dynamic behaviour, a partly heuristic model is proposed for this resonator. A model structure will be used which is rooted in a finite element description and which has a pre-defined complexity. Compared to the heuristic model presented in Section 3.2, so far a (complete) match between the model and experiments has not been obtained.

The outline for this case study II is as follows. First, in Section 3.3.1, a description of the dog-bone resonator will be given and experimental results for this resonator will be presented. Next, in Section 3.3.2, the partly heuristic modelling approach that may describe the dynamic effects observed in the measurements will be presented very briefly. This section will not provide an extremely detailed model derivation, but will mainly sketch the applied modelling approach. From simulation results, given in Section 3.3.3, it will become clear that the proposed model cannot describe the experimentally observed behaviour very well. Section 3.3 is concluded with a discussion.

3.3.1 Experiments using a dog-bone resonator

Resonator description

The dog-bone resonator under investigation is a single-crystal silicon longitudinal, or bulk resonator. A photo of a dog-bone resonator and its connections is depicted in Figure 3.17(a). The resonator is produced from SOI wafers, using the same process as described in Section 3.2.1 for the clamped-clamped beam MEMS resonator. A close-up view of the dog-bone resonator is depicted in Figure 3.17(b). This resonator consists of two masses (resonator heads) that are connected by two parallel beams. Each beam is connected to the fixed layer world by one support. Holes in the resonator heads are present for etching the oxide layer of the SOI wafer.

A schematic representation of the dog-bone resonator, similar to Figure 3.17(b) is depicted

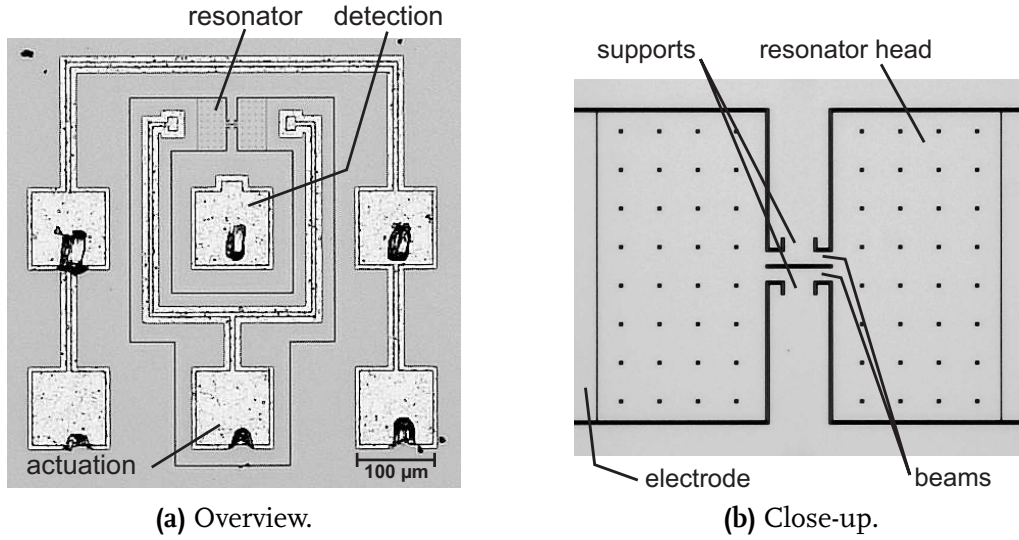


Figure 3.17 / Pictures of the dog-bone resonator.

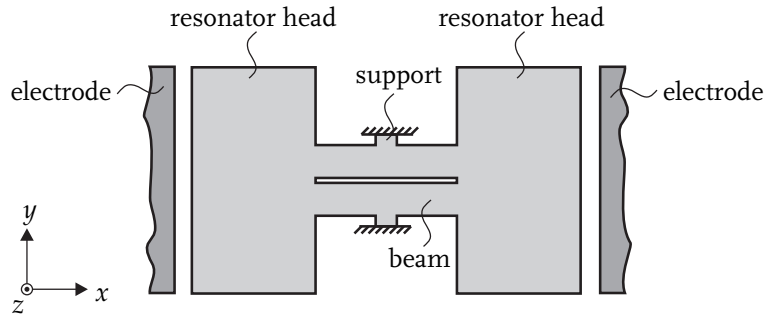


Figure 3.18 / Schematic representation of the dog-bone resonator.

in Figure 3.18. The resonator x - and y -direction are oriented along the $[100]$ and $[010]$ direction in the single crystal silicon, respectively (see also Appendix A.1.1). On the left and right side of the resonator, electrodes are present which are used for electrostatic actuation. The intended motion of the resonator consists of longitudinal stretching in the x -direction, in which the two heads of the resonator vibrate in anti-phase. In this way, anchor loss through the supports is supposed to be less than for the clamped-clamped beam resonator, which should result in a high Q -factor, see also (4.14) in Section 4.3.3. Furthermore, as can be seen in Figures 3.17(b) and 3.18, the resonator heads are quite large and are suspended through small beams. As a result, the dog-bone resonator has a low out-of-plane stiffness and may show out-of-plane vibrations (in z -direction), which are undesired. In order to excite the desired mode of the dog-bone resonator, both a bias voltage V_{dc} and an ac voltage amplitude V_{ac} are applied over the electrode gaps. The bias voltage is used for pre-stressing the resonator, whereas the ac voltage drives the resonator into vibration. Both the resonator heads and the beams stretch due to the excitation. However, the deformation in the resonator heads is substantially smaller than the deformation in the beams. Typical resonance frequencies for the desired bulk (longitudinal) mode of the resonator range from 10 to 25 MHz.

Amplitude-frequency curves

For the experiments, the same custom-built set-up (available at the NXP-TSMC Research Center) is used as for the clamped-clamped beam MEMS resonator, see Section 3.2. The dog-bone resonator is located in a vacuum chamber (pressure $p = 4.6 \times 10^{-4}$ mbar). The steady-state dynamic behaviour of the dog-bone resonator is investigated experimentally by constructing amplitude-frequency plots. For this purpose, the ac excitation frequency f is swept up and down around the bulk mode vibration frequency of the resonator. The output of the resonator is detected piezoresistively (see also Section 4.3.7), by sending a current of 1 to 3 mA through the beams of the resonator. This is schematically depicted in Figure 3.19. Due to deformation of the resonator, the beams are stretched and compressed, which causes a change in their resistance values. This resistance change is measured as a voltage change in V_{out} , of which only the ac component is measured, using a bias tee, see Figure 3.19.

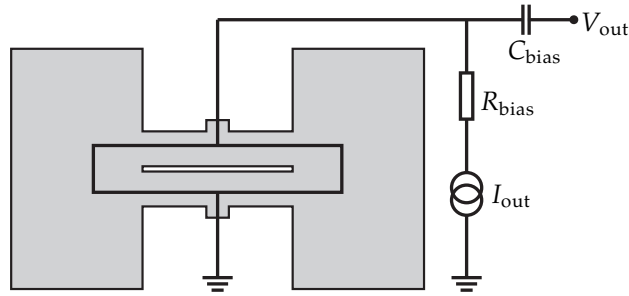


Figure 3.19 / Measurement circuit and current path through the resonator .

Two typical amplitude-frequency responses that have been measured for the dog-bone resonator are depicted in Figure 3.20. In Figure 3.20(a), the dog-bone resonator response shows no frequency hysteresis. For both the sweep up and the sweep down, an almost similar response is observed. For a higher V_{ac} -value, for which the amplitude-frequency curve is depicted in Figure 3.20(b), frequency hysteresis is observed. The response of the resonator depends on the direction in which a frequency sweep is performed: when the resonator is excited at, for instance, 15.335 MHz, the response may have a peak to peak amplitude of either 0.31 V or 1.56 V, depending on the excitation history. Furthermore, apparently a plateau for the amplitude is present for the high-amplitude solution during the frequency sweep down.

Additionally, the time signals in certain frequency regions of the plateau show low-frequent beating of the high-frequent response. Such a typical beating response is depicted in Figure 3.21, which shows the measured piezoresistive output voltage at an excitation frequency of 15.335 MHz for the sweep down.

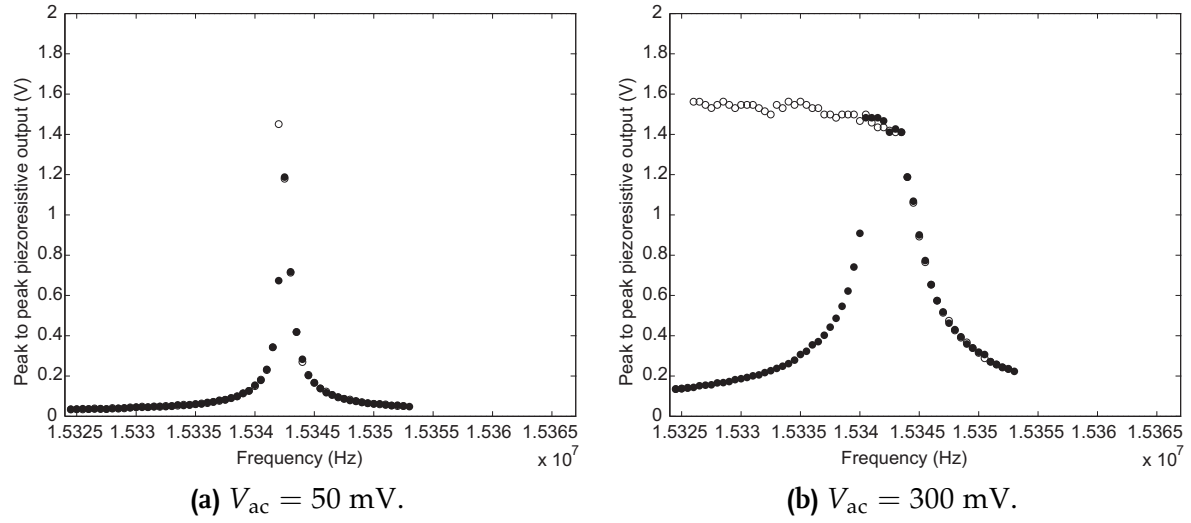


Figure 3.20 / Amplitude-frequency curves at a bias voltage of $V_{dc} = 45 \text{ V}$ and two different V_{ac} -values. \bullet : sweep up; \circ : sweep down.

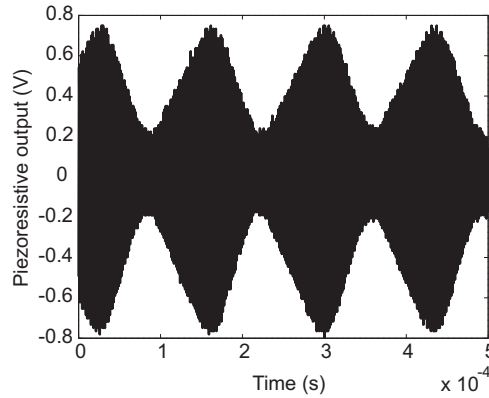


Figure 3.21 / Typical time history showing beating behaviour.

Mode coupling between in-plane and out-of-plane modes

The experimentally observed beating phenomenon depicted in Figure 3.21 is probably caused by an energy exchange between the desired in-plane mode and some undesired out-of-plane mode(s). This may be a phenomenon called mode coupling. According to, for instance, Iwatsubo and Saigo (1973), Roberts and Cartmell (1984) or Cartmell and Roberts (1988), mode coupling may appear in a nonlinear, parametrically driven system, such as the dog-bone resonator, when linear combinations of harmonic resonance frequencies of vibration modes are near the excitation frequency or near the harmonic frequency of the desired vibration mode. In that case, coupling of vibration modes may occur when (see Nayfeh and Mook, 1977):

$$nf_1 \approx f_i \pm f_j, \quad n \in \mathbb{N}, \quad (3.14)$$

where f_1 denotes the harmonic resonance frequency of the desired mode (in this case, the in-plane mode) and where f_i and f_j denote harmonic resonance frequencies of two other modes (which could be out-of plane, in this case).

In order to experimentally investigate the energy exchange and the possibly nonlinear mode coupling effect, experiments have been carried out using a Polytec MSA-400 Micro System Analyzer. This system can be operated as a laser-doppler vibrometer and is able to determine out-of-plane displacements in microsystems with frequencies from 50 kHz up to 20 MHz. The vibrometer measures only in the z -direction (see Figure 3.18), thereby ignoring x - and y -displacements. As stated before, in-plane vibrations (in x -direction) are detected piezoresistively.

Mode coupling is investigated by measuring the piezoresistive in-plane response and the out-of-plane displacement (by integrating the velocities measured with the vibrometer). By means of an external trigger, the two signals are measured simultaneously, such that information on the phase between them can be obtained.

For the measurements, which will be described next, different dog-bone resonators are used. The excitation settings are $V_{dc} = 35$ V and $V_{ac} = 100$ mV and the excitation frequency is set to $f = 16.7724$ MHz. In Figure 3.22, both the in-plane and out-of-plane time signals are displayed. The maximum out-of-plane displacement is thus 34 nm. Although the vertical axes of the graphs in Figure 3.22 do not have the same unit, it can be seen that some kind of energy exchange is present between in-plane and out-of-plane movements. An increase in out-of-plane displacement is related to a decrease in the piezoresistive response. Spectral analysis of the out-of-plane signal (Figure 3.22) in the Polytec system reveals that the out-of-plane movements mainly consist of a 7.25 MHz and a 9.52 MHz contribution. Note that the sum of the out-of-plane response frequencies equals the in-plane excitation frequency indicating that some kind of mode coupling,

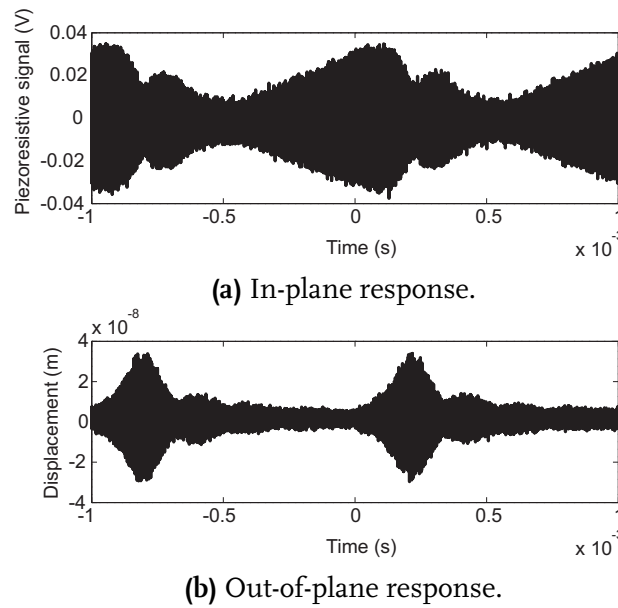


Figure 3.22 / Measured piezoresistive in-plane signal and out-of-plane displacement.

according to (3.14) may be present.

For a different dog-bone resonator, with a nominal desired in-plane resonance frequency around 19.13 MHz, similar behaviour has been observed. Again, the out-of-plane response has been measured using the laser vibrometer system. An example of a typical shape of the out-of-plane motion measured for this resonator is depicted in Figure 3.23. The excitation settings are $V_{dc} = 86.5$ V and $V_{ac} = 150$ mV with an excitation frequency already mentioned above. The frequency of the observed out-of-plane mode is much lower, 494 kHz, but the vibration displacement is substantial: up to 46.15 nm. Again, this shows that some coupling mechanism is present between (desired) in-plane vibration modes and (undesired) out-of-plane modes.

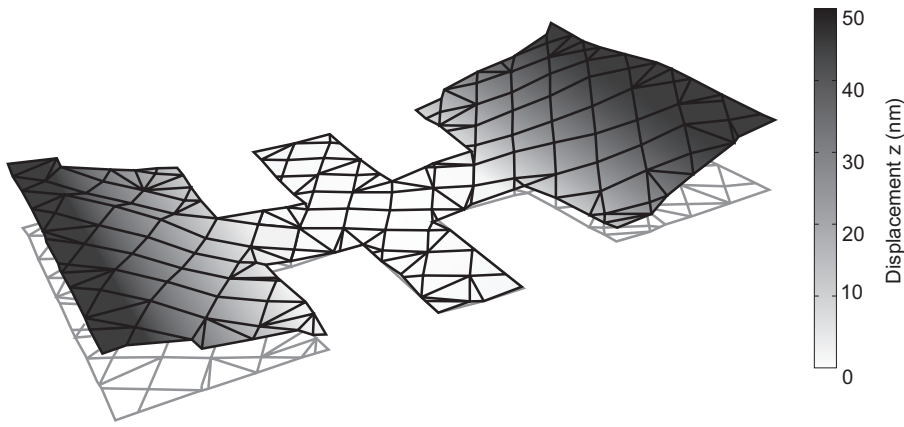


Figure 3.23 / Measured out-of-plane displacement of a resonator with a resonance frequency around 19.13 MHz. In grayscale, the out-of-plane displacement profile of the resonator is depicted at maximum displacement. The grey mesh indicates the undeformed shape.

3.3.2 Modelling approach

In this section, the partly heuristic modelling approach that has been applied for the dog-bone MEMS resonator will be described briefly. As stated before, the applied approach will not lead to a good match between the simulations and experiments. The interested reader is referred to van den Hoven (2008) for a detailed description of the model derivation. For case study I, described in Section 3.2, experimentally observed frequency hysteresis demanded for a Duffing-based heuristic model. However, for the experimentally observed behaviour of the dog-bone resonator, described in Section 3.3.1, it is more difficult to assume a specific model structure beforehand. Although a periodically forced van der Pol oscillator with cubic stiffness, or a two DOF periodically forced model with internal resonances, see (3.14), may show frequency hysteresis (Figure 3.20) and beating behaviour (Figure 3.21), a different approach will be utilised in this section.

The following partly heuristic modelling approach will be applied. Since coupling be-

tween in-plane and out-of plane modes is experimentally observed, a 2D model description that is able to couple vibration modes in x -direction to vibrations modes in z -direction, is followed. In this approach, a finite element description for the dog-bone resonator is used for determining the linear natural frequencies and eigenmodes. Next, a nonlinear strain-displacement relation will be applied for coupling the in-plane and out-of-plane vibrations. Out-of-plane excitation will be introduced by a lumped description for the electrostatic forces and moments for tapered electrodes. Finally, the numerical implementation of the model will be described.

Vibration modes

A detailed drawing of the dog-bone resonator and its dimensions is depicted in Figure 3.24. Gaps between the resonator heads and the electrodes are denoted by d_1 and d_2 , for resonator heads 1 and 2, respectively. A set of nominal dimensions is used for modelling the dynamic behaviour of the dog-bone resonator. The dimensions are listed in Table 3.2. These dimensions correspond to dog-bone resonator, that is symmetric around $x = 0$, since $w_1 = w_4$, $l_1 = l_4$, $w_2 = w_3$ and $l_2 = l_3$. In practice, asymmetry may be present due to production tolerances.

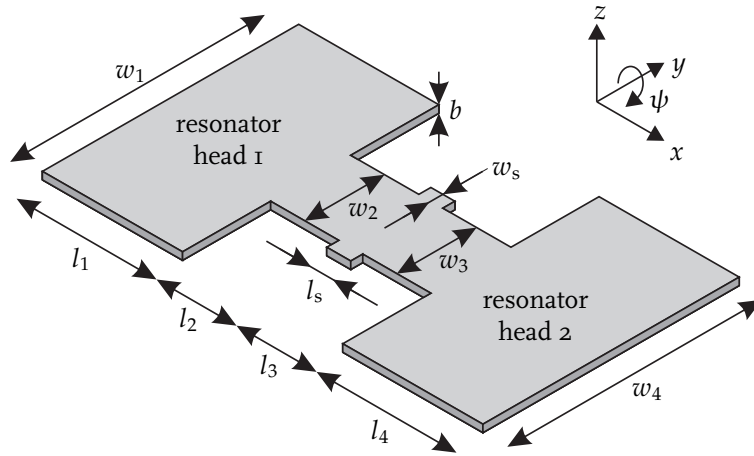


Figure 3.24 / Schematic 2D representation of the dog-bone resonator.

In order to describe the resonator in a finite element formulation, it is divided into n beam elements in x -direction. Each element has 2 nodes, such that a total of $n + 1$ nodes is obtained. Each node of an element has three DOF, displacements in x - and z -direction and rotation ψ around the y -axis, see Figure 3.24. Therefore, the model has a total of $3n + 3$ DOF. Displacement in the y -direction is not modelled. The gap in the resonator, see Figures 3.17(b) and 3.18, is not explicitly included in the model (the parallel beams connecting the resonator heads are modelled as a single beam).

Each of the beam elements contributes to the total mass and stiffness matrix. The specific contribution depends on the type of element that is selected. For the resonator

Table 3.2 / Nominal dimensions of the dog-bone resonator.

Parameter	Value (μm)	Parameter	Value (μm)
l_1	35	w_1	64
l_2	20	w_2	20
l_3	20	w_3	20
l_4	35	w_4	64
l_s	6	w_s	3
$d_1 = d_2$	335	b	1.5

considered here, Timoshenko beam elements are chosen, which take into account the effect of shear deformation in z -direction. The element mass and stiffness matrices, which can be found, for instance, in Przemieniecki (1968), are assembled into the system mass and stiffness matrix. Furthermore, the influence of the suspension of the beams of the resonator, having dimensions w_s and l_s , (see Figure 3.24) is accounted for by adding additional mass and stiffness terms to the corresponding nodes in the assembled mass and stiffness matrix. For the suspension, also Timoshenko beam elements are used (van den Hoven, 2008). Material parameters that are used for the element matrices are given in Table 3.3.

Table 3.3 / Physical parameter values for the dog-bone resonator.

Parameter	Value	Unit
ρ	2329	kg m^{-3}
E	130.02	GPa
G	79.51	GPa
ν	0.2785	(-)

By means of the assembled system mass matrix \mathbf{M} and stiffness matrix \mathbf{K} , where $\mathbf{M}, \mathbf{K} \in \mathbb{R}^{(3n+3) \times (3n+3)}$, the undamped, free vibrations of the system can be derived from the following equation of motion:

$$\mathbf{M}\ddot{\mathbf{x}} + \mathbf{K}\mathbf{x} = \mathbf{0}, \quad (3.15)$$

where $\mathbf{x} = [x_1 \ z_1 \ \psi_1 \ \dots \ x_{n+1} \ z_{n+1} \ \psi_{n+1}]^T$, $\mathbf{x} \in \mathbb{R}^{(3n+3)}$ denotes the column with the nodal displacements in x and z -direction and rotation ψ around the y -axis. Solution of the undamped eigenvalue problem:

$$[-(2\pi f_i)^2 \mathbf{M} + \mathbf{K}] \boldsymbol{\phi}_i = \mathbf{0}, \quad (3.16)$$

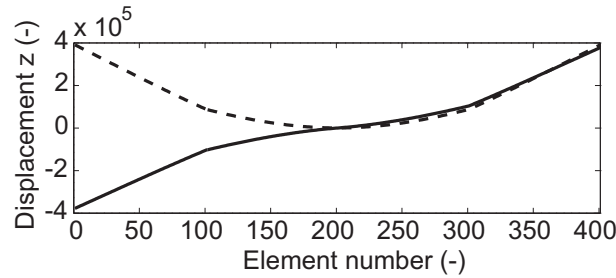
yields $3n + 3$ eigenfrequencies f_i and eigenmodes $\boldsymbol{\phi}_i$. The eleven lowest eigenfrequencies are listed in Table 3.4. The eleventh eigenfrequency is listed to show that frequencies for higher modes rapidly increase. The natural frequencies have been calculated for a finite element discretisation in the x -direction using $n = 400$ elements. Each part, with

Table 3.4 / Eigenfrequencies corresponding to the lowest eleven modes of the 2D dog-bone resonator model for the parameter values listed in Tables 3.2 and 3.3.

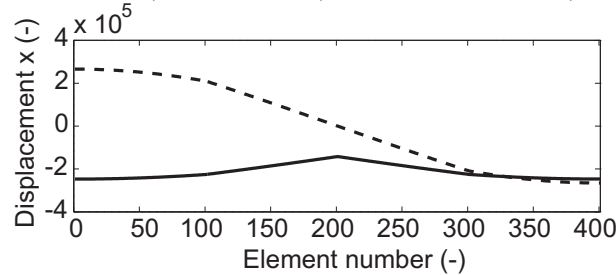
Mode	f_i (MHz)	Direction
1	0.280188	out-of-plane
2	0.355752	out-of-plane
3	2.787124	out-of-plane
4	3.241353	out-of-plane
5	9.318476	out-of-plane
6	10.158065	out-of-plane
7	14.351257	in-plane
8	18.907414	out-of-plane
9	20.575010	out-of-plane
10	22.653739	in-plane
11	30.204426	out-of-plane

length l_i , $i = 1, 2, 3, 4$ (see Figure 3.24), has been divided into 100 elements in x -direction.

A graphical representation of modes 1 and 2, and modes 7 and 10 is depicted in Figure 3.25. These correspond to the first two out-of-plane modes and the first two in-plane modes, respectively. The eigenmodes are normalised with respect to the mass matrix. Note that the linear in-plane and out-of-plane modes are uncoupled. Mode 10 (dashed line in Figure 3.25(b)) is the desired mode of the dogbone resonator. This mode corresponds to an anti-symmetric motion in x -direction around the middle node (node 201).



(a) First (mode 1, solid line) and second (mode 2, dashed line) out-of-plane modes.



(b) First (mode 7, solid line) and second (mode 10, dashed line) in-plane modes.

Figure 3.25 / First two out-of-plane (a) and in-plane (b) modeshapes. Modes are mass-matrix normalised and mode numbers refer to Table 3.4.

The second out-of-plane mode corresponds with the experimentally observed vibration shape in Figure 3.23. The four modes, depicted in Figure 3.25 will be used for introducing coupling between in-plane and out-of-plane vibrations later. Notice the piecewise continuous nature of the eigenmodes at noted 101 and 301, due to the discontinuity in width between the resonator beams and heads, see Figure 3.24.

Excitation: electrostatic forces and moments

As stated earlier, the desired in-plane vibration mode of the dog-bone resonator is actuated electrostatically. Both a bias voltage V_{dc} and an ac voltage with amplitude V_{ac} and excitation frequency f are applied to the electrodes of the resonator:

$$V(t) = V_{dc} + V_{ac} \sin(2\pi ft) \quad (3.17)$$

The electrostatic force resulting from the voltage difference over the electrode gap, depends on the gap size. It acts on the first and the last node in the finite element model. The distance between the electrodes and the resonator is not completely constant in the z -direction, due to the production process. Therefore, the gap may not be constant in z direction, since both the resonator head and the electrodes have a slightly slanted face, see Figure 3.26. This effect is called tapering and it results in out-of-plane excitation. Namely, since the electrostatic force varies over the gap height, next to the electrostatic force in the x -direction, also a bending moment around the y -axis and a force in the z -direction is introduced on the first and the last node in the model. In a first approximation for the model, it will be assumed that the electrostatic field lines will remain directed in the x -direction, such that the electrostatic force in the z -direction will be zero.

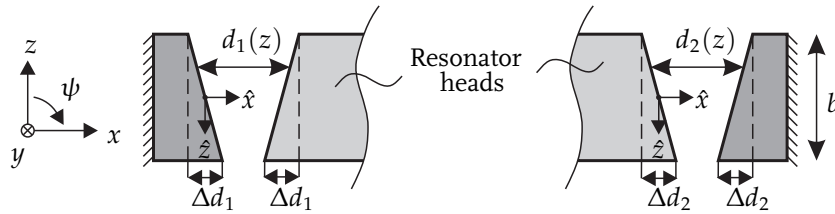


Figure 3.26 / Tapering of the gaps between resonator heads and electrodes. Local coordinates \hat{x} and \hat{z} are introduced for describing the tapering.

The electrostatic forces in x -direction, $F_1(x_1)$ and $F_{n+1}(x_{n+1})$, acting on the first and last node in the model, respectively, vary with the z direction due to tapering. Therefore, they can be elaborated as an integral expression over the gap height:

$$F_1(x_1) = -\frac{\epsilon_0 w_1 V^2}{2} \int_{-\frac{b}{2}}^{\frac{b}{2}} \frac{1}{(d_1(\hat{z}) + x_1)^2} d\hat{z} = -\frac{\epsilon_0 b w_1 V^2}{2(d_1 - \Delta d_1 + x_1)(d_1 + \Delta d_1 + x_1)}, \quad (3.18a)$$

$$F_{n+1}(x_{n+1}) = \frac{\epsilon_0 w_4 V^2}{2} \int_{-\frac{b}{2}}^{\frac{b}{2}} \frac{1}{(d_2(\hat{z}) - x_{n+1})^2} d\hat{z} = \frac{\epsilon_0 b w_4 V^2}{2(d_2 - \Delta d_2 - x_{n+1})(d_2 + \Delta d_2 - x_{n+1})}, \quad (3.18b)$$

where $\epsilon_0 = 8.854 \cdot 10^{-12}$ F/m is the permittivity in vacuum and where the gaps are described in terms of their local coordinate \hat{z} :

$$d_1(\hat{z}) = d_1(0) - \frac{2\Delta d_1}{b}\hat{z}, \quad d_2(\hat{z}) = d_2(0) - \frac{2\Delta d_2}{b}\hat{z}, \quad (3.19)$$

see Figure 3.26. In (3.18), d_1 and d_2 are used as shorthand notation for $d_1(0)$ and $d_2(0)$. Since the electrostatic excitation varies in the z -direction, it exerts a bending moment on the first and last node. These moments $M_1(x_1)$ and $M_{n+1}(x_{n+1})$ can be elaborated in a similar way as the forces $F_1(x_1)$ and $F_{n+1}(x_{n+1})$:

$$\begin{aligned} M_1(x_1) &= \frac{\epsilon_0 w_1 V^2}{2} \int_{-\frac{b}{2}}^{\frac{b}{2}} \frac{\hat{z}}{(d_1(\hat{z}) + x_1)^2} d\hat{z}, \\ &= \frac{\epsilon_0 b^2 w_1 V^2}{8} \left(\frac{1}{(d_1 - \Delta d_1 + x_1)\Delta d_1} + \frac{\ln(d_1 - \Delta d_1 + x_1)}{\Delta d_1^2} \right. \\ &\quad \left. + \frac{1}{(d_1 + \Delta d_1 + x_1)\Delta d_1} - \frac{\ln(d_1 + \Delta d_1 + x_1)}{\Delta d_1^2} \right), \end{aligned} \quad (3.20a)$$

$$\begin{aligned} M_{n+1}(x_{n+1}) &= -\frac{\epsilon_0 w_4 V^2}{2} \int_{-\frac{b}{2}}^{\frac{b}{2}} \frac{\hat{z}}{(d_2(\hat{z}) - x_{n+1})^2} d\hat{z}, \\ &= -\frac{\epsilon_0 b^2 w_4 V^2}{8} \left(\frac{1}{(d_2 - \Delta d_2 - x_{n+1})\Delta d_2} + \frac{\ln(d_2 - \Delta d_2 - x_{n+1})}{\Delta d_2^2} \right. \\ &\quad \left. + \frac{1}{(d_2 + \Delta d_2 - x_{n+1})\Delta d_2} - \frac{\ln(d_2 + \Delta d_2 - x_{n+1})}{\Delta d_2^2} \right), \end{aligned} \quad (3.20b)$$

where $d_1(\hat{z})$ and $d_2(\hat{z})$ are given in (3.19).

Coupling between in-plane and out-of-plane modes

Apart from the bending moments due to tapering (3.20), no other coupling between in-plane and out-of-plane modes is present, since the eigenmodes are decoupled. However, such a coupling or energy exchange between in-plane and out-of-plane modes has been observed in the experiments. This coupling has to be caused by some excitation mechanism, which can be either direct (due to tapering) or parametric. From some initial simulations with the model, it has become clear that excitation of out-of-plane modes cannot be described by the direct excitation due to tapering only. Therefore, the in-plane and out-of-plane modes of the dog-bone resonator will be coupled through a nonlinear strain-displacement relation. For this purpose, the strain ϵ_x in x -direction is described as (Reddy and Singh, 1981):

$$\epsilon_x = \frac{\partial u}{\partial x} + \frac{1}{2} \left(\frac{\partial w}{\partial x} \right)^2 - z \frac{\partial^2 w}{\partial x^2}. \quad (3.21)$$

In the derivation of the model, which will be described next, the first two in-plane and out-of-plane modes of the dog-bone resonator (see Figure 3.25) will be used. This combination

of eigenmodes does not obey coupling relation (3.14), but mode 2 does resemble the experimentally observed vibration quite well, see Figure 3.23.

The nonlinear (coupled) equations of motion for the dog-bone resonator will be derived using Lagrange's equations (Meirovitch, 2001; Thomsen, 2003):

$$\frac{d}{dt} \left(\frac{\partial \mathcal{T}}{\partial \dot{\mathbf{q}}} \right) - \frac{\partial \mathcal{T}}{\partial \mathbf{q}} + \frac{\partial \mathcal{U}_{\text{in}}}{\partial \mathbf{q}} = \mathbf{F}_{\text{nc}}^T, \quad (3.22)$$

where \mathcal{T} denotes the kinetic energy, \mathcal{U}_{in} denotes the internal or strain energy and \mathbf{F}_{nc} denotes a column with generalised forces and moments. Column $\mathbf{q} = [q_1 \ q_2 \ q_7 \ q_{10}]^T$ contains the time-dependent generalised coordinates of the first two out-of-plane modes (q_1 and q_2) and the first two in-plane modes (q_7 and q_{10}). Note that the index corresponds with the mode number as listed in Table 3.4.

The kinetic energy \mathcal{T} and the strain energy \mathcal{U}_{in} of the dog-bone resonator with volume \mathcal{V} can be calculated from:

$$\mathcal{T} = \frac{1}{2} \rho \int_{\mathcal{V}} (\dot{u}^2 + \dot{w}^2) d\mathcal{V}, \quad (3.23)$$

$$\mathcal{U}_{\text{in}} = \frac{1}{2} \int_{\mathcal{V}} E \varepsilon_x^2 d\mathcal{V}, \quad (3.24)$$

where u and w describe the displacement fields in the x - and z direction of the resonator, respectively, and where E denotes Young's modulus. The generalised non-conservative forces and moments will be elaborated later. In (3.24), the term ε_x denotes the strain in x -direction.

In order to evaluate the expressions for the kinetic energy (3.23) and strain energy (3.24), expressions based on temporal and spatial derivatives of the displacement fields u and w have to be integrated over the resonator volume \mathcal{V} . These displacement fields will be based on the previously calculated eigenmodes related to the first two in-plane ($\boldsymbol{\phi}_7$ and $\boldsymbol{\phi}_{10}$) and out-of-plane ($\boldsymbol{\phi}_1$ and $\boldsymbol{\phi}_2$) vibration shapes of the dog-bone resonator, see Table 3.4 and Figure 3.25. Since no analytical expressions are available for the eigenmodes, each of them will be approximated by sixth-order piecewise continuous polynomials. The polynomials are piecewise continuous due to the piecewise nature of the eigenmodes. Namely, the x -direction is divided into four parts having length l_i , $i = 1, 2, 3, 4$, see Figure 3.24. In this way, u and w can be approximated by separation of variables as follows:

$$u(x, t) = q_7(t) \alpha_7(x) + q_{10}(t) \alpha_{10}(x), \quad (3.25a)$$

$$w(x, t) = q_1(t) \alpha_1(x) + q_2(t) \alpha_2(x), \quad (3.25b)$$

where the piecewise continuous polynomials $\alpha_i(x)$ are given by:

$$\alpha_i(x) = \begin{cases} \alpha_{i,1}(x), & x \in [-(l_1 + l_2), -l_2], \\ \alpha_{i,2}(x), & x \in [-l_2, 0], \\ \alpha_{i,3}(x), & x \in [0, l_3], \\ \alpha_{i,4}(x), & x \in [l_3, l_3 + l_4]. \end{cases} \quad \text{for } i = 1, 2, 7, 10. \quad (3.26)$$

At the boundaries, the modeshapes are continuous, implying $\alpha_{i,1}(-l_2) = \alpha_{i,2}(-l_2)$, $\alpha_{i,2}(0) = \alpha_{i,3}(0)$ and $\alpha_{i,3}(l_3) = \alpha_{i,4}(l_3)$. For the sake of convenience, the arguments of (3.25) will be omitted in the following.

By using the displacement fields (3.25) and the expressions for the modeshapes (3.26), the kinetic energy and the internal energy can be evaluated, by splitting them in parts. This yields for the kinetic energy:

$$\mathcal{T} = \frac{\rho b}{2} \left[w_1 \int_{-(l_1+l_2)}^{l_2} (\dot{u}^2 + \dot{w}^2) dx + w_2 \int_{-(l_2)}^0 (\dot{u}^2 + \dot{w}^2) dx + w_3 \int_0^{l_3} (\dot{u}^2 + \dot{w}^2) dx + w_4 \int_{l_3}^{(l_3+l_4)} (\dot{u}^2 + \dot{w}^2) dx \right]. \quad (3.27)$$

Note that the kinetic energy is independent of \mathbf{q} , which yields $\frac{\partial \mathcal{T}}{\partial \mathbf{q}} = \mathbf{0}$ in (3.22). For the potential energy, a similar approach is used, where (3.25) is used in the expression for ε_x , see (3.21). Additionally, terms related to the support stiffness are included. Details can be found in van den Hoven (2008).

The column \mathbf{F}_{nc} with generalised nonconservative forces contains damping forces as well as expressions related to the electrostatic forces and moments, see (3.18) and (3.20). The damping forces are derived from a so-called Rayleigh dissipation function \mathcal{R} , see, for instance, Mallon et al. (2006), which reads (based on mass-matrix normalised eigenmodes):

$$\mathcal{R}(\dot{\mathbf{q}}) = \frac{1}{2} \int_{-(l_1+l_2)}^{(l_3+l_4)} \left[b_1 \left(\dot{q}_1 \frac{\partial w}{\partial q_1} \right)^2 + b_2 \left(\dot{q}_2 \frac{\partial w}{\partial q_2} \right)^2 + b_7 \left(\dot{q}_7 \frac{\partial u}{\partial q_7} \right)^2 + b_{10} \left(\dot{q}_{10} \frac{\partial u}{\partial q_{10}} \right)^2 \right] dx, \quad (3.28)$$

where $b_i = 2\xi_i\omega_i$, $i = 1, 2, 7, 10$ contain non-dimensional damping coefficients ξ_i for the respective modes. The generalised forces related to damping can be found from $\mathbf{F}_{\text{nc,damping}}^T = -\frac{\partial \mathcal{R}}{\partial \dot{\mathbf{q}}}$. For the electrostatic forces (3.18) and moments (3.20), the displacements x_1 and x_{n+1} are needed. These are found by evaluating the in-plane displacement u (3.25a) at $x = -(l_1 + l_2)$ and at $x = l_3 + l_4$, respectively. A detailed expression for the derivation of \mathbf{F}_{nc} can be found in van den Hoven (2008).

By using Lagrange's equations (3.22), the four coupled equations of motion for the dog-bone resonator can be derived. The system of ODEs can be written as:

$$\mathbf{M}\ddot{\mathbf{q}} + \mathbf{f}_{\text{in}}(\mathbf{q}) = \mathbf{F}_{\text{nc}}(\mathbf{q}, \dot{\mathbf{q}}, t), \quad (3.29)$$

where $\mathbf{M} \in \mathbb{R}^{4 \times 4}$ denotes the mass matrix, $\mathbf{f}_{\text{in}}(\mathbf{q}) \in \mathbb{R}^4$ denotes the column with internal nonlinear elastic forces, including the coupling between in-plane and out-of-plane deformations. $\mathbf{F}_{\text{nc}}(\mathbf{q}, \dot{\mathbf{q}}, t) \in \mathbb{R}^4$ is the column with non-conservative damping and electrostatic forces (which are time dependent due to $V(t)$). Further details can be found in van den Hoven (2008).

Numerical approach

Similar to the clamped-clamped beam resonator, the simulation model for the dog-bone resonator consists of a state-space description of (3.29). The state column is defined as $\mathbf{x} = [\mathbf{q}^T \quad \dot{\mathbf{q}}^T]^T$, such that (3.29) can be written as $\dot{\mathbf{x}} = \mathbf{f}(\mathbf{x}, t)$, where

$$\mathbf{f}(\mathbf{x}, t) = \begin{bmatrix} \dot{\mathbf{q}} \\ \mathbf{M}^{-1}[\mathbf{F}_{nc}(\mathbf{q}, \dot{\mathbf{q}}, t) - \mathbf{f}_{in}(\mathbf{q})] \end{bmatrix}. \quad (3.30)$$

Next, the steady-state nonlinear dynamic behaviour of the dog-bone resonator is investigated using a similar approach as described in Section 3.2.2, based on numerical collocation and continuation techniques in AUTO (Doedel et al., 1998), see also Section 2.4.4. For this purpose, the model has been written to non-dimensional form.

Periodic solutions will be presented in terms of x - and z -displacements at the ends of the resonator heads. The piezoresistive detection has been found not to result in different results (van den Hoven, 2008). Results will be discussed in Section 3.3.3.

3.3.3 Numerical results

Numerical simulations are performed with the model (3.29) in order to determine the nonlinear steady-state dynamic behaviour of the dog-bone resonator. In Figure 3.27, amplitude-frequency curves are depicted for the dog-bone resonator with the nominal geometry as listed in Table 3.2. For now, the tapering of the gaps is also assumed symmetric: $\Delta d_1 = \Delta d_2 = 50$ nm. These values are a worst-case scenario with respect to production tolerances. Results are shown for the in-plane and out-of-plane displacement of the left-most point (node 1) on resonator head I, see Figure 3.24. Results for the other end of the dog-bone resonator are the same due to symmetry. In the simulations, the frequency f is varied around the desired in-plane beam mode (around 22.6 MHz). At

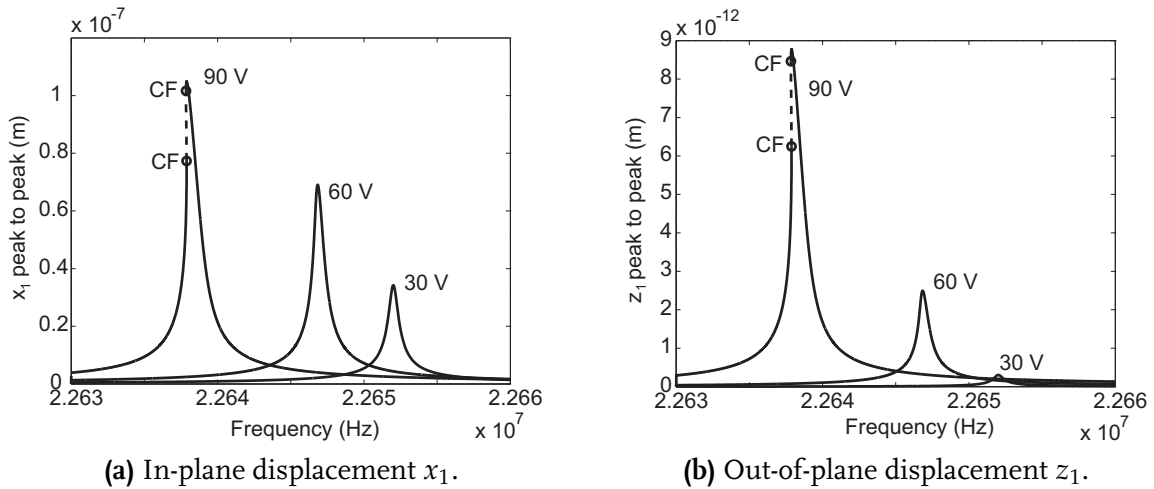


Figure 3.27 / Amplitude-frequency curves for the model with the nonlinear coupling terms for $V_{ac} = 300$ mV and three different V_{dc} -values.

an ac excitation amplitude of $V_{ac} = 300$ mV, results for three different bias voltages are depicted: $V_{dc} = 30, 60$ and 90 V.

The non-dimensional damping coefficients, which are used in the Rayleigh dissipation function (3.28), are set to $\xi_1 = 3.8 \cdot 10^{-5}$, $\xi_2 = 4.9 \cdot 10^{-5}$, $\xi_7 = 4.7 \cdot 10^{-4}$ and $\xi_{10} = 8.3 \cdot 10^{-4}$ in order to obtain an in-plane quality factor of about $Q = 35000$ and an out-of-plane quality factor of about $Q = 10000$. These values are estimated based on experiments, see van den Hoven (2008). Although the in-plane response has a peak to peak amplitude of over 100 nm, see Figure 3.27(a), the calculated out-of-plane response is only very small (in picometer range), see Figure 3.27(b). The measured out-of-plane response, see Figure 3.22(b) is in the order of 10^{-8} m. Furthermore, from the simulations it also follows (not depicted) that no resonance occurs at the asymmetric in-plane eigenmode at frequency f_7 , which corresponds to the fact that the dog-bone resonator is symmetric with respect to the plane $x = 0$.

In case of an asymmetric dog-bone resonator, in which the gaps and the tapering are set to $d_1 = 355$ nm, $d_2 = 315$ nm, $\Delta d_1 = 60$ nm and $\Delta d_2 = 40$ nm, the simulation results are about the same as the results in depicted in Figure 3.27. In addition, around f_7 , a small in-plane response is observed, due to asymmetry of the dog-bone resonator. However, the experimentally observed energy exchange between in-plane and out-of-plane modes, see Figure 3.22, has not been found in the numerical simulations.

In Noijen et al. (2007) and Mallon et al. (2008), a similar modelling approach as used here is applied to derive and analyse the equations of motion of macro-scale buckling problems. It is shown that dynamic buckling can yield an unstable harmonic resonance peak, resulting in a beating chaotic time response in which energy is exchanged between in-plane and out-of-plane modes. However, in Noijen et al. (2007) and Mallon et al. (2008), a much larger number of modes is taken into account. Therefore, it is possible that, by increasing the number of modes, such coupling between in-plane and out-of-plane modes may occur at lower excitation values, which corresponds to experimental results. This is still under investigation.

3.3.4 Discussion

The partly heuristic model, proposed in Section 3.3.2 is found to be unable to describe the experimentally observed mode-coupling behaviour (Section 3.3.1). Compared with the experimentally measured out-of-plane response, the finite element based 2D model predicts out-of-plane movements that are several orders-of-magnitude smaller. A nonlinear strain displacement relation is used for coupling the in-plane and out-of-plane motions. and tapering of the electrode gaps serves as an excitation mechanism for out-of-plane modes.

The proposed partly heuristic model for the dog-bone resonator has a fixed model structure with an a-priori defined complexity. The models is unable to describe the experimentally observed coupling between in-plane and out-of-plane modes. Furthermore, the model cannot describe the shape of the resonance peak as well as the plateau for the amplitude, observed in the experiments. The main reason for this is that the model structure

is not accurate enough in terms of coupling between in-plane and out-of-plane motion (number of modes) and in terms of the excitation mechanisms for out-of-plane modes. In the current model, only two in-plane and two out-of-plane modes are included. Inclusion of more in-plane and out-of-plane modes may result in a better description of the behaviour of the resonator. Furthermore, only tapering of the electrodes is included for out-of-plane excitation. Fringing field-effects and an accurate description of the electric field for tapered electrodes may result in more accurate results.

As described above, the partly heuristic modelling approach for case study II clearly shows shortcomings in terms of experimentally observed effects that can be described. In order to improve this, it is recommended to use a fully first-principles based approach for deriving the model of the dog-bone resonator. In this way, an improved description of in-plane and out-of-plane (parametric) excitation effects can be derived. This will provide a systematic approach for including a large variety of excitation and nonlinear dynamic effects that may be relevant for the dog-bone resonator.

3.4 Conclusions

Heuristic modelling has been applied to two case studies. For the case study of the clamped-clamped beam MEMS resonator (Section 3.2), a good quantitative match between experiments and simulations with the heuristic model has been obtained. This means that the chosen heuristic model structure, a Duffing-based model with electrostatic (parametric) excitation, is well-suited for describing the dynamic behaviour. However, because of the heuristic nature of the proposed model, it is not capable of predicting the dynamic behaviour for a full range of excitation parameters. At each excitation setting, a best fit has been made in order to obtain an optimal match between simulation and experiment. This severely limits the predictive capabilities of the obtained model.

For the second case study, concerning a dog-bone MEMS resonator (Section 3.3), the applied partly heuristic modelling approach so far has proven to be unable to describe the experimentally observed mode coupling behaviour. The main reasons for this is the incorrect model structure with respect to the number of in-plane and out-of-plane modes together with the excitation mechanism for out-of-plane modes. Especially by using the lumped approach for the electrostatic actuation, essential effects (fringing fields, non-parallel electric field in the electrode gaps) are not modelled correctly. Furthermore, whether the proposed multi-model captures the experimentally observed behaviour, depends to a large extent on the number and type of modes that are included, which, in turn depends on the complexity and the specific type of resonator considered.

A solution to the abovementioned shortcomings of heuristic modelling lies in a fundamental approach based on first-principles. Compared to the heuristic modelling approach, which takes place directly at the device level, one has to go one step back in the modelling levels, namely to the physical level, see Figure 1.2.2. Once physical level descriptions (typically, PDEs) have been obtained for relevant physical effects, model reduc-

tion techniques can be applied to derive a reduced-order model that potentially captures the experimentally observed behaviour better. This will be described in the next chapters.

Multiphysics modelling framework

Abstract / This chapter describes the multiphysics modelling framework for deriving device level models from the physical modelling level. First, some philosophy behind the modelling approach will be detailed. Next, involved physical domains for MEMS resonators are introduced and (multi-physical) effects occurring in these domains are described in detail by their governing equations. Finally, the modelling framework is presented in terms of an approach for deriving reduced-order models from the physical level models.

4.1 Introduction

From the two case studies of heuristic modelling, presented in Chapter 3, it has become clear that, for accurate predictive modelling, a first-principles based approach is required. For the clamped-clamped beam MEMS resonator of Section 3.2, the proposed lumped or descriptive device level model is capable of capturing some, but not all of the experimentally observed dynamical responses. Model parameters can be fine-tuned such that the best possible fit is obtained for a certain excitation setting (see Figure 3.12), but the predictive modelling capabilities have been found to be rather restrictive. For the dog-bone resonator, see Section 3.3, the partly heuristic model that has been proposed, has been found to be unable to describe the experimentally observed behaviour. However, this holds for the specific model considered here. Other heuristic models may be able to describe the experimentally observed behaviour. These are typical modelling issues that are related (and inherent) to heuristic modelling.

In order to overcome these issues, a first-principles based modelling framework will be presented in this chapter. The goal of the modelling framework is to derive device level (reduced-order) models from the physical modelling level (see also Figure 1.1) in an analytical or functional representation, for instance, ODEs with actual physical parameters. The models are intended for fast and accurate simulation of nonlinear dynamics of MEMS. The modelling approach will be focussed on MEMS resonators, but is not restricted to this application field within microsystems engineering. The approach may

also be applied to other microstructures in which the dynamic behaviour is of importance, such as resonant sensors, resonant filters, switches and variable capacitors.

The MEMS resonators considered in this work provide a promising alternative for conventional quartz crystals in oscillator circuits, see Section 2.2. The dynamic behaviour of these resonators is one of the key phenomena that determines the oscillator performance (Section 2.3) and has to be included in device level resonator models. Moreover, several different nonlinear effects may show up in the steady-state dynamic behaviour, depending on the specific resonator layout (see Chapter 3). The multiphysics modelling framework, created from a mechanical engineering point of view, will provide a straightforward approach for investigating the nonlinear dynamic behaviour in MEMS resonators, thereby providing a solution to the modelling requirements listed in Section 1.2.4.

Furthermore, the multiphysics models derived using the modelling framework will be validated extensively by means of experiments. Heuristic modelling, as described in Chapter 3, may have rather limited predictive capabilities. Whether a heuristic model is able to capture experimentally observed behaviour depends to a large extent on the model structure. The modelling framework, presented in Chapter 4 will provide a straightforward approach for the derivation of first-principles based multiphysics models with much better predictive qualities than heuristic models.

The majority of MEMS resonators for oscillators is operated in vacuum and makes use of the electrostatic actuation/detection principle (see Section 2.2.2). Therefore, in the current approach, the modelling framework will be confined to electrostatically actuated MEMS resonators that are operated in vacuum. In general, three different physical domains are involved in the modelling of these devices, see Figure 4.1: mechanical, electrical and thermal. Due to operation in vacuum, the fluidic domain is not included.

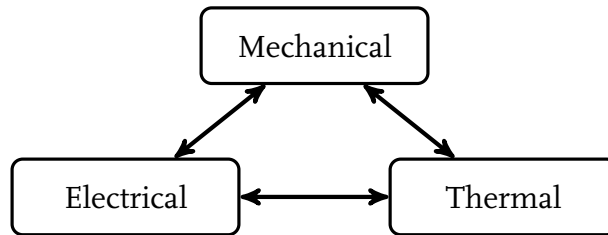


Figure 4.1 / Involved physical domains for MEMS resonators operating in vacuum.

In Section 4.2, the philosophy behind the modelling framework and the essence of first-principles based modelling will be described. Next, in Section 4.3, the relevant physical effects in each of these domains will be explained, together with the corresponding governing equations and constitutive relations at the physical level. Some effects are purely single-domain of nature, whereas others – the multiphysical effects – typically result from coupling across two physical domains. In Section 4.4, the modelling framework will be presented in terms of a methodology for deriving reduced-order models from the coupled equations at physical level by means of Galerkin discretisation. Subsequently, numerical solution and experimental validation takes place.

4.2 Modelling philosophy

The essence of modelling boils down to the selection of a limited amount of relevant physical effects to be included at a certain level of detail in a model. However, it is difficult to know in advance what effects have to be taken into account and what level of detail suffices.

For this purpose, the first-principles based multiphysics modelling framework will start from the physical level, for instance, from distributed-parameter descriptions. Relevance of effects can be addressed once physical effects that may influence the dynamic behaviour of MEMS resonators have been included. Effects that (at first sight) are relevant will be described in Section 4.3. The level of detail of the model can be varied in the Galerkin discretisation step that is applied to arrive at a reduced-order model. Often, it is unclear beforehand how much detail should be put in a first-principles based model. A more detailed model is not necessarily a better model.

A heuristic approach based on extensive experimental characterisation may also result in a correct description of experimentally observed behaviour. However, such a data-based model, consisting of, for instance, a heuristic model combined with look-up tables, may be limited in predictive capabilities, especially when variations like fabrication tolerances are relevant.

Furthermore, models resulting from a heuristic approach or from the first-principles based modelling framework presented in this chapter may be the same. Namely, using the modelling framework, reduced-order models with a relatively low number of DOF will be created (see also Section 1.2.4 for modelling requirements). These models are similar to lumped models. However, the main advantage of the first-principles based models over heuristic models is that actual physical parameters will appear in the coefficients that characterise the reduced-order (lumped) model. In this way, the models provide (more) insight into the influence of physical parameters and the sensitivity of a certain model response to such parameters.

In line with this modelling philosophy, the first-principles based multiphysics models that are derived using the framework will:

- enable fast and accurate simulation of (nonlinear) dynamic behaviour of MEMS resonators;
- allow for addressing the relevance of individual (multiphysical) effects;
- form a pre-design tool for dynamic response analysis;
- be complementary to conventional finite element simulations (that can be used for very complex geometries), allowing for fast and accurate (preliminary) simulations.

By satisfying these demands, the models can be used to gain insight in relevant physical effects as well as to predict the dynamic behaviour of the system under investigation.

4.3 Relevant physical effects

As has become clear from the previous section, three physical domains are involved in the modelling of MEMS resonators (Figure 4.1). In each of these domains, several physical effects may play a role, depending on the specific MEMS resonator layout. An overview of relevant effects, categorised into the three physical domains, is presented in Figure 4.2. This figure does not list all possible effects that may occur in MEMS in general, but only presents an overview of effects that are considered to be relevant for the modelling of MEMS resonators.

Several multiphysics effects are present in Figure 4.2. Electrostatic actuation and capacitive detection (both including fringing fields) couple mechanical deformation to capacitance changes and electrostatic force. Thermoelastic damping results from a coupling between the heat equation in the thermal domain and structural dynamics in the mechanical domain through the thermoelastic material behaviour. In the next sections, all effects depicted in Figure 4.2 will be discussed in detail by means of physical level descriptions. Additionally, nonlinearities that may arise will be described where appropriate.

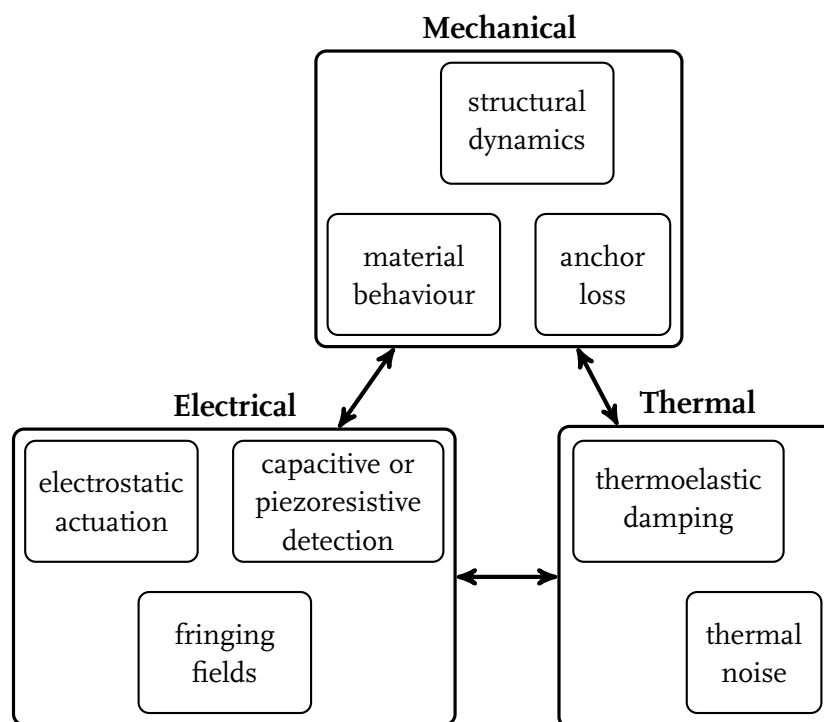


Figure 4.2 / Involved physical effects for MEMS resonators, categorised per domain (see also Figure 4.1).

4.3.1 Structural dynamics

The structural dynamics part in the mechanical domain is mainly governed by the geometry, the material (Si), the type of the micromechanical resonator and its characteristic vibration shape (see also Section 2.2.3). The underlying fundamental equations are the same for all types of resonators, but the specific form of the resulting PDEs may be different for flexural resonators and bulk resonators, for instance.

Beam- and plate-like structures have been widely used and studied in the microsystems community. At the physical level, distributed modelling approaches are used for resonators with deformation that takes place in the whole body of the resonator, for instance flexural and longitudinal resonators. Lumped approaches are used for resonators with localised deformation, such as torsional resonators or comb drive resonators.

For systems such as beams with distributed parameters, vibration can be described by partial differential equations (PDEs) and their associated boundary conditions, for instance, the beam equation, plate equation or wave equation. Several methods are available for deriving the PDEs for elastic solids, see, for instance Reddy and Rasmussen (1982), Weaver et al. (1990), Meirovitch (2001) and Reddy (2007). The governing equations can be classified into three categories: kinematics (strain-displacement relations), kinetics (conservation of momentum) and constitutive relations (stress-strain relations). Kinematics and kinetics are described in this section, whereas constitutive equations will follow in Section 4.3.2 on material behaviour.

Kinematics

The displacements \mathbf{u} of a material particle of a body \mathcal{B} can be expressed in terms of a reference coordinate system. For instance, in a Cartesian reference frame, the displacement can be written as $\mathbf{u} = (u, v, w)$. The deformation can be measured in terms of the Green-Lagrange strain tensor \mathbf{E} :

$$\mathbf{E} = \frac{1}{2} [\nabla \mathbf{u} + (\nabla \mathbf{u})^T + \nabla \mathbf{u} \cdot (\nabla \mathbf{u})^T], \quad (4.1)$$

where ∇ denotes the gradient operator with respect to the material coordinates. Components of \mathbf{E} are denoted by η_{ij} . In general, nonlinear strain-displacement relations result from (4.1). For small deformations, the last product in (4.1) may be omitted, yielding the infinitesimal strain tensor $\boldsymbol{\varepsilon}$ (whose components are denoted by ε_{ij}):

$$\boldsymbol{\varepsilon} = \frac{1}{2} [\nabla \mathbf{u} + (\nabla \mathbf{u})^T]. \quad (4.2)$$

Kinetics

Consider a material body \mathcal{B} with a volume \mathcal{V} , bounded by a surface \mathcal{S} . External forces \mathbf{T} (per unit surface area) and \mathbf{f} (per unit mass) are acting on the body \mathcal{B} .

One possible way of deriving the equations of motions of the body is by using the principle of conservation of linear momentum (Newton's second law of motion), leading to:

$$\nabla \cdot \boldsymbol{\sigma} + \rho \mathbf{f} = \rho \frac{\partial^2 \mathbf{u}}{\partial t^2}, \quad (4.3)$$

where ρ is the material density and $\boldsymbol{\sigma}$ is the stress tensor. (4.3) is supplemented by the boundary conditions for the displacement and/or stress vector:

$$\mathbf{u} = \hat{\mathbf{u}}, \quad \text{and/or} \quad \boldsymbol{\sigma} \cdot \hat{\mathbf{n}} = \hat{\mathbf{T}}, \quad (4.4)$$

where $\hat{\mathbf{u}}$ and $\hat{\mathbf{T}}$ are specified displacement and stress vectors, respectively, and where $\hat{\mathbf{n}}$ denotes the outward normal.

Alternatively, the equations of motion may be derived using energy principles and variational methods based on the kinetic energy \mathcal{T} , the internal (or strain) energy \mathcal{U}_{in} and the external work \mathcal{W}_{ex} of a material body \mathcal{B} . This is the method that will be used in this work. Hamilton's principle (Meirovitch, 2001; Reddy, 2007) states that *of all possible paths that a material particle could travel from its position at time t_1 to its position at time t_2 , its actual path will be one for which the integral*

$$\int_{t_1}^{t_2} (\mathcal{T} - \mathcal{U}_{\text{in}} - \mathcal{W}_{\text{ex}}) \, dt \quad (4.5)$$

is an extremum (with t_1 and t_2 arbitrary). A necessary condition for this to hold is that the first variation of the integrand is zero:

$$\int_{t_1}^{t_2} (\delta \mathcal{T} - \delta \mathcal{U}_{\text{in}} - \delta \mathcal{W}_{\text{ex}}) \, dt = 0. \quad (4.6)$$

The energy functions in (4.6) are given by (see Reddy, 2007):

$$\delta \mathcal{T} = \frac{1}{2} \delta \int_{\mathcal{V}} \rho \frac{\partial \mathbf{u}}{\partial t} \cdot \frac{\partial \mathbf{u}}{\partial t} \, d\mathcal{V}, \quad (4.7)$$

$$\delta \mathcal{U}_{\text{in}} = \int_{\mathcal{V}} \boldsymbol{\sigma} : \delta \mathbf{E} \, d\mathcal{V}, \quad (4.8)$$

$$\delta \mathcal{W}_{\text{ex}} = - \left(\int_{\mathcal{V}} \mathbf{f} \cdot \delta \mathbf{u} \, d\mathcal{V} + \int_{\mathcal{S}} \mathbf{T} \cdot \delta \mathbf{u} \, d\mathcal{S} \right), \quad (4.9)$$

where ' $:$ ' denotes the double dot product in (4.8). The negative sign in (4.9) indicates that the work is performed on the body \mathcal{B} . Similar to (4.3)–(4.4), the energy approach (4.6)–(4.9) yields a set of equations of motion and the associated essential (geometric) and natural (force) boundary conditions for the structural dynamics.

4.3.2 Material behaviour

In addition to the kinematics and kinetics described in Section 4.3.1, constitutive equations are needed to describe the material behaviour. These equations relate the stress

tensor σ in a material to the associated Green-Lagrange strain tensor E (4.1) or infinitesimal strain tensor ε (4.2).

The MEMS resonators under investigation in this work are made of single-crystal silicon, which has both electrical and mechanical properties that make it very suitable for microfabrication, see for instance Petersen (1982) or (Stemme, 1991). Single-crystal silicon is an anisotropic material, which means that its elastic behaviour depends on the orientation of the material. An extensive overview of silicon as an engineering material is presented in Appendix A. Taking into account the anisotropy, the constitutive equations for silicon can be written in component form as:

$$\sigma_{ii} = C_{11}\eta_{ii} + C_{12}(\eta_{jj} + \eta_{kk}), \quad (4.10a)$$

$$\tau_{ij} = C_{44}\gamma_{ij} \quad (i \neq j), \quad (4.10b)$$

where σ_{ii} , τ_{ij} , η_{ii} and γ_{ij} ($= 2\eta_{ij}$), ($i, j = 1, 2, 3$) denote normal stress, shear stress, normal Green-Lagrange strain and shear Green-Lagrange strain, respectively. The indices 1, 2 and 3 correspond with the three principal directions in the material, see Appendix A.1.2. Only three independent material constants are present in (4.10a)–(4.10b): C_{11} , C_{12} and C_{44} . Alternatively, strains can be written as a function of stresses as:

$$\eta_{ii} = S_{11}\sigma_{ii} + S_{12}(\sigma_{jj} + \sigma_{kk}), \quad (4.11a)$$

$$\gamma_{ij} = S_{44}\tau_{ij} \quad (i \neq j), \quad (4.11b)$$

which contain three independent compliance coefficients S_{11} , S_{12} and S_{44} . The values of the second-order elastic constants C_{ij} and S_{ij} are given in Table A.1. These constants can be related to the more widely used quantities of Young's modulus E and Poisson's ratio ν by relations presented in Appendix A.1.2.

Furthermore, for large deformations, nonlinear effects may arise in the constitutive equations for silicon. From literature, see for instance Seeger and Buck (1960) and Hiki (1981), it is known that silicon exhibits a physical nonlinearity, resulting in deviation from linear Hooke's law (4.10a)–(4.10b). As a result, the elastic constants become a function of the strain, see (A.31) in Appendix A.4.2. So-called third-order elastic constants describe this behaviour. Their values are listed in Table A.2.

In case of homogeneous uni-axial loading, the effects can be taken into account in a straightforward way (Kim and Sachse, 2000). The derivation of nonlinear Young's modulus for this type of loading is presented in Appendix A.4.3. Young's modulus can be written as a function of the Green-Lagrange strain η_{11} as:

$$E(\eta_{11}) = E_0 + E_1\eta_{11} + E_2\eta_{11}^2 + \dots, \quad (4.12)$$

where E_1 and E_2 denote linear and quadratic corrections to the linear Young's modulus E_0 . This expression can be included in the nonlinear constitutive equation for the stress:

$$\sigma_{11} = E(\eta_{11})\eta_{11} = (E_0 + E_1\eta_{11} + E_2\eta_{11}^2 + \dots)\eta_{11}. \quad (4.13)$$

The derivation of the constants in (4.12) is presented in Appendix A.4.3. A similar approach has been reported in Kaajakari et al. (2003a) and Kaajakari et al. (2004b). Based on these calculated constants, (4.13) can be used to determine that a 1% stress deviation from linear theory is present at a Green-Lagrange strain of $\eta_{11} = 0.0144$.

4.3.3 Loss mechanisms

Several different loss mechanisms may be present in MEMS resonators. For instance, intrinsic material losses, thermoelastic damping, surface losses and losses through the mounting of a MEMS device to the substrate (so-called anchor loss). Since the resonators are operated in vacuum, fluidic loss mechanisms like air damping, acoustic radiation and viscous drag have negligible influence. The amount of dissipation in a structure can be expressed by means of a total mechanical quality factor Q_{tot} , which can be expressed as (Tilmans et al., 1992):

$$Q_{\text{tot}} = 2\pi \frac{\mathcal{W}}{\Delta\mathcal{W}}, \quad (4.14)$$

where \mathcal{W} denotes the total energy stored in the resonator and $\Delta\mathcal{W}$ is the total energy dissipated per cycle of vibration. All loss mechanisms contribute to the total energy dissipated. Expression (4.14) is general in nature and holds for both linear and nonlinear systems. Furthermore, a quality factor Q_i can be attributed to each loss mechanism, see for instance Yang et al. (2002), Hao and Xu (2009) or Kaajakari (2009). The expression for Q_{tot} becomes:

$$\frac{1}{Q_{\text{tot}}} = \sum_{i=1}^n \frac{1}{Q_i}, \quad (4.15)$$

where a total of n loss mechanisms is present. Several of the individual loss mechanisms are described next.

Anchor loss is a loss mechanism in which vibration energy of the MEMS resonator is dissipated by transmission through the resonator support(s), also called anchors. This loss mechanism is important for MEMS resonators, since the resonator vibration induces shear or normal stress in its supports. This loss mechanism will be described in Section 4.3.4.

Intrinsic internal, or material losses depend on the purity, on the number of dislocations and on the thermoelastic losses of the material used. In general, the losses other than thermoelastic damping are very small for a single-crystal material (see Kaajakari (2009) and Appendix A.1.3). It has lower losses than a poly-crystal material and it also has less dislocations. Therefore, for resonators constructed from single-crystal silicon, the most important internal loss mechanism is thermoelastic damping, see also Roszhart (1990). This loss mechanism will be described in Section 4.3.5.

Furthermore, surface losses by surface defects or adsorbates may be present. These losses are influenced by the surface roughness, by formation of an oxide layer and by surface contamination (Yang et al., 2002). Surface loss mechanisms may be relevant for microstructures that approach nanoscale, but have been found to be not significant for clean silicon microresonators, see Kaajakari (2009). Therefore, this loss mechanism is not considered here.

4.3.4 Anchor loss

Forces and moments exerted on the resonator supports (anchors) are caused by vibration of the resonator. They excite elastic propagating waves in the substrate, such that the support structure will absorb some of the vibration energy of the resonator (Hao et al., 2003; Park and Park, 2004a).

In literature, analytical work has been done on the calculation of the amount of energy dissipated per cycle. See for instance Hao et al. (2003), Park and Park (2004a,b), Hao and Ayazi (2007) and Hao and Xu (2009). Especially Hao and Xu (2009) present a thorough overview of the origin and calculation of support loss for clamped-clamped beam MEMS resonators. The anchors of the beam act as excitation sources (shear stress or normal stress) on the substrate and generate waves. These waves cause dissipation by carrying away energy. Analytical expressions for the energy dissipation ΔW related to anchor loss are derived in terms of the shear or normal stress at the beam ends and the corresponding vibration displacements. Next, by means of (4.14), the quality factor of the resonator can be calculated, which can be incorporated into the modelling framework as a damping term.

Anchor losses can be reduced by mechanically isolating the vibrating elements from the substrate. For instance, one could suspend the resonator at nodal (non-vibrating) points via thin beams to the substrate. Alternatively, one could use an approach in which the vibration in the structure is more or less balanced by using symmetry. Examples of such structures have been discussed in Stemme (1991) and in Tilmans et al. (1992). However, for each specific resonator type, it is advisable to investigate the effect of the dimensions of the anchors. For instance, Q -factors have been found to depend in a nonlinear way on the stem radius in a disk resonator suspended from a stem in the middle (Paci et al., 2006).

4.3.5 Thermoelastic damping

As has been described in Section 4.3.3, thermoelastic damping is the most important internal loss mechanism for resonators constructed from single-crystal silicon.

In a thermoelastic solid (any solid with a non-zero thermal expansion coefficient), a coupling exists between the strain field due to mechanical deformation and the temperature field in the solid. General theory on thermoelasticity can be found in Boley and Weiner (1960) and Nowinski (1978). The coupling between the mechanical and thermal domain provides an energy dissipation mechanism that allows the system to relax to an equilibrium through irreversible heat flow. The heat flow follows from local temperature gradients which are caused by local strain gradients through the thermal expansion coefficient. This fundamental energy dissipation mechanism is called thermoelastic damping. It poses an upper limit to the quality factor of any constructed resonator in which deformation takes place.

The calculations of thermoelastic damping start with the classical papers by Zener (1937, 1938, 1960), and Zener et al. (1938). A relation for the thermoelastic Q -factor for a reed (beam) in flexural vibration is derived, based on a series approximation for the temperature profile in the beam:

$$Q^{-1} = \frac{E\alpha^2 T_0}{\rho c_p} \frac{\omega\tau}{1 + (\omega\tau)^2}, \quad (4.16)$$

where E is the Young's modulus of the beam, α is the thermal expansion coefficient, T_0 is the nominal temperature and c_p is the heat capacity per unit volume at constant pressure. ω is the beam vibration frequency (for arbitrary flexural vibration mode) and τ is the thermal relaxation time given by

$$\tau = \frac{h^2 \rho c_p}{\pi^2 k}, \quad (4.17)$$

where h is the beam width, ρ is the material mass density and k is the thermal conductivity. Thermal properties of single-crystal silicon can be found in Appendix A.2. The heat conduction in the beam is assumed to take place in the width direction of the beam only (not along the length). The relation for the Q -factor (4.16) exhibits a so-called Lorentzian behaviour as a function of $\omega\tau$ and has a maximum value of $E\alpha^2 T_0 / 2c_p$ at $\omega\tau = 1$. This can be understood as follows. When the frequency ω is much smaller than the effective relaxation rate $1/\tau$ of the system, it remains approximately in static equilibrium and very little energy is dissipated. If the vibration frequency is much higher than the relaxation rate $\omega \gg 1/\tau$, the system has no time to relax, which, again, results in little dissipation. Only when the frequency ω is near the relaxation rate $1/\tau$, thermal dissipation plays a role. Especially for MEMS, this is indeed the case, since, due to their small dimensions, the thermal relaxation time τ and the vibration frequency ω are close together.

In papers by Alblas (1961) and Shieh (1975, 1979) a more extensive approach to thermoelastic coupling is presented, based on partial differential equations for the elastic body dynamics and the first law of thermodynamics. Moreover, in Shieh (1975, 1979), thermoelastic vibration and damping for Timoshenko beams is addressed. In Lord and Shulman (1967), the effect of finite thermal conduction speed is investigated. This results in a heat conduction equation that is second order with respect to time, instead of first order. However, at room temperature, the characteristic time constant of the finite velocity of conduction of silicon is very low ($\mathcal{O}(10^{-13})$ s), so the generalised theory reduces to the conventional coupled theory (first law of thermodynamics).

Lifshitz and Roukes (2000) have extended Zener's approach to an explicit solution for the thermoelastic coupling for (MEM) beam resonators. Starting from the Euler-Bernoulli beam equation and the heat equation (both including thermoelastic coupling), harmonic motion is assumed. In this case, the solution to the heat equation can be found explicitly and can be substituted back into the beam equation. The complex-valued temperature profile results in a complex, frequency-dependent, stiffness in the beam equation. The reasoning behind the complex stiffness is that the real part of the stiffness is in phase with the elastic deformation, whereas the imaginary part is out of phase, thereby causing

dissipation. The following expression for the Q -factor is derived:

$$Q^{-1} = \frac{E\alpha^2 T_0}{\rho c_p} \left(\frac{6}{\xi^2} - \frac{6}{\xi^3} \frac{\sinh \xi + \sin \xi}{\cosh \xi + \cos \xi} \right), \quad (4.18)$$

where

$$\xi = h \sqrt{\frac{\omega \rho c_p}{2k}}. \quad (4.19)$$

Variables in (4.18) and (4.19) are the same as used in (4.16) and (4.17). Good correspondence is found with the expression (4.16) from Zener (1937).

Nayfeh and Younis (2004) have extended the approach of Lifshitz and Roukes (2000) to the two-dimensional problem of thermoelastic damping in microplates, by making use of a similar complex-valued temperature profile. Duwel et al. (2006) have used finite element simulations to solve the coupled mechanical-thermal eigenvalue problem from which the Q -factor of the resonator can be calculated. Prabhakar and Vengallatore (2008) have investigated the additional effect of heat conduction along the length of the beam, instead of the 1D heat conduction in transverse direction assumed in previous papers. The proposed 2D approach is found to result in a larger effect of thermoelastic damping, yielding a lower Q -factor.

For the multiphysics modelling framework, the thermoelasticity equations in general form are required. These can be found in Boley and Weiner (1960) and Nowinski (1978). The so-called Duhamel-Neumann relations relate stresses and strains via the stiffness coefficients and thermal coefficients. The thermoelastic equivalent of (4.10a)–(4.10b) becomes:

$$\sigma_{ii} = C_{11}\eta_{ii} + C_{12}(\eta_{jj} + \eta_{kk}) + \beta_{ii}\theta, \quad (4.20a)$$

$$\tau_{ij} = C_{44}\gamma_{ij} + \beta_{ij}\theta \quad (i \neq j), \quad (4.20b)$$

where β_{ij} are the thermal moduli and θ is the temperature difference $\theta = T - T_0$ with respect to a reference temperature T_0 . The thermoelastic version of (4.11a)–(4.11b) becomes:

$$\eta_{ii} = S_{11}\sigma_{ii} + S_{12}(\sigma_{jj} + \sigma_{kk}) + \alpha_{ii}\theta, \quad (4.21a)$$

$$\gamma_{ij} = S_{44}\tau_{ij} + \alpha_{ij}\theta \quad (i \neq j), \quad (4.21b)$$

where α_{ij} denote the thermal expansion coefficients. For silicon, no thermal expansion occurs in shear direction ($\alpha_{ij} = 0$ for $i \neq j$) and the thermal expansion coefficient is the same for the three principal directions $\alpha_{ii} = \alpha$ for $i = 1, 2, 3$ (see Appendix A.2.2). As a result, $\beta_{ij} = 0$ (for $i \neq j$) and $\beta_{ii} = \beta$ for $i = 1, 2, 3$. Using these expressions, (4.20)–(4.21) can be simplified. Furthermore, for this special case, β can be related to α by:

$$\beta = -\frac{\alpha}{S_{11} + 2S_{12}} = -(C_{11} + 2C_{12})\alpha. \quad (4.22)$$

The general form of the heat equation is found from the first law of thermodynamics. For material with cubic symmetry, such as single-crystal silicon, this becomes (Nowinski, 1978):

$$k\nabla^2\theta - \rho c_p \frac{\partial\theta}{\partial t} + T_0\beta \frac{\partial e}{\partial t} = 0, \quad (4.23)$$

where ∇^2 is the Laplacian operator and e denotes the dilatation:

$$e = \eta_{11} + \eta_{22} + \eta_{33}. \quad (4.24)$$

In general, also the other physical effects (Sections 4.3.1–4.3.7) may depend on temperature. For instance, stiffness parameters depend on temperature (see Appendix A.2.4). However, in the current approach, these effects are omitted; only thermoelastic damping will be considered.

4.3.6 Electrostatic actuation and fringing fields

The MEMS resonators considered in this work are actuated electrostatically, see also Section 2.2.2. Background on electrostatics can be found in, for instance Griffiths (1999). Consider Figure 4.3, where a parallel plate capacitor is depicted schematically. The plates are separated by a distance d and have a surface A . The top plate has a surface charge density σ_e and the bottom plate has a surface charge density of equal magnitude but of opposite sign. The total charge of a plate equals $q_e = \sigma_e A$. The electrical field between the plates has a value of σ_e/ϵ_0 , where ϵ_0 denotes the permittivity of vacuum. The parallel

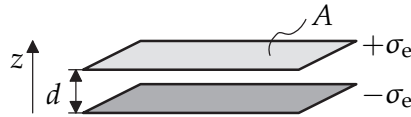


Figure 4.3 / Parallel plate capacitor consisting of two plates, each having an area A and an opposite charge density, and that are separated by a distance d .

plate capacitor in Figure 4.3 has a capacitance of (Griffiths, 1999):

$$C = \frac{\epsilon_0 A}{d}, \quad (4.25)$$

and the stored electrical energy in the capacitor equals:

$$\mathcal{W}_e = \frac{1}{2}CV^2 = \frac{1}{2}\frac{q_e^2}{C}, \quad (4.26)$$

where V denotes the voltage difference over the capacitor plates and where $q_e = CV$. The electrostatic attracting force F_e , acting on the capacitor plates if one moves the the top plate in Figure 4.3 over a distance dz , can be calculated from (Griffiths, 1999):

$$F_e = -\frac{d\mathcal{W}_e}{dz} = \frac{1}{2}\frac{q_e^2}{C^2}\frac{dC}{dz} = \frac{1}{2}V^2\frac{dC}{dz}. \quad (4.27)$$

Note that the total charge q_e on the capacitor is assumed constant. In MEMS resonators, displacement dz typically results from mechanical deformation (vibration) of the resonator.

In general, the plates of a capacitor have finite dimensions. As a result, the approximation for a parallel plate capacitor (4.25) is no longer completely valid. The electric field is no longer uniform between the capacitor plates and zero elsewhere, but is influenced by the plate boundaries and dimensions. These effects are called fringing field effects. As an illustration, Figure 4.4(a) depicts the electric field for an ideal parallel plate capacitor. Fringing field effects are depicted in Figure 4.4(b).

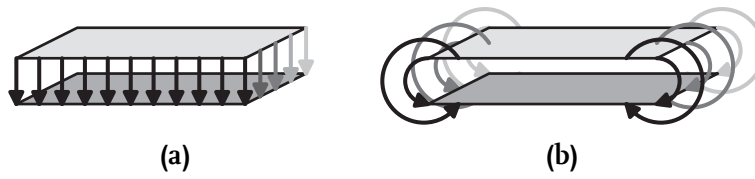


Figure 4.4 / Sketch of the electric fields for a parallel plate capacitor: (a) ideal parallel plate and (b) fringing fields.

The total capacitance C_{tot} of the capacitor, including fringing field effects, can be written as:

$$C_{\text{tot}} = C_{\text{pp}} + C_f, \quad (4.28)$$

where C_{pp} denotes the ideal parallel plate capacitance, given by (4.25), and C_f denotes the fringing field contribution. The general trend of fringing fields is to increase the effective capacitance of the capacitor. Only for relatively simple geometries, analytical calculations of the fringing field can be performed using so-called Schwartz-Christoffel conformal mapping techniques, see Palmer (1937). Furthermore, Chang (1976), van der Meijs and Fokkema (1984), and Barke (1988) provide extensions to this approach. An overview of different expressions for calculating the contribution of fringing fields is given in Leus and Elata (2004).

For the case of electrostatically actuated microbeams, work on electrostatic actuation (including fringing field effects) has been reported in Osterberg (1995), Osterberg and Senturia (1997), Krylov and Maimon (2004), Krylov and Seretensky (2006) and Batra et al. (2006a,b, 2007, 2008). This will be described in detail in Chapter 5.

4.3.7 Capacitive or piezoresistive detection

The motion of the resonator can be detected capacitively or piezoresistively (see also Section 2.2.2). Only these two methods are considered in this work and will be described next.

Capacitive detection

Motion of the MEMS resonator will result in motion of one (or both) of the capacitor plates. This, in turn, results in generation of an electrical current. Often, one of the plates of the capacitor is fixed and is used as the measurement electrode. For a capacitor with capacitance $C_{\text{tot}}(z)$, depending on the plate position z of the movable plate, see Figure 4.3, the current i_c will result from temporal changes in the charge q_e of the capacitor:

$$\begin{aligned} i_c &= \frac{dq_e}{dt} = \frac{d(C_{\text{tot}}(z)V(t))}{dt} \\ &= V(t) \frac{dC_{\text{tot}}(z)}{dt} + C_{\text{tot}}(z) \frac{dV(t)}{dt} = \underbrace{V(t) \frac{dC_{\text{tot}}(z)}{dz} \frac{dz}{dt}}_{i_c} + \underbrace{C_{\text{tot}}(z) \frac{dV(t)}{dt}}_{i_{ac}}, \end{aligned} \quad (4.29)$$

where $V(t)$ denotes the time-dependent voltage difference applied to the moving plate (measurement electrode) of the capacitor. The first term in (4.29), related to the time-derivative of the capacitance C_{tot} is often called the motional current i_c and the second one is called the ac current i_{ac} , see also Kaajakari et al. (2005a). For capacitively sensed MEMS resonators, the motional i_c current will always be present. However, if only a dc voltage is applied to the measurement electrode, i_{ac} will vanish. Furthermore, the measured output voltage of the resonator depends on the exact layout of the measurement circuit.

Piezoresistive detection

When silicon is subjected to stress, the piezoresistance effect results in a resistance change, see, for instance, Kanda (1991). In order to understand the principle, consider a silicon bar with length l , thickness b and width h . The resistance of the bar is defined as (Kanda, 1991):

$$R = \frac{\rho_0 l}{bh}, \quad (4.30)$$

where ρ_0 is the resistivity of silicon in Ωm . For thin films, ρ_0/b can be written as the sheet resistance R_{sheet} in Ω . When the bar with resistance R , see (4.30), is stretched, a change in resistance ΔR occurs, which can be related to the dimensional changes of the bar and the change in resistivity by

$$\frac{\Delta R}{R} = \frac{\Delta l}{l} - \frac{\Delta b}{b} - \frac{\Delta h}{h} + \frac{\Delta \rho}{\rho_0}. \quad (4.31)$$

The last term in (4.31), the change in resistivity, is the dominant term for semiconductor gauges with about a factor 50 (Kanda, 1991). Therefore, dimensional changes ΔL , Δb and Δh will be neglected. When silicon is subjected to a uni-axial stress σ , the change in resistance is (Kanda, 1982, 1991):

$$\frac{\Delta R}{R} \approx \frac{\Delta \rho}{\rho_0} = \pi_1 \sigma, \quad (4.32)$$

where π_1 denotes the longitudinal piezoresistive coefficient in Pa^{-1} . In general, anisotropic behaviour plays a role for the piezoresistance coefficient (Kanda, 1982, 1991), but this will not be considered here. Furthermore, the piezoresistive coefficient is influenced by both the impurity concentration and temperature, see Kanda (1982) and Tufte and Stelzer (1963).

Piezoresistive sensing uses a constant current i_s , sent through a piezoresistive element. The resistance change ΔR results in a voltage change that can be measured. The output voltage then equals:

$$V_{\text{out}} = i_s(R + \Delta R) = i_s R(1 + \pi_1 \sigma). \quad (4.33)$$

Additional details on piezoresistive sensing can be found in Kaajakari (2009).

4.3.8 Thermal noise

Thermal noise is a combined thermal-electrical effect, caused by thermal agitation of electrons inside electrical conductors. This noise is called Johnson-Nyquist or thermal noise (Johnson, 1928; Nyquist, 1928) and has already been described in Section 3.2.2. For completeness of the modelling framework, the equation describing the root mean square (rms) of the noise voltage v_n generated in a resistor is repeated here:

$$v_n = \sqrt{4k_B T R \Delta f}, \quad (4.34)$$

where k_B denotes Boltzmann's constant, T denotes absolute temperature, R is the resistor value and Δf is the bandwidth in which the noise is measured.

4.4 Modelling framework

In Section 4.3, the governing equations at physical level have been described for effects that are relevant for the modelling of MEMS resonators. Three different methods that can be applied for creating reduced-order models have been listed in Section 1.2.2. Analytical derivation by applying modal reduction or approximation techniques will be applied in this work, since first-principles-based governing equations are available for the relevant physical effects. Approximation techniques that can be applied are, for instance, modal basis functions (Senturia et al., 1997), modal projection techniques (Mehner et al., 2003), or the Galerkin method (Hung and Senturia, 1999; Meirovitch, 2001). These techniques are weighted residual techniques, in which a solution is assumed in the form of a linear combination of trial functions (also called series discretisation). In this work, the Galerkin method will be applied, since it can be readily applied to nonlinear systems as well. In the next section, this method will be described in detail. Finally, Section 4.4.2 will give an overview of the multiphysics modelling framework.

4.4.1 Construction of reduced-order models

The Galerkin method can be used as an approximation method to obtain solutions to both linear and nonlinear PDEs. The method is general in scope and can be applied to conservative as well as nonconservative systems (Meirovitch, 2001). Consider a system of governing equations and boundary conditions for a domain (or volume) \mathcal{V} , with boundary \mathcal{S} , in vector form:

$$\mathcal{L}(\mathbf{v}) = \mathbf{g}(\mathbf{v}, t), \quad \mathbf{v} \in \mathcal{V}, \quad (4.35a)$$

$$\mathcal{B}(\mathbf{v}) = \mathbf{0}, \quad \mathbf{v} \in \mathcal{S}, \quad (4.35b)$$

where \mathcal{L} denotes a vector of (nonlinear) differential operators, \mathbf{v} is a vector of state variables, and $\mathbf{g}(\mathbf{v}, t)$ is a forcing function which may depend on the state variables and time t . \mathcal{B} denotes a vector of operators describing the boundary conditions. In general, the state solution $\mathbf{v}(x, y, z, t)$ is a function of Cartesian coordinates (x, y, z) and of time t . Typically, for the physical level models considered, \mathcal{L} consists of the PDEs from the structural dynamics part, derived using (4.6)–(4.9), together with the heat equation PDE (4.23). The part related to the structural dynamics contains both first- and second-order time derivatives of \mathbf{v} , whereas the part related to the heat equation only contains first-order time derivatives of \mathbf{v} . In general, \mathbf{v} is a function of the displacements \mathbf{u} that are relevant for the description of the structural dynamics, see Section 4.3.1. In system (4.35), \mathcal{L} , \mathcal{B} and \mathbf{g} are known and the goal is to determine \mathbf{v} .

An approximate solution $\hat{\mathbf{v}}(x, y, z, t)$ for $\mathbf{v}(x, y, z, t)$ in (4.35) is sought in a separable form as a series expansion of spatially varying basis functions $\boldsymbol{\varphi}_i(x, y, z)$ and $\boldsymbol{\psi}_j(x, y, z)$ and time-varying coefficients $q_i(t)$ and $r_j(t)$:

$$\hat{\mathbf{v}}(x, y, z, t) = \sum_{i=1}^n q_i(t) \boldsymbol{\varphi}_i(x, y, z) + \sum_{j=1}^n r_j(t) \boldsymbol{\psi}_j(x, y, z). \quad (4.36)$$

For sake of convenience, the coefficients of the basis functions have been separated into a part that is second-order time-dependent (terms with $q_i(t)$) and the part that is first-order time dependent (terms with $r_j(t)$). The choice of the corresponding basis functions $\boldsymbol{\varphi}_i(x, y, z)$ and $\boldsymbol{\psi}_j(x, y, z)$ depends on the specific system considered. In general, they are chosen such that boundary conditions (4.35b) for the PDEs (4.35a) are satisfied a priori. The coefficients $q_i(t)$ and $r_j(t)$ are also called generalised coordinates or generalised degrees of freedom (DOFs). The series approximation (4.36) is truncated at order n .

For known basis functions, the Galerkin method can be used to derive a system of ODEs in the coefficients $q_i(t)$ and $r_j(t)$. For this purpose, the residual $\mathcal{L}(\hat{\mathbf{v}}) - \mathbf{g}(\hat{\mathbf{v}}, t)$ is requested to be orthogonal to each of the basis functions. This can be written as:

$$\left. \begin{aligned} \int_{\mathcal{V}} \boldsymbol{\varphi}_i^T [\mathcal{L}(\hat{\mathbf{v}}) - \mathbf{g}(\hat{\mathbf{v}}, t)] d\mathcal{V} &= 0, \\ \int_{\mathcal{V}} \boldsymbol{\psi}_j^T [\mathcal{L}(\hat{\mathbf{v}}) - \mathbf{g}(\hat{\mathbf{v}}, t)] d\mathcal{V} &= 0, \end{aligned} \right\} \forall i, j \in [1, \dots, n]. \quad (4.37)$$

Elaboration of (4.37) results in the following set of equations:

$$\mathbf{M}\ddot{\mathbf{q}} + \mathbf{f}_{\text{in}}(\mathbf{q}, \dot{\mathbf{q}}, \mathbf{r}) = \mathbf{f}_{\text{ex}}(\mathbf{q}, t), \quad (4.38a)$$

$$\mathbf{T}\dot{\mathbf{r}} = \mathbf{f}_{\text{th}}(\mathbf{r}, \dot{\mathbf{q}}), \quad (4.38b)$$

where both second-order and first-order equations in time are grouped according to the state columns with generalised DOFs, $\mathbf{q} = [q_1, \dots, q_n]^T$ and $\mathbf{r} = [r_1, \dots, r_n]^T$, respectively. The other quantities in (4.38) have already been defined in (2.8).

Next, (4.38) can be rewritten to $\mathbf{f}_{\text{st}}(\mathbf{q}, \mu) = \mathbf{0}$ or $\dot{\mathbf{x}} = \mathbf{f}(\mathbf{x}, \mu)$, for calculation of static equilibrium points \mathbf{q}_e or periodic solutions $\mathbf{x}_p(t)$, respectively. Subsequently, numerical continuation of solutions can take place. This has already been explained in Section 2.4.

Numerous examples of the Galerkin method, applied to MEMS can be found, for instance, in Tilmans and Legtenberg (1994), Zhao et al. (2004), Krylov and Maimon (2004) and Younis et al. (2007). General approaches, without a specific MEMS application, can be found in Hung et al. (1997), Gabbay et al. (2000), Mehner et al. (2000) and Nayfeh et al. (2005).

4.4.2 Framework overview

With the physical level descriptions for the relevant effects (Section 4.3) and the Galerkin method for creating reduced-order models from this description (Section 4.4.1), the multiphysics modelling framework can be defined. A schematic overview of the framework is depicted in Figure 4.5.

The framework starts with the various physical level descriptions for a MEMS resonator. Blocks with physical effects and their governing equations are depicted in Figure 4.5. The physical models are based on (4.1), (4.6)–(4.9), (4.12), (4.14), (4.20) and (4.23), (4.27), (4.28), (4.29) or (4.33) and (4.34). Energy principles and the variational method (Hamilton's principle) are used for the structural dynamics, since these allow for straightforward inclusion of nonlinear effects. Thermoelasticity is directly included in the constitutive equations. Thermoelastic coupling is present between the heat equation and the structural dynamics part. The Green-Lagrange strain tensor is coupled to both the constitutive equations and the heat equation (in the latter through the dilatation (4.24)). Fringing field effects are included in both the electrostatic actuation and capacitive detection. Finally, thermal noise is present in the detected output of the resonator.

Once the modelling on the physical level has been completed, Galerkin discretisation is performed to obtain a reduced-order model from the physical level descriptions. This step is based on (4.35)–(4.37). As will become clear from Chapter 5, it may be required to perform the numerical simulations based on models in non-dimensional form. Otherwise, the difference in orders of magnitude between, for instance, typical vibration frequencies of $\mathcal{O}(10^6)$ Hz and displacements of $\mathcal{O}(10^{-7})$ m may cause difficulties for numerical simulation. Therefore, before Galerkin discretisation, the physical level description may be written to non-dimensional form. As a result, the basis functions for Galerkin discretisation will also be in non-dimensional form.

By application of the Galerkin method, a device level model is derived from the physical level description. This model, consisting of a system of ODEs, is still in a functional description, based on parameters that can be related to actual physical properties and dimensions of the resonator. Therefore, the model is very suitable for fast and accurate simulation of the nonlinear dynamics of MEMS resonators and for parameter studies. Furthermore, due to the followed approach, individual physical effects can still be distinguished and their relevance can be addressed.

The device level model (4.38) can be rewritten to forms that are suitable for numerical simulation. Static or dynamic analysis can be performed. In the static analysis, equilibrium points \mathbf{q}_e and their stability are calculated (see Section 2.4.2). This type of simulation is typically used for pull-in analysis of electrostatically actuated microstructures. In this way, pull-in curves can be determined, in which a structural displacement is depicted versus a static actuation voltage, which acts as the bifurcation parameter μ . In the dynamic analysis, periodic solutions \mathbf{x}_p and their stability are determined (see Section 2.4.3), which is relevant for determine steady-state oscillations of MEMS resonators. Amplitude-frequency curves can be calculated by setting the excitation frequency as the bifurcation parameter μ and by calculating the system response as a function of this frequency. These nonlinear equivalents of frequency response functions have already been introduced in Chapter 3.

Experimental validation is an integral part of the modelling framework. Results from numerical simulations using device level models are compared with experimental ones. If the numerical simulations have been performed based on a non-dimensional model, the results are translated back to dimensional form. Furthermore, experimental validation may have impact on the modelling assumptions (on the physical level) and on the Galerkin discretisation approach (choice and number of basis functions). Therefore, it may lead to model refinements.

In general, relatively simple structural elements (such as beams and plates) are used in the first step of the framework (physical level). These structures have the advantage that suitable basis functions for Galerkin discretisation may be found in a straightforward way. Often these shape functions are based on the linear, undamped modeshapes of the structure under consideration.

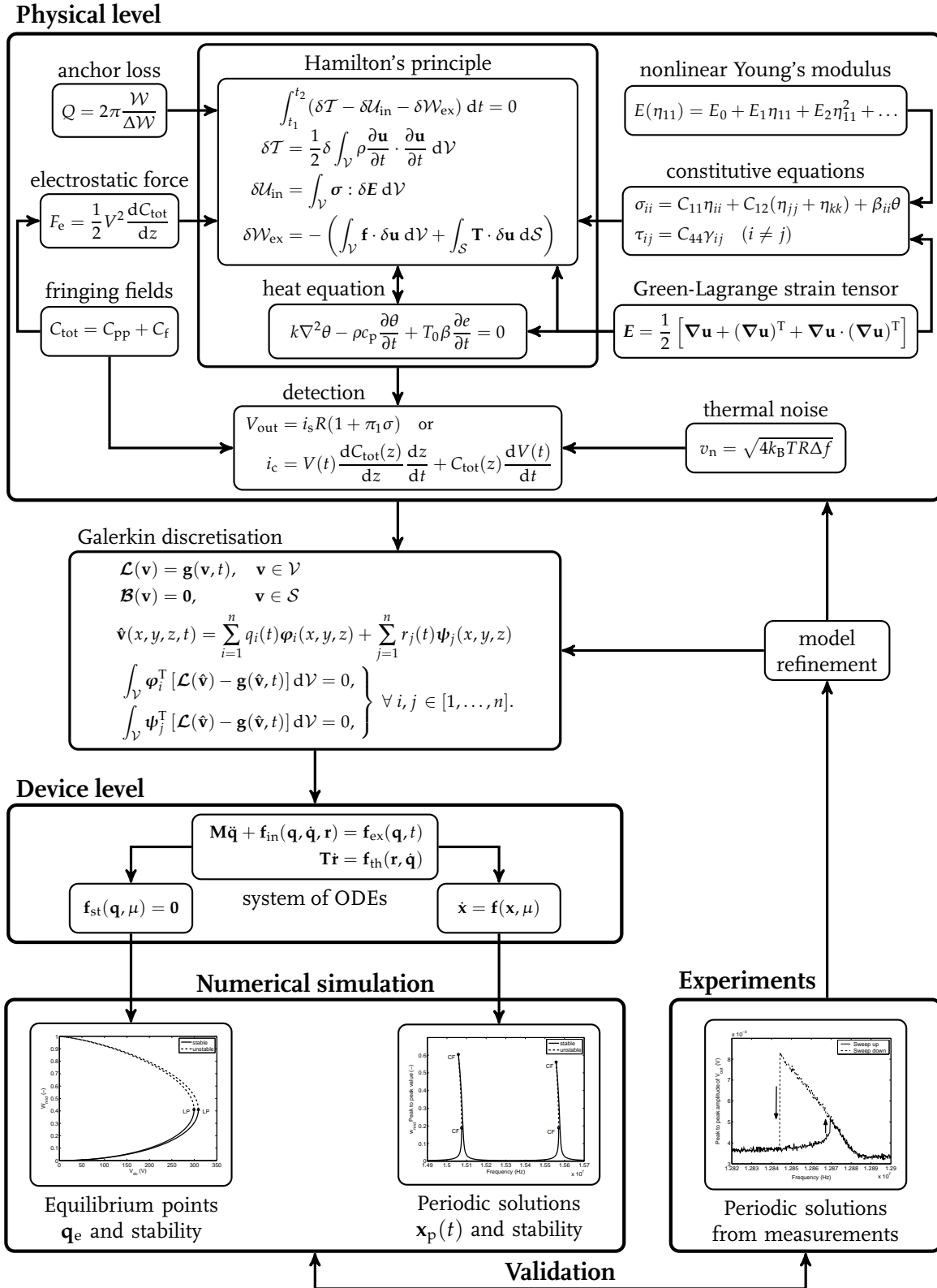


Figure 4.5 / Schematic overview of the multiphysics modelling framework for a MEMS resonator.

Modelling of a clamped-clamped beam MEMS resonator¹

Abstract / In this chapter, the first-principles based modelling framework is applied to a case study of a clamped-clamped beam MEMS resonator. Several models, having varying level of complexity and including various effects are derived. The models are partly validated by means of finite element simulations. Extensive numerical simulation is performed to address the influence of individual nonlinear effects. Finally, a comparison of the different models motivates the choice for the optimal model and concludes this chapter.

5.1 Introduction

In the previous chapter, the multiphysics modelling framework for dynamic simulation of MEMS resonators has been defined. In this chapter, the framework will be applied to the same MEMS resonator as used in Section 3.2: an electrostatically actuated clamped-clamped beam. The heuristic model of Section 3.2 cannot describe the dynamics of this resonator to their full extent, or in a predictive sense. One important reason for this is that various physical phenomena that may play a role (see Section 4.3) have only been included in a descriptive, lumped manner. As a result, different nonlinear dynamic effects have been gathered into a single, effective nonlinear stiffness function (3.5), thereby losing the ability to discern between contributions of single nonlinear effects.

The effective nonlinear stiffness function, together with the electrostatic actuation has been able to describe the overall, Duffing-like behaviour (see Section 3.2.3). However, due to the lumped form of the model, no insight can be gained into how physical dimensions and parameters contribute to the overall dynamic behaviour through individual physical effects (see Section 4.3). By means of the modelling framework of Chapter 4, in this chapter, a straightforward approach will be applied to arrive at a first-principles

¹Parts of this chapter have been presented in Mestrom et al. (2008b).

based multiphysics model of the clamped-clamped beam resonator. All relevant effects (defined in the framework) will be included, allowing for investigation of their individual contributions.

The outline of this chapter is as follows. In Section 5.2, physical level models for the clamped-clamped beam resonator will be derived using the modelling framework. The models will be rewritten to non-dimensional form and will be discretised using Galerkin discretisation. Using this approach, reduced-order models of varying complexity will be obtained. Next, in Section 5.3, some aspects of the reduced-order models are validated by means of finite element simulations. Simulation results for the derived models will be presented in Section 5.4, where an extensive investigation of individual nonlinear dynamic effects will be performed. Additionally, the different models will be compared. This serves as a motivation for the choice of the optimal, or most promising model, which will be validated experimentally in Chapter 6, and leads to the conclusions in Section 5.5.

5.2 Models of the clamped-clamped beam MEMS resonator

The clamped-clamped beam MEMS resonator, considered in this chapter, has already been depicted in Figure 3.1. Schematically, the resonator is depicted again in Figure 5.1(a). The resonator is both actuated and sensed electrostatically. The voltages on the electrodes are denoted by V_1 and V_2 and the corresponding electrode gaps are d_1 and d_2 , respectively. Voltage V_1 consists of a dc (V_{dc}) and an ac (V_{ac}) component, whereas voltage V_2 on the output electrode consists only of a dc voltage V_{dc} . The coordinate system is chosen such that the x -direction is along the length of the beam, y is in thickness direction and z is in transverse direction. Displacements in (x, y, z) -direction are denoted by (u_0, v_0, w_0) , respectively. Figure 5.1(b) depicts an idealisation of the beam resonator having a length l , a width h and a thickness b . The beam is clamped on both ends and its dynamic transverse deflection is denoted by $w_0(x, t)$, where t denotes time. Figure 5.1(c) shows

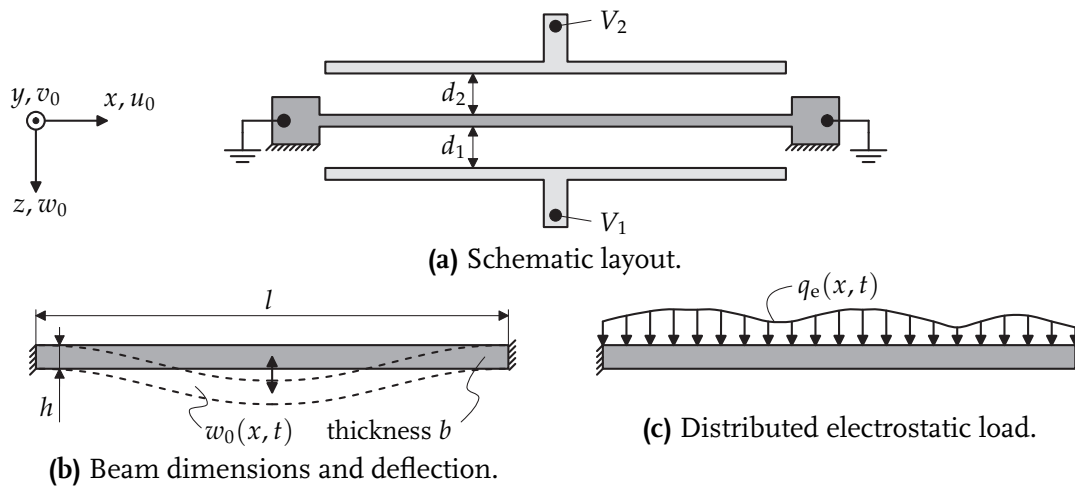


Figure 5.1 / Schematic representation of the clamped-clamped beam resonator.

the distributed load, acting on the beam. This load comprises the combined excitation from the electrostatic forces acting between the beam and the two electrodes.

The resonator output results from capacitive detection using electrode 2 in Figure 5.1(a). Only the motional current i_c in (4.29) (see Section 4.3.7) will be present, since $V_2 = V_{dc}$.

At this point, it is useful to list the nominal values for the dimensions and the electrode gaps of the clamped-clamped beam resonator, which will be used in the experiments in Chapter 6. The values are listed in Table 5.1. For experimental validation, beams with two different thickness values b will be used. The dimensions listed in Table 5.1 will have implications with respect to the modelling, see Section 5.2.1.

Table 5.1 / Nominal dimensions of the beam resonator and the electrode gaps.

Dimension	Value	Unit
l	44	μm
h	4	μm
b	1.4 or 10	μm
d_1, d_2	330	nm

5.2.1 Assumptions

Several general assumptions, related to the mechanical domain, underly the models that will be derived in this section. These are the following:

1. beam theory is assumed for modelling the beam. This implies that
 - displacements are independent of coordinate y , see Figure 5.1, such that the beam can be considered as 2D;
 - no stress or strain is present in z -direction (σ_{zz} and ε_{zz} are not included);
 - Euler-Bernoulli or Timoshenko beam theory can be used;
2. finite strains are assumed, instead of infinitesimal strains. As a result, strain components are evaluated according to the Green-Lagrange strain tensor, instead of the infinitesimal strain tensor (see Section 4.3.1). In this way, geometric nonlinear effects can be taken into account;
3. in-plane displacements u_0 are much smaller than transverse displacements w_0 : $u_0 \ll w_0$. Finite element simulations have confirmed that u_0 is two to three orders of magnitude smaller than w_0 ;
4. axial inertia is neglected (u_0 -motion is assumed stationary);

5. properties like Young's modulus E , mass density ρ and shear modulus G are assumed to be constant along the beam length, as well as its width h and thickness b (implying constant area $A = bh$ and second moment of area $I = \frac{1}{12}bh^3$);
6. the clamping on the beam edges is assumed to be ideal.

Several different theories exist for describing the (dynamic) behaviour of beams (Han et al., 1999; Wang et al., 2000). Classical Euler-Bernoulli beam theory is adequate for slender beam structures, that is, for structures with a small width-to-length ratio h/l , see, for instance Weaver et al. (1990), Rao (1995) and Meirovitch (2001). In this theory, transverse shear is neglected. However, for non-slender beams, having a relatively large width-to-length ratio, transverse shear may play a significant role. Timoshenko beam theory (Timoshenko, 1921, 1922) includes both shear deformation and rotary inertia. In addition to the transverse deflection field $w_0(x, t)$ of Euler-Bernoulli beam theory, a shear deformation field $\varphi(x, t)$ is assumed, together with related inertia terms. See also Appendix B.1 on beam theory.

From the nominal dimensions of the beam, listed in Table 5.1, it becomes clear the width-to-length ratio is relatively large ($h/l = 1/11$), which implies that slender beam theory (Euler-Bernoulli) may no longer be adequate for describing the beam deformation. In order to investigate the effect of shear deformation, both Euler-Bernoulli and Timoshenko beam theory will be used.

5.2.2 Physical level models

Based on the governing equations for the effects that play a role (see Section 4.3), three different physical level models will be derived for the clamped-clamped beam resonator. Used theories and included effects in these models are summarised in Table 5.2.

Table 5.2 / Used theories and included effects in the three different models (E: Euler-Bernoulli; T: Timoshenko).

Model	beam theory	anchor loss	fringing fields	thermo-elasticity	nonlinear elasticity
<i>I</i>	E	✓	✓	✗	✓
<i>II</i>	E	✓	✓	✓	✗
<i>III</i>	T	✓	✓	✓	✗

All three models include fringing field effects and anchor loss. Anchor loss will be included into the models after they have been written to non-dimensional form and have been discretised using the Galerkin method, see Section 5.2.6 The beam motion in all three models is detected capacitively, see Section 4.3.7. An expression for the motional current i_c , see (4.29), will be presented. Actually, this expression will be an improved version of (3.6) used in Chapter 3. As stated before in Section 5.2.1, two options are available

for beam theory. Models *I* and *II* are derived according to Euler-Bernoulli beam theory, whereas model *III* is based on Timoshenko beam theory. Moreover, only model *I* includes nonlinear material effects (nonlinear Young's modulus (4.12)). Only for uni-axial loading, (4.12) can be derived in a straightforward way, see Appendix A.4.3 and Kim and Sachse (2000). Therefore, this is only done for model *I* which is based on Euler-Bernoulli beam theory. Due to the complexity of this model, thermoelastic effects have not been included. However, models *II* and *III* both include thermoelastic effects. The resulting PDEs for the three models will be presented in the next subsections. Detailed derivations, using Hamilton's principle (Section 4.5), can be found in Appendix B.2.

Model I

The PDE of model *I*, describing the transverse deflection w_0 ($w_0(x, t)$) according to Euler-Bernoulli beam theory is the following:

$$\begin{aligned} \rho A \frac{\partial^2 w_0}{\partial t^2} - \rho I \frac{\partial^4 w_0}{\partial x^2 \partial t^2} + \left[E_0 I + E_1 I \left(\frac{\partial w_0}{\partial x} \right)^2 + \frac{3E_2 I}{4} \left(\frac{\partial w_0}{\partial x} \right)^4 \right. \\ \left. + \frac{9E_2 I h^2}{20} \left(\frac{\partial^2 w_0}{\partial x^2} \right)^2 \right] \frac{\partial^4 w_0}{\partial x^4} + \left[2E_1 + 9E_2 I \left(\frac{\partial w_0}{\partial x} \right)^2 \right] \left(\frac{\partial^2 w_0}{\partial x^2} \right)^3 \\ + \left[6E_1 I \frac{\partial w_0}{\partial x} + 9E_2 I \left(\frac{\partial w_0}{\partial x} \right)^3 + \frac{9E_2 I h^2}{10} \frac{\partial^3 w_0}{\partial x^3} \right] \frac{\partial^2 w_0}{\partial x^2} \frac{\partial^3 w_0}{\partial x^3} \\ - \left[\int_0^l \left\{ \frac{E_0 A}{2I} \left(\frac{\partial w_0}{\partial x} \right)^2 + \frac{E_1 A}{4I} \left(\frac{\partial w_0}{\partial x} \right)^4 + \frac{E_1 I}{I} \left(\frac{\partial^2 w_0}{\partial x^2} \right)^2 \right. \right. \\ \left. \left. + \frac{E_2 A}{8I} \left(\frac{\partial w_0}{\partial x} \right)^6 + \frac{3E_2 I}{2I} \left(\frac{\partial w_0}{\partial x} \right)^2 \left(\frac{\partial^2 w_0}{\partial x^2} \right)^2 \right\} dx + N_0 \right] \frac{\partial^2 w_0}{\partial x^2} = q_e. \end{aligned} \quad (5.1)$$

As stated before, ρ is the material mass density, $A = bh$ is the surface area and $I = \frac{1}{12}bh^3$ is the second moment of area. N_0 is the initial axial tension in the beam. A negative axial tension corresponds to a compressive load. Buckling is not considered in the model, since the buckling stress ($\frac{N_0}{A}$) for out-of-plane buckling of the thin beam ($b = 1.4 \mu\text{m}$) is over 350 MPa. Other parameters have already been introduced in Section 5.2.1 and in (4.12). The second term on the left-hand side of (5.1) denotes rotary inertia. Terms with E_0 ($E_0 = E$ in models *II* and *III*) are related to linear elasticity, whereas terms with E_1 and E_2 are related to higher-order elasticity effects.

The clamped edges of the beam translate to the following boundary conditions for (5.1):

$$\frac{\partial w_0}{\partial x} = 0, \quad w_0 = 0 \quad \text{at} \quad x = 0, l. \quad (5.2)$$

The distributed electrostatic load q_e ($q_e(x, t)$) acting on the beam, includes first-order fringing field correction terms (Osterberg, 1995; Osterberg and Senturia, 1997) and is

given by (see Appendix B.2.5):

$$q_e = \frac{\epsilon_0 b V_1^2(t)}{2(d_1 - w_0)^2} \left(1 + 0.65 \frac{d_1 - w_0}{b} \right) - \frac{\epsilon_0 b V_2^2}{2(d_2 + w_0)^2} \left(1 + 0.65 \frac{d_2 + w_0}{b} \right), \quad (5.3)$$

where the voltages on the electrodes (see Figure 5.1) are given by:

$$V_1(t) = V_{dc} + V_{ac} \sin(2\pi ft) \quad \text{and} \quad V_2 = V_{dc}. \quad (5.4)$$

As a result, excitation (5.3) contains both direct and parametric terms, since, where the parametric excitation acts on the linear and the nonlinear terms. Such an excitation has also been described in Rhoads et al. (2006). Furthermore, the expression for the electrostatic forcing q_e is in line with recently reported work on an electrostatically actuated microbeam (Krylov et al., 2005; Krylov, 2007).

The output current, resulting from capacitive detection of the motion of the beam will be derived in Section 6.4.4 and is given by:

$$\begin{aligned} i_{out} = & \frac{V_{ac}}{R_b} \sin(2\pi ft) + 2\pi ft V_{ac} (C_b + C_s) \cos(2\pi ft) \\ & + V_{dc} \int_0^l \frac{\epsilon_0 b}{(d_2 + w_0)^2} \left(1 + 0.65 \frac{d_2 + w_0}{b} \right) \frac{\partial w_0}{\partial t} dx. \end{aligned} \quad (5.5)$$

The last term on the right-hand side is the motional current i_c , resulting from vibration of the beam. First-order fringing field effects are included in this term. Furthermore, the first two terms in the right-hand side of (5.5), containing resistance R_b and capacitances C_b and C_s , are related to parasitic effects in the measurement circuit of the resonator.

Model II

The PDE of model II, describing the beam transverse deflection w_0 according to Euler-Bernoulli beam theory reads as:

$$\begin{aligned} \rho A \frac{\partial^2 w_0}{\partial t^2} - \rho I \frac{\partial^4 w_0}{\partial x^2 \partial t^2} + EI \frac{\partial^4 w_0}{\partial x^4} + \frac{\partial^2 M_T}{\partial x^2} \\ - \left[\frac{EA}{2l} \int_0^l \left(\frac{\partial w_0}{\partial x} \right)^2 dx + N_0 - \frac{1}{l} \int_0^l N_T dx \right] \frac{\partial^2 w_0}{\partial x^2} = q_e, \end{aligned} \quad (5.6)$$

where the thermoelastic moment M_T and the thermoelastic axial force N_T are given by:

$$M_T = E\alpha b \int_{-\frac{h}{2}}^{\frac{h}{2}} z \theta dz, \quad N_T = E\alpha b \int_{-\frac{h}{2}}^{\frac{h}{2}} \theta dz, \quad (5.7)$$

where α denotes the thermal expansion coefficient. The boundary conditions for (5.6) are the same as in (5.2) and the electrostatic force distribution q_e has already been given in (5.3)–(5.4). The output current is again given by (5.5). Apart from the terms with M_T and N_T , (5.6) equals (5.1), with $E_1 = E$ and $E_2 = E_3 = 0$.

The heat equation, describing the thermal field θ ($\theta(x, z, t)$) of the beam is given by (see also Appendix B):

$$\rho c_p \frac{\partial \theta}{\partial t} = k \frac{\partial^2 \theta}{\partial z^2} - T_0 \alpha E \frac{\partial}{\partial t} \left[\frac{1}{2} \left(\frac{\partial w_0}{\partial x} \right)^2 - z \frac{\partial^2 w_0}{\partial x^2} \right], \quad (5.8)$$

where c_p is the heat capacity of per unit volume at constant pressure and k is the thermal conductivity. $\theta = T - T_0$ is the difference between the instantaneous temperature T and the equilibrium temperature T_0 . Coupling between the mechanical domain and the thermal domain is present through the terms M_T and N_T in (5.6) and terms with w_0 in (5.8). Finally, (5.8) is subject to the boundary conditions:

$$\frac{\partial \theta}{\partial z} = 0 \quad \text{at} \quad z = \pm \frac{h}{2}, \quad (5.9)$$

denoting insulation, or zero heat flux, at the top and bottom boundaries of the beam.

Model III

Model III is based on Timoshenko beam theory. Both shear deformation and rotary inertia are included in the PDEs:

$$\begin{aligned} \rho A \frac{\partial^2 w_0}{\partial t^2} - k_s G A \left(\frac{\partial \varphi}{\partial x} + \frac{\partial^2 w_0}{\partial x^2} \right) \\ - \left[\frac{EA}{2l} \int_0^l \left(\frac{\partial w_0}{\partial x} \right)^2 dx + N_0 - \frac{1}{l} \int_0^l N_T dx \right] \frac{\partial^2 w_0}{\partial x^2} = q_e. \end{aligned} \quad (5.10a)$$

$$\rho I \frac{\partial^2 \varphi}{\partial t^2} - EI \frac{\partial^2 \varphi}{\partial x^2} + \frac{\partial M_T}{\partial x} + k_s G A \left(\varphi + \frac{\partial w_0}{\partial x} \right) = 0, \quad (5.10b)$$

In addition to the PDE for the transverse displacement w_0 (5.10a), an additional, coupled PDE (5.10b) describes the shear deformation field φ ($\varphi(x, t)$). Parameter k_s is the so-called shear correction factor, which accounts for the difference between the actual shear force over the width of the beam (z -direction) and the constant shear force predicted by Timoshenko theory. From Kaneko (1975), the best value of k_s for a rectangular cross section (determined from theory and experiments) is determined to be:

$$k_s = \frac{5 + 5\nu}{6 + 5\nu}, \quad (5.11)$$

where ν denotes Poisson's ratio. The thermoelastic moment M_T and the thermoelastic axial force N_T are the same as given in (5.7).

The boundary conditions for (5.10), corresponding to clamped edges, are:

$$w_0 = 0, \quad \varphi = 0 \quad \text{at} \quad x = 0, l. \quad (5.12)$$

The electrostatic forcing q_e in (5.10a) is given in (5.3)–(5.4) and the output current is given in (5.5). Furthermore, the heat equation reads:

$$\rho c_p \frac{\partial \theta}{\partial t} = k \frac{\partial^2 \theta}{\partial z^2} - T_0 \alpha E \frac{\partial}{\partial t} \left[\frac{1}{2} \left(\frac{\partial w_0}{\partial x} \right)^2 + z \frac{\partial \varphi}{\partial x} \right], \quad (5.13)$$

and is subject to the same boundary conditions as model II (5.9). Coupling between the mechanical domain and the thermal domain is present through the terms M_T, N_T and terms with w_0, φ in (5.10) and (5.13), respectively

5.2.3 Models in non-dimensional form

As indicated in the description of the modelling framework, Section 4.4.2, it is required for numerical simulation to put the models in non-dimensional form. In this way, vibration frequencies of $\mathcal{O}(10^6)$ Hz and displacements of $\mathcal{O}(10^{-7})$ m, for instance, are scaled such that they become approximately of the same order. For this purpose, introduce the non-dimensional parameters:

$$\bar{x} = \frac{x}{l}, \quad \bar{w}_0 = \frac{w_0}{d}, \quad \bar{t} = t \sqrt{\frac{EI}{\rho A l^4}}, \quad \bar{z} = \frac{z}{h}, \quad \text{and} \quad \bar{\theta} = \frac{\theta}{T_0}. \quad (5.14)$$

As a result, temporal and spatial derivatives become:

$$\frac{\partial}{\partial \bar{t}} = \sqrt{\frac{\rho A l^4}{EI}} \frac{\partial}{\partial t}, \quad \frac{\partial}{\partial \bar{x}} = l \frac{\partial}{\partial x}, \quad \text{and} \quad \frac{\partial}{\partial \bar{z}} = h \frac{\partial}{\partial z}. \quad (5.15)$$

Note that the shear deformation ϕ is already in non-dimensional form. By using (5.14) and (5.15), the three models can be written to non-dimensional form. For notational convenience, the bars, denoting non-dimensional quantities, will be omitted. New parameters will be introduced for the non-dimensionalised models, which are related to physical parameters in (5.1)–(5.13). These parameters are given first:

$$c_{1,E} = \frac{\alpha E d_1 h}{\rho c_p l^2} (-), \quad c_2 = \frac{\alpha E d_1^2}{\rho c_p l^2} (-), \quad c_{1,T} = \frac{\alpha E h}{\rho c_p l} (-), \quad (5.16a)$$

$$c_b = \frac{b}{d_1} (-), \quad c_d = \frac{d_2}{d_1} (-), \quad c_{e1} = \frac{E_1 d_1^2}{E_0 l^2} (-), \quad (5.16b)$$

$$c_{e2} = \frac{E_2 d_1^4}{E_0 l^4} (-), \quad c_{e3} = \frac{E_2 d_1^2 h^2}{E_0 l^4} (-), \quad c_k = \frac{k l^2}{c_p h^3} \sqrt{\frac{12}{\rho E}} (-), \quad (5.16c)$$

$$c_l = \frac{d_1}{l} (-), \quad c_m = 6 \frac{d_1^2}{h^2} (-), \quad c_r = \frac{h^2}{12 l^2} (-), \quad (5.16d)$$

$$c_s = 12 \frac{G l^2}{E h^2} (-), \quad c_v = \frac{6 \epsilon_0 l^4}{E d^3 h^3} (\text{V}^{-2}), \quad c_{M,E} = 12 \frac{\alpha T_0 l^2}{d_1 h} (-), \quad (5.16e)$$

$$c_{M,T} = 12 \frac{\alpha T_0 l}{h} (-), \quad c_N = 12 \frac{\alpha T_0 l^2}{h^2} (-), \quad c_\sigma = 12 \frac{l^2}{E h^2} (\text{m}^2 \text{N}^{-1}). \quad (5.16f)$$

Parameters c_v and c_σ are not in non-dimensional form, but are scaled conveniently. In this way, excitation voltages V_{dc} and V_{ac} can be applied in V and the axial tension $\sigma_0 = \frac{N_0}{A}$ can be applied in Pa. Furthermore, as will become clear from Section 5.2.7, the output current i_{out} (5.5) does not need to be rewritten to non-dimensional form, since it is calculated afterwards. The non-dimensional PDEs for models *I*, *II* and *III* will be given next.

Model I

After applying (5.14)–(5.15), the PDE (5.1) for the flexural vibration becomes:

$$\begin{aligned} \frac{\partial^2 w_0}{\partial t^2} - c_r \frac{\partial^4 w_0}{\partial x^2 \partial t^2} + \left[1 + c_{e1} \left(\frac{\partial w_0}{\partial x} \right)^2 + \frac{3}{4} c_{e2} \left(\frac{\partial w_0}{\partial x} \right)^4 + \frac{9}{20} c_{e3} \left(\frac{\partial^2 w_0}{\partial x^2} \right)^2 \right] \frac{\partial^4 w_0}{\partial x^4} \\ + \left[2c_{e1} + 9c_{e2} \left(\frac{\partial w_0}{\partial x} \right)^2 \right] \left(\frac{\partial^2 w_0}{\partial x^2} \right)^3 + \left[6c_{e1} \frac{\partial w_0}{\partial x} + 9c_{e2} \left(\frac{\partial w_0}{\partial x} \right)^3 \right. \\ + \left. \frac{9}{10} c_{e3} \frac{\partial^3 w_0}{\partial x^3} \right] \frac{\partial^2 w_0}{\partial x^2} \frac{\partial^3 w_0}{\partial x^3} - \left[\int_0^1 \left\{ c_m \left(\frac{\partial w_0}{\partial x} \right)^2 + \frac{1}{2} c_{e1} c_m \left(\frac{\partial w_0}{\partial x} \right)^4 \right. \right. \\ + \left. c_{e1} \left(\frac{\partial^2 w_0}{\partial x^2} \right)^2 + \frac{1}{4} c_{e2} c_m \left(\frac{\partial w_0}{\partial x} \right)^6 + \frac{3}{2} c_{e3} \left(\frac{\partial w_0}{\partial x} \right)^2 \left(\frac{\partial^2 w_0}{\partial x^2} \right)^2 \right\} dx \\ + c_\sigma \sigma_0 \left. \right] \frac{\partial^2 w_0}{\partial x^2} = c_v \left[V_1^2 \frac{1 + 0.65c_b(1 - w_0)}{(1 - w_0)^2} - V_2^2 \frac{1 + 0.65c_b(c_d + w_0)}{(c_d + w_0)^2} \right], \quad (5.17) \end{aligned}$$

where the parameters are given in (5.16), and where σ_0 is the axial stress in the beam. The non-dimensional boundary conditions become:

$$\frac{\partial w_0}{\partial x} = 0, \quad w_0 = 0 \quad \text{at} \quad x = 0, 1. \quad (5.18)$$

Model II

The PDE for flexural vibration w_0 of the beam in model *II* in non-dimensional form is given as:

$$\begin{aligned} \frac{\partial^2 w_0}{\partial t^2} - c_r \frac{\partial^4 w_0}{\partial x^2 \partial t^2} + \frac{\partial^4 w_0}{\partial x^4} + c_{M,E} \int_{-\frac{1}{2}}^{\frac{1}{2}} \frac{\partial^2 \theta}{\partial x^2} z dz \\ - \left[c_m \int_0^1 \left(\frac{\partial w_0}{\partial x} \right)^2 dx + c_\sigma \sigma_0 - c_N \int_0^1 \int_{-\frac{1}{2}}^{\frac{1}{2}} \theta dz dx \right] \frac{\partial^2 w_0}{\partial x^2} \\ = c_v \left[V_1^2 \frac{1 + 0.65c_b(1 - w_0)}{(1 - w_0)^2} - V_2^2 \frac{1 + 0.65c_b(c_d + w_0)}{(c_d + w_0)^2} \right], \quad (5.19) \end{aligned}$$

where Leibniz's rule for differentiation under the integral sign (see for instance Kreysig, 2006) is used for evaluating $\frac{\partial^2 M_T}{\partial x^2}$ in (5.6), using M_T from (5.7).

The non-dimensional form of (5.8) becomes:

$$\frac{\partial \theta}{\partial t} = c_k \frac{\partial^2 \theta}{\partial z^2} + \left[c_{1,E} z \frac{\partial^3 w_0}{\partial x^2 \partial t} - c_2 \frac{\partial w_0}{\partial x} \frac{\partial^2 w_0}{\partial x \partial t} \right]. \quad (5.20)$$

Parameters used in (5.19)–(5.20) are given in (5.16). The boundary conditions for (5.19) are given by (5.18) and those for (5.20) become:

$$\frac{\partial \theta}{\partial z} = 0 \quad \text{at} \quad z = \pm \frac{1}{2}. \quad (5.21)$$

Model III

In non-dimensional form, the PDEs for the beam in model III become:

$$\begin{aligned} \frac{\partial^2 w_0}{\partial t^2} - k_s \left(\frac{1}{c_1} \frac{\partial \varphi}{\partial x} + \frac{\partial^2 w_0}{\partial x^2} \right) - \left[c_m \int_0^1 \left(\frac{\partial w_0}{\partial x} \right)^2 dx + c_\sigma \sigma_0 - c_N \int_0^1 \int_{-\frac{1}{2}}^{\frac{1}{2}} \theta dz dx \right] \frac{\partial^2 w_0}{\partial x^2} \\ = c_v \left[V_1^2 \frac{1 + 0.65 c_b (1 - w_0)}{(1 - w_0)^2} - V_2^2 \frac{1 + 0.65 c_b (c_d + w_0)}{(c_d + w_0)^2} \right], \end{aligned} \quad (5.22a)$$

$$c_r \frac{\partial^2 \varphi}{\partial t^2} - \frac{\partial^2 \varphi}{\partial x^2} + c_{M,T} \int_{-\frac{1}{2}}^{\frac{1}{2}} \frac{\partial \theta}{\partial x} z dz + k_s c_s \left(\varphi + c_1 \frac{\partial w_0}{\partial x} \right) = 0, \quad (5.22b)$$

together with the boundary conditions:

$$w_0 = 0, \quad \varphi = 0 \quad \text{at} \quad x = 0, l. \quad (5.23)$$

The non-dimensional form of (5.13) becomes:

$$\frac{\partial \theta}{\partial t} = c_k \frac{\partial^2 \theta}{\partial z^2} - \left[c_{1,T} z \frac{\partial^2 \varphi}{\partial x \partial t} + c_2 \frac{\partial w_0}{\partial x} \frac{\partial^2 w_0}{\partial x \partial t} \right], \quad (5.24)$$

which has to obey boundary conditions (5.21).

5.2.4 Galerkin discretisation

In general, Galerkin discretisation is suited for both linear and nonlinear PDEs (Meirovitch, 2001). For nonlinear PDEs, a system of nonlinear ODEs results after discretisation. Now that the three models have been put into non-dimensional form, reduced-order (device level) models can be derived by applying Galerkin discretisation, see (4.35)–(4.37) in Section 4.4.1. For each of the non-dimensional PDEs in models I, II and III, their field variables can be expressed as a sum of spatial basis functions that, a priori, satisfy the imposed boundary conditions. The time-dependent coefficients of these

Table 5.3 / Overview of the PDEs, the fields and their corresponding Galerkin discretisation per model (subscript E: Euler-Bernoulli; T: Timoshenko).

Model	PDE(s)	boundary conditions	fields	generalised coordinates	basis functions
<i>I</i>	(5.17)	(5.18)	$w_0(x, t)$	$q_i(t)$	$W_{E,i}(x)$
<i>II</i>	(5.19)	(5.18)	$w_0(x, t)$	$q_i(t)$	$W_{E,i}(x)$
	(5.20)	(5.21)	$\theta(x, z, t)$	$r_i(t)$	$\Theta_{E,i}(x, z)$
<i>III</i>	(5.22b)	(5.23)	$\varphi(x, t)$	$p_i(t)$	$\Phi_{T,i}(x)$
	(5.22a)	(5.23)	$w_0(x, t)$	$q_i(t)$	$W_{T,i}(x)$
	(5.24)	(5.21)	$\theta(x, z, t)$	$r_i(t)$	$\Theta_{T,i}(x, z)$

basis functions are called generalised coordinates or generalised DOFs. An overview of the governing equations, their boundary conditions, the involved fields and their Galerkin discretisation is given in Table 5.3 for the three derived models.

Since both model *I* and model *II* are based on Euler-Bernoulli beam theory, the transverse deflection of the beam can be expressed as

$$w_0(x, t) = \sum_{i=1}^n q_i(t) W_{E,i}(x), \quad (5.25)$$






where basis functions $W_{E,i}(x)$ satisfy boundary conditions (5.18) a priori. In order to create a reduced-order model using Galerkin discretisation, the series (5.25) is truncated at order n . Similarly, other basis functions listed in Table 5.3 are used for series expansion of their corresponding fields.

An important aspect of Galerkin discretisation is the choice of basis functions. These have to be chosen carefully in order to obtain accurate results. Often, eigenmodes of a PDE are used. An overview of the expressions for the basis functions is given in Table 5.4. Next to the mathematical expressions, a graphical representation of the first basis function is depicted. A detailed derivation of the basis functions in Table 5.4 is given in Appendix B.3.

With respect to the mechanical part of the model, linear, undamped eigenmode shapes are used as basis functions. Non-dimensional mode shapes $W_{E,i}(x)$ for the Euler-Bernoulli beam in models *I* and *II* (with $\sigma_0 = 0$ in (5.17) and (5.19), respectively) are found from Blevins (1979). Mode shape pairs $\Phi_{T,i}(x)$ and $W_{T,i}(x)$ for the Timoshenko beam in model *III* are derived from the linear, homogeneous version (with $\sigma_0 = 0$) of (5.22) using a separation of variables method, described in, for instance, Han et al. (1999). For both $W_{E,i}(x)$ and $\Phi_{T,i}(x)$, $W_{T,i}(x)$, roots of the frequency equation (also listed in Table 5.4) are used in the mode shape coefficients.

Basis functions $\Theta_{E,i}(x, z)$ and $\Theta_{T,i}(x, z)$ for the thermal field $\theta(x, z)$ have been derived from linearised versions of the heat equations, that is, without the term with coefficient c_2 in (5.20) and (5.24). Their detailed derivation, based on separation of variables, is also presented in Appendix B.3. The temperature distribution in the basis functions for the thermal field can be understood as follows. Thermoelasticity results in a temperature

Table 5.4 / Basis functions for the fields w_0 and θ and a graphical representation of the first basis function ($i = 1$).

Function	Expression	Graph for $i = 1$
$W_{E,i}(x)$	$\cosh \lambda_i x - \cos \lambda_i x - \sigma_i (\sinh \lambda_i x - \sin \lambda_i x)$ $\sigma_i = \frac{\cosh \lambda_i - \cos \lambda_i}{\sinh \lambda_i - \sin \lambda_i}$ where λ_i are the roots of the frequency equation: $\cos \lambda \cosh \lambda - 1 = 0$	
$\Phi_{T,i}(x)$	$\alpha_i \sin a_i x + \beta_i \sinh b_i x + \alpha_i \sigma_i (\cos a_i x - \cosh b_i x)$	
$W_{T,i}(x)$	$\cos a_i x - \cosh b_i x - \sigma_i (\sin a_i x - \frac{\alpha_i}{\beta_i} \sinh b_i x)$ $\sigma_i = \frac{\cos a_i - \cosh b_i}{\sin a_i - \frac{\alpha_i}{\beta_i} \sinh b_i}$ $a_i = \sqrt{(c_r + \frac{1}{k_s c_s}) \frac{\omega_i^2}{2} + \frac{1}{2} \sqrt{(c_r + \frac{1}{k_s c_s})^2 \omega_i^4 + 4(\omega_i^2 - \frac{c_r}{k_s c_s} \omega_i^4)}}$ $b_i = \sqrt{-(c_r + \frac{1}{k_s c_s}) \frac{\omega_i^2}{2} + \frac{1}{2} \sqrt{(c_r + \frac{1}{k_s c_s})^2 \omega_i^4 + 4(\omega_i^2 - \frac{c_r}{k_s c_s} \omega_i^4)}}$ $\alpha_i = \frac{(k_s c_s a_i^2 - \omega_i^2) c_1}{k_s c_s a_i} \quad \beta_i = \frac{(k_s c_s b_i^2 + \omega_i^2) c_1}{k_s c_s b_i}$ where ω_i are the roots of the frequency equation, using $a_i, b_i, \alpha_i, \beta_i$: $\alpha^2 \sin a \sinh b + 2\alpha\beta \cos a \cosh b - \beta^2 \sin a \sinh b - 2\alpha\beta = 0$	
$\Theta_{E,i}(x, z)$	$c_{1,E} \frac{d^2 W_{E,i}(x)}{dx^2} (z + \frac{1}{2\pi} \sin 2\pi z)$	
$\Theta_{T,i}(x, z)$	$-c_{1,T} \frac{d\Phi_{T,i}(x)}{dx} (z + \frac{1}{2\pi} \sin 2\pi z)$	

increase for compression and a temperature decrease for tension. Consider basis function $\Theta_{E,1}(x, z)$, depicted in Table 5.4. Its mathematical expression contains the second derivative of $W_{E,1}(x)$ with respect to x . For the mechanical basis function $W_{E,1}(x)$, also depicted in Table 5.4, at the left edge, the top side is under tension, and the bottom side is under compression. In the thermal basis function $\Theta_{E,1}(x, z)$, this would result in a positive temperature at the top side and a negative temperature at the bottom side. From the graphical representation of $\Theta_{E,1}(x, z)$, this is indeed observed to be the case.

An important aspect related to discretisation of the electrostatic forcing function (right-hand side in (5.17), (5.19) and (5.22a)) is the following. Consider, for instance, substitution of $\sum q_i W_{E,i}$ (shorthand notation for (5.25)) into the right-hand side (RHS) of (5.17), giving:

$$\text{RHS} = c_v \left[V_1^2 \frac{1 + 0.65c_b(1 - \sum q_i W_{E,i})}{(1 - \sum q_i W_{E,i})^2} - V_2^2 \frac{1 + 0.65c_b(c_d + \sum q_i W_{E,i})}{(c_d + \sum q_i W_{E,i})^2} \right]. \quad (5.26)$$

For the N^{th} equation of the reduced-order system, multiplication with $W_{E,N}$ and integration over x from 0 to 1 has to take place, see (4.37). Due to the denominator terms

in (5.26), no explicit, or analytic, solution can be obtained for this integral. For the basis functions $W_{T,i}$ for the Timoshenko beam, the same problem arises.

Three possible solutions are available for coping with this issue. One may

1. linearise or make a Taylor expansion of the electrostatic forcing term in order to get rid of the denominators that make an analytic solution impossible. This has been applied in, for instance, Tilmans and Legtenberg (1994) and Younis et al. (2003);
2. pre-multiply the PDE with the (common) denominator terms in (5.26), such that the electrostatic forcing is taken into account in an exact way. This method has been used in Younis et al. (2003) and Nayfeh and Younis (2005), for instance;
3. integrate (5.26) directly, using numerical methods (for instance, numerical quadrature). This method has been applied in, for instance Krylov et al. (2005), Krylov (2007) and Krylov et al. (2008).

For large-amplitude motion (for instance, up to dynamic pull-in), Taylor-expansion (option 1) is only very limitedly applicable, since the electrostatic forcing function is approximated accurately only in a small region, even if a large number of terms is taken into account. This is caused by the $1/w_0^2$ behaviour of the electrostatic forcing functions. Option 2 yields a computationally very complex model if a large number of modes is used for Galerkin discretisation. Furthermore, this option results in a state-dependent mass matrix in the reduced-order model, which may become singular during numerical simulation. Option 3 is the computationally more demanding option, but allows for straightforward inclusion of the electrostatic forcing terms and an exact representation. In this thesis, the last option is chosen. Fast calculation is still possible, by using carefully selected numerical quadrature routines, see also Section 5.2.7.

5.2.5 Reduced-order models

By application of Galerkin discretisation, using the basis functions described in the previous section (see Table 5.4), reduced-order models of varying order have been derived. From Figure 5.1, it can be seen that the electrodes span the whole beam length. For this reason, only symmetric modes will be included as basis functions for the Galerkin discretisation of $w_0(x, t)$ and $\varphi(x, t)$. This approach is also followed in, for instance, Younis et al. (2003) and Nayfeh et al. (2005). For models *I* and *II*, this translates to: $W_{E,i}(x)$, with $i = 1, 3, 5, \dots$ and for model *III*: $\Phi_{T,i}(x)$, $W_{T,i}(x)$, with $i = 1, 3, 5, \dots$. For the sake of convenience, arguments of the basis functions will be omitted in the following.

For model *I*, only a single-mode discretisation has been derived, due to mathematical complexity of the higher-order derivatives and their products in (5.17). For models *II* and *III*, 1, 2 and 3-mode discretisations have been derived. In the following, the expressions for the single-mode Galerkin discretisation of models *I*, *II* and *III* will be given and some model features will be discussed. In order to be able to implement damping related

to anchor loss, additional (other than thermoelastic) damping terms will be introduced into the models by means of modal viscous damping terms. Expressions for multi-mode Galerkin discretisations for models *II* and *III* can be found in Appendix B.4.

Model I

For the single-mode discretisation of (5.17), using $w_0 = q_1 W_{E,1}$, the general form for the reduced-order model can be written as (see also (4.38)):

$$\mathbf{M}\ddot{\mathbf{q}} + \mathbf{f}_{\text{in}}(\mathbf{q}, \dot{\mathbf{q}}) = \mathbf{f}_{\text{ex}}(\mathbf{q}, t), \quad (5.27)$$

where the quantities in (5.27) are elaborated as:

$$\mathbf{q} = q_1, \quad (5.28a)$$

$$\mathbf{M} = 1 - c_r \int_0^1 \frac{\partial^2 W_{E,1}}{\partial x^2} W_{E,1} dx, \quad (5.28b)$$

$$\begin{aligned} \mathbf{f}_{\text{in}}(\mathbf{q}, \dot{\mathbf{q}}) = & \lambda_1^4 q_1 + c_1 \dot{q}_1 - q_1 \left[c_m \left\{ q_1^2 \int_0^1 \left(\frac{\partial W_{E,1}}{\partial x} \right)^2 dx + \frac{1}{2} c_{e1} q_1^4 \int_0^1 \left(\frac{\partial W_{E,1}}{\partial x} \right)^4 dx \right. \right. \\ & + \left. \frac{1}{4} c_{e2} q_1^6 \int_0^1 \left(\frac{\partial W_{E,1}}{\partial x} \right)^6 dx \right\} + c_{e1} q_1^2 \int_0^1 \left(\frac{\partial^2 W_{E,1}}{\partial x^2} \right)^2 dx + \frac{3}{2} c_{e3} q_1^4 \int_0^1 \left(\frac{\partial W_{E,1}}{\partial x} \right)^2 \left(\frac{\partial^2 W_{E,1}}{\partial x^2} \right)^2 dx \\ & + c_\sigma \sigma_0 \int_0^1 \frac{\partial^2 W_{E,1}}{\partial x^2} W_{E,1} dx + c_{e1} \lambda_1^4 q_1^3 \int_0^1 \left(\frac{\partial W_{E,1}}{\partial x} \right)^2 W_{E,1}^2 dx + \frac{3}{4} c_{e2} \lambda_1^4 q_1^5 \int_0^1 \left(\frac{\partial W_{E,1}}{\partial x} \right)^4 W_{E,1}^2 dx \\ & + \frac{9}{20} c_{e3} \lambda_1^4 q_1^3 \int_0^1 \left(\frac{\partial^2 W_{E,1}}{\partial x^2} \right)^2 W_{E,1}^2 dx + 6 c_{e1} q_1^3 \int_0^1 \frac{\partial W_{E,1}}{\partial x} \frac{\partial^2 W_{E,1}}{\partial x^2} \frac{\partial^3 W_{E,1}}{\partial x^3} W_{E,1} dx \\ & + 9 c_{e2} q_1^5 \int_0^1 \left(\frac{\partial W_{E,1}}{\partial x} \right)^3 \frac{\partial^2 W_{E,1}}{\partial x^2} \frac{\partial^3 W_{E,1}}{\partial x^3} W_{E,1} dx + \frac{9}{10} c_{e3} q_1^3 \int_0^1 \left(\frac{\partial^3 W_{E,1}}{\partial x^3} \right)^2 \frac{\partial^2 W_{E,1}}{\partial x^2} W_{E,1} dx \\ & + 2 c_{e1} q_1^3 \int_0^1 \left(\frac{\partial^2 W_{E,1}}{\partial x^2} \right)^3 W_{E,1} dx + 9 c_{e2} q_1^5 \int_0^1 \left(\frac{\partial W_{E,1}}{\partial x} \right)^2 \left(\frac{\partial^2 W_{E,1}}{\partial x^2} \right)^3 W_{E,1} dx, \end{aligned} \quad (5.28c)$$

$$\mathbf{f}_{\text{ex}}(\mathbf{q}, t) = c_v \int_0^1 \left[V_1^2 \frac{1 + 0.65 c_b (1 - q_1 W_{E,1})}{(1 - q_1 W_{E,1})^2} - V_2^2 \frac{1 + 0.65 c_b (c_d + q_1 W_{E,1})}{(c_d + q_1 W_{E,1})^2} \right] W_{E,1} dx. \quad (5.28d)$$

Parameter λ_1 in (5.28c) denotes the first root of the frequency equation for the Euler-Bernoulli beam, see also Table 5.4. The term with c_1 on the right-hand side of (5.28c) is included to introduce viscous damping. It can be observed from the internal forces (5.28c) that the model is nonlinear in the state q_1 . Furthermore, the electrostatic force, including fringing field effects, is also nonlinear in q_1 .

Model II

The single-mode discretisation of (5.19) and (5.20), using $w_0 = q_1 W_{E,1}$ and $\theta = r_1 \Theta_{E,1}$, results in the following reduced-order model in general form:

$$\mathbf{M}\ddot{\mathbf{q}} + \mathbf{f}_{\text{in}}(\mathbf{q}, \dot{\mathbf{q}}, \mathbf{r}) = \mathbf{f}_{\text{ex}}(\mathbf{q}, t), \quad (5.29a)$$

$$\mathbf{T}\dot{\mathbf{r}} = \mathbf{f}_{\text{th}}(\mathbf{r}, \dot{\mathbf{q}}), \quad (5.29b)$$

where (5.29a) corresponds to the discretised version of (5.19) and (5.29b) to (5.20). The quantities in (5.29) are given by:

$$\mathbf{q} = q_1, \quad (5.30a)$$

$$\mathbf{r} = r_1, \quad (5.30b)$$

$$\mathbf{M} = 1 - c_r \int_0^1 \frac{\partial^2 W_{E,1}}{\partial x^2} W_{E,1} dx, \quad (5.30c)$$

$$\begin{aligned} \mathbf{f}_{in}(\mathbf{q}, \dot{\mathbf{q}}, \mathbf{r}) = & \lambda_1^4 q_1 + c_1 \dot{q}_1 + c_{M,E} \int_0^1 \int_{-\frac{1}{2}}^{\frac{1}{2}} r_1 \frac{\partial^2 \Theta_{E,1}}{\partial x^2} W_{E,1} z dz dx \\ & - q_1 \left[c_m q_1^2 \int_0^1 \left(\frac{\partial W_{E,1}}{\partial x} \right)^2 dx + c_\sigma \sigma_0 \right] \int_0^1 \frac{\partial^2 W_{E,1}}{\partial x^2} W_{E,1} dx, \end{aligned} \quad (5.30d)$$

$$\mathbf{f}_{ex}(\mathbf{q}, t) = c_v \int_0^1 \left[V_1^2 \frac{1 + 0.65 c_b (1 - q_1 W_{E,1})}{(1 - q_1 W_{E,1})^2} - V_2^2 \frac{1 + 0.65 c_b (c_d + q_1 W_{E,1})}{(c_d + q_1 W_{E,1})^2} \right] W_{E,1} dx, \quad (5.30e)$$

$$\mathbf{T} = \int_0^1 \int_{-\frac{1}{2}}^{\frac{1}{2}} \Theta_{E,1}^2 dz dx, \quad (5.30f)$$

$$\mathbf{f}_{th}(\mathbf{r}, \dot{\mathbf{q}}) = c_k r_1 \int_0^1 \int_{-\frac{1}{2}}^{\frac{1}{2}} \frac{\partial^2 \Theta_{E,1}}{\partial z^2} \Theta_{E,1} dz dx + c_{1,E} \dot{q}_1 \int_0^1 \int_{-\frac{1}{2}}^{\frac{1}{2}} \frac{\partial^2 W_{E,1}}{\partial x^2} \Theta_{E,1} z dz dx. \quad (5.30g)$$

Due to the fact that the basis functions $\Theta_{E,i}$ are anti-symmetric with respect to $z = 0$, they will vanish during integration from $-\frac{1}{2}$ to $\frac{1}{2}$ over z . As a result, terms with c_N and c_2 in (5.19) and (5.20), respectively have vanished and are not found in the reduced-order model (5.29)–(5.30). Again, viscous modal damping is introduced by the term with coefficient c_1 in (5.30d). Furthermore, it can be seen that (thermoelastic) coupling is present between the mechanical part 5.29a and thermal part 5.29b by means of variables $\dot{\mathbf{q}}$ and \mathbf{r} . Moreover, compared to model *I*, only a single nonlinear term arises in (5.30d), which is related to the mid-plane stretching term of the beam (parameter c_m). The electrostatic forcing function (5.30e) is the same as the one in model *I*.

Model III

The single-mode discretisation of (5.22)–(5.24), using $\varphi = p_1 \Phi_{T,1}$, $w_0 = q_1 W_{T,1}$ and $\theta = r_1 \Theta_{T,1}$, results in the following reduced-order model:

$$\mathbf{M} \ddot{\mathbf{q}} + \mathbf{f}_{in}(\mathbf{q}, \dot{\mathbf{q}}, \mathbf{r}) = \mathbf{f}_{ex}(\mathbf{q}, t), \quad (5.31a)$$

$$\mathbf{T} \dot{\mathbf{r}} = \mathbf{f}_{th}(\mathbf{r}, \dot{\mathbf{q}}), \quad (5.31b)$$

where (5.31a) contains the discretised versions of (5.22) and (5.31b) contains the discretised version of (5.24). The terms in (5.31) are given by:

$$\mathbf{q} = [p_1 \quad q_1]^T, \quad (5.32a)$$

$$\mathbf{r} = r_1, \quad (5.32b)$$

$$\mathbf{M} = \begin{bmatrix} c_r \int_0^1 \Phi_{T,1}^2 dx & 0 \\ 0 & \int_0^1 W_{T,1}^2 dx \end{bmatrix}, \quad (5.32c)$$

$$\mathbf{f}_{\text{in}}(\mathbf{q}, \dot{\mathbf{q}}, \mathbf{r}) = \mathbf{C} \begin{bmatrix} \dot{p}_1 \\ \dot{q}_1 \end{bmatrix} + \mathbf{c}_r(r_1) + \mathbf{K}(q_1) \begin{bmatrix} p_1 \\ q_1 \end{bmatrix}, \quad (5.32d)$$

$$\mathbf{f}_{\text{ex}}(\mathbf{q}, t) = \begin{bmatrix} 0 \\ c_v \int_0^1 \left[V_1^2 \frac{1+0.65c_b(1-q_1 W_{T,1})}{(1-q_1 W_{T,1})^2} - V_2^2 \frac{1+0.65c_b(c_d+q_1 W_{T,1})}{(c_d+q_1 W_{T,1})^2} \right] W_{T,1} dx \end{bmatrix}, \quad (5.32e)$$

$$\mathbf{T} = \int_0^1 \int_{-\frac{1}{2}}^{\frac{1}{2}} \Theta_{T,1}^2 dz dx, \quad (5.32f)$$

$$\mathbf{f}_{\text{th}}(\mathbf{r}, \dot{\mathbf{q}}) = c_k r_1 \int_0^1 \int_{-\frac{1}{2}}^{\frac{1}{2}} \frac{\partial^2 \Theta_{T,1}}{\partial z^2} \Theta_{T,1} dz dx - c_{1,T} \dot{q}_1 \int_0^1 \int_{-\frac{1}{2}}^{\frac{1}{2}} \frac{\partial \Phi_{T,1}}{\partial x} \Theta_{T,1} z dz dx, \quad (5.32g)$$

where matrices \mathbf{C} , $\mathbf{c}_r(r_1)$ and $\mathbf{K}(q_1)$ in (5.32d) are given by:

$$\mathbf{C} = \begin{bmatrix} c_{1,\varphi} \int_0^1 \Phi_{T,1}^2 dx & 0 \\ 0 & c_{1,w} \int_0^1 W_{T,1}^2 dx \end{bmatrix}, \quad (5.33a)$$

$$\mathbf{c}_r(r_1) = \begin{bmatrix} r_1 c_{M,T} \int_0^1 \int_{-\frac{1}{2}}^{\frac{1}{2}} \frac{\partial \Theta_{T,1}}{\partial x} \Phi_{T,1} z dz dx \\ 0 \end{bmatrix}, \quad (5.33b)$$

$$\mathbf{K}(q_1) = \begin{bmatrix} k_s c_s \int_0^1 \Phi_{T,1}^2 dx - \int_0^1 \frac{\partial^2 \Phi_{T,1}}{\partial x^2} \Phi_{T,1} dx & k_s c_s c_1 \int_0^1 \frac{\partial W_{T,1}}{\partial x} \Phi_{T,1} dx \\ -\frac{k_s c_s}{c_1} \int_0^1 \frac{\partial \Phi_{T,1}}{\partial x} W_{T,1} dx & -k_{22}(q_1) \int_0^1 \frac{\partial^2 W_{T,1}}{\partial x^2} W_{T,1} dx \end{bmatrix}, \quad (5.33c)$$

with, in the (2,2) element of $\mathbf{K}(q_1)$:

$$k_{22}(q_1) = k_s c_s + c_m q_1^2 \int_0^1 \left(\frac{\partial W_{T,1}}{\partial x} \right)^2 dx + c_\sigma \sigma_0. \quad (5.33d)$$

Similar to model *II*, terms that are linear in the basis functions $\Theta_{T,i}$ (c_N and c_2 in (5.22a) and (5.24), respectively) vanish during integration over z from $-\frac{1}{2}$ to $\frac{1}{2}$. Similar to model *I* and *II*, viscous modal damping is introduced in the discretised model by terms $c_{1,\varphi}$ and $c_{1,w}$ in (5.33a).

Similar to model *II*, for model *III* only two nonlinear terms arise in the single-mode discretisation: Midplane stretching is included through the parameter c_m in (5.33d) and electrostatic forcing is present in (5.32e).

Finally, in model *III*, thermoelastic coupling (by means of variables $\dot{\mathbf{q}}$ and \mathbf{r}) is present between the mechanical (5.31a) and thermal part (5.31b) (this is also similar to model *II*).

5.2.6 Modelling of anchor loss

Next to thermoelastic damping, the most important source of dissipation is assumed to be anchor loss, since the resonator operates in vacuum, see also Sections 4.3.3 and (4.3.4). Anchor loss is implemented in the reduced-models by means of viscous modal damping: parameter c_1 in (5.28c), c_1 in (5.30d) and $c_{1,\varphi}$ and/or $c_{1,w}$ in (5.33a). In the multi-mode Galerkin discretisations (see Appendix B.4), each vibration mode is accompanied by a mechanical loss term. In (5.28c), for instance, coefficient c_1 can be regarded as $c_1 =$

2ξ , where ξ denotes the classical non-dimensional damping coefficient of a 1DOF mass-spring-damper system and is related to the Q -factor by:

$$Q = \frac{1}{2\xi}. \quad (5.34)$$

For models *II* and *III*, similar considerations hold. In order to calculate the anchor loss of the vibrating beam, the expression for the Q -factor (4.14) is used, for which both the energy loss $\Delta\mathcal{W}$ per cycle and the total energy stored in the beam \mathcal{W} are needed. For a linear 1DOF mass-spring-damper system, relations (4.14) and (5.34) are equivalent. Because, another dissipation mechanism next to anchor loss is present in the system (thermoelastic damping), in this section $\Delta\mathcal{W}$ refers to energy dissipation through anchor loss and is based on analytic relations derived by Hao et al. (2003) and Hao and Xu (2009). The general approach in Hao and Xu (2009) assumes (see also Section 4.3.4) that the dissipation per cycle can be calculated as the integral of the stress at the suspension multiplied by the displacement in the suspension that is induced by this stress:

$$\Delta\mathcal{W} = \pi \int_{\text{clamped region}} \text{stress} \cdot \text{displacement}. \quad (5.35)$$

The displacement in the substrate is calculated from 2D elastic wave theory describing the elastic wave propagation (Hao and Xu, 2009). For a beam, clamped on both sides, the clamped edges act as shear stress excitation sources on the substrate. From Hao and Xu (2009), the energy loss is then given by:

$$\Delta\mathcal{W} = \pi h^2 b \tau_0^2 \left[\frac{(3 - \nu)(1 + \nu)}{4E} + \frac{\Pi}{\pi E} \right], \quad (5.36)$$

where Π is given by the integral

$$\Pi = \int_0^1 \left[\frac{\zeta^2(1 - \nu^2)}{\sqrt{1 - \zeta^2}} \cos\left(\sqrt{1 - \zeta^2} \frac{\omega l}{c_L}\right) + 2(1 + \nu) \sqrt{1 - \zeta^2} \cos\left(\sqrt{1 - \zeta^2} \frac{\omega l}{c_L}\right) \right] d\zeta. \quad (5.37)$$

In (5.37) ζ is the integration variable, ω is the resonant frequency of the beam and c_L is the longitudinal wave propagation velocity in the substrate defined according to:

$$c_L^2 = \frac{E}{\rho(1 - \nu^2)}. \quad (5.38)$$

In order to derive expressions for the total energy stored in the beam, the vibration is assumed to be both linear and harmonic. In that case, the stored energy equals:

$$\mathcal{W}_E = \frac{\omega_i^2}{2} \int_V \rho W_{E,i}^2(x) dV = \frac{\rho A \omega_i^2}{2} \int_0^l W_{E,i}^2(x) dx \quad (5.39)$$

according to Euler-Bernoulli beam theory (models *I* and *II*) and:

$$\begin{aligned} \mathcal{W}_T &= \frac{\omega_i^2}{2} \int_V (\rho W_{T,i}^2(x) + \rho (z \Phi_{T,i}(x))^2) dV \\ &= \frac{\omega_i^2}{2} \left(\rho A \int_0^l W_{T,i}^2(x) dx + \rho I \int_0^l \Phi_{T,i}^2(x) dx \right) \end{aligned} \quad (5.40)$$

according to Timoshenko beam theory (model *III*). In (5.39) and (5.40) ω_i denotes the natural frequency of mode i . Furthermore, the shear forces at the clamped ends of the beam are:

$$\tau_{0,E} = -\frac{EI}{A} \frac{\partial^3 W_{E,i}(x)}{\partial x^3} \bigg|_{x=0,l} \quad \text{for Euler-Bernoulli,} \quad (5.41)$$

$$\tau_{0,T} = k_s G \left(\frac{\partial W_{T,i}(x)}{\partial x} + \Phi_{T,i}(x) \right) \bigg|_{x=0,l} \quad \text{for Timoshenko beam theory.} \quad (5.42)$$

For the nominal beam dimensions, listed in Table 5.1, the Q -factors related to anchor loss can be calculated using (5.36)–(5.42) and (4.14). This gives $Q_E \approx 450$ and $Q_T \approx 120$ for models *I*–*II* and model *II*, respectively.

Some remarks on these values are the following. Firstly, the anchor loss for the Timoshenko beam is higher than for the Euler-Bernoulli beam. This is expected, since the Timoshenko beam shows more shear force, resulting in more dissipation.

Secondly, the calculated Q -factors are found to be independent of the beam thickness b (Table 5.1). Namely, the energy loss per cycle (5.36) is linear in b , whereas the stored energy is also linear in b (through A and I), see (5.39) and (5.40).

Finally, the values for the Q -factor are very low and roughly an order of magnitude smaller than experimentally determined Q -factors (this will become clear from Chapter 6). In the theory presented in Hao et al. (2003) and Hao and Xu (2009), all waves that are radiated into the semi-infinite substrate due to the shear force at the clamped edges are assumed to be lost. This assumption is not valid for the beam considered in this work, see for instance Figure 3.3. Wave reflections may occur in the suspensions of the beam due to finite dimensions of the substrate. Reflected waves result in less energy loss and, therefore, a higher Q -factor. Since this effect cannot be quantified in a straightforward way, (tuning) freedom will be allowed in the numerical simulations with respect to the Q -factor related to anchor loss (see Section 6.5).

5.2.7 Numerical implementation

The reduced-order models that have been derived in Section 5.2.5 have to be written in the form $\mathbf{f}_{\text{st}}(\mathbf{q}, \mu) = \mathbf{0}$ or $\dot{\mathbf{x}} = \mathbf{f}(\mathbf{x}, \mu)$, for calculation of equilibrium points \mathbf{q}_e or periodic solutions $\mathbf{x}_p(t)$, respectively (see Section 2.4). First, however, the integrals in the reduced-order models, stemming from Galerkin discretisation, have to be evaluated numerically. Apart from these integrals, the models remain in symbolic form, allowing for parameter studies. The procedure for deriving the models is as follows.

In the first step, the equations of motion (5.27)–(5.33) are implemented in symbolical form in the software package MAPLE², which is very suitable for symbolic mathematical calculations. The integrals in (5.28), (5.30) and (5.32)–(5.33) are evaluated numerically

²Waterloo Maple Inc, Maple 12.

using adaptive Gauss-Kronrod quadrature (Piessens et al., 1983). The combination of trigonometric and hyperbolic functions in the basis functions, see Table 5.4, requires that these integrals are evaluated numerically. Next, the equations are rewritten to forms that are suitable for analysis of equilibrium points or periodic solutions. As mentioned before, apart from the evaluated integrals, they are still in symbolic form.

In order to calculate equilibrium points and their stability, the resulting equations, $\mathbf{f}_{\text{st}}(\mathbf{q}, \mu) = \mathbf{0}$, are exported from MAPLE to MATLAB³. Stability can be determined from the eigenvalues of the Jacobian at an equilibrium point, see also Section 2.4.2. Once a solution has been determined, numerical continuation for equilibrium points can take place. Path-following routines (see also Section 2.4.4) for studying bifurcations of equilibrium points have been written in MATLAB. Furthermore, routines for evaluating the state-dependent discretised electrostatic forcing (5.26) using numerical quadrature are implemented.

The dynamic equations, in the form of $\dot{\mathbf{x}} = \mathbf{f}(\mathbf{x}, \mu)$, are exported to Fortran code, which can be used in AUTO (Doedel et al., 1998) for calculating periodic solutions and their bifurcations. Additionally, local derivative information in terms of the Jacobians $\frac{\partial \mathbf{f}(\mathbf{x}, \mu)}{\partial \mathbf{x}}$ and $\frac{\partial \mathbf{f}(\mathbf{x}, \mu)}{\partial \mu}$ is calculated symbolically in MAPLE and exported as well, since it allows for faster computation. For this purpose, the issue of evaluating (5.26) and its derivative arises. Custom-made functions for evaluating the discretised electrostatic forcing and its derivatives are written in Fortran, such that they can be evaluated using Fortran numerical integration routines directly.

Finally, in case of calculation of periodic solutions, the output current i_{out} of the resonator can be calculated as a postprocessing step, using (5.5). Again, this will be clarified in Chapter 6. Results presented in Section 5.4 will be presented in terms of displacements, since they will be used for comparison between the three derived models.

5.3 Validation with finite element solutions

In order to validate some aspects of the three models that have been derived, finite element (FE) simulations can be used. For this purpose, Comsol Multiphysics⁴ will be used, which is very suited for multiphysics calculations. Simulations will be performed for the nominal beam geometry listed in Table 5.1, using physical parameter values as listed in Table 5.5. The thickness b of the beam only has influence for the fringing field calculations. The x -axis of the beam is oriented in the $[100]$ direction. Therefore, Young's modulus and Poisson's ratio are given by (A.8) and (A.9). In the next three sections, a comparison between results from FE simulations and results from models *I*, *II* and *III* will be made.

³The Mathworks, Inc., Matlab 7.5.0 (R2007b).

⁴COMSOL AB, Comsol Multiphysics 3.4

Table 5.5 / Physical parameter values for the reduced-order models.

Parameter	Value	Unit
ρ	2329	kg m^{-3}
E	130.02	GPa
ν	0.2785	(-)
k	156	$\text{W m}^{-1} \text{K}^{-1}$
c_p	716	$\text{J kg}^{-1} \text{K}^{-1}$
α	$2.616 \cdot 10^{-6}$	K^{-1}
T_0	300	K

5.3.1 Natural frequencies and mode shapes

First, the natural frequencies and mode shapes will be compared. For this purpose, a modal analysis simulation is carried out in Comsol Multiphysics. The FE results are compared with natural frequencies according to Euler-Bernoulli beam theory (models *I* and *II*) and Timoshenko beam theory (model *III*). These have been calculated as solutions of the frequency equations listed in Table 5.4.

In Comsol, the beam has been modeled as a two-dimensional structure. Three different mesh sizes are used. The finest mesh has 8 elements over the beam width h and 320 elements along the beam length l . The calculation is a plane stress analysis and the element type is quadratic. This type of element includes shear effects, so no explicit choice for exclusion of shear is possible. The two edges of the beam at $x = 0, l$ are clamped and anisotropic material behaviour, using the stiffness coefficients from Table A.1, has been implemented. Results for modes 1 through 7 are shown in Table 5.6. Both the FE results and the analytical results are listed.

From Table 5.6 it can be seen that no large differences are present between the 16×160 mesh and the 32×320 mesh. Therefore, the 32×320 mesh is considered fine enough for the modes considered. The natural frequencies calculated using Comsol match those

Table 5.6 / Natural frequencies of the first 7 modes of the beam (MHz). Three different mesh sizes are used in Comsol Multiphysics.

Mode	Comsol Multiphysics			Model <i>II</i>	Model <i>III</i>
	8×80	16×160	32×320	Euler-Bernoulli	Timoshenko
1	15.351	15.350	15.349	15.869	15.323
2	40.503	40.498	40.497	43.743	40.422
3	75.331	75.322	75.320	85.753	75.155
4	117.444	117.431	117.426	141.754	117.111
5	165.019	164.999	164.993	211.757	164.454
6	216.650	216.623	216.615	295.759	215.775
7	271.307	271.273	271.264	393.762	270.047

calculated using Timoshenko beam theory very well. In this way, confidence is gained in the results from Timoshenko beam theory. The natural frequencies from Euler-Bernoulli beam theory are significantly higher than the FE results or the results from Timoshenko. The difference increases with the number of the mode. This is expected, since for higher mode numbers, shear deformation has a larger influence.

In Figure 5.2, the modeshapes of symmetric modes 1, 3 and 5 are depicted. It has already been explained why only the symmetric modes will be taken into account for Galerkin discretisation. Figure 5.2(a) shows the FE modeshapes and Figure 5.2(b) and (c) show the Euler-Bernoulli and Timoshenko base functions (modeshapes), respectively. At first sight, all three sets of mode shapes look very similar. However, closer inspection shows that both the FE and Timoshenko modeshapes have a nonzero slope at $x = 0, l$, whereas the Euler-Bernoulli modeshapes do have a zero slope (as imposed by the boundary conditions (5.2)). This can be observed most clearly for mode 5. Therefore, the Timoshenko modeshapes match the FE modeshapes better in terms of boundary conditions.

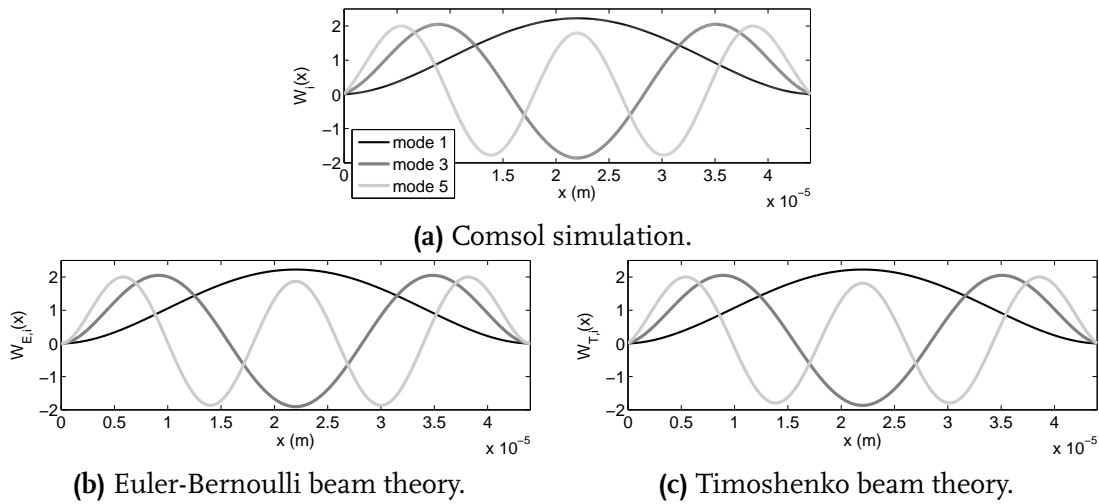


Figure 5.2 / Modeshapes of modes 1, 3 and 5.

5.3.2 Thermoelastic modeshapes and damping

Simplified expressions for the Q -factor related to thermoelastic damping in beams have been derived for beams in Zener's classical papers (Zener, 1937, 1938), see (4.16)–(4.17), and, in an improved form, in Lifshitz and Roukes (2000), see (4.18)–(4.19). In principle, these expressions are independent of the modeshape, but in both of the theories, the Q -factor depends on the beam vibration frequency ω . The thermal time constant (4.17) associated with thermal relaxation can be calculated from the beam dimensions and the physical parameter values. This yields $\tau = 1.733 \cdot 10^{-8}$ s/rad, corresponding to a thermal vibration frequency of 9.184 MHz, which is indeed in the range of the beam natural frequencies. In order to calculate the Q -factor of the beam with nominal dimensions, vi-

bration frequencies according to two beam theories can be used, see Table 5.6. Results for modes 1, 3 and 5 are listed in Table 5.7. From the results it can be seen that the Q -factors

Table 5.7 / Q -factors for modes 1, 3 and 5, calculated according to Zener theory (4.16) (Zener, 1937, 1938) and Lifshitz (4.18) (Lifshitz and Roukes, 2000) using natural frequencies from Euler-Bernoulli or Timoshenko beam theory, see Table 5.6.

Mode	Euler-Bernoulli		Timoshenko	
	Zener	Lifshitz	Zener	Lifshitz
1	14319	14449	14079	14211
3	58508	55801	51454	49466
5	143098	129650	111271	102118

predicted by both Zener and Lifshitz are lower for the beam vibrating at natural frequencies according to Timoshenko beam theory. Furthermore, for mode 1, the Q -factors are all in the same range. For higher modes, the differences increase, which can be attributed to the differences between the frequencies (Euler-Bernoulli versus Timoshenko), that is also increasing, see Table 5.6.

Next, calculations for thermoelastic damping have been performed in Comsol Multiphysics. These are based on Duwel et al. (2006) and the calculation method presented there. This method is based on a mutual coupling between the stress-strain analysis module and the heat transfer module. Mechanical deformation forms a heat source in the material according to the dilatation term e (4.24) in (4.23) and the temperature, calculated in the thermal domain, causes thermoelastic strains in the material through the thermoelastic constitutive law (4.21). The 32×320 mesh, already mentioned in Section 5.3.1, is used in Comsol Multiphysics. From a transient analysis, the complex eigenvalues λ_c of the coupled system can be calculated. The imaginary parts $\text{Im}\{\lambda_c\}$ denote the angular natural frequencies and the Q -factors can be determined from (Duwel et al., 2006):

$$Q = \left| \frac{\text{Im}\{\lambda_c\}}{2\text{Re}\{\lambda_c\}} \right|. \quad (5.43)$$

In model *II* (Euler-Bernoulli) and *III* (Timoshenko), the eigenvalues are calculated from the linearisation of the model around $(\mathbf{q}, \dot{\mathbf{q}}, \mathbf{r}) = (\mathbf{0}, \mathbf{0}, \mathbf{0})$. Next, the eigenvalues can be calculated from the Jacobian of the system and the damped natural frequency and the Q -factor can be determined. Results of this investigation are depicted in Table 5.8. It can be seen that the damped natural frequencies of model *II* (Euler-Bernoulli) and model *III* (Timoshenko) are slightly below the undamped frequencies, see Table 5.6. This is expected as damping is known to reduce the natural frequency. Interestingly, however, for the Comsol Multiphysics simulations, this is the other way around: the damped natural frequencies are (slightly) higher than the undamped ones. No explanation for this effect has been found. Nevertheless, the damped natural frequencies from Comsol Multiphysics match the ones from the Timoshenko beam model (model *III*) very well.

Furthermore, for the first mode, the Q -factor from the Comsol Multiphysics simulations

Table 5.8 / Damped natural frequencies and Q -factors according to FE simulations (32×320 mesh) and according to calculations in this work.

	Comsol Multiphysics		Model II		Model III	
Mode	f (MHz)	Q (-)	f (MHz)	Q (-)	f (MHz)	Q (-)
1	15.350	14324	15.799	14549	15.321	15260
3	75.323	49700	82.962	56688	75.144	62891
5	165.003	100111	194.790	131674	164.428	157693

and the Euler-Bernoulli model is in line with the one predicted in Table 5.7 by the theories of Zener and Lifshitz. For the Timoshenko model, the Q -factor is slightly higher, which contradicts the observation in Table 5.7, where Timoshenko beam theory results in lower Q -factors. However, the agreement for mode 1 gives confidence in the first-principles based modelling approach in models II and III. For higher modes, the difference between the Q -factors of models II and III and those from Comsol Multiphysics increases. The Comsol Multiphysics values agree very well with the Lifshitz values listed in Table 5.7.

Results for mode 1 in Table 5.8 are also depicted graphically in Figure 5.3, where the temperature part $\Theta(x, z)$ of the modeshapes is depicted as a temperature distribution (in K) over the beam. All temperature modeshapes have been scaled similarly. Figures 5.3(a) and (b) show the results from the simulation in Comsol Multiphysics. The explanation for the temperature distribution has already been given in Section 5.2.4. Figure 5.3(c) shows a contour plot of the basis function $\Theta_{E,1}(x, z)$ (see also Table 5.4 for the temperature field in model II). Figure 5.3(d) shows $\Theta_{T,1}(x, z)$ for model III. The contour plots in Figure 5.3(c) and (d) have been normalised to the same amplitude as Figure 5.3(b), such that they can be compared. It can be seen that the temperature distribution in the finite

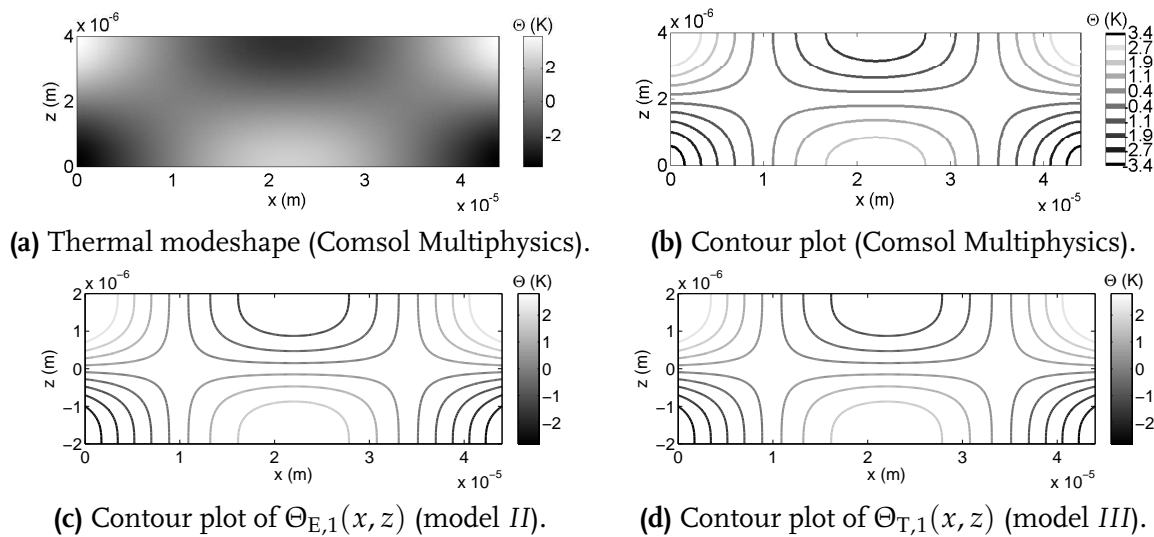


Figure 5.3 / Thermoelastic modeshapes: (a) and (b) calculates from Comsol Multiphysics; (c) and (d) basis functions for Euler-Bernoulli and Timoshenko models, respectively.

element simulation is captured very well in the basis functions $\Theta_{E,1}(x, z)$ and $\Theta_{T,1}(x, z)$. Therefore, these are believed to serve as suitable basis functions for Galerkin discretisation. Results for modes 3 and 5 show a similar match between the FE solutions and the basis functions.

Summarising, although there is a difference between Q -factors of models *II* and *III* and those from Comsol Multiphysics simulations or classical theory (Zener, 1937; Lifshitz and Roukes, 2000), a good match is obtained between the thermoelastic mode-shape and the basis functions $\Theta_{E,i}(x, z)$ and $\Theta_{T,i}(x, z)$ that are used in Galerkin discretisation. A major disadvantage of the classical theory is that only an expression for the Q -factor is calculated, under the assumption of small harmonic motions. The approach in this work allows for straightforward and explicit inclusion of thermoelastic effects in the multiphysical nonlinear models through coupling between the mechanical and thermal physical field. Furthermore, thermoelastic damping is not the only loss mechanism present in flexural MEMS resonators. Additional loss mechanisms like anchor loss, see Section 5.2.6, also cause dissipation. In practice, a single overall Q -factor Q_{tot} is measured, see also (4.15) in Section 4.3.3, which can be related to the dissipation through anchor loss Q_a and thermoelastic damping Q_{th} as:

$$\frac{1}{Q_{\text{tot}}} = \frac{1}{Q_a} + \frac{1}{Q_{\text{th}}}, \quad (5.44)$$

Because of relation (5.44), it is difficult to distinguish between the different loss mechanisms in measurements. Although the values for Q_a , derived in Section 5.2.6, suggest that anchor loss will be the dominant contribution in (5.44), thermoelastic damping will not be neglected. Namely, as will become clear from Section 6.5, the calculated Q_a are much too low.

5.3.3 Fringing field effects

The final aspect of the model that is validated by means of finite element simulations is the effect of fringing fields. For this purpose, consider the schematic representation of the beam and its cross-section in Figure 5.4. Note that in the cross-section, Figure 5.4(b), the electrodes are much larger than the beam. This may not be apparent from Figure 5.4(a), but corresponds to the situation in practice, see Figure 3.3. The cross-section is in the y - z

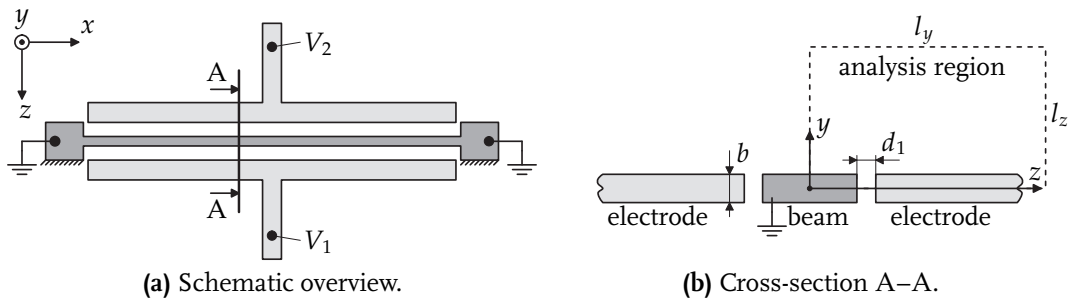


Figure 5.4 / Schematic overview of the analysis for fringing field effects.

plane and shows the analysis region for the fringing fields, having a dimension of l_y and l_z in y - and z -direction, respectively. Due to symmetry, the region spans only the positive y -direction. The Comsol Multiphysics analysis is performed with the beam grounded and with the electrode in positive z -direction having a voltage V . In Comsol, the capacitance can be calculated from an electrostatic analysis. The analysis region dimensions l_y and l_z have influence on the calculated capacitance values. Therefore, Comsol simulations have been performed for varying values of l_y and l_z . Typical simulation results are depicted in Figure 5.5, for the two different thickness values b of the beam, see Table 5.1. The grayscale in this figure indicates the voltage, normalised to a maximum value of 1 and the black lines denote the electrical field lines. It can be seen that fringing fields are present between the beam and the electrode. Simulation results are listed in Table 5.9.

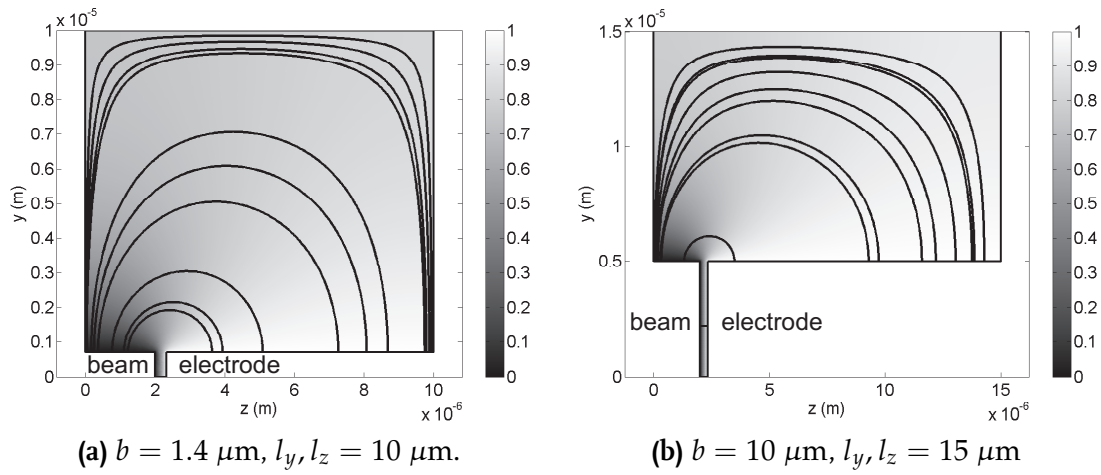


Figure 5.5 / Fringing field effects for two geometries and analysis regions.

According to parallel plate theory (4.25), the capacitance between the beam and a single electrode is given by

$$C_{\text{pp}} = \frac{\epsilon_0 b l}{d_1}. \quad (5.45)$$

With inclusion of first-order fringing field correction, see for instance Osterberg (1995) and Osterberg and Senturia (1997), the total capacitance becomes:

$$C_{\text{tot}} = \frac{\epsilon_0 b l}{d_1} \left[1 + \frac{2d_1}{\pi b} + \frac{2d_1}{\pi b} \ln \left(\frac{\pi b}{d_1} \right) \right], \quad (5.46)$$

where the parallel plate capacitance (5.45) can be recognised in the first term in the right-hand side of (5.46). The electrostatic forcing q_e with first-order fringing field correction (5.3) is also based on (5.46).

Table 5.9 lists the results for two different values of the beam thickness b and the nominal geometry of Table 5.1. Analytically calculated capacitance values, according to (5.45) and (5.46) are listed as well as simulation results from Comsol Multiphysics.

Table 5.9 / Results for the fringing field capacitance calculations.

Analysis type		Capacitance in (fF)	
		$b = 1.4 \mu\text{m}$	$b = 10 \mu\text{m}$
parallel plate (5.45)		1.65278	11.80558
fringing field corrected (5.46)		2.54313	13.18356
Comsol	$l_y, l_z = 5 \mu\text{m}$	2.56923	–
Multiphysics	$l_y, l_z = 10 \mu\text{m}$	2.64167	12.77934
	$l_y, l_z = 15 \mu\text{m}$	2.65984	12.81066
	$l_y, l_z = 20 \mu\text{m}$	2.67532	12.83034
	$l_y, l_z = 25 \mu\text{m}$	2.68346	12.84224

From Table 5.9, several observations can be made. Firstly, fringing field effects play a significant role for the two beams under investigation in this chapter. Secondly, fringing fields have a larger effect for the thin beam ($b = 1.4 \mu\text{m}$) than for the thick beam ($b = 10 \mu\text{m}$). The parallel plate approximation (5.45) significantly underestimates the capacitance value. The value, obtained from the fringing field corrected capacitance (5.46), is up to 6% lower than the value from Comsol Multiphysics, depending on the size of the analysis region. For the thick beam, the effect of fringing fields is less pronounced. The parallel plate capacitance is approximately 10% lower than the fringing field corrected one. From the finite element simulations, it follows that (5.46) slightly overestimates the capacitance (up to 3% for $l_y, l_z = 25 \mu\text{m}$).

Although the fringing field effect is slightly underestimated for thin beams ($b = 1.4 \mu\text{m}$) and slightly overestimated for thick beams ($b = 10 \mu\text{m}$), it may still be concluded that (5.46) serves as a useful first-order approximation for fringing field effects. The analytical expression (5.46) allows for inclusion of fringing fields in functional form in the electrostatic forcing (5.3), which is very useful for fast simulation with models *I* to *III*.

5.4 Simulation results and model comparison

From Section 5.3, confidence has been gained with respect to several separate physical aspects of the models. In this section, simulations with the reduced-order models will be performed, in order to investigate the influence of the various physical effects on the static and dynamic behaviour of the clamped-clamped beam MEMS resonator. For the beam, the nominal geometry, listed in Table 5.1 will be used, together with model parameter values of Table 5.5. As indicated in Section 5.2.7, results will be presented in terms of displacements, instead of the output current i_{out} . Furthermore, results obtained in the next two sections will be compared to results from literature. First, in Section 5.4.1, pull-in curves will be determined from a static analysis, studying equilibrium points and their stability. Next, in Section 5.4.2, amplitude-frequency curves will be calculated from the full nonlinear dynamic analysis in which periodic solutions and their stability are determined.

5.4.1 Equilibrium points and stability

The analysis of equilibrium points and their stability is typically used for pull-in analysis of electrostatically actuated microstructures. As stated in Section 2.4.2, pull-in is a phenomenon that may occur when the electrostatic force overcomes the mechanical force, such that the electrodes snap together. This happens at a the so-called pull-in voltage V_{pi} . In order to study equilibrium points and their stability for the three models, they have been rewritten to the form $\mathbf{f}_{\text{st}}(\mathbf{q}, \mu) = \mathbf{0}$, which is numerically implemented in MATLAB, see Section 5.2.7. Essentially, this boils down to setting all time derivatives in models *I* to *III* to zero. Furthermore, only a single electrode is used in the static analysis (see Figure 5.1):

$$V_1 = V_{\text{dc}}, \quad V_2 = 0. \quad (5.47)$$

Equilibrium points of the system are calculated as a function of the dc voltage V_{dc} , which acts as the bifurcation parameter μ . Numerical continuation, or path-following, is applied to follow the branch of equilibrium points. It is convenient to introduce the midpoint displacement w_{mid} (at $x = 0.5$) as a response quantity. It is defined for the non-dimensional basis functions as:

$$w_{\text{mid}} = \sum_{i=1}^n q_i W_{\text{E},i}(0.5) \quad \text{or} \quad w_{\text{mid}} = \sum_{i=1}^n q_i W_{\text{T},i}(0.5), \quad (5.48)$$

depending on whether the model is based on Euler-Bernoulli or Timoshenko beam theory, respectively. By multiplying w_{mid} with d_1 , see (5.14), the dimensional midplane displacement can be calculated. Furthermore, physical effects (see Section 4.3) that are relevant for equilibrium positions and their stability are mid-plane stretching (a geometric nonlinear effect) in the beam and fringing fields in the electrostatic actuation. In models *I* to *III*, these effects have been included and are quantified by a non-dimensional coefficient, see Section 5.2.5. Coefficient c_{m} is related to mid-plane stretching and c_{b} accounts for fringing field effects. By setting one (or both) of these coefficients to zero, the respective effect can be switched off.

In order to compare the three different models, first, the static analysis is performed for the single-mode discretisation. The axial initial stress σ_0 is set to zero for now. Some results for the three models are depicted in Figure 5.6 for the thin beam ($b = 1.4 \mu\text{m}$). On the horizontal axis, the bifurcation parameter V_{dc} is indicated. On the vertical axis w_{mid} is depicted ranging from 0 to d_1 (see Table 5.1). In Figure 5.6, four different so-called pull-in curves can be seen. The curves consist of a stable lower part and an unstable upper part. Local stability of the system follows from an eigenvalue analysis, see Section 2.4.2. The transition from the stable to the unstable part is accompanied by a limit point (LP) bifurcation. For a voltage V_{dc} that increases above the pull-in voltage V_{pi} at this bifurcation point, no stable solution of the system can be found, and pull-in will occur. An increase of the voltage beyond V_{pi} results in a sudden ‘snap’ of the beam to the electrode.

Furthermore, it can be seen in Figure 5.6 that model *III* has the lowest pull-in voltage, $V_{\text{pi}} = 299.44 \text{ V}$, and that models *I,II* without the effect of fringing fields ($c_{\text{b}} = 0$) have

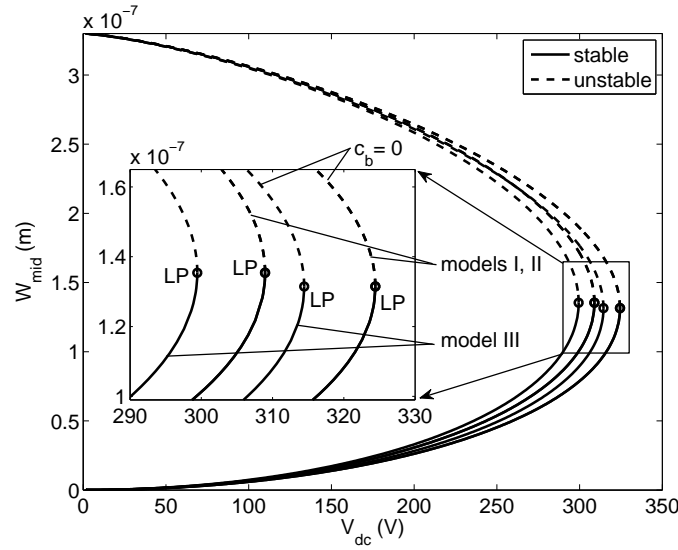


Figure 5.6 / Static equilibrium curves for the single mode models *I*, *II* and *III*. $c_b = 0$ indicates: simulation without fringing fields.

the highest pull-in voltage, $V_{pi} = 324.42$ V. All simulations show a similar midpoint displacement w_{mid} at the bifurcation point. Further numerical results are given in Table 5.10 for both the thin and the thick beam. For the sake of convenience, midplane displacements are given in non-dimensional form. The pull-in displacement for an ideal parallel plate approximation with a uniform gap equals $w = 0.33$, see for instance Senturia (2001). Simulations with the single-mode models take approximately 30 seconds on a Pentium IV computer, depending on the stepsize in V_{dc} . From these numerical results, it becomes clear that there is virtually no difference between models *I* and *II* in terms of pull-in voltages and midpoint displacements at pull-in. Therefore, for static analysis, material nonlinear effects provide no added value to the model but only increase the model

Table 5.10 / Results for models *I*, *II* and *III* for the single-mode discretisation.

Thin beam: $b = 1.4 \mu\text{m}$								
Model	$c_b, c_m = 0$		$c_b = 0$		$c_m = 0$		Full model	
	V_{pi} (V)	w_{mid} (-)	V_{pi} (V)	w_{mid} (-)	V_{pi} (V)	w_{mid} (-)	V_{pi} (V)	w_{mid} (-)
<i>I</i>	324.30	0.3980	324.42	0.3985	308.82	0.4100	308.95	0.4103
<i>II</i>	324.29	0.3980	324.42	0.3984	308.82	0.4099	308.95	0.4104
<i>III</i>	314.31	0.3980	314.43	0.3984	299.31	0.4100	299.44	0.4103

Thick beam: $b = 10 \mu\text{m}$								
Model	$c_b, c_m = 0$		$c_b = 0$		$c_m = 0$		Full model	
	V_{pi} (V)	w_{mid} (-)	V_{pi} (V)	w_{mid} (-)	V_{pi} (V)	w_{mid} (-)	V_{pi} (V)	w_{mid} (-)
<i>I</i>	324.30	0.3980	324.42	0.3985	321.98	0.3998	322.10	0.4002
<i>II</i>	324.29	0.3980	324.42	0.3984	321.97	0.3998	322.10	0.4002
<i>III</i>	314.31	0.3980	314.43	0.3984	312.06	0.3999	312.18	0.4003

complexity. Model *III*, based on Timoshenko beam theory, shows pull-in voltages that are approximately 10 V lower than model *I* and *II*, which are based on Euler-Bernoulli beam theory. This is caused by the additional shear flexibility in the model *III*. Inclusion of fringing fields results in a pull-in voltage that is approximately 15 V lower. Compare, for instance, the ‘full model’ case with a case in which $c_b = 0$. The effect of midplane stretching is very small. For all three models parameter c_m has negligible influence, which is caused by the small ratio of d_1 to h , see (5.16) and Table 5.1. However, it will become clear from Section 5.4.2 that this parameter does play a role in dynamical simulations.

Results for the thick beam ($b = 10 \mu\text{m}$) show a similar trend. Here, however, the effect of fringing fields is less pronounced, resulting only in a difference of approximately 2 V in the pull-in voltage. This has already become clear in the finite element validation of the fringing field approximation in Section 5.3.3. In fact, fringing fields cause the only difference between the results for the thin and thick beam. The reason for this is that the thickness dimension, as defined in Figure 5.1, normally does not play a role in models based on beam theory. For fringing field effects, however, it does play a role. Also for the thick beam, midplane stretching only has a marginal influence on the response values.

Next, an analysis is performed in which the effect of taking into account multiple modes is investigated. As already indicated in Section 5.2.5, multi-mode discretisations are available for models *II* and *III* only. Results from this analysis are given in Table 5.11, again for the thin and the thick beam. Durations of the numerical simulation range from 15 seconds for the single-mode models up to 120 seconds for model *III* with 3-modes on a Pentium IV computer. From these results, it can be concluded that, for the beam under investigation, inclusion of more modes does not result in significantly different pull-in voltages or midpoint displacements.

Table 5.11 / Results for models *II* and *III* for single and multi-mode discretisations.

Model	Modes	$b = 1.4 \mu\text{m}$		$b = 10 \mu\text{m}$	
		V_{pi} (V)	w_{mid} (-)	V_{pi} (V)	w_{mid} (-)
<i>II</i>	1	308.95	0.4104	322.10	0.4002
	1, 3	309.12	0.4087	322.27	0.3986
	1, 3, 5	309.11	0.4089	322.27	0.3988
<i>III</i>	1	299.44	0.4103	312.18	0.4003
	1, 3	299.65	0.4084	312.39	0.3983
	1, 3, 5	299.63	0.4088	312.38	0.3986

As a result, it can be concluded for the static analysis that a single mode model is accurate enough. For the nominal geometry, simulation results show that shear deformation may not be neglected and that fringing field effects are significant (this was already found in Section 5.3.3). Therefore, model *III*, with inclusion of fringing fields appears to be the most accurate model for the beam under investigation.

Comparison with literature

As an additional validation of both models *II* and *III* and the analysis of equilibrium points and their stability, several comparisons with pull-in analyses reported in literature will be performed.

In Osterberg (1995) and Osterberg and Senturia (1997), a linear Euler-Bernoulli beam model has been proposed as a means for determining the pull-in voltage for, among others, a clamped-clamped beam (or plate-like) device. Material parameters for the beam are: $E = 169$ GPa, $\nu = 0.06$, $b = 50$ μm , $h = 3$ μm and $d_1 = 1$ μm . Due to the plate-like structure of the silicon beam, an effective Young's modulus of $E/(1 - \nu^2)$ (plate modulus) is used. Furthermore, the electrostatic actuation in Osterberg and Senturia (1997) contains the same fringing field correction as used in this work. The governing partial differential equation for the beam has been solved by a finite difference relaxation solver. Pull-in voltages have been reported for six test cases with varying lengths l and initial stress values σ_0 . These are listed in Table 5.12. Additionally, 3D numerical simulations results from MEMCAD⁵ have been listed.

In order to make a fair comparison with results from this work, numerical simulations with model *II* (which is also based on Euler-Bernoulli beam theory) have been performed, including up to three modes in the discretisation, indicated by 1; 1, 3 or 1, 3, 5. The results are also depicted in Table 5.12. From the comparison, it can be seen that quite a

Table 5.12 / Pull-in voltage V_{pi} (V) for several parameter values. Comparison between results reported in Osterberg and Senturia (1997) and simulations with model *II*.

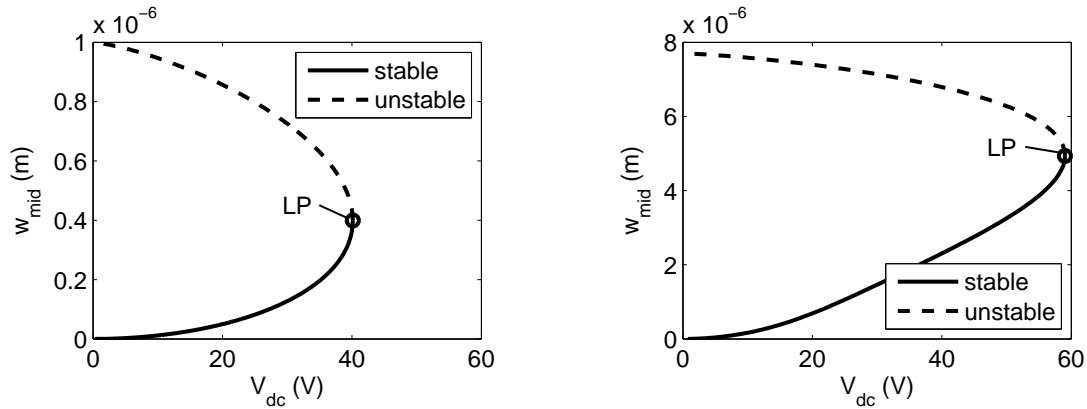
Parameters		This work, model <i>II</i>				
l (μm)	σ_0 (MPa)	Osterberg	MEMCAD	1	1, 3	1, 3, 5
250	0	39.5	40.1	39.39	39.41	39.41
	100	56.9	57.6	58.32	58.13	58.06
	-25	33.7	33.6	33.00	32.95	32.95
350	0	20.2	20.3	20.10	20.11	20.11
	100	35.4	35.8	36.71	36.41	36.32
	-25	13.8	13.7	12.96	12.82	12.81

good agreement is obtained, already for single-mode simulations. The MEMCAD value is taken as reference value. Depending on the specific parameter values, agreement between MEMCAD values and model *II* results is achieved within 2% .

Next a comparison is made between this work and recently reported results from Krylov (2007) and Krylov et al. (2008). In Krylov (2007), a silicon microbeam is investigated. The beam is modelled using an Euler-Bernoulli beam model in which both fringing field and midplane stretching effects are included. By means of Galerkin discretisation, a reduced-order model is created in the same way as has been done in Section 5.2.5. For a

⁵Microcosm Technologies, Cambridge, MA; renamed Coventor, Inc., software: CoventorWare

beam with parameters $E = 169$ GPa, $\nu = 0.28$, $l = 800$ μm , $b = 50$ μm , $h = 14.4$ μm and $d_1 = 1$ μm , a pull-in voltage of $V_{\text{pi}} = 40.17$ V is reported. Simulations with model *II* yield $V_{\text{pi}} = 40.13$ V, $V_{\text{pi}} = 40.15$ V and $V_{\text{pi}} = 40.15$ V for the mode 1, mode 1,3 and mode 1,3,5 discretisations, respectively. A very good agreement is obtained. The pull-in curve for the single-mode simulation is depicted in Figure 5.7(a).



(a) Results for the beam in Krylov (2007). (b) Results for the beam in Krylov et al. (2008).

Figure 5.7 / Pull-in curves calculated for comparison with two recent works.

Also in Krylov et al. (2008), the pull-in behaviour of electrostatically actuated microstructures is investigated in detail. A similar modelling method is applied as in Krylov (2007) and the work presented in this thesis. However, a different expression for fringing field effects is used, based on van der Meijs and Fokkema (1984) and Batra et al. (2006b). For a beam with parameters $E = 169$ GPa, $\nu = 0.28$, $l = 1000$ μm , $b = 30$ μm , $h = 2.1$ μm and $d_1 = 7.7$ μm , a pull-in voltage of 60 V is reported. Simulations with model *II* yield $V_{\text{pi}} = 59.04$ V, $V_{\text{pi}} = 58.34$ V and $V_{\text{pi}} = 57.65$ V for the mode 1, mode 1,3 and mode 1,3,5 discretisations, respectively. Differences with Krylov et al. (2008) may be attributed to the different expression for the fringing field effects. Again, the pull-in curve for the single-mode discretisation is depicted in Figure 5.7(b).

Finally, further information on analysis and modelling with respect to pull-in of electrostatically actuated microstructures can be found in, for instance, Pamidighantam et al. (2002), and Rochus et al. (2005, 2006). In Pamidighantam et al. (2002), both the effects of fringing fields and charge redistribution are taken into account. The latter is reported to result in a reduction of the effective electrode area, due to charge movement, once the beam deforms. In Rochus et al. (2005) and Rochus et al. (2006), a monolithic finite element formulation for electromechanical coupling is proposed, in which the electric and mechanical fields are solved simultaneously in the same formulation.

5.4.2 Periodic solutions and stability

The analysis of steady-state periodic solutions allows for determining stationary oscillations of MEMS resonators. For instance, for MEMS resonators that are used in oscillators, both the frequency of oscillation and the oscillation amplitude are important. Furthermore, amplitude-frequency curves can be calculated, which are the nonlinear equivalent of frequency response functions. In order to study periodic solutions and their stability for the three MEMS resonator models, they are rewritten in the form $\dot{\mathbf{x}} = \mathbf{f}(\mathbf{x}, \mu)$. The ODEs are numerically implemented in Fortran code, which is used by AUTO97 (Doedel et al., 1998) for calculation and numerical continuation of periodic solutions, that is, resonator oscillations, see Section 2.4.3. The excitation voltages on the two electrodes are set to their values in (5.4). Excitation parameters are the voltages V_{dc} and V_{ac} and the excitation frequency f . In order to calculate amplitude-frequency curves, the frequency f in the ac part of V_1 will act as the bifurcation parameter μ .

Similar to the equilibrium point analysis in previous section, the deflection w_{mid} at the midpoint of the beam will be the response quantity for the results. However, since periodic solutions will be calculated, w_{mid} is a function of t . Therefore, the peak to peak value of w_{mid} will be considered.

First, simulations are performed in order to investigate what physical effects (see Section 4.3) are relevant for periodic solutions. This will be done for excitation settings $V_{dc} = 40$ V and $V_{ac} = 125$ mV in V_1 and V_2 (5.4). As has become clear from (5.16) in Section 5.2.3, the physical effects are quantified by a non-dimensional coefficient. This parameter can be set to 0 for switching the effect off, just as has been done in Section 5.4.1. In the following, c_m denotes the midplane stretching effect, c_b denotes fringing field effects and c_r denotes rotary inertia. Unless stated otherwise, the effect of anchor loss is not included, since its low Q -factor would render most of the individual physical effects invisible. This will become clear at the end of this section.

Results of a simulation study for a single-mode discretisation of models *I* and *II*, both based on Euler-Bernoulli beam theory, are depicted in Figure 5.8. The results are presented for the thin beam, $b = 1.4$ μm . Model *I* does not contain thermoelastic damping. In order to be able to compare its response with the response of model *II*, a version of model *II* without thermoelasticity is used. In both models a quality factor of $Q = 15000$ is used, which corresponds approximately with the quality factor related to thermoelastic damping, see Tables 5.7 and 5.8 for mode 1.

Figure 5.8 shows the amplitude-frequency plot models *I* and *II* under influence of various physical effects. On the horizontal axis, the excitation frequency is plotted and on the vertical axis, the peak to peak value of w_{mid} is shown. Stable periodic solutions are indicated by solid lines, whereas unstable periodic solutions are indicated by dashed lines. Cyclic fold bifurcations (indicated by CF) mark the transitions between stable and unstable periodic solutions, see also Section 2.4.3.

Several observations can be made from Figure 5.8, which, in fact, shows 8 response curves. Firstly, it can be seen that there is no visible difference between the amplitude-frequency responses of model *I* and model *II*. Therefore, it can be concluded that the

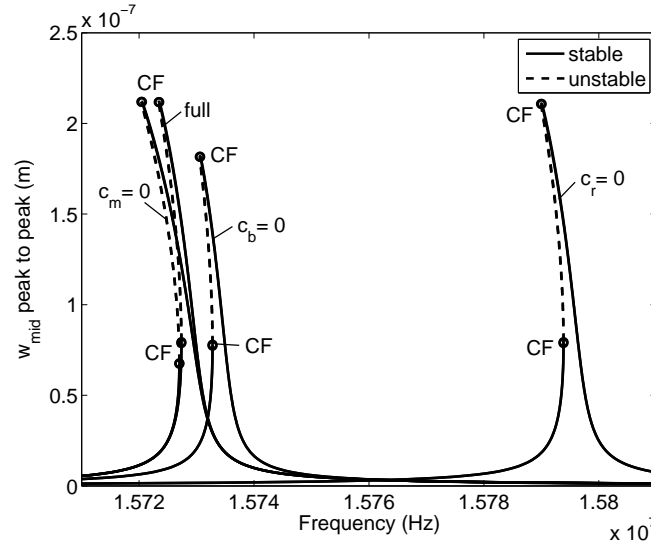


Figure 5.8 / Eight amplitude-frequency curves including various effects for models *I* and *II*. No visible differences are present between models *I* and *II*. c_b : fringing fields, c_m : midplane stretching, c_r : rotary inertia. Excitation values: $V_{dc} = 40$ V and $V_{ac} = 125$ mV.

influence of nonlinear elastic effects is not significant for the beam under investigation. This has been observed in Section 5.4.1 for the equilibrium point analysis as well.

Secondly, exclusion of midplane stretching (c_m), fringing fields (c_b) and rotary inertia (c_r) effects do have significant influence on the amplitude frequency curve, compared to the ‘full’ analysis, in which all effects are included, see Figure 5.8. All resonance peaks show softening nonlinear behaviour, since these bend to lower frequencies.

As expected, if midplane stretching is not included (curve with $c_m = 0$), more softening nonlinear behaviour occurs. In the equilibrium point analysis, this effect did not play a significant role, but for periodic solutions, it does. Furthermore, it will become clear later on that the midplane stretching effect is necessary to be able to describe the transition from hardening to softening nonlinear behaviour for increasing V_{dc} .

From comparison of the curves ‘full’ and $c_b = 0$, it can be seen that exclusion of fringing fields results in a higher resonance frequency with a lower peak value. This is expected, since fringing fields increase the effective capacitance between the electrodes and the beam. As a result, the effective stiffness decreases, resulting in a lower resonance frequency, and the electrostatic force increases, resulting in a higher amplitude. The effective stiffness, given for the lumped model in (3.8) in Section 3.2.2 depends on the capacitance, the gap and the dc voltage.

Inclusion of rotary inertia (parameter c_r) increases the inertia of the beam, thereby increasing the effective, or vibrating, mass of the beam. Therefore, if rotary inertia is taken into account, the resonance frequency is lower than for the case $c_r = 0$. Especially for the relatively wide beam (large h/l -ratio), this effect does play a role.

Next, a similar analysis is performed for models *II* and *III*, both with thermoelastic effects

included. Results for model *II* are virtually the same as already depicted in Figure 5.8, but with slightly lower amplitude, since the Q -factor for thermoelastic damping equals $Q = 14549$ for model *II* (see Table 5.8) instead of $Q = 15000$ used in Figure 5.8. For model *III*, results are depicted in Figure 5.9. In model *III*, rotary inertia is included automatically, since this serves as the inertia term in the PDE for the shear deformation field φ , see (5.22b).

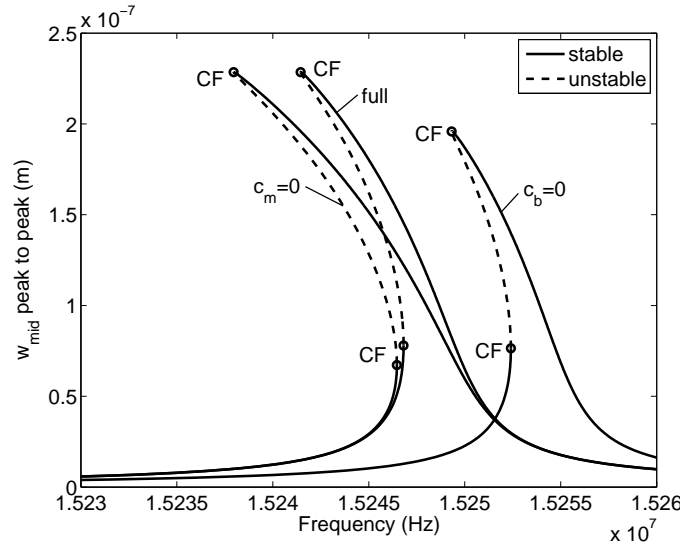


Figure 5.9 / Amplitude-frequency curves including various effects for model *III*. c_b : fringing fields and c_m : midplane stretching. Excitation values: $V_{dc} = 40$ V and $V_{ac} = 125$ mV.

Trends for model *III* are similar to those observed in Figure 5.8. If midplane stretching is not included ($c_m = 0$), more softening nonlinear behaviour results and if fringing fields ($c_b = 0$) are not included, a higher resonance frequency and a lower amplitude results. Furthermore, the resonance frequency for model *III* is lower than the one for models *I* and *II*, compare the scale of the horizontal axis in Figure 5.9 with Figure 5.8. This is in line with the difference in natural frequencies between Timoshenko and Euler-Bernoulli beam theory, see Table 5.8.

In conclusion, from Figures 5.8 and 5.9 it follows that both midplane stretching and fringing field effects have to be included in the analysis of periodic solutions, since they have significant influence. In addition, for model *II*, rotary inertia is of importance.

In order to investigate the effect of taking into account multiple basis functions (modes) in the Galerkin discretisation, simulations with models *II* and *III* have been performed using mode 1, modes 1, 3 and modes 1, 3, 5. All physical effects are included. The excitation settings are the same as used previously: $V_{dc} = 40$ V and $V_{ac} = 125$ mV. Amplitude-frequency curves for these simulations are depicted in Figure 5.10(a) for model *II* and in Figure 5.10(b) for model *III*. In each of these figures, three amplitude-frequency curves are depicted that virtually coincide (showing no visible differences).

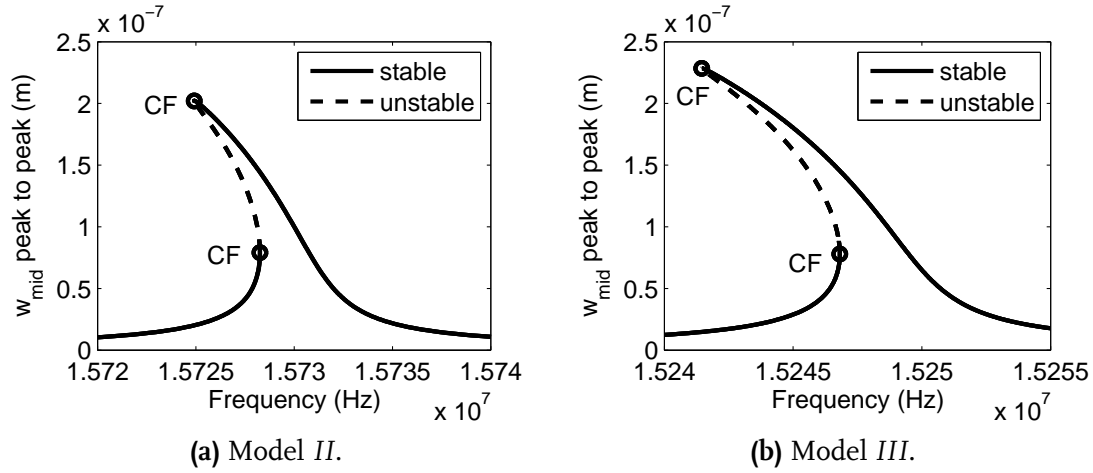


Figure 5.10 / Results for three different (1, 2 and 3 DOF) discretisations, $V_{dc} = 40$ V and $V_{ac} = 125$ mV. For each of the models, the results almost coincide.

From the results, it becomes clear that the single-mode and multi-mode models almost give the same results around the first harmonic resonance frequency. The clamped-clamped beam MEMS resonator considered in this work is mainly operated around its first harmonic resonance frequency. Therefore, it has no added value to include more modes in the simulation model. This corresponds with the conclusion in the equilibrium point analysis in Section 5.4.1, where the single-mode results already give a good prediction of the pull-in voltage for the beam under investigation.

However, in systems with low damping, a situation might occur in which a higher mode with a harmonic resonance frequency f_i shows an n^{th} superharmonic resonance at the first harmonic resonance peak with natural frequency f_1 . This may happen when $f_i/n \approx f_1$, where $i, n = 2, 3, 4, \dots$. This effect is described in, for instance, Fey et al. (1990) and is very sensitive to damping. In the numerical simulations, performed with modes 1, 3 and modes 1, 3, 5, this effect has not been observed. Furthermore, in the experiments, described in Section 6.5, this effect is also not observed, although it may be disguised due to the presence of measurement noise. The superharmonic resonances may occur more easily if the modes are internally resonant. This is not the case here, see for instance Younis and Nayfeh (2003), where the authors find that a three-to-one internal resonance does not occur for a clamped-clamped microbeam.

Furthermore, it can be seen that the height of the resonance peaks is higher for model III than for model II. Reasons for this are twofold. Firstly, the Q -factor in model III is somewhat higher than the one in model II, see Table 5.8. This results in a higher amplitude. Secondly, in model III, which is based on Timoshenko beam theory, additional flexibility is introduced by including the shear deformation field. This results in more deformation and, hence, higher resonance peaks.

Now that it has become clear for the beam considered, that it suffices to use the single-mode discretisation including all physical effects, except material nonlinearities (model I), additional simulations for other excitation settings will be performed. These excitation

settings are listed in Table 5.13 and are chosen such that the product $V_{dc}V_{ac}$, which is a measure for the harmonic excitation amplitude (due to V^2 -terms in the excitation), is constant. Therefore, these settings will result in approximately the same amplitudes of the response.

Table 5.13 / Excitation settings for simulations with models *II* and *III*.

Excitation settings	
V_{dc} (V)	V_{ac} (mV)
10	500
20	250
30	167
40	125

Simulation results for these settings are depicted in Figures 5.11 and 5.12 for models *II* and *III*, respectively. The results show that the type of nonlinear dynamic behaviour changes with the excitation settings. For bias voltages of $V_{dc} = 30$ and 40 V, softening nonlinear behaviour is observed, due to dominating softening nonlinear behaviour of the electrostatic actuation. This has already been observed in Figures 5.8–5.10.

At $V_{dc} = 10$ V, effective hardening nonlinear behaviour is present, since the resonance peak bends to higher frequencies. Apparently, the hardening effect from midplane stretching (parameter c_m) dominates the softening behaviour of the electrostatic actuation. If midplane stretching is omitted ($c_m = 0$), softening nonlinear behaviour is found, since the remaining nonlinear dynamic effect, electrostatic forcing, has a softening nonlinear nature. This motivates the inclusion of midplane stretching in the models.

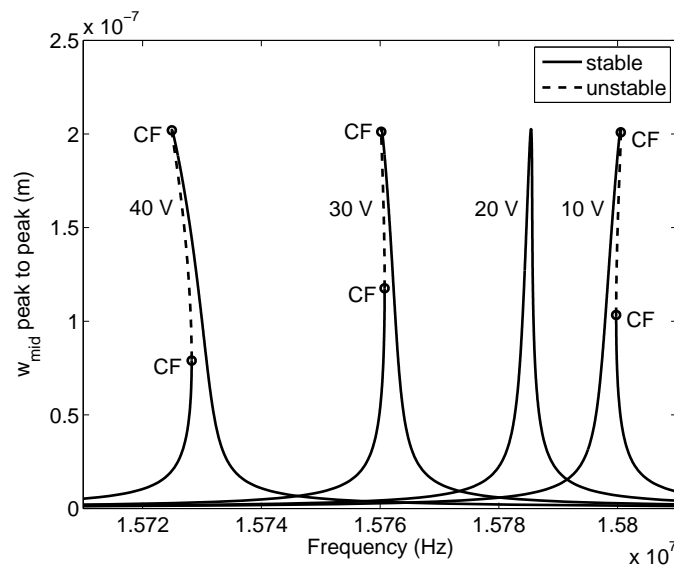


Figure 5.11 / Amplitude-frequency curves for model *II* for excitation values listed in Table 5.13.

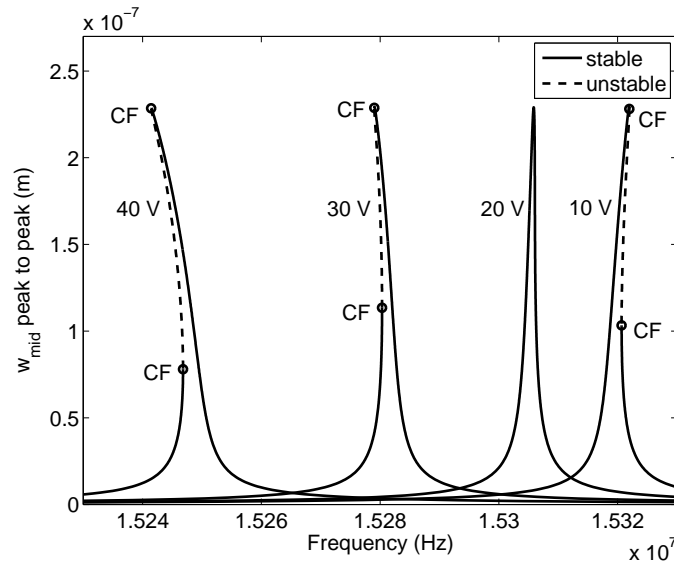


Figure 5.12 / Amplitude-frequency curves for model *III* for excitation values listed in Table 5.13.

Namely, although midplane stretching does not give significantly different results for the equilibrium point analysis (Section 5.4.1), it is an essential effect for the analysis of the dynamic behaviour.

At the intermediate value of $V_{dc} = 20$ V, a resonance without frequency hysteresis results, indicating a balance between midplane stretching (hardening) and electrostatic actuation (softening).

For excitation values higher than those listed in Table 5.13, even richer nonlinear dynamic behaviour may occur. However, the dominant nonlinear effect will be softening, resulting from the electrostatic actuation (see also Section 7.4.5). Eventually, the response may end in dynamic pull-in (Nayfeh et al., 2007). An extensive investigation of hardening to softening transitions in a purely parametrically excited comb-drive resonator is reported in Rhoads et al. (2006).

Apart from the different ranges for the resonance frequencies, the responses of models *II* and *III* are almost the same. As explained earlier, the amplitude for model *II* is somewhat lower than that of model *III*. Simulations with the thick beam ($b = 10$ μm) show similar trends as depicted in Figures 5.8–5.12 for the thin beam. The only difference is that the influence of fringing fields is less pronounced, an aspect which has been found in the analysis of equilibrium points as well, see Section 5.4.1.

Finally, to conclude this section on periodic solutions, the effect of anchor loss is investigated. In Figure 5.13, simulation results are presented for model *II*, where a Q -factor of 450 is used. This value corresponds to the analytically calculated value for anchor loss in model *II* in Section 5.2.6. Simulations have been performed for the excitation values listed in Table 5.13. The results show that for the (low) theoretical Q -factor related to anchor loss, no frequency hysteresis is found near the first harmonic resonance peak for

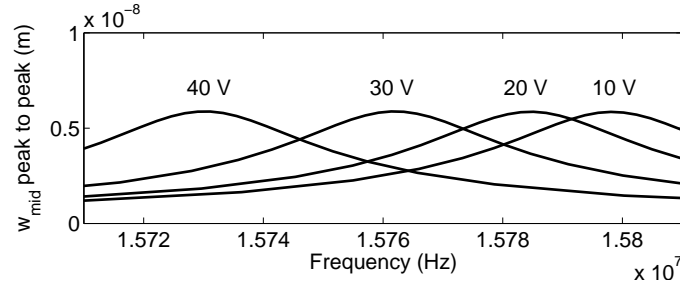


Figure 5.13 / Amplitude-frequency curves for model *II* for excitation values listed in Table 5.13. Anchor loss is included using a Q -factor of 450, see Table 5.8.

all excitation settings of Table 5.13. Differences in responses, related to various physical effects, see Figures 5.8–5.12 can no longer be observed. All (subtle) effects are damped due to the low Q -factor. Results for model *III*, including anchor loss are very similar to those depicted in Figure 5.13. They only show a resonance peak at lower frequencies, corresponding to those of Figure 5.12.

Comparison with literature

One of the first experimental observations of nonlinear dynamical effects in a MEMS resonator has been reported in Andres et al. (1987). Here, a hardening nonlinear response has been measured in a silicon resonant pressure sensor. Other hardening nonlinear responses have been observed in a comb drive resonator in Pratt et al. (1991) and in a beam resonator in Zook et al. (1992).

Theoretical work on the amplitude-frequency effect has been presented in Tilmans et al. (1992) and Tilmans and Legtenberg (1994), where the resonance frequency of a clamped-clamped beam microresonator has been determined by employing Rayleigh's (or Rayleigh-Ritz's) energy method, see for instance Weaver et al. (1990).

Yao and MacDonald (1996) describe the first experimental observation of both hardening and softening nonlinear dynamic behaviour in the same micromechanical device, depending on the excitation values. A similar trend as in Figures 5.11 and 5.12 has been observed.

Most of the literature before the year 2000 on nonlinear dynamic effects are based on lumped, Duffing-like modelling approximations, with the exception of Tilmans et al. (1992) and Tilmans and Legtenberg (1994). A different modelling approach, like the one described in this chapter, has been presented in Abdel-Rahman et al. (2002), Younis and Nayfeh (2003) and Younis et al. (2003). In these references, an Euler-Bernoulli beam model, including midplane stretching, has been used (like model *II*) to describe the nonlinear dynamics of a microbeam that is actuated by a single electrode. After single-mode Galerkin discretisation, a perturbation technique, the method of multiple scales (Nayfeh, 1981), is applied to determine an approximate solution to the amplitude-frequency curve of the microbeam. This technique assumes small nonlinearities.

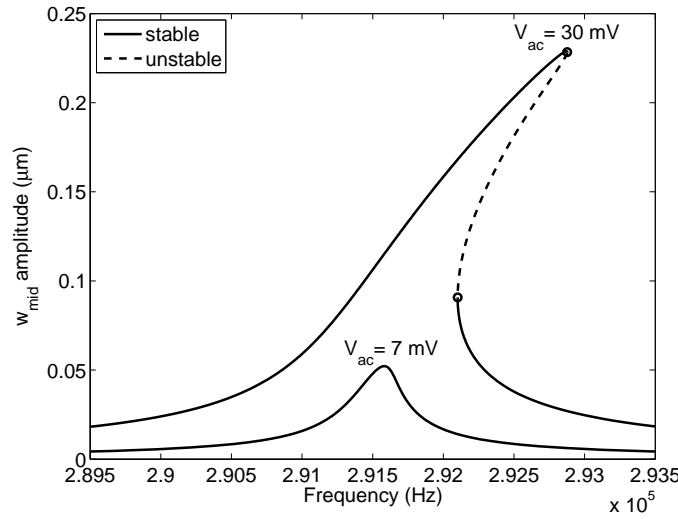


Figure 5.14 / Amplitude-frequency curves calculated for $V_{dc} = 8$ V and two V_{ac} -values, using clamped-clamped microbeam parameters from Younis and Nayfeh (2003).

A typical example from Younis and Nayfeh (2003) is based on Gui et al. (1998) and describes the steady-state nonlinear dynamic response of a silicon clamped-clamped microbeam with parameters $E = 166$ GPa, $\nu = 0.22$, $b = 100$ μm , $h = 1.5$ μm and $d_1 = 1$ μm , subject to an initial axial force of $N_0 = 0.00011$ N. The Q -factor of the beam is 900. At a bias voltage of $V_{dc} = 8$ V two amplitude-frequency curves have been calculated based on the perturbation method, for $V_{ac} = 7$ mV and $V_{ac} = 30$ mV. Peak amplitudes for the midpoint displacement w_{mid} at these excitation settings are 0.04 μm and 0.16 μm , respectively, and a hardening nonlinear response has been observed for $V_{ac} = 30$ mV. In order to make a fair comparison with these results, simulations with model II, also based on Euler-Bernoulli beam theory, have been performed. The results are depicted in Figure 5.14. Note that on the vertical axis, the maximum amplitude of the midpoint oscillation w_{mid} is plotted, which is also the response measure in Younis and Nayfeh (2003).

The simulated responses match those described in Younis and Nayfeh (2003) very well in a qualitative sense: the amplitude-frequency curves in Younis and Nayfeh (2003) have virtually the same shape as those in Figure 5.14. However, since numerical calculation of periodic solutions (using AUTO97) is used in the current work, no approximation to the nonlinear dynamic solution has to be made. Therefore, the amplitudes determined from the simulations with model II are found to be 0.05 μm and 0.23 μm , for $V_{ac} = 7$ mV and $V_{ac} = 30$ mV, respectively. This is up to 44% higher than the values reported in Younis and Nayfeh (2003).

5.5 Conclusions

Based on the comparison with finite element simulations described in Section 5.3 and the numerical simulation results described in Section 5.4, a comparison between models *I*, *II* and *III* can be made.

Some model aspects have been validated with finite element simulations using Comsol Multiphysics. These are the natural frequencies, thermoelastic damping and fringing fields. A good correspondence has been obtained for the natural frequencies of the finite element calculations and those of model *III*. The thermal modeshape and the *Q*-factor related to thermoelastic damping in models *II* and *III* match well with the FEM results for the first mode. For higher modes, the match becomes worse. Furthermore, the fringing field between the resonator and the electrodes can be approximated quite well with the first-order fringing field correction from Osterberg and Senturia (1997), see Section 5.3.3.

For both the static analysis (equilibrium points) and the dynamic analysis (periodic solutions), it has become clear that the effect of nonlinear material behaviour does not play a role, since it gives no significantly different simulation results. Therefore, model *II* is preferred over model *I*, since the former allows for straightforward inclusion of the relevant effect of thermoelastic damping.

Furthermore, for the static analysis of model *II* and *III* (Section 5.4.1), fringing field effects provide an improvement in the models, although their influence is less pronounced for the thick beam ($b = 10 \mu\text{m}$). By means of finite element simulations, this effect has also been verified, see Section 5.3.3. The effect of midplane stretching has been found to be hardly noticeable in the responses for equilibrium calculations (pull-in curves) for the nominal geometry of the beam (Table 5.1).

Moreover, from a comparison with literature, it has been found that models based on a single-mode Galerkin discretisation already yield a good estimate of the pull-in voltage. For the nominal beam geometry considered here, a single-mode discretisation is enough. If a larger electrode gap is present, a multi-mode discretisation may give slightly better results, since the inclusion of more modes may result in a better description of the deflection profile of the deformed beam.

In the dynamic analysis, both fringing fields and midplane stretching effects do play a significant role. Thermoelastic damping plays a role as well. For the first mode, both models *II* and *III* have a thermoelastic damping implementation that results in *Q*-factors that are in agreement with values from both literature (Zener, 1937, 1938; Lifshitz and Roukes, 2000) and finite element simulations. For higher modes, models *II* and *III* estimate the *Q*-factor too high. However, for the beam considered it has been shown that single-mode Galerkin discretised models yield results that are accurate enough. The use of multiple modes does not result in significant improvements.

Additionally, for model *II*, rotary inertia influences the response significantly. Therefore, it has to be included in the model. Furthermore, anchor loss has been found to results in very high damping in the system. It will become clear in Chapter 6 that the *Q*-factor calculated by the analytical anchor loss calculations in Section 5.2.6 is too low.

Developed dynamic model *II* has been validated with results from literature. The numerical method for determining periodic solutions in this work enables direct calculation of amplitude frequency curves, so that approximations to the response do not have to be made.

From a comparison of models *II* and *III*, it has become clear that the effect of shear deformation has to be included in the model, since this results in lower stiffness of the beam. For the static analysis, this results in lower pull-in voltages and for the dynamic analysis, this results in lower resonance frequencies. The above motivates the choice for the single-mode discretisation of model *III* as the best model, with all physical effects included, except for anchor loss.

Another important conclusion from Section 5.4.2 is that, regardless of the physical effects included, the overall dynamic behaviour of the clamped-clamped beam MEMS resonator still features frequency hysteresis as a response, see Figures 5.8–5.12, which may be described by a Duffing-based model. Actually, in Section 3.2, the proposed heuristic model for the clamped-clamped beam resonator has been a Duffing-based model with electrostatic actuation. This lumped model, has proven to be a good initial estimate for describing the measured responses. However, in the heuristic model, small parameter value changes are necessary to describe the behaviour for varying excitation settings.

In summary, the lumped, Duffing-based model with electrostatic actuation of Section 3.2 is able to describe some, but not all aspects of the dynamic behaviour of the clamped-clamped beam MEMS resonator for a certain excitation setting. Furthermore, the lumped parameters of this model have not been related to physical dimensions and physical parameters of the MEMS resonator. In order to capture the subtle details in the dynamic response, such as the transition from hardening to softening nonlinear behaviour, or the influence of the various physical effects, a first-principles based modelling approach is required. The approach, as proposed in Chapter 4 has been applied in this chapter to arrive at several models of the clamped-clamped beam MEMS resonator of varying complexity. The models are still in symbolic form, without physical parameters that have to be lumped into effective stiffness or mass quantities. Based on a simulation study, the influence of various physical effects has been judged, thereby motivating the choice for the single-mode discretisation of model *III* as the most suitable model. Experimental verification of this model will follow in Chapter 6.

Experiments on a clamped-clamped beam MEMS resonator¹

Abstract / In this chapter, the experimental validation of the derived models for the clamped-clamped beam MEMS resonator is described. The experimental set-up and two measurement techniques are described in detail. Small signal analysis is used to characterise the MEMS resonator in its linear regime using an electrical circuit representation. A custom-built Labview interface is used for measuring nonlinear dynamic responses. By using the two measurement techniques, relevant resonator parameters for the multiphysics models are determined. Finally, validation of the models takes place by confronting simulation results with experiments.

6.1 Introduction

An essential part in the multiphysics modelling framework presented in Chapter 4, is experimental validation. This is the ultimate test for assessing the validity of the derived models. Experimental validation is used to determine and evaluate the influence of the various physical effects that are included in the multiphysics model. Some iteration between experiments and modelling may be necessary, see Figure 4.5, since experiments may give rise to model refinements in terms of values of the model parameters or the structure of the model.

In order to verify the multiphysics models for the clamped-clamped beam resonator, derived in Chapter 5, experimental validation will be performed in this chapter. Experimental facilities and expertise at the NXP-TSMC Research Center, have been available for this purpose. In Chapter 5, model *III* has been determined to be the best model for the clamped-clamped beam MEMS resonator. Extensive validation of this model will take place for MEMS resonators with two different thickness values (see Table 5.1). As

¹Some results of this chapter have been presented in Mestrom et al. (2008b) and Mestrom et al. (2009a).

will become clear, two measurement techniques can be used for experimental characterisation, small signal analysis using network analyzer measurements and nonlinear measurements. The first method is a common method in electrical engineering for approximating the behavior of nonlinear devices with linear equations. The method has been used for characterising the MEMS resonator under small excitation values, for which the resonators are assumed to operate in their linear regime. By using this approach, resonator parameters such as the Q -factor and parasitic electric effects can be estimated from an electrical equivalent circuit representation. The second technique is able to measure MEMS resonator responses during operation under arbitrary excitation conditions. For these measurements, the resonator can also be operated in its nonlinear regime.

The outline of this chapter is as follows. First, a description of the clamped-clamped beam MEMS resonator will be given in Section 6.2. The measurement set-up and the two measurement techniques will be described in Section 6.3. Next, in Section 6.4, resonator parameter estimation by means of an electrical circuit representation will be described, and the measurement circuit will be introduced. The actual validation of model *III*, which has been derived in Chapter 5, will take place in Section 6.5. Here, results from the measurements are confronted with simulation results for MEMS resonators with two different thickness values. Finally, the chapter is ended with conclusions in Section 6.6.

6.2 Clamped-clamped beam MEMS resonator

Similar to the resonator described in Section 3.2, the steady-state behaviour of clamped-clamped beam MEMS resonators is experimentally investigated in this chapter. The resonators are available from the NXP-TSMC Research Center. A schematic picture of the resonator layout is depicted in Figure 6.1. The beam can be seen in the center. Six aluminum bond pads are located around the beam. These fit the ground-signal-ground probes that are used during the measurements. The outer four bond pads are connected to 'ground', such that the beam itself is grounded. The middle two bond pads are used for actuation and measurement purposes. Resonators are fabricated on SOI wafers. The production process of the resonators has already been described in Section 3.2.1.

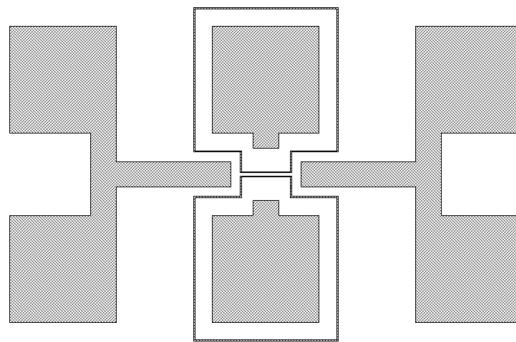


Figure 6.1 / Schematic layout of the clamped-clamped beam resonator. Thick lines are etched trench lines, used for isolation and transduction purposes.

The resonator beams have a nominal dimension (length l , width h and thickness b) as listed in Table 5.1 and have a typical resonance frequency around 13 to 14 MHz. Resonators with different gap sizes have been developed. From device to device, both the beam dimensions and the electrode gaps may vary slightly due to production tolerances. These parameters can be identified from measurements. Both the beam length and the electrode gaps influence the dynamic behaviour of the beam (l influences the resonance frequency, the gaps influence the nonlinear electrostatic softening). Two SEM pictures of a nominally 44 μm long beam are depicted in Figure 6.2. Actual lengths are measured to be slightly less than their nominal design value, as indicated in Figure 6.2.

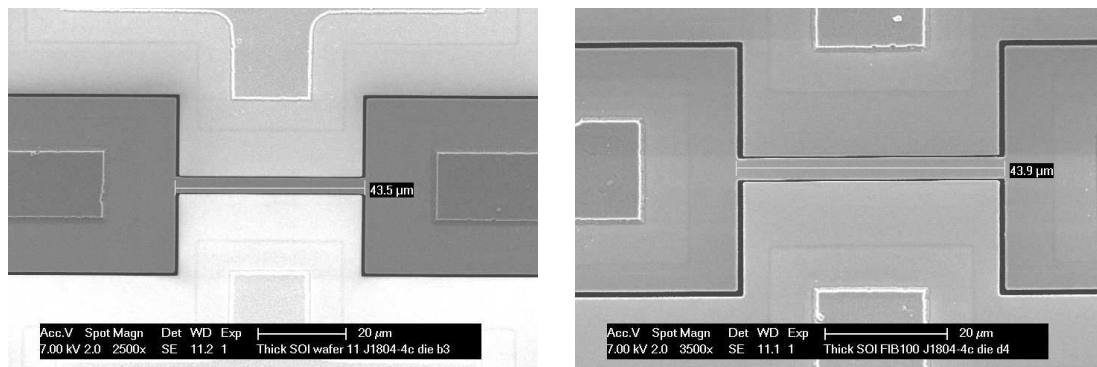


Figure 6.2 / SEM pictures of two clamped-clamped beam resonators.

Dimensions of the beam width and the electrode gaps are depicted in Figure 6.3, for two different beams. For the resonators depicted in the figure, the nominal gaps are designed to be around 200 nm and 300 nm, respectively. However, deviations of $\pm 10\%$ are very common, see Figure 6.3.

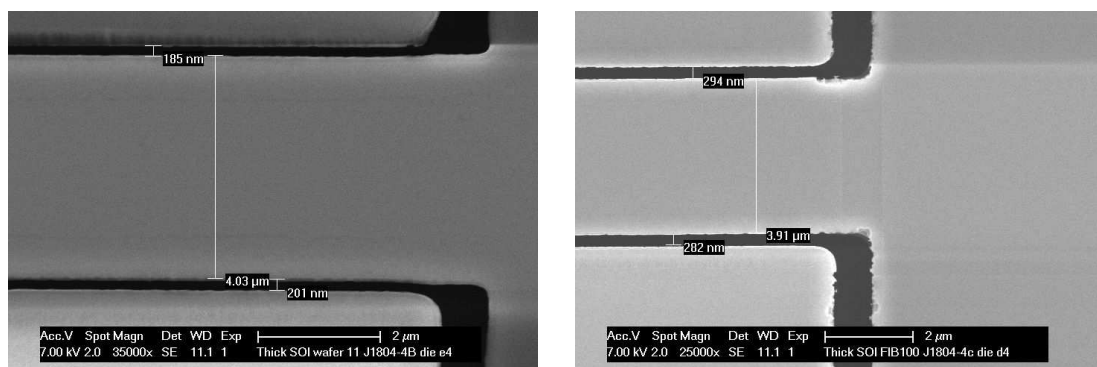


Figure 6.3 / Detailed SEM pictures with dimensions of the gaps and the beam width.

6.3 Measurement set-up and techniques

6.3.1 Set-up overview

At the NXP-TSMC Research Center, a custom-built set-up is available for MEMS resonator measurements. It consists of the following components (see also Bontemps, 2006).

Measurements are performed in vacuum, in order to exclude squeeze film or air damping effects. The resonator is placed inside an aluminum vacuum chamber. The vacuum in the chamber is maintained by a Pfeiffer vacuum pump. After closing the lid of the vacuum chamber, the pump is able to reach a pressure of below 0.01 mbar in 5 to 10 minutes. The operational pressure of the pump is $5 \cdot 10^{-5}$ mbar.

The six aluminum bond pads of a MEMS resonator, see Figure 6.1, are used for actuation and detection purposes. These bond pads are designed in such a way that they fit the two three-electrode (ground-signal-ground) probes that are used during the measurements. The probing of the resonator is done with the aid of a camera. The two probes are Süss MicroTec Z-probes. A close-up of a wafer with the Z-probes is depicted in Figure 6.4.

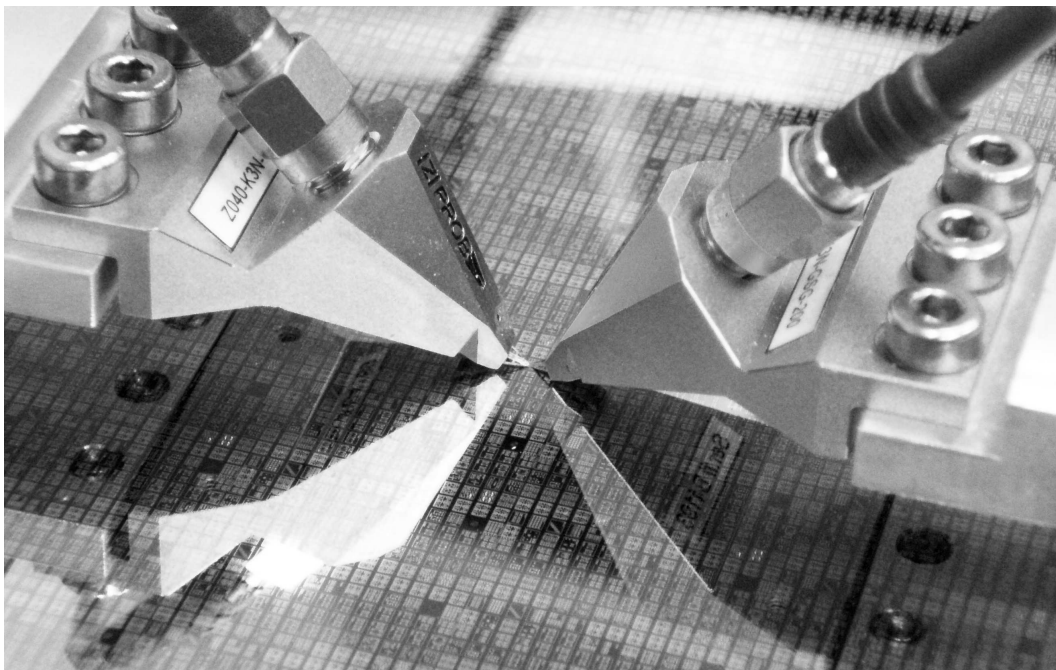


Figure 6.4 / Close-up of the Z-probes connected to a resonator on a wafer.

A Keithley 230 voltage source is used to supply the bias voltage V_{dc} to the resonator. Furthermore, an Agilent 33250A signal generator is available for providing the ac driving signal V_{ac} to excite the resonator, see also Section 6.3.2.

6.3.2 Measurement techniques

A schematic drawing of the clamped-clamped beam resonator has already been depicted in Figures 3.1 and 5.1. The clamped-clamped beam resonator contains two electrode gaps. During measurements, both the electrodes are biased by a dc voltage. In addition, each of the two electrodes can also be used as either an ac input or output, depending on the type of measurement that is performed. Therefore, the resonator can be considered as a two-port network.

Two possible measurement options, which will be described in Sections 6.3.3 and 6.3.4, are available for MEMS resonators:

1. small-signal (linear) analysis using a network analyzer;
2. nonlinear measurement using a LabView² interface.

In general, the electrical measurement set-up has a form as depicted in Figure 6.5(a). In this figure, the set-up is depicted in case a network analyzer measurement is performed. The resonator is located on the left. A dc (or bias) voltage is applied to the two electrodes

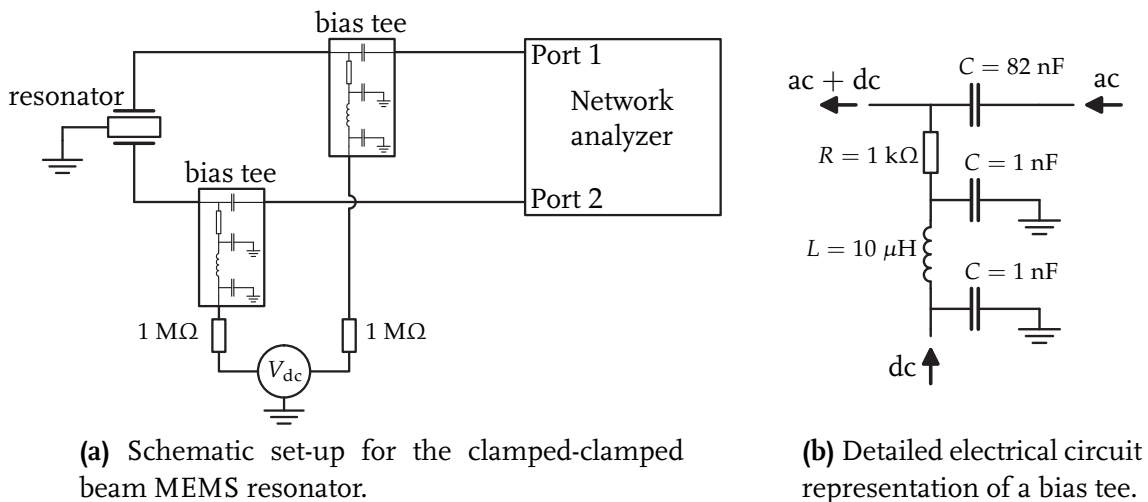


Figure 6.5 / Schematic electrical measurement set-up for a dual-gap resonator.

of the resonator by means of bias tees. The bias tees shield the network analyzer from the bias voltage while they allow coupling of ac and dc voltages to and from the resonator, at the same time. Schematically, the equivalent circuit of the bias tees used (PicoSecond 5530A) is depicted in Figure 6.5(b). Furthermore, $1\text{ M}\Omega$ resistors are included (see Figure 6.5(a)) in order to avoid parasitic cross-talk between the bias tees and to make sure that the network analyzer is not damaged in case the resonator is shorted.

²National Instruments Corporation, NI Labview 8.2.

6.3.3 Network analyzer measurements

Measurements on the MEMS resonator by means of a network analyzer are based on small signal analysis. The response of the system is assumed to be harmonic and linear. An Agilent Technologies E5071C (9 kHz–4.5 GHz) ENA Series Network Analyzer is used for the measurements. During the measurements, a dc voltage V_{dc} is applied to the resonator and a two-port measurement of S-parameters (scattering parameters) is performed. This will be explained later.

A range of excitation frequencies is set through which the network analyzer sweeps (only upwards) the frequency of the signal of its two ports. In this way, the resonator is excited harmonically at a certain frequency. The measured response consists of the output of the system at the same frequency as the excitation frequency. For this purpose, the measured signal is filtered with a very narrow bandpass filter (typically, the pass-band is set to 50 Hz for all measurements). Measurements (single sweeps) take roughly 6 to 7 minutes each.

The network analyzer measures S-parameters, which are a function of the frequency. For a detailed description of these non-dimensional parameters, see, for instance, Gonzalez (1997). Several advantages of S-parameters are the following:

- S-parameters relate to signal flow, rather than to applied voltages and currents;
- they are measured in a matched impedance setting (typically a load and source of 50 Ω), since open and short-circuit type of measurements are difficult to realise;
- effects of cables, bias tees and the network analyzer itself can be eliminated by proper calibration.

A schematic representation of a two-port network is depicted in Figure 6.6. The resonator acts as the two-port device in the center. Incident complex voltage waves (a_1, a_2) and

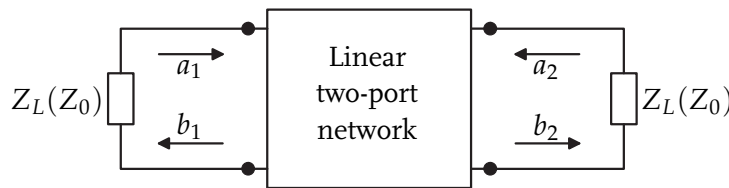


Figure 6.6 / Schematic representation of a two-port network.

reflected complex voltage waves (b_1, b_2) are also depicted. The reference impedance Z_L is assumed to be positive and real. By convention, it will be replaced by Z_0 , see also Figure 6.6. During measurements, impedance matching in the network analyzer realises that $Z_0 = 50 \Omega$ and that either $a_1 = 0$ or $a_2 = 0$. The linear relations describing this two-port network are:

$$b_1 = S_{11}a_1 + S_{12}a_2, \quad (6.1a)$$

$$b_2 = S_{21}a_1 + S_{22}a_2, \quad (6.1b)$$

where the S-parameters are defined as

$$S_{11} = \left. \frac{b_1}{a_1} \right|_{a_2=0} \quad (\text{input reflection coefficient; output properly terminated}), \quad (6.2a)$$

$$S_{12} = \left. \frac{b_1}{a_2} \right|_{a_1=0} \quad (\text{reverse transmission coefficient; input properly terminated}), \quad (6.2b)$$

$$S_{21} = \left. \frac{b_2}{a_1} \right|_{a_2=0} \quad (\text{forward transmission coefficient; output properly terminated}), \quad (6.2c)$$

$$S_{22} = \left. \frac{b_2}{a_2} \right|_{a_1=0} \quad (\text{output reflection coefficient; input properly terminated}). \quad (6.2d)$$

S-parameters are gain (transmission) and reflection parameters. In analogy to optics, S_{11} and S_{22} are the same as optical reflection coefficients, whereas S_{12} and S_{21} are the same as optical transmission coefficients. However, the S-parameters depend on the wave frequency (in this case, the ac excitation frequency) and, therefore, they have to be determined over a relevant range of frequencies.

Furthermore, since the clamped-clamped beam MEMS resonator is a symmetric device, S_{12} is equal to S_{21} . Due to noise, however, these may differ slightly. Therefore, $S_{12}(= S_{21})$ is set to the average of the measured two values.

As described earlier, calibration of the network analyzer allows for compensation in the measured S-parameters for the effect of cables, probes, bias tees and the network analyzer itself. Calibration consists of four steps, termed SOLT (short-open-load-trans), and has been performed on a Süss MicroTec CSR-8 calibration substrate.

6.3.4 Labview measurements

The second measurement technique, allowing for measurements in the nonlinear regime, uses a LabView interface that enables automated measurements. The electrical set-up of Figure 6.5 is changed slightly, such that the Agilent signal generator is included, which sets V_{ac} on port 1 (input). Furthermore, a Tektronix TDS3032B sampling scope is connected to port 2 (output) with a 40 dB amplifier placed in between the output and the scope. The output is measured as a voltage V_{out} .

The LabView interface is able to control the dc voltage source, the ac signal generator and the sampling scope. The scope has a sampling buffer of 10 000 points, which are captured by the LabView interface and written to data files. The measurement program is capable of setting the excitation frequency f and can perform stepped frequency sweeps in positive and negative direction through a fully customisable frequency range. At each frequency, after 2 s, the output voltage V_{out} is measured. Depending on the number of frequency points, a single measurement, consisting of a sweep up directly followed by a sweep down, may take from ten minutes to over an hour.

From some initial measurements, it has been found that a lot of noise is present in the output V_{out} . The noise may even dominate the resonator output signal when it has a

small amplitude (away from resonance frequencies or for small ac excitation amplitudes). Partly, the noise can be attributed to thermal noise (see also Section 3.2.2), but it also stems from the amplifier and scope. The amplifier has a bandwidth of 150 MHz. In order to reduce the influence of noise, filtering is applied to the measured time signals. An 8th-order low-pass Butterworth filter with a cut-off frequency of 100 MHz is used to filter the signals. Since the resonators have a fundamental frequency of around 13 to 14 MHz, filtering with a cut-off frequency of 100 MHz will not significantly affect the fundamental frequency components. In order to illustrate this, original and filtered time signals have been plotted in Figure 6.7. Especially when the system response shows a large output amplitude (Figure 6.7(b)), filtering is observed to influence the resonator output signal only very little. Furthermore, it does not change the qualitative nature of the response. Based on the filtered time signals, peak to peak values of the response can be calculated. By doing this for a range of excitation frequencies, the peak to peak values can be used to construct amplitude-frequency curves of the system. This can be done for both sweep directions.

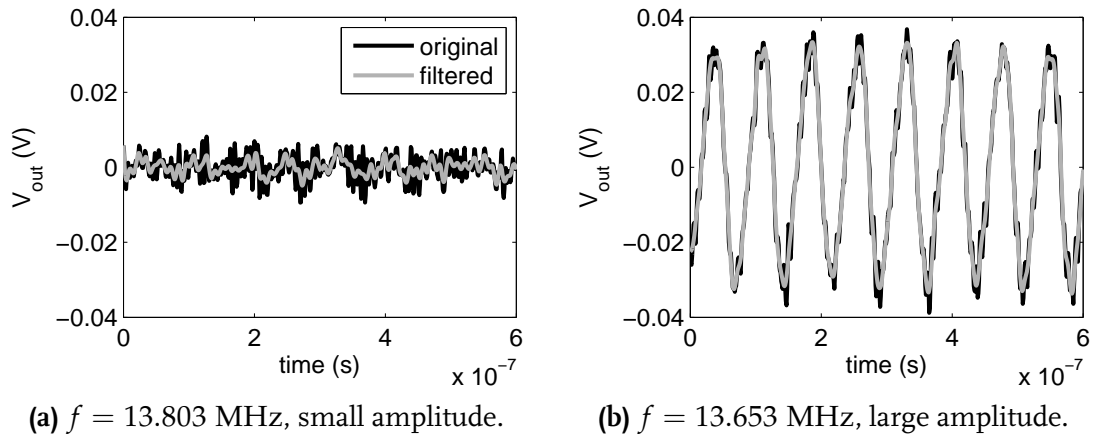


Figure 6.7 / Example of two original and filtered time histories.

6.4 Electrical circuit representation and parameter estimation

The network analyzer measurements can be used to investigate various effects related to the MEMS resonator. By means of an electrical equivalent circuit, insight can be gained in motional (related to the resonator itself) and parasitic effects. This approach and the method for estimating the linear resonator parameters, such as the Q -factor and the natural frequency of the beam, will be described in the following Sections.

6.4.1 Electrical equivalent circuit

A possible representation for a MEMS resonator operating in its linear regime is an electrical equivalent RLC -circuit, similar to the representation of a quartz crystal (Salt, 1987; Hewlett-Packard Company, 1997a) and the lumped model in (3.11)–(3.12). A more detailed electrical model (Bontemps, 2006) is depicted in Figure 6.8. In this figure, the

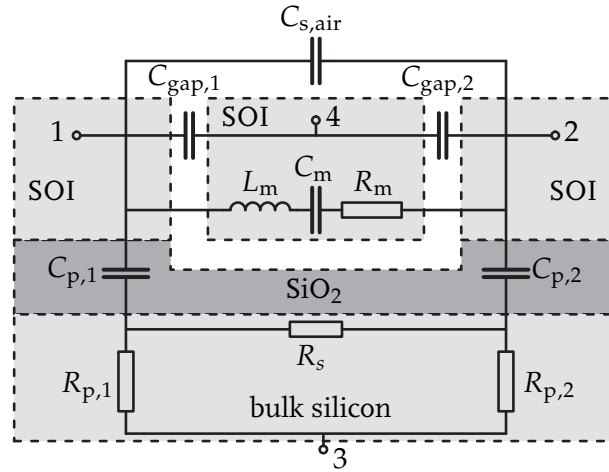


Figure 6.8 / Detailed equivalent circuit of the clamped-clamped beam resonator, in which physical parasitic effects are indicated.

RLC -circuit of the resonator itself can be seen in the center. The layers of the SOI wafer are indicated by the grey parts (Si: light grey, SiO_2 : dark grey). The substrate is the bulk silicon layer at the bottom of Figure 6.8. Several parasitic resistors and capacitors (indicated by subscripts p and s) can be seen around the resonator. $C_{s,\text{air}}$ denotes the shunt capacitance between the two resonator electrodes and $C_{\text{gap},1}$ and $C_{\text{gap},2}$ denote the capacitances over the electrode gaps. R_s denotes a parasitic shunt resistance through the bulk silicon layer and $C_{p,i}$ and $R_{p,i}$ ($i = 1, 2$) denote the bondpad capacitances and the resistance between the bond pads and the bulk silicon substrate for the two electrodes. Furthermore, terminals 1 and 2 are the ac input and output ports of the resonator. Terminal 3 is on the bulk silicon layer and terminal 4 is used for grounding of the resonator.

In general, the behaviour of a two-port device, such as the clamped-clamped beam MEMS resonator, at a fixed frequency can be represented in terms of a Π -network (or T-network) of three complex impedances, see for instance Gonzalez (1997) or Nilsson and Riedel (2008). Any complex impedance can be written as a parallel combination of a resistor and a capacitor. Note that this is a purely mathematical description, which allows for negative resistance or capacitance values. Alternatively, a series combination of a resistor and a capacitor could be used. Figure 6.9 depicts the Π -network that describes the parasitics around the resonator. The parasitic components in Figure 6.9 are not completely identical to those in Figure 6.8, but can represent the same circuit (after some elaboration). Figure 6.9(a) shows the situation when a bias voltage V_{dc} is applied, whereas Figure 6.9(b) shows the situation when $V_{\text{dc}} = 0$ V. In both cases, $V_{\text{ac}} \neq 0$ V. For the

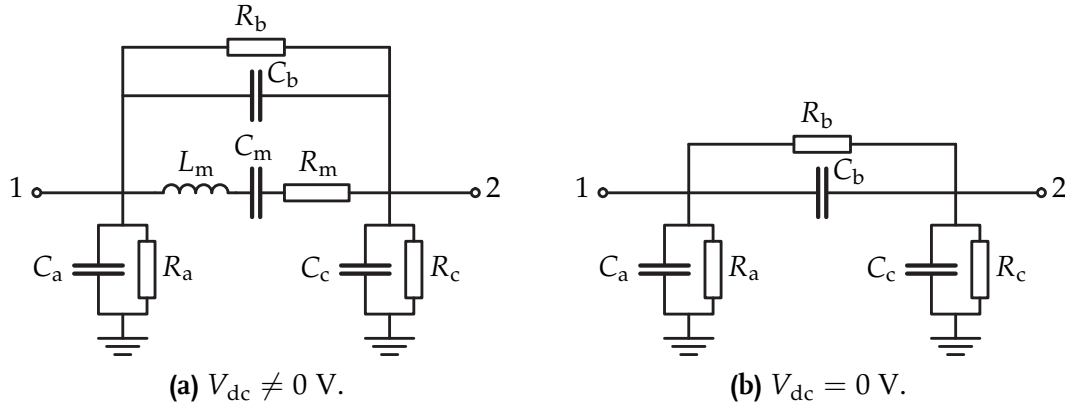


Figure 6.9 / Equivalent resonator circuit (Π -network).

case $V_{dc} = 0$ V, no (harmonic) response occurs and the motional branch (subscript m) is omitted. All parasitics depicted in Figure 6.8 are represented by three resistance and capacitance values R_i and C_i ($i = a, b, c$), respectively. A simplified graphical representation of the Π -network of Figure 6.9(a) is depicted in Figure 6.10(a). The two-port network representation of the resonator is depicted in Figure 6.10(b).

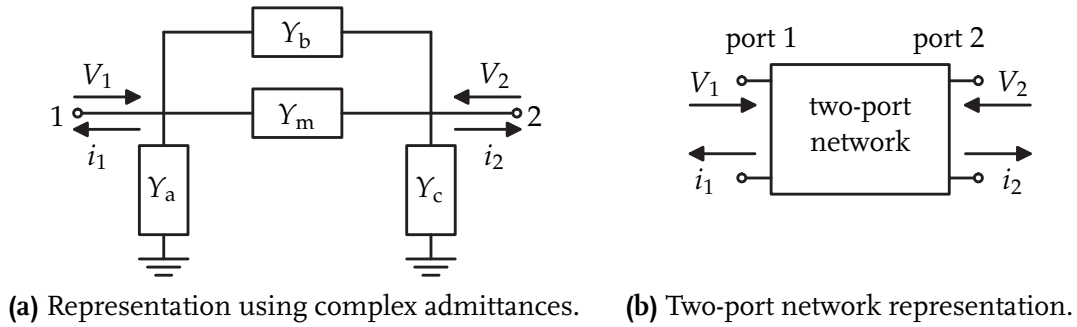


Figure 6.10 / Representation of the Π -network of Figure 6.9(a).

The complex admittances in Figure 6.10(a) are given by:

$$Y_i = \frac{1}{R_i} + j\omega C_i, \quad i = a, b, c, \quad (6.3a)$$

$$Y_m = \frac{1}{R_m + j\omega L_m + 1/(j\omega C_m)} + j\omega C_s. \quad (6.3b)$$

The last term in (6.3b), $j\omega C_s$, is optionally present in case of an additional (different from $C_{s,air}$ in Figure 6.8) shunt capacitance in the resonator. This will be explained in Sections 6.4.3 and 6.4.4. The motional branch is omitted ($Y_m = 0$) for the case $V_{dc} = 0$ V, since no transduction of the ac excitation is transmitted to the resonator (as described earlier).

6.4.2 Y-parameters calculation

From the Π -network representation of the MEMS resonator, it is possible to obtain the Y-parameters of the system. Y-parameters, or admittance parameters (see, for instance Gonzalez, 1997) determine the relation between current and voltage in a two-port network as depicted in Figure 6.10(b):

$$i_1 = Y_{11}V_1 + Y_{12}V_2, \quad (6.4a)$$

$$i_2 = Y_{21}V_1 + Y_{22}V_2, \quad (6.4b)$$

Application of Kirchoff's current law to the electrical circuit of Figure 6.10(a), allows for expressing the Y-parameters expressed in terms of the admittances Y_a , Y_b , Y_c and Y_m :

$$Y_{11} = Y_a + Y_b + Y_m, \quad (6.5a)$$

$$Y_{12} = Y_{21} = -(Y_b + Y_m), \quad (6.5b)$$

$$Y_{22} = Y_c + Y_b + Y_m. \quad (6.5c)$$

Furthermore, the Y-parameters relate to the measured S-parameters of the network (see Section 6.3.3) as follows (Gonzalez, 1997; Hewlett-Packard Company, 1997b):

$$Y_{11} = \frac{(1 + S_{22})(1 - S_{11}) + S_{12}S_{21}}{(1 + S_{11})(1 + S_{22}) - S_{12}S_{21}}Y_0, \quad (6.6a)$$

$$Y_{12} = \frac{-2S_{12}}{(1 + S_{11})(1 + S_{22}) - S_{12}S_{21}}Y_0, \quad (6.6b)$$

$$Y_{21} = \frac{-2S_{21}}{(1 + S_{11})(1 + S_{22}) - S_{12}S_{21}}Y_0, \quad (6.6c)$$

$$Y_{22} = \frac{(1 + S_{11})(1 - S_{22}) + S_{12}S_{21}}{(1 + S_{11})(1 + S_{22}) - S_{12}S_{21}}Y_0, \quad (6.6d)$$

where the characteristic admittance Y_0 (used for normalisation) is given by:

$$Y_0 = \frac{1}{Z_0} = \frac{1}{50} \Omega^{-1}, \quad (6.7)$$

see also Figure 6.6. Similar to the S-parameters, symmetry of the resonator implies $Y_{12} = Y_{21}$.

If two S-parameter measurements are performed for a certain frequency range of interest, one for $V_{dc} \neq 0$ and one for $V_{dc} = 0$ V, the corresponding Y-parameters can be calculated using (6.6). Note that for the case when $V_{dc} = 0$ V, $Y_m = 0$, see Figure 6.9(b). Next, by using (6.5), the four admittances in Figure 6.10(a) can be determined using:

$$Y_a = (Y_{11} + Y_{12}) \Big|_{V_{dc}=0 \vee V_{dc} \neq 0}, \quad (6.8a)$$

$$Y_b = -Y_{12} \Big|_{V_{dc}=0}, \quad (6.8b)$$

$$Y_c = (Y_{22} + Y_{12}) \Big|_{V_{dc}=0 \vee V_{dc} \neq 0}, \quad (6.8c)$$

$$Y_m = Y_{12} \Big|_{V_{dc}=0} - Y_{12} \Big|_{V_{dc} \neq 0}. \quad (6.8d)$$

6.4.3 Parasitic and motional parameters

Once the admittance parameters Y_a , Y_b , Y_c and Y_m have been determined, it is possible to extract the values of the parasitic resistors and capacitors. The parameters R_i and C_i , ($i = a, b, c$) of the parasitic admittances Y_a , Y_b and Y_c are assumed constant over the frequency range considered. Therefore, they are averaged over the frequency ($\langle \dots \rangle$ denotes average):

$$R_i = \left\langle \frac{1}{\text{Re}\{Y_i\}} \right\rangle, \quad C_i = \left\langle \frac{\text{Im}\{Y_i\}}{\omega} \right\rangle, \quad \text{for } i = a, b, c. \quad (6.9)$$

For the motional admittance Y_m , the determination of the parameters is slightly more complicated. The admittance (6.3b), without the additional parasitic term, has an analogy with a second-order linear dynamical system:

$$Y_m = \frac{1}{R_m + j\omega L_m + 1/(j\omega C_m)} + j\omega C_s = \frac{j\omega A}{\omega_V^2 - \omega^2 + j\omega\omega_V/Q} + j\omega C_s, \quad (6.10)$$

where the parameters in the latter part of (6.10) are given by:

$$\omega_V^2 = \frac{1}{L_m C_m}, \quad A = \frac{1}{L_m}, \quad \text{and} \quad Q = \frac{1}{R_m} \sqrt{\frac{L_m}{C_m}}. \quad (6.11)$$

The angular resonance frequency under application of a bias voltage V_{dc} is denoted by ω_V . Furthermore, the estimated Q -factor is a measure for all dissipation mechanisms in the resonator, so it contains contributions of anchor loss, thermoelastic damping and possible other dissipation mechanisms. For a given (measured) Y_m over a frequency range of interest, parameters (6.11) can be found by numerically fitting the response (6.10) to the measured values. Optimisation routines in Matlab are used for this purpose. Examples of such fitted responses will be described in Section 6.5.

Finally, it is of interest how parasitic and motional parameters that are used for electrical characterisation of the resonator behave under changes of the applied bias voltage V_{dc} . The parasitic parameters Y_a , Y_b and Y_c are assumed to be constant, but the motional parameters in Y_m will change due to the parametric excitation of the resonator, see (3.8). Therefore, it is of interest how parameters, R_m , L_m and C_m , or ω_V , A and Q (6.10)–(6.11), change with V_{dc} . In accordance with (3.8), the angular resonance frequency ω_V (or f_V , in Hz) shows an overall trend given by:

$$f_V^2 = f_0^2 - \alpha_f V_{dc}^2, \quad (6.12)$$

where f_0 is the first natural frequency of the microbeam without application of a bias voltage and α_f denotes the proportionality constant. Validity of relation (6.12) can be easily shown by considering the lumped model description in (3.8) in Section 3.2.2. Examples of how (6.12) can be used will be given in Section 6.5.

6.4.4 Measurement circuit

For the measurements in the nonlinear regime, using the Labview set-up, a slightly different approach holds. These measurements are not performed in a matched impedance setting, as is the case for the S-parameters measurement using the network analyser, see Section 6.3.3. The measurement circuit is similar to the one depicted in Figure 6.10(a) and is depicted in Figure 6.11(a). It can be seen that, apart from the resonator, the same

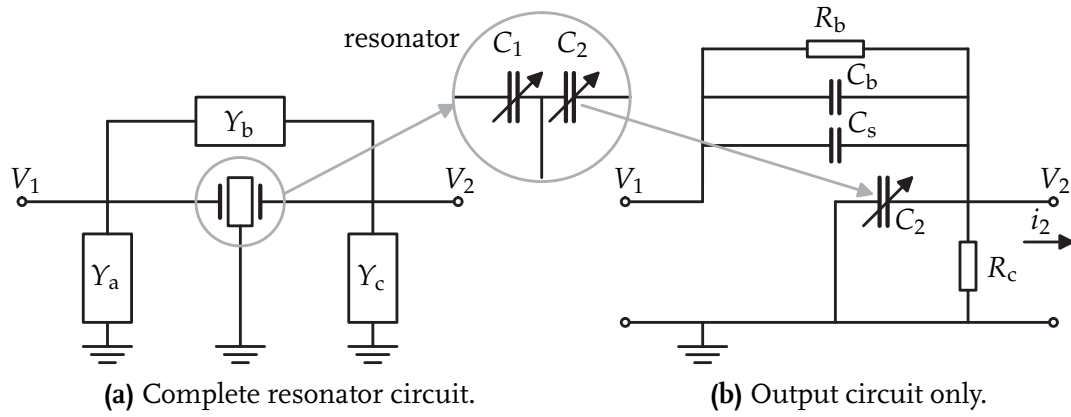


Figure 6.11 / Measurement circuit for the Labview measurements.

parasitic impedances Y_a , Y_b and Y_c (6.3a) as in Figure 6.10(a) are present. The resonator can be considered as a pair of varying capacitors C_1 and C_2 , denoting electrode gaps 1 and 2, respectively. V_1 and V_2 denote the voltages applied to the electrodes and equal, see also (5.4):

$$V_1(t) = V_{dc} + V_{ac} \sin(2\pi ft) \quad \text{and} \quad V_2 = V_{dc}. \quad (6.13)$$

Parts of the circuit in Figure 6.11(a) that contribute to the measured resonator output are depicted in Figure 6.11(b). Parasitics in Y_a do not influence the output at port 2. Furthermore, variable capacitor C_2 of the resonator is used for output measurements. At port 2, a constant voltage V_{dc} is present (6.13). Therefore only the resistance part R_c of Y_c is relevant. It can be seen in Figure 6.11(b) that parasitics stemming from Y_b have been included, as well as the optionally present additional shunt capacitance C_s .

The output current i_2 can be found using Kirchoff's current law and equals:

$$i_2 = \frac{V_1 - V_2}{R_b} + (C_b + C_s) \frac{d(V_1 - V_2)}{dt} - \frac{d(C_2 V_2)}{dt} - \frac{V_2}{R_c}. \quad (6.14)$$

Using (6.13) gives:

$$i_2 = \frac{V_{ac}}{R_b} \sin(2\pi ft) + 2\pi ft V_{ac} (C_b + C_s) \cos(2\pi ft) - V_{dc} \frac{dC_2}{dt} - \frac{V_{dc}}{R_c}. \quad (6.15)$$

The capacitance C_2 , including fringing field effects equals (see also (5.46) and

Osterberg and Senturia (1997)):

$$C_2 = \int_0^l \frac{\epsilon_0 b}{d_2 + w_0} \left[1 + \frac{2(d_2 + w_0)}{\pi b} + \frac{2(d_2 + w_0)}{\pi b} \ln \left(\frac{\pi b}{d_2 + w_0} \right) \right] dx, \quad (6.16)$$

such that the time derivative of C_2 can be elaborated as:

$$\frac{dC_2}{dt} = \frac{\partial C_2}{\partial w_0} \frac{\partial w_0}{\partial t} = - \int_0^l \frac{\epsilon_0 b}{(d_2 + w_0)^2} \left(1 + 0.65 \frac{d_2 + w_0}{b} \right) \frac{\partial w_0}{\partial t} dx. \quad (6.17)$$

Furthermore, as shown in Figure 6.5 in Section 6.3.2, a bias tee is present to decouple the dc component from i_2 . Therefore, the term $\frac{V_{dc}}{R_c}$ in (6.15) is omitted. Substituting (6.17) in (6.15) gives the output current:

$$i_{out} = \frac{V_{ac}}{R_b} \sin(2\pi ft) + 2\pi ft V_{ac} (C_b + C_s) \cos(2\pi ft) + V_{dc} \int_0^l \frac{\epsilon_0 b}{(d_2 + w_0)^2} \left(1 + 0.65 \frac{d_2 + w_0}{b} \right) \frac{\partial w_0}{\partial t} dx, \quad (6.18)$$

which is measured on a 50 Ω resistor R_{50} . Therefore the measured output voltage equals

$$V_{out} = R_{50} i_{out}. \quad (6.19)$$

In the simulation model which will be used in the next section for validation, (6.18) has been included as a postprocessing step, in which the integral is evaluated numerically (using Gaussian quadrature) based on the calculated beam deflection w_0 .

An important difference between the current approach and the one presented in Section 3.2.2 is that in (6.18) the contributions of parasitics have been included explicitly. This will result in an improved match between the shape of the amplitude-frequency curves of the experiments and the simulations. Namely, the inclusion of parasitics will result in an anti-resonance in the amplitude-frequency curve for the output at a frequency slightly higher than the resonance frequency, as will become clear from Section 6.5. Furthermore, contrary to what has been done in Section 3.2.2, there is no need for modelling the bias tee separately as in (3.6), since this does not affect the ac component of the measured output. The bias tee is considered to be transparent, such that i_{out} is exactly the ac part of i_c in (6.15), apart from a possible small phase shift.

Finally, note that the Labview measurements are not performed in a matched impedance setting. Due to the impedance mismatch (the resonator has a rather high impedance of $\mathcal{O}(10^5) \Omega$), the actual, measured output voltage V_{out} , will be lower than the calculated output from the model. This will become clear in the next section.

6.5 Experimental results and model validation

6.5.1 Validation approach

By using the measurement techniques and electrical parameters calculation techniques, presented in Sections 6.3 and 6.4, respectively, experimental validation of the simulation

model is performed. From the modelling side, it has become clear from Section 5.5 that model *III* is best suitable for describing the dynamic behaviour of the clamped-clamped beam resonator under investigation. To recapitulate, model *III* is based on Timoshenko beam theory and includes all relevant physical effects. However, the analytically derived expression for the Q -factor due to anchor loss is very low (see Section 5.2.6) and is therefore omitted for now. A single-mode Galerkin discretisation has been found to suffice for accurately describing the dynamic behaviour of the resonator. This model will be validated with experiments in the next two sections, for both the thick ($b = 10 \mu\text{m}$) and thin ($b = 1.4 \mu\text{m}$) MEMS resonator. First, however, the validation approach will be explained.

Effects like under-etching and finite production tolerances may lead to deviations from the nominal beam geometry. Therefore, some model parameters have to be adjusted in order to obtain the best match between simulations and experiments. Due to the first-principles based modelling approach, actual physical parameters are still present in symbolical form in the model. Most model parameters can be obtained directly from actual physical dimensions of the MEMS resonator and from physical properties of single-crystal silicon. However, the electrical parameters of the measurement circuit, the beam length l (to correct for under-etching), the dimensions of the electrode gaps d_1 and d_2 and the Q -factor related to anchor loss have to be determined experimentally. A straightforward experimental-numerical approach for determining these parameters consists of the following steps:

1. **network analyzer measurements:** over a range of V_{dc} -values:
 - (a) determine parasitics parameters $R_i, C_i, i = a, b, c$ (6.9). Only R_b and C_b are needed in (6.18);
 - (b) identify (fit) motional parameters R_m, L_m and C_m , as a function of V_{dc} , using (6.10). Optionally, identify parasitic capacitance C_s . Calculate f_V and Q (6.11) as a function of V_{dc} ;
 - (c) determine f_0 by fitting (6.12) to the f_V - V_{dc} -curve;
2. determine the beam length l in simulation model *III*, such that the simulated f_0 matches the measured value;
3. **Labview measurements:** over a range of V_{dc} values:
 - (a) use parasitics from step 1(a), the averaged Q -factor, C_s from step 1(b) and length l from step 2 for simulations with the numerical model;
 - (b) tune electrode gaps d_1 and d_2 such that the simulated resonance frequencies match the experimental ones for the range of V_{dc} -values considered. Assume, for now, that $d_1 = d_2$;
 - (c) tune the Q -factor to obtain a match the shapes of the resonance peaks. The Q -factor is a key parameter for the resonance peak height and the location of cyclic fold bifurcations;

4. validate the simulation model by comparing its results with experiments performed at other V_{dc} and V_{ac} excitation values.

In step 2, the length l of the beam in the model is selected to obtain a natural frequency f_0 in the simulation model that matches the experimental one. Reasons for adjusting the beam length are the following. Due to under-etching, the effective beam length may be slightly higher than the nominal length, see Table 5.1. However, this cannot be seen from SEM pictures. Furthermore, in model *III*, ideal clamping of the beam ends is assumed, in which both the rotation and shear deformation are zero (5.12). In practice, the clamping is not ideal, resulting in increased flexibility of the suspension of the beam. This can be compensated for by increasing the length l of the beam.

Furthermore, in step 3(b), $d_1 = d_2$ is used, which means that the electrode gaps around the beam are assumed to be equal. However, due to production tolerances, electrode gaps may differ from their nominal dimensions, see Figure 6.3. Therefore, the influence of asymmetric electrode gaps $d_1 \neq d_2$ will be investigated as well. If this is not explicitly stated, however, numerical results in the next two sections are calculated using $d_1 = d_2$.

Finally, physical parameter values that are used for the simulations with model *III* are obtained from literature, see also Appendix A. These parameter values are listed in Table 6.1.

Table 6.1 / Physical parameter values used in the simulations with model *III*.

Parameter	Value	Unit
ρ	2329	kg m^{-3}
E	130.02	GPa
G	79.51	GPa
ν	0.2785	(-)
k	156	$\text{W m}^{-1} \text{K}^{-1}$
c_p	716	$\text{J kg}^{-1} \text{K}^{-1}$
α	$2.616 \cdot 10^{-6}$	K^{-1}
T_0	300	K

6.5.2 Results for the thick beam

Network analyzer measurements

First, results for the thick clamped-clamped beam MEMS resonator will be presented. The beam has a thickness of $b = 10 \mu\text{m}$ and a width of $h = 4 \mu\text{m}$. Network analyzer measurements have been performed for a range of V_{dc} -values from 20 to 70 V, in steps of 5 V. The ac-excitation is set to $V_{ac} = 158 \text{ mV}$. A reference measurement at $V_{dc} = 0 \text{ V}$ has been performed in order to be able to calculate the Y-parameters according to (6.6)–

(6.8). In this way, the motional (Y_m) and parasitic admittances (Y_a , Y_b and Y_c) have been calculated. Parameters R_i and C_i of the parasitics are calculated using (6.9) and (6.10) is used to fit the motional impedance Y_m . An example of a measured and fitted Y_m is depicted in Figure 6.12. No additional parasitic term C_s is present in the motional impedance. Note that outside the resonance peak, a lot of noise is present. From the fit

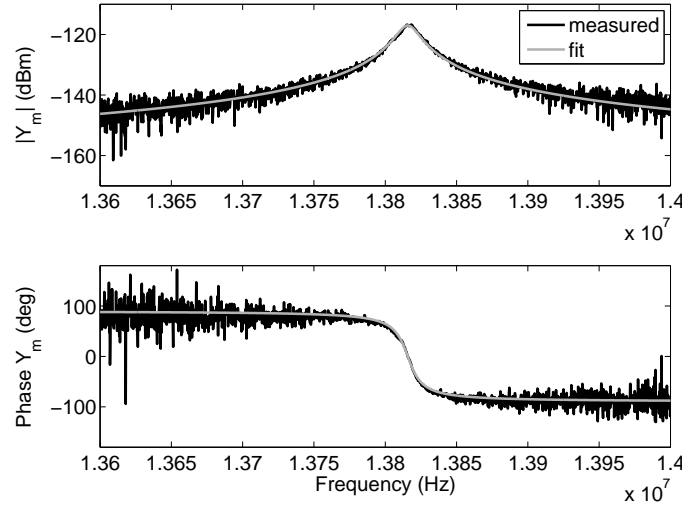


Figure 6.12 / Measured and fitted Y_m at $V_{dc} = 25$ V for the thick beam.

of motional impedance Y_m , the resonance frequency f_V and the Q -factor are calculated using (6.11). These are depicted in Figures 6.13(a) and (b), respectively, as a function of V_{dc} . The natural frequency f_0 can be determined by fitting (6.12) to the f_V - V_{dc} curve. Next, the length of the beam l has been adjusted such that the first natural frequency in the simulation model corresponds to the experimental value. Values for relevant parasitic components (see (6.18)) have been listed in Table 6.2. Values for the averaged Q -factor, natural frequency f_0 and the beam length l are also listed. Note that the value of R_b listed in Table 6.2 is negative, which is allowed in the purely mathematical description (using a resistor in parallel with a capacitor) for the parasitic impedance Y_b , see also Section 6.4.1. Furthermore, the averaged Q -factor is listed. This is an effective Q -factor,

Table 6.2 / Parameters for the model of the thick beam, determined from the network analyzer measurements.

Parameter	Value	Unit
R_b	-24.256	M Ω
C_b	1.980	fF
C_s	0	F
f_0	13.8389	MHz
Q	910	(-)
l	46.37	μm

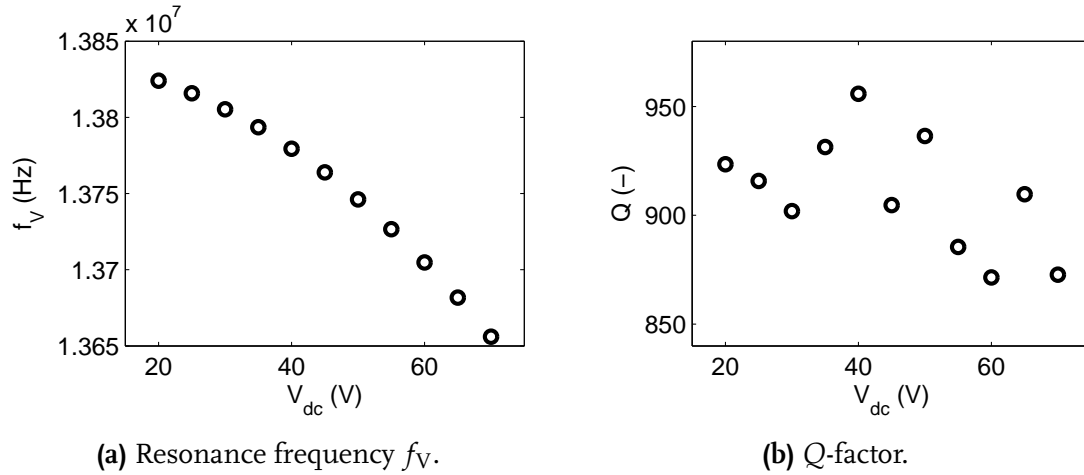


Figure 6.13 / Resonance frequency f_V and Q -factor as a function of V_{dc} .

in which all dissipation effects are included. Its value serves as an indication, or initial guess for the Q -factor that is to be determined by matching simulation results to the Labview measurements.

Labview measurements

Next, Labview measurements are performed for various V_{ac} and V_{dc} excitation settings. First, for an ac excitation amplitude of $V_{ac} = 500$ mV, the influence of a variation in V_{dc} has been investigated. V_{dc} is varied between 20 and 70 V in steps of 10 V. Measurement results for these settings are depicted in Figure 6.14(a), as a series of amplitude-frequency curves. On the horizontal axis, the excitation frequency is depicted and on the vertical axis, the peak to peak value of V_{out} is shown. It can be seen that for higher V_{dc} -values, the amplitude of the response is larger (due to stronger excitation) and the resonance frequency is lower, see also Section 5.4.2. The latter effect has already been observed from the network analyzer measurements, see Figure 6.13(a).

Simulations with model *III* (single mode discretisation) have been performed, in which V_{out} is included, using (6.18)–(6.19). Values for the parasitics, R_b , C_b and C_s are given in Table 6.2. By comparison between simulation and experimental results, it is straightforward to determine values for equal electrode gaps $d_1 = d_2$, since the resonance frequency at a certain V_{dc} -value changes significantly with the value of the electrode gaps. Additionally, the Q -factor is adjusted such that the shapes of the simulated resonance peaks match the experimental ones.

In the experimental results, depicted in Figure 6.13(a), it can be seen that no frequency hysteresis has been observed. However, the resonance peaks bend a little to lower frequencies, as can be observed most clearly for $V_{dc} = 60$ and 70 V. In the simulations, the Q -factor has to be high enough to capture this effect as well.

In this way, electrode gaps of $d_1 = d_2 = 360$ nm are found, and an overall Q -factor of $Q = 1320$. Simulation results are depicted in Figure 6.14(b). By comparing the experimental

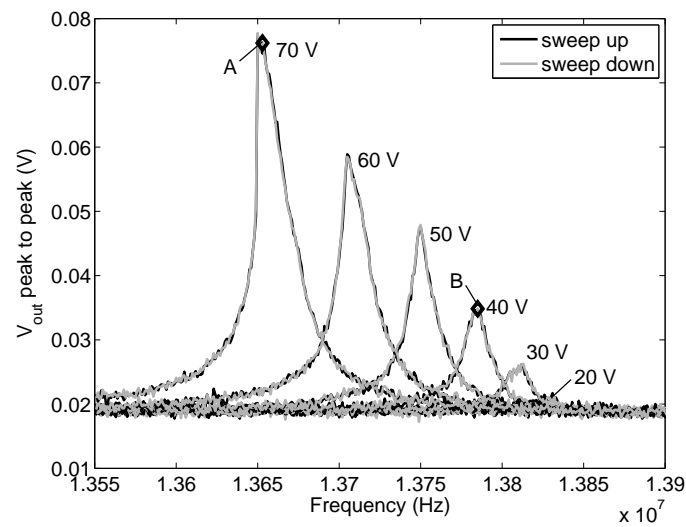
and simulated responses, it can be seen that a good match has been obtained. Simulated and measured resonance peaks are located at the same frequencies and they also have similar shapes. Especially for the response at 70 V, it can be seen that the resonance peak is slightly tilted to lower frequencies, due to the electrostatic softening effect. However, no frequency hysteresis occurs, due to the low quality factor of the system.

As already indicated in Section 5.2.6 and in (5.44), the overall Q -factor is related to Q_a (anchor loss) and Q_{th} (thermoelastic damping) and possible unmodelled dissipative effects. Anchor loss has been implemented as modal damping, see Section 5.2.6. Values for the individual Q -factors are: $Q_a = 1600$ and $Q_{th} = 14570$. The overall Q -factor of 1320 is found from $Q_{tot} = (Q_a^{-1} + Q_{th}^{-1})^{-1}$ (5.44). This Q -factor is higher than the value of 910 determined from the network analyzer measurements, see Table 6.2.

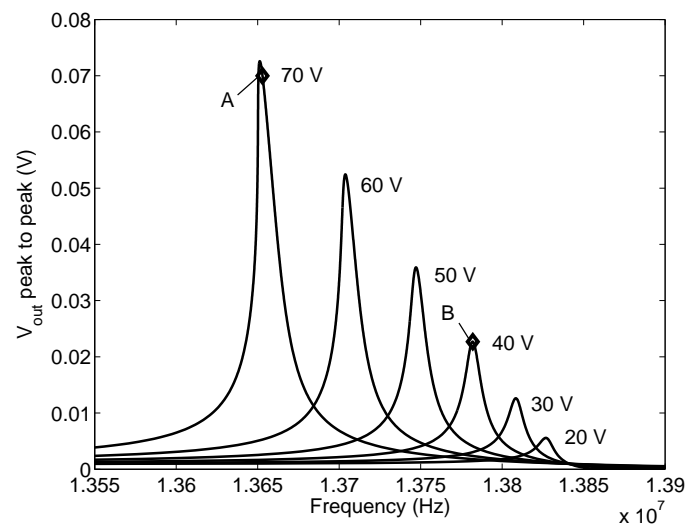
Finally, for points A and B, indicated in Figures 6.14(a) and (b), parts of the time histories have been depicted in Figure 6.15. Again, also here it can be seen that a good match between the measured and simulated responses has been obtained. The shape of the simulated output voltage signals matches the measured ones very well. Due to the lower voltage amplitude of the signal at point B, the effect of noise is more pronounced (see Figure 6.15(b)).

A mismatch in amplitude between the measured and simulated amplitude-frequency curves can be observed from Figure 6.14. The mismatch is not caused by the fact that only a single mode is taken into account in the Galerkin discretisation, since simulations with 2 and 3 modes show amplitude-frequency responses that coincide with those depicted in Figure 6.14. Instead, the mismatch can be attributed to two effects. Firstly, the Labview measurements are not performed in a matched impedance configuration. The motional resistance R_m , which determines the impedance at the peak of the resonance, has been determined from the fit of Y_m to the network analyzer measurements. It ranges from 90 k Ω up to 1 M Ω . Since the output is measured on a 50 Ω resistor (6.19), the measured peak to peak value of V_{out} will be lower than the actual amplitude. Secondly, (thermal) noise results in an additional off-set. This off-set is largest when the resonator output is small, for instance, at non-resonance frequencies, compare Figures 6.14(a) and (b). The effect can also be observed in Figure 6.15(b), where the noise results in a larger amplitude.

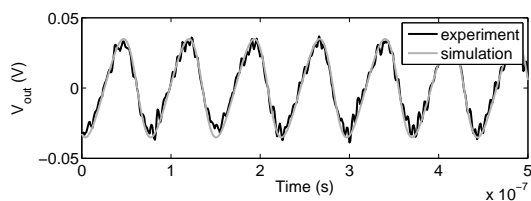
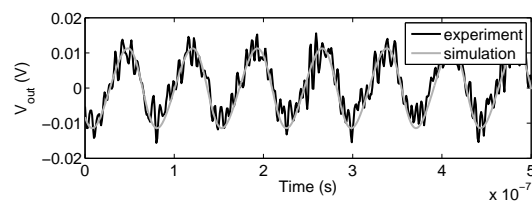
The description of the measurement circuit, as shown in Figure 6.11, is an improvement with respect to the one used in Section 3.2.2. It is both more accurate and more in line with the real experimental set-up since the effect of parasitics is included as well, see (6.18). This has consequences with respect to the thermal noise considerations. Using the more accurate description of the measurement circuit for the Labview measurements, the effect of thermal noise is found to be much less than previously described in Section 3.2.



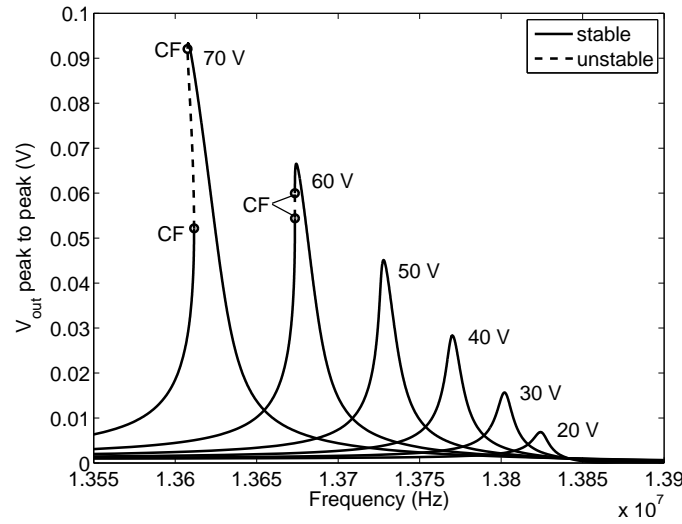
(a) Experimental results.



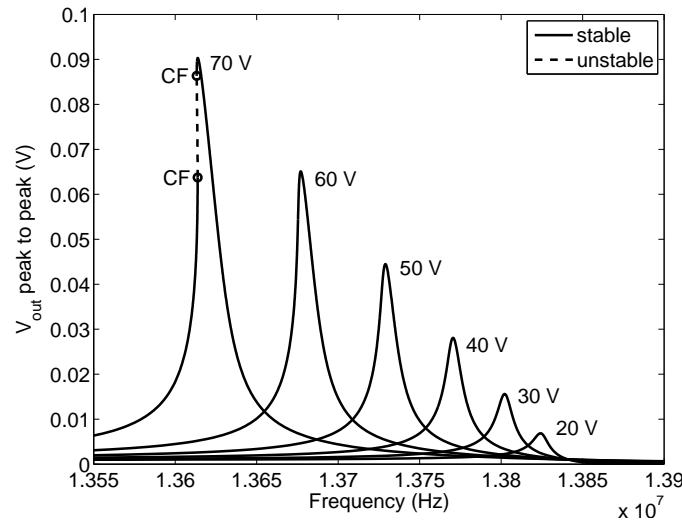
(b) Simulation results.

Figure 6.14 / Amplitude-frequency curves for $V_{ac} = 500$ mV and varying V_{dc} .(a) Time signal at point A, $f = 13.653$ MHz.(b) Time signal at point B, $f = 13.783$ MHz.**Figure 6.15** / Parts of time histories at selected points in Figure 6.14.

In order to investigate the effect of asymmetric electrode gaps, simulations have been performed for the resonator with one electrode gap 10% smaller, that is: $d_1 = 324$ nm or $d_2 = 324$ nm. Simulation results for the same excitation settings as in Figure 6.14 are depicted in Figure 6.16. From these results it can be seen that a smaller electrode gaps results in stronger electrostatic actuation. Namely, both an increase in amplitude and a decrease in frequency is observed, with respect to results depicted in Figure 6.14(b). Furthermore, for the case with $d_1 = 324$ nm, a small amount of frequency hysteresis occurs for $V_{dc} = 60$ and 70 V. For the case $d_2 = 324$ nm, frequency hysteresis occurs only at $V_{dc} = 70$ V. The transitions from stable to unstable periodic solutions and vice versa are characterised by cyclic fold (CF) bifurcations. The difference between Figure 6.16(a) and



(a) $d_1 = 324$ nm, $d_2 = 360$ nm.

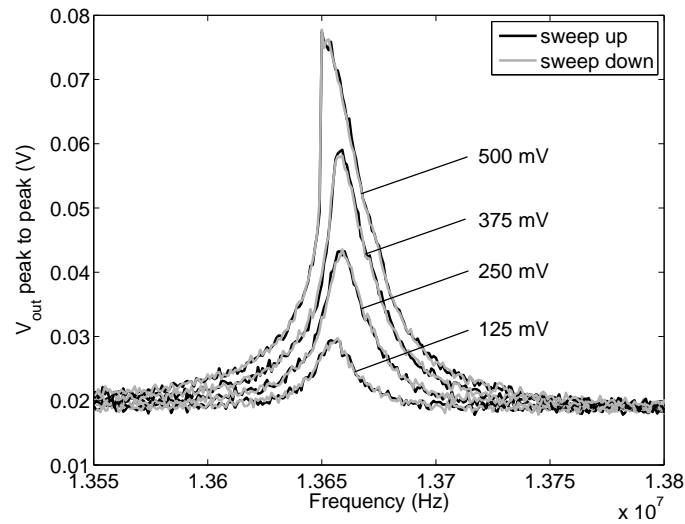


(b) $d_1 = 360$ nm, $d_2 = 324$ nm.

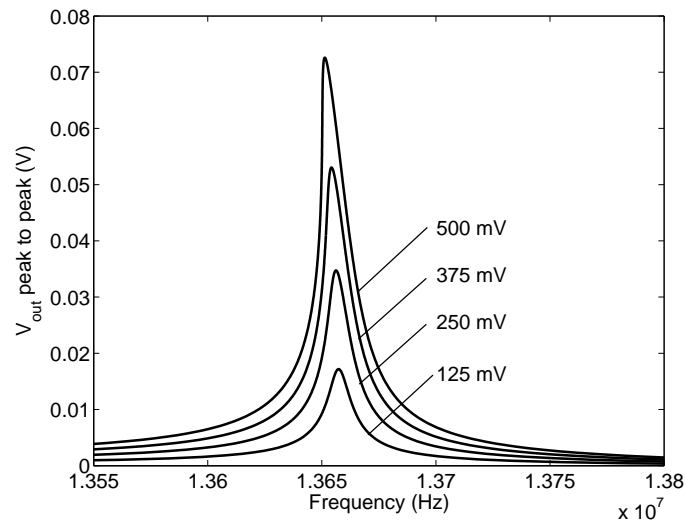
Figure 6.16 / Simulated amplitude-frequency curves, similar to Figure 6.14, using asymmetric electrode gaps.

(b) stems from the fact that electrode 1 is used for ac excitation, whereas electrode 2 is used for ac detection. A smaller gap at electrode 1 results in a stronger excitation. As a result, the electrostatic softening effect in the simulation with $d_1 = 324$ nm (Figure 6.16(a)) is more pronounced than in the simulation with $d_2 = 324$ nm (Figure 6.16(b)).

Finally, the influence of the ac excitation value V_{ac} is investigated at a bias voltage of $V_{dc} = 70$ V. For this purpose, V_{ac} is increased from 125 mV to 500 mV in steps of 125 mV. In Figure 6.17, both experimental and numerical results are depicted. Comparison of Figures 6.17(a) and (b) again gives a good match, taking into account the effects of impedance mismatch and noise.



(a) Experimental results.



(b) Simulation results.

Figure 6.17 / Amplitude-frequency curves for $V_{dc} = 70$ V and varying V_{ac} .

6.5.3 Results for the thin beam

Network analyzer measurements

The second MEMS resonator under investigation is the thin beam, which has a thickness of $b = 1.4 \mu\text{m}$ and a width of $h = 4 \mu\text{m}$. Network analyzer measurements have been performed for a range of V_{dc} -values from 20 to 40 V, in steps of 5 V. The ac-excitation is set to $V_{\text{ac}} = 50 \text{ mV}$. A reference measurement at $V_{\text{dc}} = 0 \text{ V}$ has been performed. Using a similar approach as for the thick beam, see Section 6.5.2, the motional (Y_{m}) and parasitic admittances (Y_{a} , Y_{b} and Y_{c}) have been determined. Parameters R_i and C_i of the parasitics have been calculated using (6.9) and (6.10) is used to fit the motional impedance Y_{m} . In contrast to the thick beam, an additional shunt capacitance is present in the description of the thin beam, denoted by C_{s} in (6.10). An example of a measured and fitted Y_{m} , for $V_{\text{dc}} = 25 \text{ V}$ is depicted in Figure 6.18.

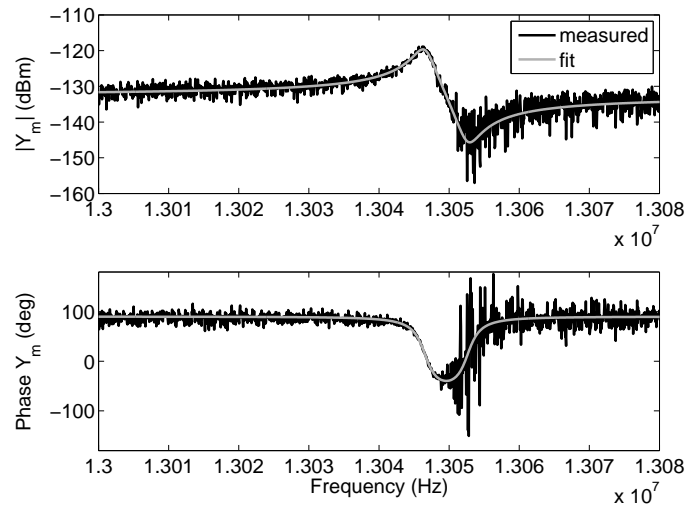


Figure 6.18 / Measured and fitted Y_{m} at $V_{\text{dc}} = 25 \text{ V}$ for the thin beam.

It can be seen that the additional parasitic capacitance C_{s} results in an anti-resonance at a frequency slightly higher than the resonance frequency. The overall parasitic effects are larger for the thin beam than for the thick beam, discussed previously. That is, the capacitance and resistance values of the parasitic components are larger, which can be observed by comparing the values for the parasitics, see Tables 6.2 and 6.3. This will have a significant influence in the Labview measurements as well, as will become clear later.

From the fit of the motional impedance Y_{m} , the resonance frequency f_{V} and the Q -factor have been identified. These are depicted for the range of V_{dc} -values in Figures 6.19(a) and (b), respectively. A numerical fit to the $f_{\text{V}}-V_{\text{dc}}$ curve, using (6.12) allows for determining the natural frequency f_0 . The beam length l has been adjusted such that the first natural frequency in the simulation model corresponds to the experimental value. Values for

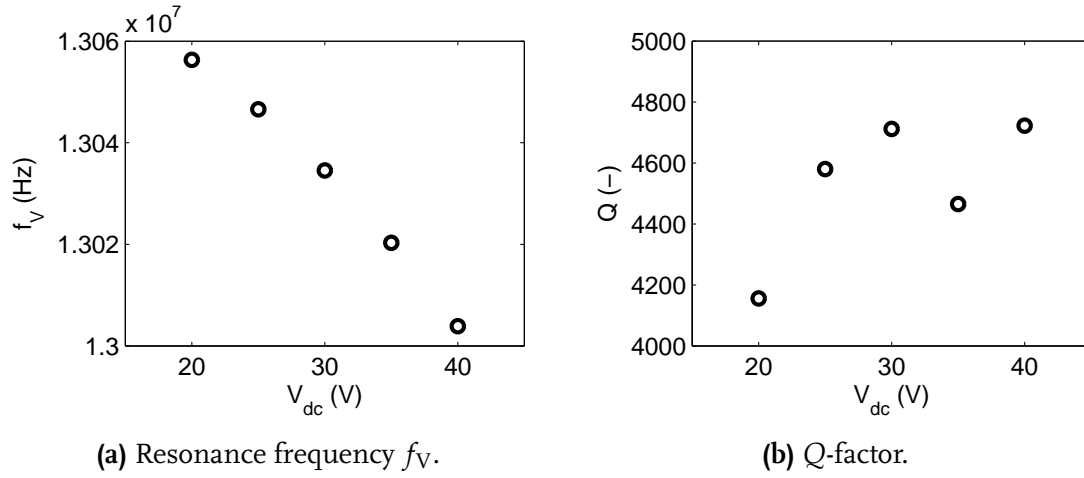


Figure 6.19 / Resonance frequency and Q -factor as a function of V_{dc} .

relevant parasitic components (see (6.18)) have been listed in Table 6.3. Values for the averaged Q -factor, natural frequency f_0 and the beam length l are also listed. Similar to the results for the thick beam, R_b has a negative value here as well. The averaged Q -factor, which will be used as an initial guess for matching the simulation model to the Labview measurements, is about 5 times higher than the Q -factor for the thick beam. The Labview measurements will be described next.

Table 6.3 / Parameters for the model of the thin beam, determined from the network analyzer measurements.

Parameter	Value	Unit
R_b	-2.9886	$G\Omega$
C_b	4.763	fF
C_s	2.393	fF
f_0	13.0724	MHz
Q	4527	(-)
l	47.75	μm

Labview measurements

Labview measurements have been performed for various V_{ac} and V_{dc} excitation settings. First, for a range of values corresponding approximately to a constant $V_{dc}V_{ac}$ product, the influence of V_{dc} is investigated, which is varied between 10 and 40 V. The product $V_{ac}V_{dc}$ roughly corresponds to the harmonic excitation amplitude (due to V^2 -terms in the excitation). Values of the excitation parameters are listed in Table 6.4.

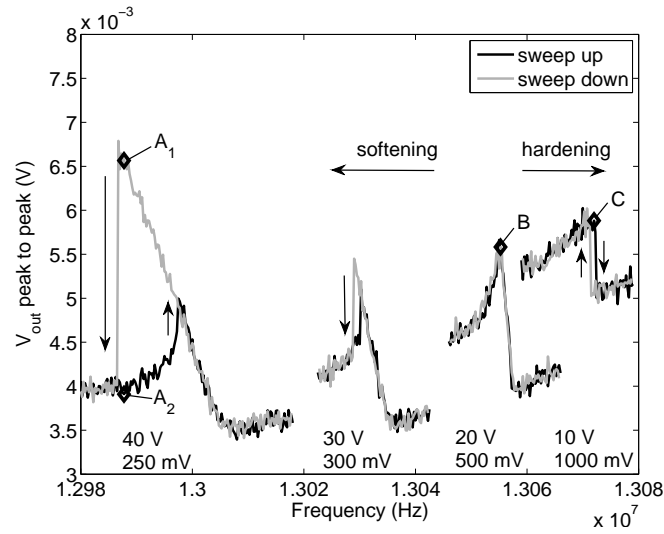
Table 6.4 / Excitation settings corresponding approximately to $V_{dc}V_{ac} = \text{constant}$.

V_{dc} (V)	V_{ac} (mV)
10	1000
20	500
30	300
40	250

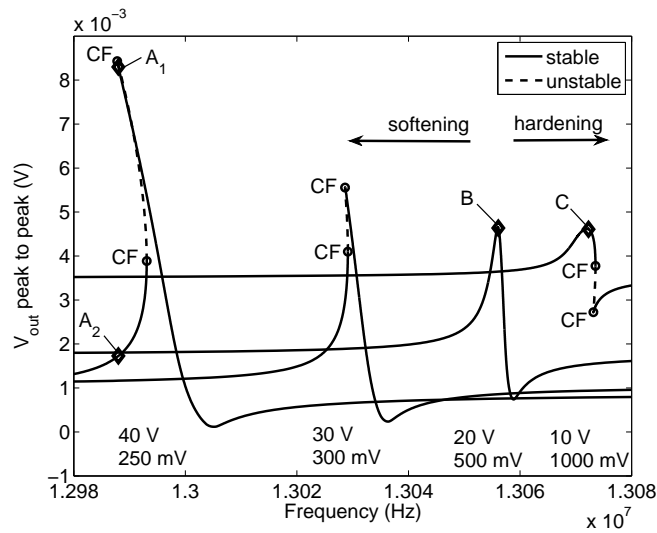
Measurement results for the settings in Table 6.4 are depicted in Figure 6.20(a), as a series of amplitude-frequency plots. Simulation results are depicted in Figure 6.20(b). It can be seen that for higher V_{dc} -values, the resonance frequency is lower. Furthermore, jumps in the measured amplitude-frequency curves indicate that for $V_{dc} = 10$ V, hardening nonlinear behaviour is observed, whereas the curves at $V_{dc} = 30$ and 40 V show softening nonlinear behaviour. The response at $V_{dc} = 20$ V, for $V_{ac} = 500$ mV shows a resonance without frequency hysteresis. Apparently, a balance is present between hardening and softening nonlinear behaviour at this bias voltage. The hardening to softening transition effect has earlier been observed in Figure 5.12. Several points on the amplitude-frequency curves in Figure 6.20(a) have been indicated. Time signals for these points are depicted in Figure 6.21 and will be discussed later.

Simulations with model *III*, single mode discretisation, have been performed. As stated before, values for the parasitics, R_b , C_b and C_s are given in Table 6.3. Using a similar approach as applied for the thick beam, values for equal electrode gaps $d_1 = d_2$ have been determined. Additionally, the Q -factor is tuned such that the shapes of the simulated resonance peaks match the experimental ones and such that the downward jump frequency in experiments corresponds with the upper cyclic fold (CF) bifurcation points in simulations. In this way, electrode gaps of $d_1 = d_2 = 342$ nm are found, and an overall Q -factor of $Q = 6210$. Simulation results are depicted in Figure 6.20(b). By comparing Figures 6.20(a) and (b), it can be seen that a good match has been obtained, since simulated and measured resonance peaks are located at the same frequencies and they also have similar shapes. However, similar to the results for the thick beam, a mismatch in amplitudes is present, which is caused by impedance mismatch and noise. Furthermore, the simulation results shows the same transition from hardening to softening nonlinear behaviour for increasing V_{dc} as the experimental results. In the simulations, cyclic fold bifurcations mark the transition from stable to unstable periodic solutions. These results have been obtained for a single-mode Galerkin discretisation. Amplitude-frequency curves, calculated using multi-mode Galerkin discretisations coincide with the single-mode results.

For points A_1 , A_2 , B and C, indicated in Figures 6.20(a) and (b), parts of their time histories have been depicted in Figure 6.21. It can be seen that a match in shape has been obtained between simulation and experimental results. The amplitude of the time histories, however, shows a mismatch. This has also been observed as a difference in amplitude between the measured and simulated amplitude-frequency curves in Figure 6.20. This effect again stems from impedance mismatch and thermal noise, similar to the results for the thick beam. The motional impedance R_m of the resonator has been determined



(a) Experimental results.



(b) Simulation results.

Figure 6.20 / Transition from hardening to softening nonlinear behaviour for varying excitation values.

from the network analyzer measurements and ranges from 396 k Ω up to 1.63 M Ω .

Furthermore, inclusion of the relation for the output voltage, based on (6.18)–(6.19), results in the anti-resonance present at a frequency slightly higher than the resonance frequency, see Figure 6.20. For reference, simulation results for the same excitation settings (Table 6.4) are depicted in terms of the peak to peak midpoint displacement w_{mid} in Figure 6.22. Here, it can be seen that the amplitude-frequency curves do not show anti-resonances slightly above the resonance frequency.

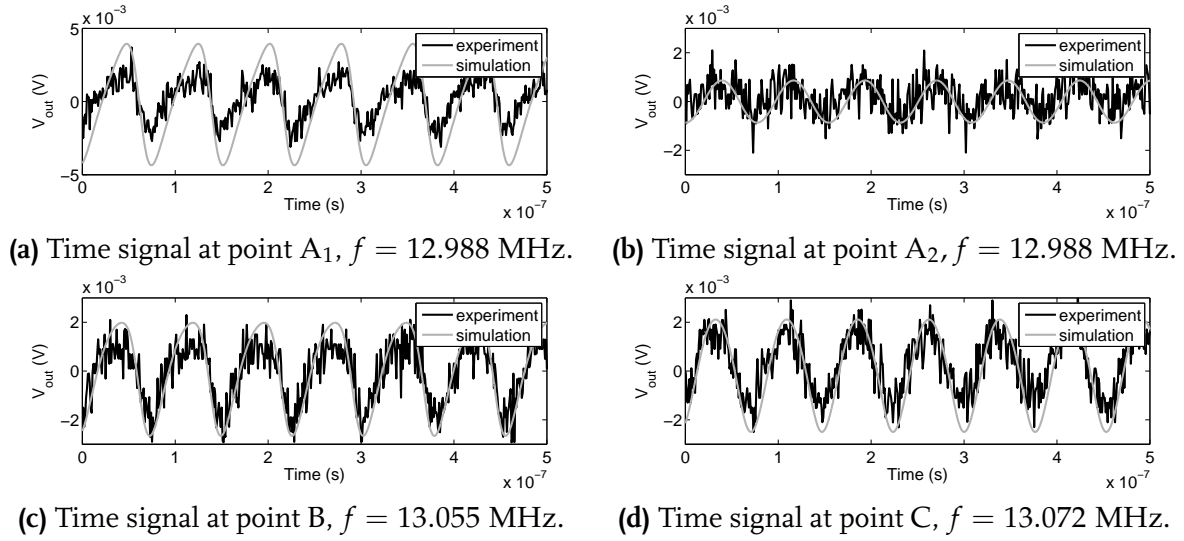


Figure 6.21 / Parts of time histories at selected points in Figure 6.2o.

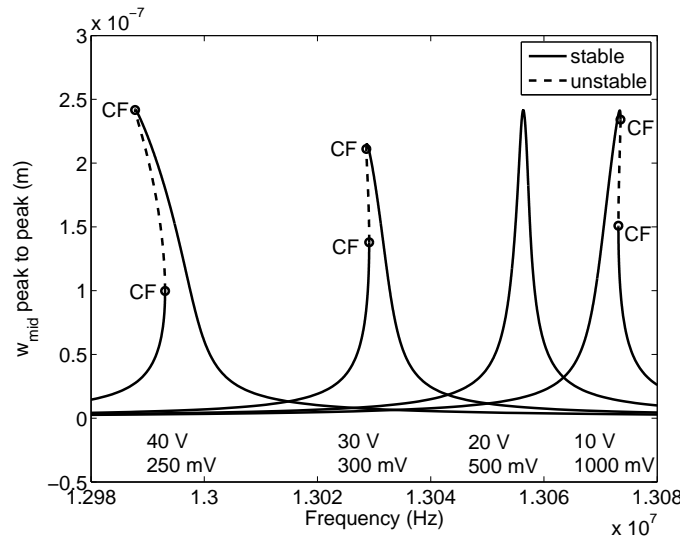


Figure 6.22 / Simulation results of Figure 6.2o(b) in terms of peak to peak midpoint displacement w_{mid} .

Based on the Q -factor that has been determined from matching the simulation results to experimental results, contributions from anchor loss and thermoelastic damping can be determined. The overall Q -factor is related to Q_a (anchor loss) and Q_{th} (thermoelastic damping) by (5.44). Anchor loss has been implemented as modal damping. Values for the Q -factors are: $Q_a = 11000$ and $Q_{\text{th}} = 14250$, giving a total of $Q = 6210$. Again, this is higher than the value of $Q = 4527$ determined from the network analyzer measurements, see Table 6.3.

The analytical derivation of anchor loss in Section 5.2.6, based on Hao et al. (2003) and Hao and Xu (2009) is found to result in a Q -factor that is significantly lower than

the experimentally determined one. The derivations in Section 5.2.6 are based on a semi-infinite substrate, into which stress waves are radiated. Wave reflections in the suspension of the beam considered in this work are probably the main cause for the higher Q -factor in the experiments. Namely, reflected waves result in less dissipation, yielding a higher Q -factor.

Next, some results are presented for other excitation values than discussed so far. For a bias voltage of $V_{dc} = 10$ V, the effect of V_{ac} is investigated by varying it from 500 to 1250 mV in steps of 250 mV. Both experimental and simulation results for these excitation settings are depicted in Figure 6.23. It can be seen that the results from the simulation model correspond reasonably well with the experimental results, apart from the amplitude values. The overall shapes of the amplitude-frequency curves correspond

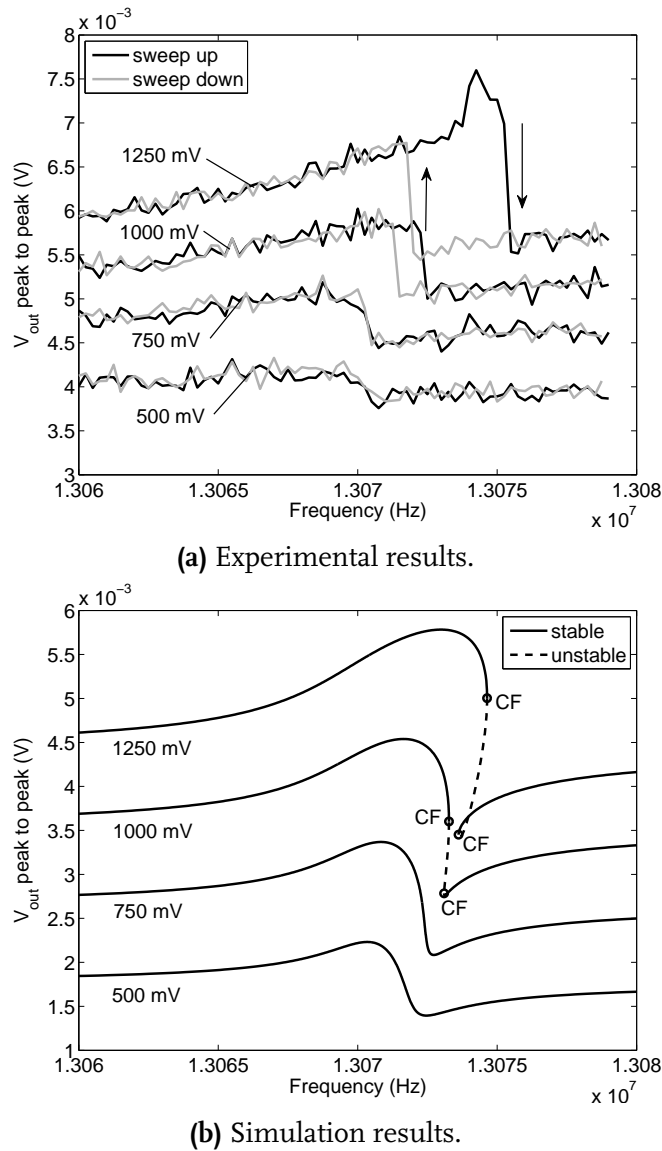


Figure 6.23 / Amplitude-frequency curves for $V_{dc} = 10$ V and varying V_{ac} .

quite well. Frequency hysteresis is observed in the experiment for $V_{ac} = 1000$ and 1250 mV. In the simulated amplitude-frequency curves for these values, unstable solution branches are present, which also give rise to frequency hysteresis. However, the location of the lower CF bifurcation points does not correspond with the frequency at which an upward jump takes place in the measured response, see, for instance, the curve for $V_{ac} = 1250$ mV. A reason for this difference has not been found.

At a different bias voltage, $V_{dc} = 40$ V, another comparison has been made between experimental and simulation results. V_{dc} is set to 40 V and V_{ac} is varied from 100 to 300 mV in steps of 100 mV. The results are depicted in Figure 6.24. Again, a good match is obtained, in which both the resonance frequency and the shape of the amplitude-frequency curves corresponds quite well. Again, the effect of the parasitics in

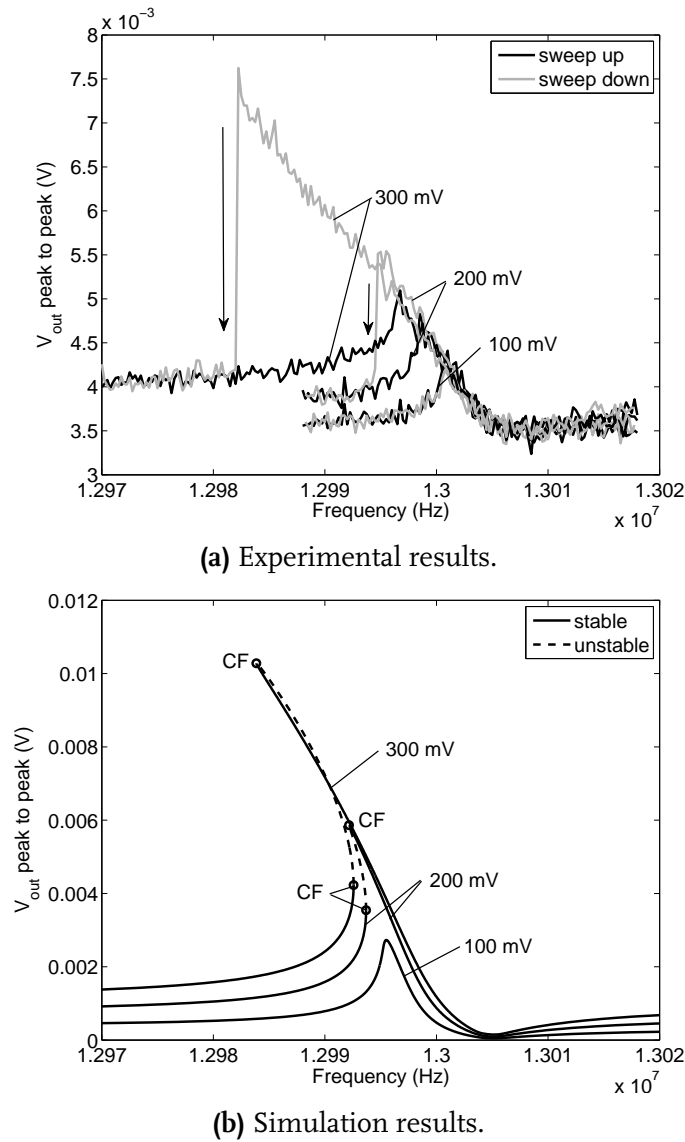
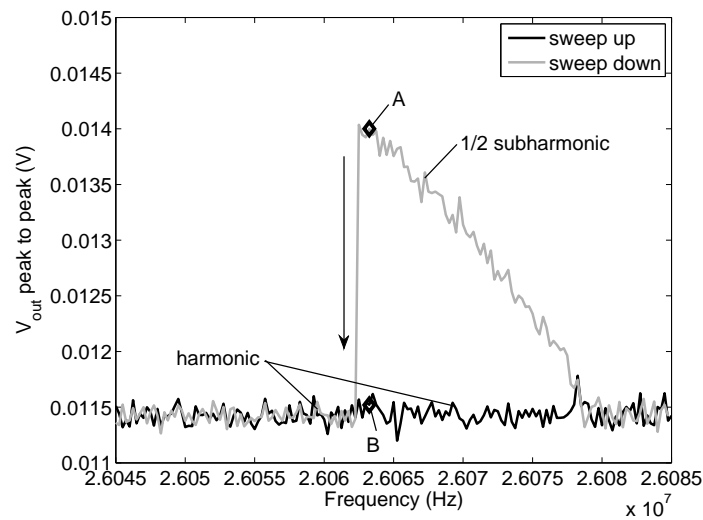


Figure 6.24 / Amplitude-frequency curves for $V_{dc} = 40$ V and varying V_{ac} .

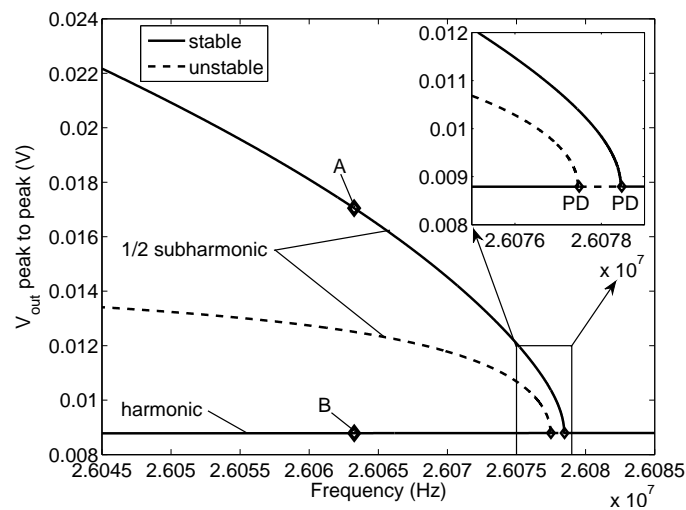
the clamped-clamped beam MEMS resonator can be observed in the measured response in Figure 6.24(a). At a frequency around 13.005 MHz, the three amplitude-frequency curves almost coincide. This effect is also predicted by the simulation model, see Figure 6.24(b). Furthermore, similar to the results in Figure 6.23, the location of the lower CF bifurcation points in the simulation results does not correspond exactly with the experimentally observed upward jumps.

Another phenomenon, which has also been observed in the measurements used for the heuristic modelling approach (Figures 3.15 and 3.16 in Section 3.2) is the presence of a $1/2$ subharmonic resonance. At excitation settings of $V_{dc} = 30$ V and $V_{ac} = 1250$ mV the $1/2$ subharmonic resonance is found at a frequency of approximately 26.07 MHz, which is twice the first harmonic resonance frequency. For a $1/2$ subharmonic resonance, the fundamental frequency in the response is half the excitation frequency. Experimental and simulation results for the $1/2$ subharmonic resonance are depicted in Figure 6.25.

In order to find the $1/2$ subharmonic resonance in the simulation model, the Q -factor has to be increased from 6210 to 7310. By comparing simulation and experimental results, a good match can be observed. From the simulation results, it becomes clear that the $1/2$ subharmonic resonance branches are initiated by two period doubling bifurcations (PD) around $f = 26.078$ MHz, see the inset in Figure 6.25(b). In Figure 6.26, time histories are depicted for points A and B, indicated in Figure 6.25. The V_{out} -signals of the simulation model correspond well with the experimental results. The period doubling effect can be observed by comparing the time history at point A (Figure 6.26(a), $1/2$ subharmonic branch) with the one at point B (Figure 6.26(b), harmonic branch). In the experiment, a jump down is observed for the sweep down at a frequency of 26.062 MHz. Due to noise in the system, the response may have jumped to the lower, harmonic, branch. In the numerical simulation, no cyclic fold bifurcation is found at this frequency. Actually, according to perturbation theory, nonlinear damping has to be present in order for the stable and unstable subharmonic branches to close in a CF bifurcation, see for instance Lifshitz and Cross (2003). In the case of Figure 6.26(b), however, the $1/2$ subharmonic branch will continue till dynamic pull-in at a frequency below 26 MHz.



(a) Experimental results.



(b) Simulation results.

Figure 6.25 / Amplitude-frequency curves for the 1/2 subharmonic resonance.

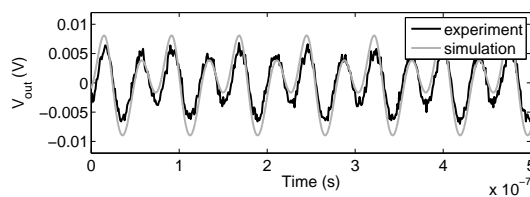
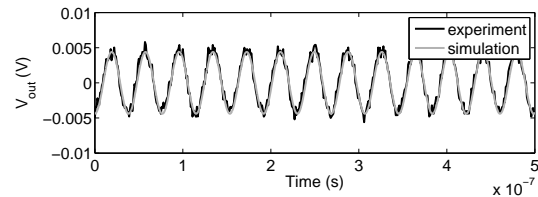
(a) Time signal at point A, $f = 26.0633$ MHz.(b) Time signal at point B, $f = 26.0633$ MHz.

Figure 6.26 / Parts of time histories at selected points in Figure 6.25.

6.6 Conclusions

After description of two different measurement techniques, an electrical equivalent circuit representation of the clamped-clamped beam MEMS resonator is introduced. The representation of the resonator in this description is only valid for small signal analysis. Next, the two measurement techniques have been applied for extensive experimental validation of the most promising simulation model of Chapter 5. For this purpose, model *III* has been used, which is based on Timoshenko beam theory, and includes relevant physical effects. However, since the analytically derived expression for the Q -factor due to anchor loss (Q_a) is very low, Q_a will be estimated based on measurements. A single-mode discretisation is found to be sufficient for accurately describing the nonlinear dynamic behaviour of the MEMS resonator under investigation.

Two clamped-clamped beam MEMS resonators have been investigated, having dimensions close to the nominal geometry given in Table 5.1. A thick ($b = 10 \mu\text{m}$) and a thin ($b = 1.4 \mu\text{m}$) beam have been used. Results show a reasonably good match between experiments and simulations with the 1DOF model. Resonance frequencies and shapes of amplitude-frequency curves, both with and without frequency hysteresis, match very well for various excitation parameters V_{dc} and V_{ac} . Therefore, confidence has been gained in the modelling approach and the model, proposed in Chapters 4 and 5, respectively.

A first major improvement, with respect to the heuristic modelling approach applied in Section 3.2 is that a more accurate description of the measurement circuit has been derived, based on the electrical equivalent circuit of the clamped-clamped beam MEMS resonator (see Sections 6.4). Electrical parameters of the measurement circuit can be identified from experiments. The description includes parasitic electrical effects and results in a good match between simulations and experiments.

Secondly, since the model (model *III*) is based on first principles, most model parameters have been obtained directly from actual physical dimensions of the MEMS resonator and from physical properties of single-crystal silicon. These model parameters have actual physical meaning (they are not lumped), which is the main benefit of using a first-principles based approach. However, the electrical parameters of the measurement circuit, the beam length l (to correct for under-etching), the dimensions of the electrode gaps d_1 and d_2 and the Q -factor related to anchor loss have to be identified experimentally. A straightforward validation approach has been proposed (Section 6.5.1) in order to identify these parameters from experiments. As a result, by using the multiphysics modelling framework together with the validation approach, a model description is obtained, in which individual physical parameters and individual effects can be distinguished. Contrary to the results of the heuristic model for the clamped-clamped beam MEMS resonator of Section 3.2, subtle variations in the response have now been captured.

Finally, in order to be able to make a fully quantitative comparison between the simulations and the experiments, their amplitude mismatch has to be addressed. The mismatch is present for the Labview measurements only and is caused by an impedance mismatch in the measurement circuit of the resonator and by (thermal) noise. As a result, a different (lower) output than the actual one is measured.

Phase feedback for nonlinear MEMS resonators in oscillator circuits¹

Abstract / In this chapter, a phase feedback approach for using nonlinear MEMS resonators in oscillator circuits is investigated. The principle of the approach is illustrated for a nonlinear Duffing resonator, which is representative for many types of MEMS resonators. Next, the approach is applied in a system level simulation, using a device level model for a clamped-clamped beam MEMS resonator. Phase feedback allows for operation of the resonator in its nonlinear regime and enables control of both the frequency of oscillation and the output power of the signal. Various aspects of phase feedback are investigated in detail and the chapter ends with conclusions.

7.1 Introduction

As indicated in Chapter 1, silicon MEMS resonators provide a promising alternative for quartz crystals as accurate timing devices in oscillator circuits for modern data and communication applications (Nguyen, 2005, 2007). Major advantages are their compact size, feasibility of integration with IC technology and low cost. In an oscillator circuit, the resonator acts as a frequency selective element, see Section 2.3. Linear behavior of the resonator is often desired, since nonlinearities in the resonator may complicate oscillator behavior and may limit the signal to noise ratio (S/N-ratio) and phase noise performance. Conventional quartz crystal resonators are not driven into nonlinear regimes, since the rather bulky quartz crystal units can store sufficient energy for oscillation while remaining linear. Therefore, quartz crystal based oscillator circuits are often limited through amplifier nonlinearities.

MEMS resonators inherently can store less energy, due to their smaller size, see Kaajakari et al. (2004a). Therefore, they are often driven into nonlinear regimes at much lower excitation amplitudes than quartz crystals. Operation in nonlinear regimes

¹This chapter is based on Mestrom et al. (2007) and Mestrom et al. (2009b).

can be circumvented by using resonator arrays to improve linearity and power handling (see Nguyen, 2007). However, the use of arrays results in larger device dimensions. Alternatively, bulk mode resonators can be used (see, for instance Mattila et al., 2002b; Pourkamali and Ayazi, 2003; Hao et al., 2004; Lin et al., 2004) but these may be more susceptible to spurious modes. Furthermore, these bulk resonators vibrate in much stiffer modes (at higher frequencies), contrary to the so-called flexural resonators on which this paper focuses. Electrostatically actuated flexural MEMS resonators intrinsically show nonlinear effects. For instance, the excitation is intrinsically nonlinear (depends on the reciprocal of the square of the gap) and the resonators are easily driven into nonlinear mechanical regimes, See Chapters 3 and 5. Furthermore, operation at low excitation values often results in an unacceptably low S/N-ratio.

In this chapter, it is shown that addressing nonlinear regimes of the MEMS resonator does not need to be a problem. Based on the heuristic device level model for the clamped-clamped beam MEMS resonator of Section 3.2, a system level approach (see Figure 1.3) for using nonlinear flexural MEMS resonators in an oscillator circuit is proposed. This so-called phase feedback technique allows for active tuning of the oscillation frequency in a closed-loop sense, by setting the phase in the feedback amplifier. The concept will be illustrated for a nonlinear Duffing resonator. The tuning freedom of the phase feedback approach will be investigated further by means of numerical simulations on a flexural MEMS resonator showing characteristic nonlinear behavior. The model for this resonator has been verified experimentally in Section 3.2 (Mestrom et al., 2008a).

Background on oscillator circuits has already been given in Section 2.3. Especially the oscillation conditions (2.2)–(2.3) are relevant for phase feedback. The outline for the remainder of this chapter is as follows. First, the open-loop response of a nonlinear Duffing resonator will be explained in Section 7.2. In Section 7.3, the phase feedback principle will be explained for this nonlinear Duffing resonator. Subsequently, the method will be applied on simulation level to an electrostatically actuated clamped-clamped beam MEMS resonator for which the nonlinearities are of Duffing-type. Simulation results will be presented in Section 7.4 and, finally, some conclusions will be drawn in Section 7.5.

7.2 Open-loop response of the Duffing resonator

The small size of MEMS resonators requires that they often have to be driven into nonlinear regimes in order to store enough energy. Nonlinear effects include, but are not limited to, geometric nonlinearities due to (relatively) large vibration amplitudes (Kaajakari et al., 2004a; Thomsen, 2003), electrostatic nonlinearities due to capacitive excitation and detection (Kaajakari et al., 2004a), and material nonlinearities like higher-order elastic effects (Kim and Sachse, 2000). These effects have been described in Chapter 4. From Chapter 5, it has become clear that these nonlinear effects may effectively be described by a simplified or lumped model with a Duffing-like structure, see also Kaajakari et al. (2004a). Therefore, without loss of generality, the principle of phase feedback will be explained for a Duffing system (which is a classical example of a nonlinear resonator),

that shows qualitatively similar nonlinear dynamic behavior to a MEMS resonator. The differential equation for the forced Duffing system is given as (Thomsen, 2003):

$$m\ddot{x} + b\dot{x} + k_1x + k_3x^3 = F_0 \cos \Omega t, \quad (7.1)$$

where x denotes some characteristic displacement and parameters m , b , k_1 and k_3 denote mass, damping, linear stiffness and cubic stiffness parameters, respectively. Depending on the sign of k_3 , the system has a hardening ($k_3 > 0$) or softening ($k_3 < 0$) spring characteristic. The forcing has an amplitude F_0 and an angular excitation frequency Ω . The Duffing oscillator is representative for certain types of MEMS resonators, as will be discussed in Section 7.3.2. By introducing parameters

$$\omega_0 = \sqrt{\frac{k_1}{m}}, \quad \xi = \frac{b}{2\sqrt{k_1 m}}, \quad \gamma = \frac{k_3}{k_1} \omega_0^2, \quad \text{and} \quad q = \frac{F_0}{m}, \quad (7.2)$$

(7.1) can be rewritten as

$$\ddot{x} + 2\xi\omega_0\dot{x} + \omega_0^2x + \gamma x^3 = q \cos \Omega t. \quad (7.3)$$

Here, ω_0 is the natural frequency of the linear system (without γ), ξ is the non-dimensional damping coefficient, γ is the nonlinearity parameter and q is the forcing parameter. An approximate solution to the response of the Duffing system to a resonant excitation ($\Omega \approx \omega_0$) can be obtained by applying the method of multiple scales, which is a perturbation technique, described in, for instance, Nayfeh (1981) or Thomsen (2003). This method can only be applied to weakly nonlinear systems. Therefore, a small book-keeping parameter $\varepsilon \ll 1$ will be introduced to indicate that the nonlinearity is weak compared to linear terms. For the case of resonant excitation, as considered here, small excitations lead to large responses, so the excitation and damping terms are scaled as well:

$$\ddot{x} + \omega_0^2x = \varepsilon(q \cos \Omega t - 2\xi\omega_0\dot{x} - \gamma x^3). \quad (7.4)$$

Here, the equation has been arranged such that the left-hand side constitutes a linear undamped system. The method of multiple scales allows for the steady-state solution of (7.4) to be written as (Thomsen, 2003):

$$x = a \cos(\Omega t - \psi) + \varepsilon \frac{\gamma}{32\omega_0^2} a^3 \cos(3(\Omega t - \psi)) + \mathcal{O}(\varepsilon^2), \quad (7.5)$$

where a is given by the solution to the so-called frequency response equation

$$q^2 = a^2 \left[(2\xi\omega_0^2)^2 + \left(\frac{3}{4}\gamma a^2 - 2\sigma\omega_0^2 \right)^2 \right] \quad (7.6)$$

and the phase ψ results from

$$\tan \psi = \frac{-\xi\omega_0}{\sigma - \frac{3\gamma}{8\omega_0} a^2}. \quad (7.7)$$

As mentioned before, parameter ε in (7.4) and (7.5) is a small bookkeeping parameter, which serves to indicate the order of approximation. Parameter σ in (7.6) and (7.7) is the frequency detuning parameter $\sigma = \Omega - \omega_0$. Furthermore, local asymptotic stability of solutions (a, ψ) holds if (Thomsen, 2003):

$$\left(\sigma - \frac{3\gamma}{8\omega_0}a^2\right)\left(\sigma - \frac{9\gamma}{8\omega_0}a^2\right) + (\xi\omega_0)^2 < 0. \quad (7.8)$$

By using (7.6)–(7.8), amplitude-frequency curves and phase-frequency curves can be approximated based on the fundamental harmonic term in (7.5) ($\varepsilon = 0$). These curves are nonlinear equivalents to the magnitude and phase curves of the Bode diagram. They are depicted in Figure 7.1 for the specific parameter values $\omega_0 = 2\pi$ rad/s, $\xi = 0.005$, $\gamma = -5 \text{ m}^{-2}\text{s}^{-2}$, and $q = 0.4 \text{ m/s}^2$. Since $\gamma < 0$, see (7.2), the system will show softening. Stability of the periodic solutions has been determined by (7.8) and is also indicated.

Figure 7.1(a) contains the amplitude-frequency curve, which depicts the normalized amplitude (a/a_{\max} , where a_{\max} is the value at the peak) of oscillation versus normalized frequency Ω/ω_0 . In practice, jumps will be observed in the steady-state nonlinear dynamic behavior of the resonator when one sweeps up and down through the fundamental resonance region. These jumps are also indicated in Figure 7.1 by the arrows. This effect is also known as frequency hysteresis. The right part shows the corresponding phase-frequency curve. Recall that both curves are based on the assumption that the system response (7.5) may be approximated by a linear response (only the first harmonic term in (7.5)). Otherwise, the term phase has no meaning for nonlinear systems. For the relatively large value of the nonlinearity used here ($\gamma = -5 \text{ m}^{-2}\text{s}^{-2}$), this may be only a very crude approximation, since the Duffing resonator may no longer be considered as a weakly nonlinear system.

For the approximation, given in (7.5), the phase can be calculated from (7.7). In Figure 7.1(b), it can be seen that the phase changes by π rad over the resonance peak, sim-

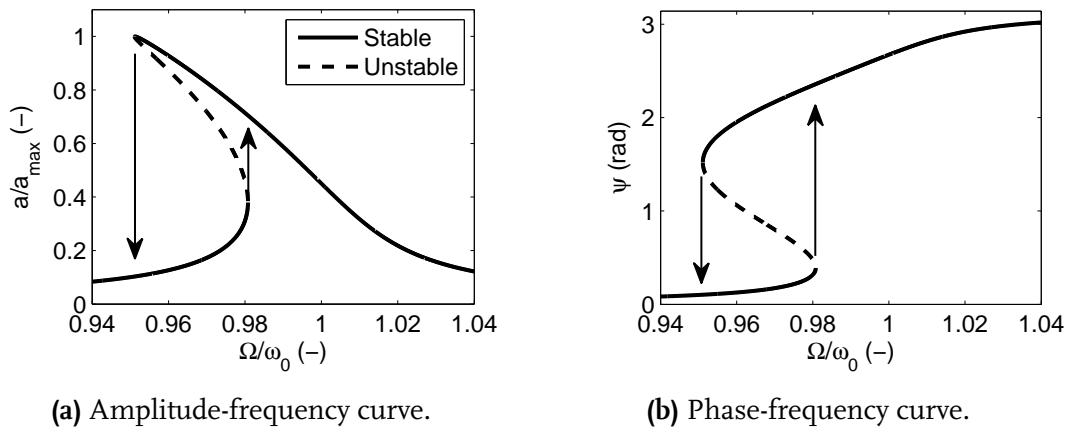


Figure 7.1 / Open-loop response for the Duffing resonator (linear natural angular frequency is ω_0).

ilar to the phase change in a linear system. Finally, note from Figure 7.1 that both the amplitude a and the phase ψ are *not* single-valued functions of the excitation frequency.

7.3 Phase feedback

7.3.1 Principle of phase feedback

In order to cope with resonator nonlinearities in an oscillator environment, a technique, described in Greywall et al. (1994) and Yurke et al. (1995), can be applied. This will be called *phase feedback*. Consider the phase-frequency curve in Figure 7.1(b) again. Although the phase is not a single-valued function of the excitation frequency, this is the case the other way around. In other words, *the frequency is a single valued function of the phase*, that is $\Omega/\omega_0 = f(\psi)$. This is depicted in Figure 7.2(a), in which the usable range for the phase is $\psi \in [0, \pi]$. Here, displacement x of (7.3) is used as the output of the resonator, see Figure 2.3, which is fed into the amplifier. Depending on what quantity of the system is used for feedback, the usable range may change. The concept of phase feedback is suitable for oscillator applications, since the resonator and amplifier together have to satisfy gain and phase requirements (2.2)–(2.3). As a result, the frequency at which the resonator oscillates can be actively controlled by setting the amplifier part of the oscillator circuit to a suitable phase condition. This idea holds under the assumption that the amplitude, the frequency and the phase of the amplifier are independent. In that case, the resonator can be forced to oscillate at a frequency of $\Omega/\omega_0 \approx 0.96$ with a phase of $\psi = \psi_R = 2$ rad (see Figure 7.2(a)), by setting the amplifier phase to $\psi_A = 2\pi - \psi_R$, see (2.2). In this way, the closed-loop behavior of the system tunes the resonator to oscillate at a high-amplitude solution (at the peak in the open-loop response in Figure 7.1(a)). The amplitude-phase curve for the Duffing resonator is depicted in Figure 7.2(b).

It will become clear in Section 7.4 that, with phase feedback, the oscillator can even operate on the unstable part of the curve of a nonlinear MEMS resonator. Namely, unstable

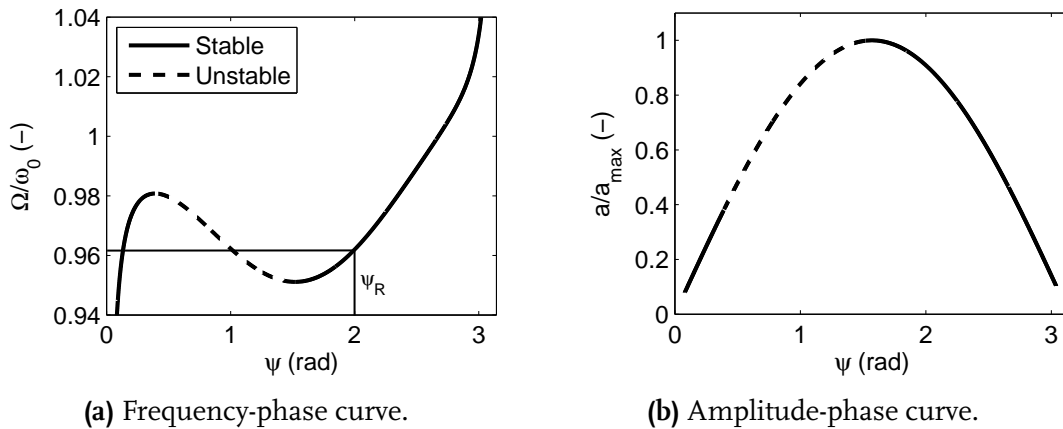


Figure 7.2 / Open-loop response of the Duffing resonator.

regions in the open-loop response (see Figure 7.1) are stabilized using phase feedback. Moreover, a resonator phase near $\psi = \pi/2$ rad not only results in high-amplitude resonator oscillations, but also in small sensitivity of the oscillation frequency to changes in phase. Namely, the frequency Ω/ω_0 is not very sensitive for changes in ψ , since the frequency-phase function is (almost) horizontal in the region around $\psi = \pi/2$ rad, see Figure 7.2. The method described above has been used in a recently developed sensitive magnetometer, described in Greywall (2005).

Two further remarks can be made with respect to the technique of phase feedback. Firstly, the proposed technique may seem to show similarities with a phase-locked loop (PLL), which can also be used for generating stable frequencies, see, for instance Best (2003). However, phase feedback is substantially different. PLLs consist of a feedback circuit in which the phase and frequency difference between the output and a reference signal are translated into a control signal. This signal is fed into a voltage-controlled oscillator (VCO) that ‘locks’ the output again to the reference signal. The main difference between PLLs and the proposed phase feedback approach is that in PLLs, a reference signal (frequency) is present to which the output should be locked. Deviations from this reference signal result in control effort that controls the output to its ‘locked’ state. For phase feedback, no reference is present, since the output frequency of the circuit can be determined by setting the phase of amplifier. In this way, phase feedback is in fact a frequency control method, similar to the control voltage that is used in a VCO. Furthermore, no control effort is needed, other than that of setting the phase in the amplifier once. By setting the amplifier phase, the resonator will act as a band-pass filter that allows only the signals that satisfy the oscillator phase condition (see (2.2)) to pass.

Secondly, the proposed phase feedback technique is not a nonlinearity cancellation technique, see, for instance Shao et al. (2008b). Cancellation of the nonlinearity of the resonator is not necessary for the principle to be applied. As will be shown in Section 7.4.2, phase feedback will cause both the frequency and the amplitude to be single-valued functions of phase ψ for the nonlinear MEMS resonator considered.

7.3.2 Application to a MEMS resonator

The phase feedback approach, described in the previous section, will be applied at system model level to a clamped-clamped beam MEMS resonator. The resonator under investigation consists of the single-crystal silicon beam of Chapter 3 with a length of $44\ \mu\text{m}$, a width of $4\ \mu\text{m}$ and a thickness of $1.4\ \mu\text{m}$. The device level model for the resonator has a Duffing-like structure and is able to describe measured nonlinear dynamical behavior rather well, see Chapter 3.

A schematic representation of the clamped-clamped beam resonator is depicted in Figure 3.1. The actuation of the resonator is realized by means of a dc (V_{dc}) and an ac (V_{ac}) voltage component, which are applied to the electrodes of the resonator by means of bias tees, see Figure 3.1. Note that the dc voltage V_{dc} is applied to both electrodes of the beam, whereas the ac voltage is applied to a single electrode.

The device level model for the resonator has been given in (3.1)–(3.3) and (3.5). Note that the resonator is excited parametrically. Although the beam vibration shape is continuous, this lumped description has been found adequate for capturing the dynamic behavior of the MEMS resonator, see Chapter 3.

The linear natural frequency of the clamped-clamped beam resonator equals $f_0 = \omega_0/(2\pi) = 1/(2\pi)\sqrt{k_1/m}$. Due to electrostatic actuation, this frequency will change slightly to $f_{0,e} = 1/(2\pi)\sqrt{k_{1,e}/m}$, where stiffness $k_{1,e}$ equals k_1 offset by a V_{dc}^2 -term: $k_{1,e} = k_1 - 2C_0V_{dc}^2/d_0^2$, see (3.8).

The output of the resonator is measured on the electrode without the ac excitation, see Figure 3.1. The output current i_{out} results from capacitive detection of the resonator motion. Only the motional i_{mot} term in (4.29) remains, giving:

$$i_{out} = \frac{dq_e}{dt} = \frac{d}{dt} \left(V_{dc} \frac{C_0 d_0}{d_0 + x} \right) = -V_{dc} \frac{C_0 d_0}{(d_0 + x)^2} \dot{x}. \quad (7.9)$$

From this equation, it can be seen that the output current is roughly proportional to minus the velocity of the resonator: $i_{out} \propto -\dot{x}$. Since the output i_{out} of the MEMS resonator will be used for phase feedback, the usable range for the resonator phase ψ_R will change from $\psi_R \in [0, \pi]$ (see the Duffing resonator in Section 7.3.1) to $\psi_R \in [\pi/2, 3\pi/2]$. This will be shown in Section 7.4.2.

In practice, the current i_{out} can be sensed and converted into a voltage by using a trans-impedance amplifier. In that case, the amplifier output voltage will be used for feedback purposes.

In order to be able to perform closed-loop simulations with phase feedback, an system level oscillator circuit model including the device level model of the nonlinear MEMS resonator has been implemented numerically in MATLAB/SIMULINK². The schematic structure is depicted in Figure 7.3. The MEMS resonator block contains a SIMULINK block diagram implementation of (3.1)–(3.3), (3.5) and (7.9).

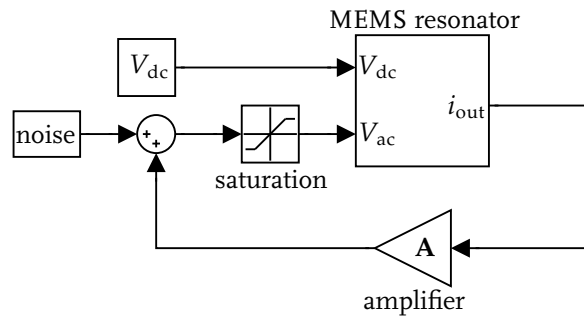


Figure 7.3 / Block diagram of the oscillator circuit with the MEMS resonator.

²The Mathworks Inc., Matlab 7.5.0 (R2007b)

The oscillator circuit consists of the MEMS resonator and an amplifier. The resonator is driven by a bias voltage V_{dc} and an input voltage $V_{in} = V_{ac}$ on the resonator ac input. The oscillator is self-starting due to (thermal) noise, see Section 2.3. The resonator output, current i_{out} , is amplified and fed back into the resonator. The input to the MEMS resonator is limited in amplitude by a saturation function. Otherwise, the oscillation amplitude might grow till the resonator shows dynamic pull-in (see also Section 7.4.5). The saturation element may also introduce additional nonlinearities in the system, but has to be included in order to be able to compare closed-loop responses with open-loop responses. This will become clear in Section 7.4. Additional (nonlinear) effects, resulting from the saturation element, are still a topic of further research.

The oscillator circuit has to satisfy the two conditions (2.2)–(2.3) in order for oscillations to occur. Therefore, the amplifier gain $\mathbf{A} = G_A(\Omega) \exp(j\psi_A(\Omega))$ has been implemented as a gain and a phase shift, which is an idealised representation. In practice, both the amplifier gain and phase depend on the input as well, and can not be set arbitrarily. Therefore, a more accurate model of the amplifier electronics would be required. However, for investigation of the principle of phase feedback, the idealised representation is used. In the block diagram (Figure 7.3), this is implemented by means of a gain and a transport delay with a delay time of $\Delta t_A = \psi_A / (2\pi f_{0,e})$, where ψ_A denotes the required amplifier phase. The simulation procedure consists of solving an initial value problem in MATLAB/SIMULINK using a fixed time step solver. Simulation results for phase feedback with the MEMS resonator will be presented in the next section.

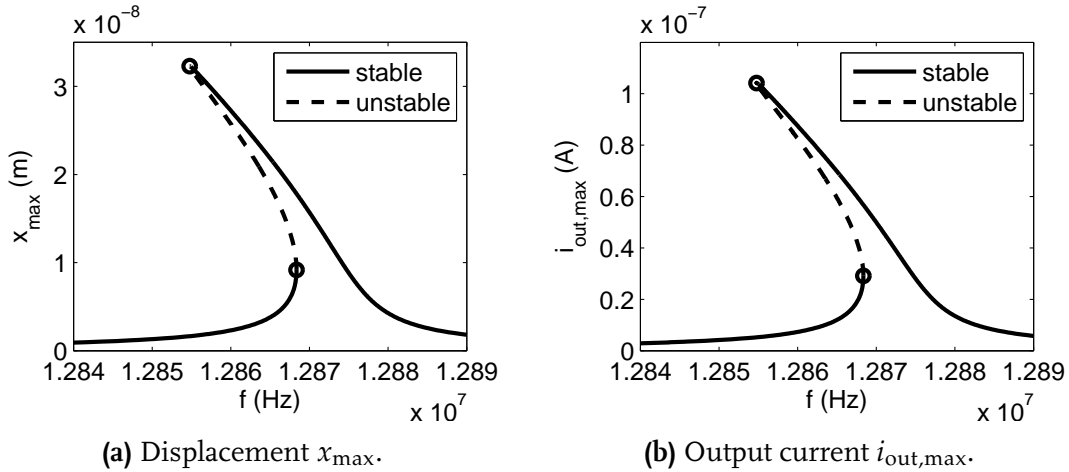
7.4 Results

7.4.1 Open-loop response of the MEMS resonator

For the results listed in this section, the set of parameter values listed in Table 7.1 has been used (see also Table 3.1). The value of V_{ac} should be interpreted as the saturation level in the saturation block in Figure 7.3. From these parameter values, the fundamental frequency can be calculated: $f_0 = 12.945$ MHz ($f_{0,e} = 12.873$ MHz). Furthermore, the amplitude-frequency curve for this parameter set has been calculated numerically using AUTO (Doedel et al., 1998) and is depicted in Figure 7.4. The maximum displacement x_{max} is plotted versus the excitation frequency $f = \Omega / (2\pi)$ in Figure 7.4(a). The circles indicate turning points in the curves. Typical vibration amplitudes are in the order of several tens of nanometers. The response is similar to that of the Duffing resonator, presented earlier (see Figure 7.1(a)). In an oscillator setting, the output current i_{out} is available, rather than the resonator displacement. The current, which is roughly proportional to $-\dot{x}$ (see (7.9)), shows an amplitude-frequency curve, see Figure 7.4(b), which is similar to that of the displacement x_{max} .

Table 7.1 / Numerical values for the model parameters.

Parameter	Value	Unit
m	0.2275	ng
b	2.721×10^{-9}	N s m ⁻¹
k_1	1.505	kN m ⁻¹
k_2	0.0	N m ⁻²
k_3	-6.2×10^{15}	N m ⁻³
k_4	0.0	N m ⁻⁴
k_5	1.2×10^{30}	N m ⁻⁵
d_0	330	nm
C_0	0.185	fF
V_{dc}	70.0	V
V_{ac}	180	mV

**Figure 7.4** / Amplitude-frequency curves for the MEMS resonator and the parameter values listed in Table 7.1.

7.4.2 Oscillator response using phase feedback

The effect of phase feedback on the resonator output is investigated by means of numerical simulations with the block diagram depicted in Figure 7.3. A typical result is shown in Figure 7.5, where the resonator output currents i_{out} without and with phase feedback are shown. In the case without feedback, Figure 7.5(a), the resonator is driven by noise only. Therefore, the resonator output to this noisy excitation is its band-pass filtered response, which will not reach a periodic solution. For feedback, the amplifier gain is chosen such that oscillations will swing up. For Sections 7.4.2 and 7.4.3, a gain value of $G_A = 10^7$ V/A is applied. More details on the influence of the gain will follow in Section 7.4.4.

The amplifier phase is set to $\psi_A = 2\pi - \pi$ rad to force the resonator to operate at $\psi_R = \pi$ rad. From Figure 7.5(b), it can be seen that it takes some time before the resonator reaches its steady-state. The time to reach steady-state depends on the excess gain

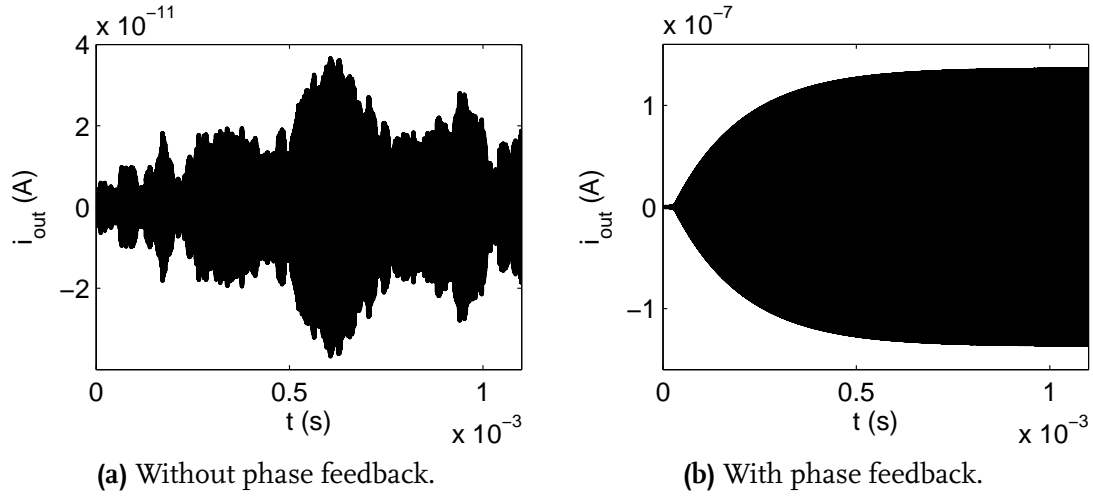


Figure 7.5 / Output current i_{out} .

in the feedback loop, see (2.3). No additional dissipation mechanism is added by phase feedback. The steady-state amplitude that the periodic solution attains depends on the amplifier gain G_A and the dissipation in the resonator, which influences G_R . Once the oscillator gain condition (2.3) becomes an equality, the amplitude stops growing. The amplifier output, which is the input of the resonator, is limited (clipped) by the saturation element, see Figure 7.3. The Q -factor of the system is a measure for the dissipation in the resonator and equals $Q = 1/(2\xi) = \sqrt{k_{1,e}m/b} = 6.8 \times 10^3$, which is not extremely high. With the electrode gaps listed in Table 7.1, the Q -factor would translate to a very large motional resistance value of $R_m = 2 \text{ M}\Omega$ in an electrical equivalent circuit representation, see (3.12) in Section 3.2.2. The motional resistance is found to result in significant contribution of thermal noise in the open-loop response. In closed-loop this effect will not be seen, because phase feedback filters the noise according to the oscillation phase condition (2.2).

In steady-state, the oscillator output is periodic. The autopower spectra of the output signals with and without phase feedback have been calculated and are depicted in Figure 7.6. In the feedback case, a resonator phase of $\psi_R = \pi \text{ rad}$ is used.

Here, the resonator output i_{out} is used as the oscillator output in order to compare the situation with and without feedback. In practice, however, the amplifier output voltage is used (see Figure 2.3). From Figure 7.6, it can be seen that the output of the circuit with phase feedback has a much higher spectral purity compared to the case without phase feedback.

Furthermore, it can be seen that the fundamental frequency in the feedback case is slightly lower than in the case without feedback. This is the result of the phase-dependence of the oscillation frequency (see Figure 7.2), where a functional relation between frequency and phase exists. In order to investigate this behavior, a simulation study has been performed in which the requested phase ψ_R of the resonator is varied between $\pi/2$ and $3\pi/2$ rad, which is the usable range for ψ_R for current (i_{out}) feedback (see also Section 7.3.2). For values of $\psi_R \in [0, \pi/2]$ and $\psi_R \in [3\pi/2, 2\pi]$ rad, no sustained oscillation

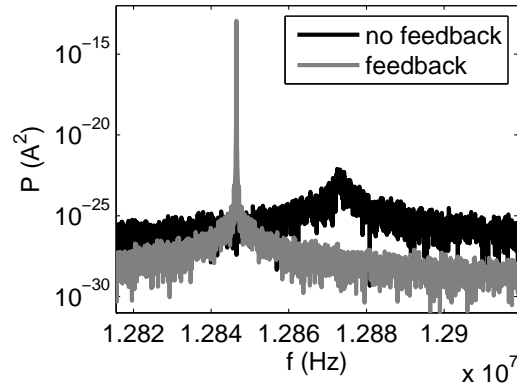


Figure 7.6 / Autopower spectrum of the oscillator output i_{out} with ($\psi_R = \pi$ rad) and without phase feedback.

tions have been observed. For each phase $\psi_R \in [\pi/2, 3\pi/2]$, and, consequently, for each amplifier phase $\psi_A = 2\pi - \psi_R$, the fundamental frequency in the output is determined. The frequency-phase curve is depicted in Figure 7.7(a). This figure is similar in shape to Figure 7.2(a), with the difference that Figure 7.7(a) depicts closed-loop results. Note that the local minimum of the analytical curve for the Duffing system in Figure 7.2 is present at $\psi_R = \pi/2$ rad, whereas in Figure 7.7(a), the local minimum for the MEMS resonator is present at $\psi_R = \pi$ rad. The difference in phase for this minimum can be related to the fact that the response of the Duffing equation is in terms of the position x , whereas the resonator output i_{out} in the oscillator circuit is roughly proportional to $-\dot{x}$, see (7.9). The region to the left of the minimum (i.e. the range $\psi_R \in [2, \pi]$ rad in Figure 7.7(a)) would correspond to the unstable part of the open-loop frequency-phase curve, similar to Figure 7.2(a). However, in case of phase feedback, no unstable part exists on the left of the minimum. Closed-loop phase feedback stabilizes the oscillation at the open-loop unstable part of the response. Furthermore, since the oscillation frequency changes with

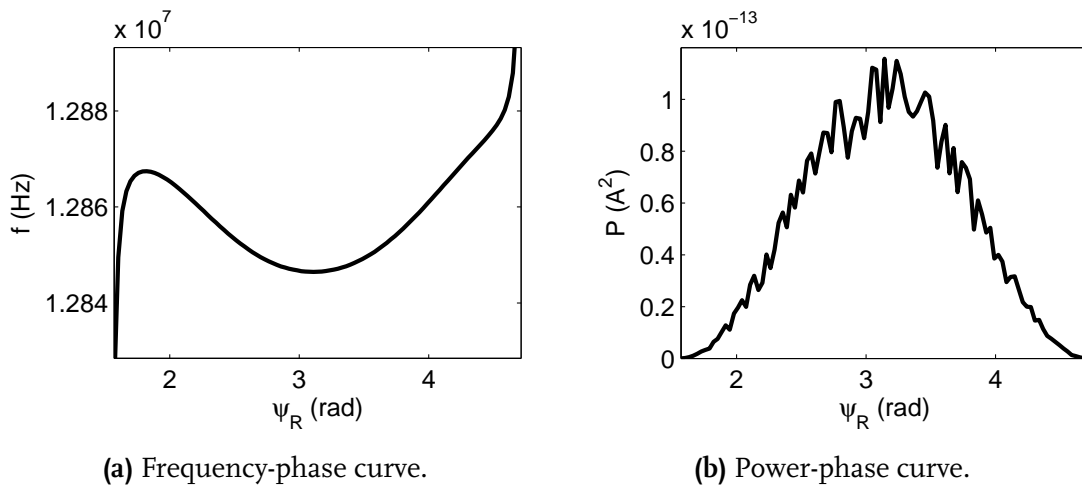


Figure 7.7 / Closed-loop response of the oscillator circuit with the MEMS resonator.

the phase, the amplifier phase provides a means for fine-tuning the oscillation frequency. For oscillator applications, a large S/N-ratio in the circuit output is desired. Required for this is a high output power and low noise. Output power is a measure for the desired fundamental frequency content. For each phase ψ_R , the power at the fundamental oscillation frequency is calculated from the resonator output and is depicted in Figure 7.7(b). This response is similar in shape to the open-loop amplitude-phase curve depicted in Figure 7.2(b). However, Figure 7.7(b) shows a jittery shape which is caused by the finite frequency resolution in the simulations. In Figure 7.7(b), it can be seen that highest power is available at a feedback phase of about $\psi_R = \pi$ rad, which can be explained as follows. In general, the most effective excitation for a system is proportional to the system velocity. A phase shift of π rad of the output signal i_{out} (which is proportional to $-\dot{x}$) will result in a signal proportional to \dot{x} that is fed back into the resonator.

Summarizing the results of this simulation study, the optimal operation point for the MEMS resonator based oscillator circuit has been determined to be at a feedback phase of $\psi_R = \pi$ rad. Here, the response is at the maximum of the output current power-phase curve (Figure 7.7(b)) and at the local minimum of the frequency-phase curve (Figure 7.7(a)), which is both very beneficial. Namely, high power results in a good fundamental harmonic signal component and in less amplifier effort needed for sustaining vibrations. The local minimum in the frequency-phase curve results in little changes in frequency for changes in phase. Additionally, since the amplifier phase ψ_A sets the resonator phase ψ_R , the amplifier phase can be used for fine-tuning the oscillation frequency of the oscillator through the frequency-phase curve in Figure 7.7(a). The concept limits are still a topic of further research. For instance, robustness of the principle with respect to process spread of both the MEMS resonator and the amplifier electronics is of interest.

To conclude this section, a phase noise plot has been calculated from Figure 7.6. This plot is depicted in Figure 7.8 (solid line), where the phase noise $\mathcal{L}(\Delta f)$ is expressed in decibels below the carrier per Hertz. It can be seen that the narrow peak in Figure 7.6 results in a good phase noise response. For reference, Figure 7.8 can be compared with

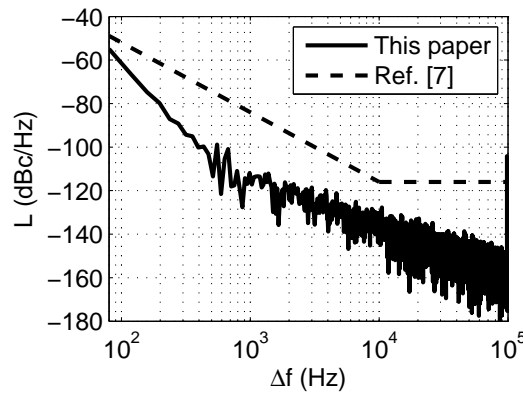


Figure 7.8 / Phase noise plot for the oscillator output (solid line), calculated from Figure 7.6. The dashed line is an approximation to the curve from Lin et al. (2004).

recently reported experimental results in Lin et al. (2004) for a clamped-clamped beam resonator with a slightly lower nominal frequency (9.34 MHz), for which an approximate curve is depicted as a dashed line in Figure 7.8. From this comparison, it follows that the results from the approach described in this paper are quite promising, since this results low phase noise. An important remark here, is that the slopes of the simulated phase noise response do not match those predicted by Leeson's equation (2.7), see Figure 2.5. A possible reasons for this mismatch is the following. Leeson's model is based on thermal noise considerations for a linear time-invariant *LC*-oscillator. The oscillator under investigation here is nonlinear, since it is based on a nonlinear MEMS resonator. The nonlinear effects in the MEMS resonator may result in additional noise upconversion. Additionally, the saturation element may introduce similar effects.

7.4.3 Influence of saturation level

Next, it is investigated what influence the saturation level in the saturation block (see Figure 7.3) has on the spectral content of the output signal. For this purpose, the saturation level in the saturation block has been varied between 20 mV and 260 mV in steps of 40 mV. First, however, the open-loop situation is investigated. Under harmonic excitation, amplitude-frequency plots of the resonator have been calculated for the various V_{ac} -values using AUTO (Doedel et al., 1998). Results, in terms of output current, are depicted in Figure 7.9. From the figure, it can be seen that the resonator response changes from almost linear (no hysteresis) to strongly nonlinear (hysteresis) for increasing V_{ac} . By using these V_{ac} -values as the saturation limits in the oscillator circuit (Figure 7.3), the transition from almost linear to nonlinear can be investigated in the closed-loop simulations. Furthermore, by varying the resonator phase (by means of setting the amplifier phase) in the usable range $\psi_R \in [\pi/2, 3\pi/2]$ rad, frequency-phase curves for the closed-

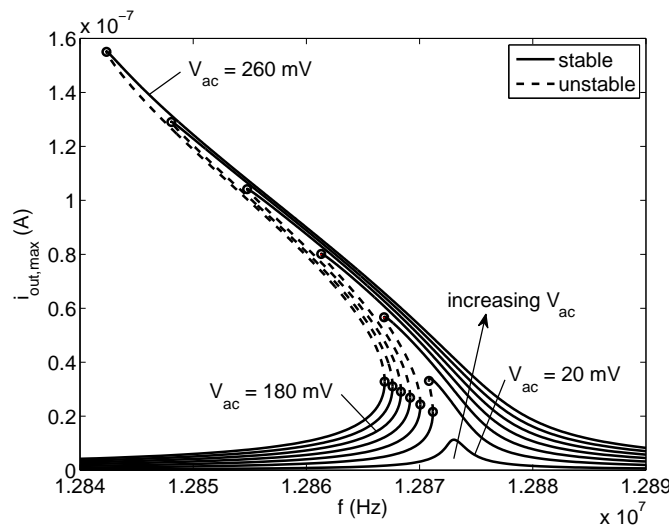


Figure 7.9 / Open-loop amplitude-frequency curve for the MEMS resonator for various V_{ac} values (constant increments of 40 mV are used).

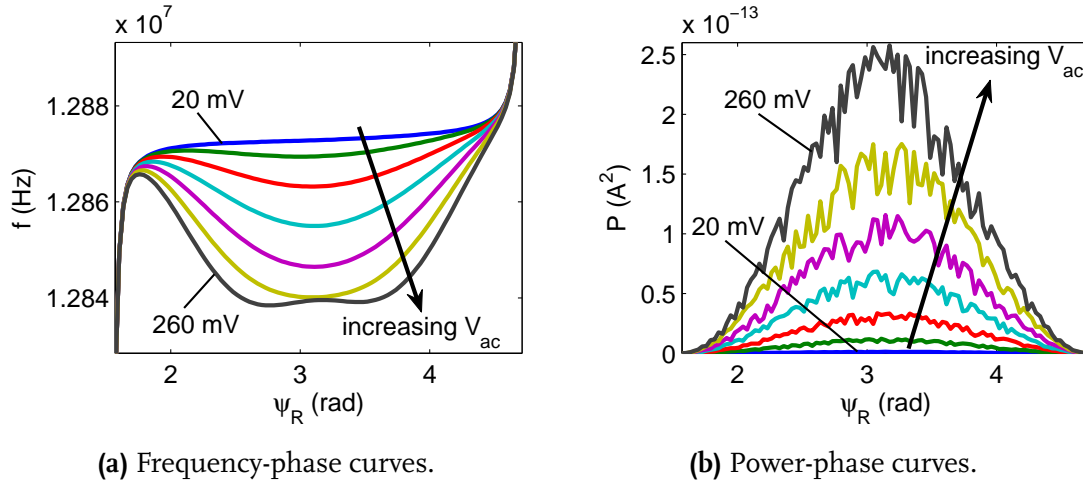


Figure 7.10 / Closed-loop responses for various saturation values V_{ac} (constant increments of 40 mV are used).

loop system can be calculated for the fundamental oscillation frequency. These are depicted in Figure 7.10(a). Similar to the amplitude-frequency responses of the resonator itself (see Figure 7.9), the frequency-phase curves can be seen to become increasingly nonlinear for higher V_{ac} -values. Only the $V_{ac} = 20$ mV simulation is (almost) linear. This value corresponds to the upper curve in Figure 7.10(a), which is monotonically increasing for increasing phase. Therefore, for linear resonators, there is almost no tuning freedom for the frequency of oscillation by setting the resonator phase ψ_R . Furthermore, the minimum in the frequency-phase curve becomes wider with increasing V_{ac} and even two (local) minima appear for $V_{ac} = 260$ mV. This is related to the increasing amount of nonlinearity in the system for larger amplitudes (term k_5 in (3.5)). A wider minimum indicates a smaller sensitivity of the oscillation frequency for the amplifier phase. Consequently, the tolerances on the phase-setting part of the feedback amplifier have to be less strict.

Furthermore, the power at the fundamental oscillation frequency for the two cases considered, is depicted in Figure 7.10(b) for varying V_{ac} . As expected, higher saturation levels result in higher output power. Furthermore, for all V_{ac} -values, the maximum power is located at a resonator phase around $\psi_R = \pi$ rad. This means that the optimal operation point in terms of frequency sensitivity for phase corresponds with the highest output power.

From Figure 7.10, it becomes clear that the two control parameters, being amplifier phase ψ_A (ψ_R , indirectly) and saturation value V_{ac} , provide a means for (fine-)tuning the frequency of oscillation as well as the output power of the oscillator. This demonstrates that phase feedback is a powerful concept for nonlinear MEMS resonators.

To conclude this section, the spectral content in the oscillator output i_{out} has been investigated for a resonator phase of $\psi_R = \pi$ rad. Results are depicted in Figure 7.11(a). As already stated above and as can be seen from Figure 7.11(a), an increasing saturation value results in a lower oscillation frequency and a higher signal power. The phase noise

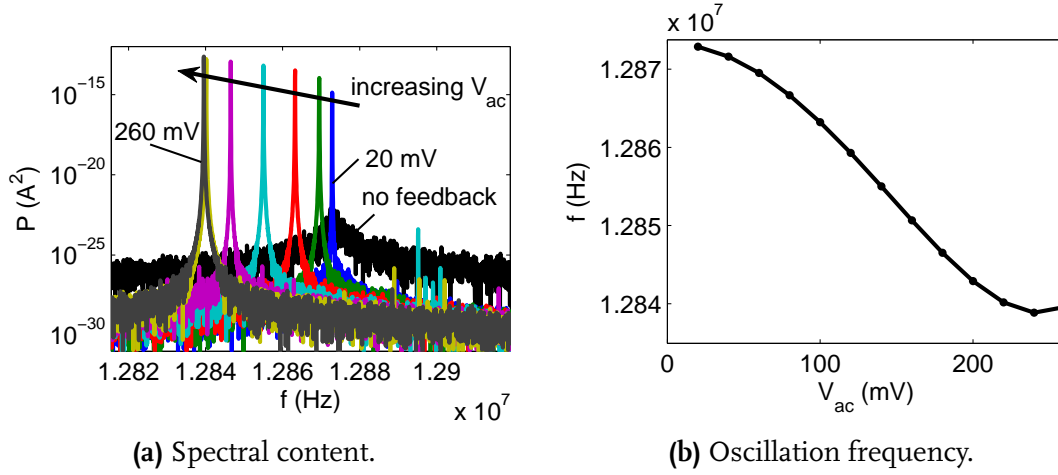


Figure 7.11 / Dependence on the saturation level V_{ac} .

responses of the oscillator for these saturation values have been calculated from the spectral content. The results are very similar to the response depicted in Figure 7.8. The oscillation frequency dependence on V_{ac} is depicted in Figure 7.11(b).

7.4.4 Influence of amplifier gain

Furthermore, the influence of the gain in the feedback amplifier has been investigated. The input to the amplifier is a current (i_{out}) and its output is a voltage, the V_{ac} input of the resonator. Therefore, the gain has a unit of V/A (Volt per Ampere).

By varying the gain in the feedback simulations, a threshold value for the gain has been determined: $G_A = 10^6$ V/A. Below this value, oscillations will not swing up. This high gain value results from the high motional resistance R_m of the resonator, see Section 7.4.2. In order to generate this amount of gain, a multi-stage amplifier will be needed. From a design perspective, another option would be to create resonators with much lower motional resistance values, by using larger electrode areas (thicker resonators) and smaller gaps.

7.4.5 Response up to dynamic pull-in

It is known from literature that MEMS resonators may exhibit dynamic pull-in (Nayfeh et al., 2007) under electrostatic forcing. Under resonance, the displacement amplitude of the MEMS beam may become large enough (x close to $\pm d_0$) for the electrostatic forcing $F_e(x, t)$ (3.2) to cause a collapse of the beam to one of the electrodes. For the open-loop response of the MEMS resonator, amplitude-frequency curves for two different V_{ac} values (500 and 635 mV) are depicted in Figure 7.12. Note that these are significantly higher V_{ac} -values than used sofar, see Figure 7.9. The inset in Figure 7.12 shows a zoom around the resonance frequency in which the upper turning point for

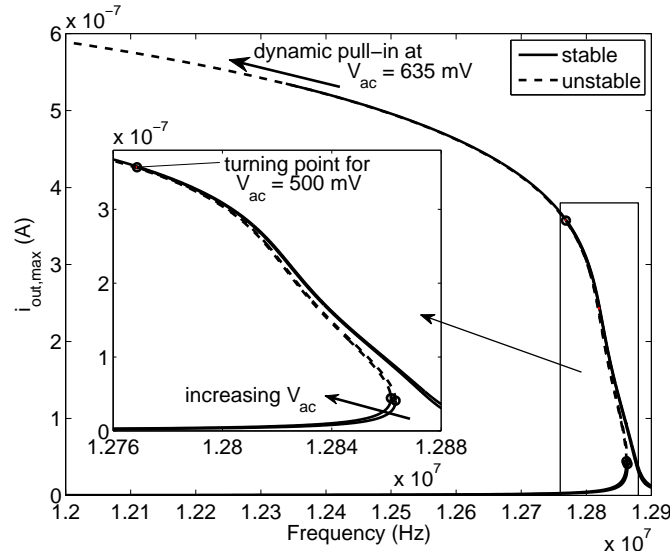


Figure 7.12 / Open-loop amplitude-frequency curve for the MEMS resonator for $V_{ac} = 500$ and 635 mV (dynamic pull-in).

$V_{ac} = 500$ mV is indicated. Dynamic pull-in has been found to occur at an ac excitation value of $V_{ac} = 635$ mV, which is indicated by the upper curve, labeled ‘dynamic pull-in’.

Phase feedback simulations have been performed for the same two V_{ac} values as in the open-loop case. An amplifier phase of $\psi_A = \pi$ rad has been used. Simulation results are shown in Figure 7.13, where the spectral content has been depicted. For $V_{ac} = 635$ mV, no dynamic pull-in is observed. It can be seen that, although the resonator does not exhibit dynamic pull-in in closed-loop, the spectral content deteriorates and shows side-bands compared to the results in Figure 7.11(a). This results in close-to-carrier side-bands in the phase noise response, which is undesired. These non-harmonic side-bands may result from an oscillator output that is no longer purely periodic. For instance, MEMS resonators have been reported to show chaotic behaviour close to pull-in values, see De and Aluru (2006).

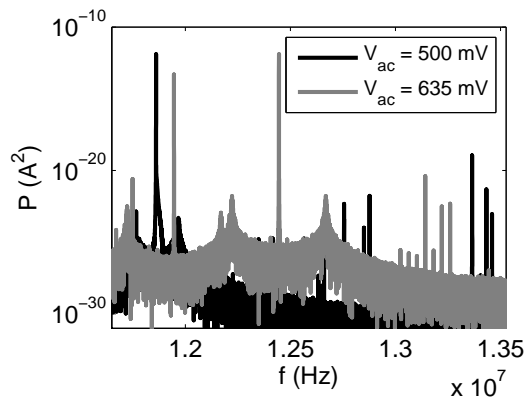


Figure 7.13 / Spectral content for two different V_{ac} values.

To conclude the analysis on dynamic pull-in, V_{ac} is increased to find the value at which the closed-loop system exhibits dynamic pull-in. This occurs at $V_{ac} = 2.3$ V, which is 3.6 times higher than the open-loop dynamic pull-in voltage. The time history of i_{out} for pull-in is shown in Figure 7.14.

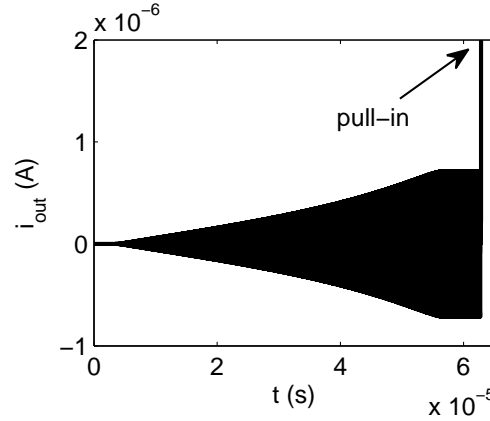


Figure 7.14 / Output current i_{out} during dynamic pull-in.

Summarizing, it can be concluded that phase feedback renders the system more robust with respect to dynamic pull-in than the open-loop case, since this occurs at higher voltages than in open-loop. However, with respect to the phase noise response, it is recommended to stay safely away from the open-loop pull-in excitation value.

7.5 Conclusion

The principle of phase feedback has been investigated for an oscillator circuit containing a nonlinear electrostatically actuated clamped-clamped beam MEMS resonator. The proposed approach is generally applicable to MEMS resonators whose dynamics can be described by a lumped Duffing-like model. A system level oscillator circuit model has been used, incorporating the device level clamped-clamped beam MEMS resonator model of Section 3.2. By means of an extensive simulation study, it has been shown that phase feedback is a powerful technique that allows for using such a nonlinear resonator in an oscillator circuit. Frequency-phase curves and power-phase curves are useful for selecting optimal operation points for the phase feedback in oscillator circuits. For the nonlinear clamped-clamped beam resonator with capacitive excitation and detection, an optimal feedback phase has been determined as $\psi_R = \pi$ rad. Furthermore, the influence of the saturation level and the gain in the circuit has been investigated. Additionally the closed-loop system has been found to be more robust with respect to dynamic pull-in than the open-loop system. However, the phase noise response deteriorates for large saturation values V_{ac} . For the proposed phase feedback approach, the control parameters amplifier phase ψ_A and saturation value V_{ac} provide a means for (fine-)tuning the frequency of

oscillation as well as the output power of the oscillator.

Based on the interesting and promising simulation results, it is recommended to experimentally investigate the described approach, in order to further validate and understand the phase feedback concept and its limitations. Furthermore, possible oscillator noise aliasing or upconversion effects stemming from nonlinearities in the resonator (see Kaajakari et al., 2005a) or from the presence of the saturation element in the oscillator circuit should be investigated. Additionally, an improved description of the amplifier part of the oscillator circuit has to be included.

Finally, other properties of the MEMS resonator based oscillator should be addressed, such as accuracy, long-term stability (aging) and temperature effects (see Section 2.3.2). Long-term stability is related to the vacuum encapsulation of the resonator. By means of long-term experiments, these effects can be addressed. Examples of experimental work in this field are documented in, for instance, Koskenvuori et al. (2004), Kaajakari et al. (2005b), Kim et al. (2005), Candler et al. (2006b) and Kim et al. (2007).

Conclusions and recommendations

Abstract / The main ideas and methods are recapitulated and conclusions with respect to the research objective are stated. Furthermore, recommendations for future work are given.

8.1 Conclusions

To recapitulate, the research objective of this thesis was to address the requirements for multiphysics modelling, stated in Section 1.2.4, with respect to the analysis of nonlinear dynamics in MEMS, see Section 1.2.3. Although the work has focussed on a specific class of MEMS, namely MEMS resonators, it is not restricted to this application field. The approach can also be applied to other fields, in which dynamics of the microstructure are of importance, such as MEMS (resonant) sensors, filters, switches and variable capacitors.

Various modelling approaches have been derived and have been presented in this thesis. They can be categorised into the modelling levels that are distinguished in the modelling of MEMS devices, see Figure 1.1.

Heuristic modelling (Chapter 3)

In Chapter 3 heuristic device level modelling has been applied to two case studies. In the first case study, a heuristic model has been proposed for an electrostatically actuated clamped-clamped beam MEMS resonator. Inspired by experimentally observed frequency hysteresis, a relatively simple, 1DOF Duffing-based dynamic model with electrostatic actuation has been proposed which typically may be capable of describing the observed nonlinear dynamic response of the resonator. The model, which has an a priori defined complexity in terms of the electrostatic actuation and its nonlinear stiffness function, is able to describe the measured behaviour relatively well for the excitation parameter settings used. However, at the same time, shortcomings of the model become clear, since subtle variations in the resonator response that are observed in the experiments can only

be described by fitting the model to each response.

In the second case study, partly heuristic modelling has been applied to a dog-bone MEMS resonator. The derived model, containing several heuristic elements, has proven to be unable to describe the experimentally observed mode coupling behaviour. The main reasons for this is the incorrect model structure with respect to the number of in-plane and out-of-plane modes together with the excitation mechanism for out-of-plane modes. Especially by using the lumped approach for the electrostatic actuation, essential effects (fringing fields, non-parallel electric field in the electrode gaps) are not modelled correctly. Furthermore, whether the proposed multi-model captures the experimentally observed behaviour, depends to a large extent on the number and type of modes that are included, which, in turn depends on the complexity and the specific type of resonator considered.

The observed shortcomings of the heuristic modelling approach for the two case studies serve as the motivation for the first-principles based approach that is described in Chapter 4.

First-principles based multiphysics modelling framework (Chapters 4, 5 and 6)

In Chapter 4, the multiphysics modelling framework for nonlinear dynamics of MEMS resonators has been presented. The philosophy behind the first-principles based modelling approach has been explained. The framework is intended for fast and accurate simulation of the nonlinear dynamic behaviour of MEMS resonators, thereby meeting the modelling requirements stated in Section 1.2.4. Based on a first-principles description and formulated at the physical modelling level for the involved physical domains (mechanical, electrical and thermal), the framework provides a straightforward approach for deriving reduced-order (or device level) models. Relevant physical effects can be included in the model in a systematic way. These effects may consist of couplings between different physical fields and may be linear or nonlinear of nature. Once the description at the physical level has been completed, a set of coupled PDEs has been obtained. Galerkin discretisation is applied to these PDEs in order to create reduced-order models of varying complexity, which are suited for fast and accurate simulation. Next, numerical simulation and validation with experiments can be performed. Experimental validation may lead to model refinements, related to the involved physical effects or to the number of basis functions included in the Galerkin discretisation.

The proposed multiphysics modelling approach has been applied to a full case study on a clamped-clamped beam MEMS resonator in Chapters 5 and 6, similar to the one investigated in Section 3.2. In Chapter 5, the modelling framework has been applied to derive models of varying level of complexity. For Galerkin discretisation, the undamped uncoupled eigenmodes of the PDEs are used as spatial basis functions. Validation of natural frequencies, modeshapes, thermoelastic damping and fringing field effects of the models has been performed by means of comparison with finite element simulations. A good match has been obtained, thereby justifying assumptions that have been made. Both for nonlinear static and nonlinear dynamic analysis, the derived models have been thoroughly compared with results from literature, yielding good correspondence.

In an extensive simulation study, the relevance of various physical effects has been addressed and an optimal model with respect to degrees of freedom and included physical effects has been chosen for the clamped-clamped beam MEMS resonator under investigation. For this MEMS resonator, nonlinear material effects have been determined to be irrelevant, whereas effects like rotary inertia and shear deformation (Timoshenko beam theory), fringing fields and thermoelastic damping have been shown to be relevant. Additionally, it has been observed that the overall dynamic behaviour of the clamped-clamped beam MEMS resonator still has a Duffing-like response, regardless of the physical effects included. This confirms that the heuristic model, used in case study I in Chapter 3, has been a good initial estimate for describing the dynamic behaviour. On the other hand, subtle differences and variations in the response can only be described using the first-principles based approach from Chapter 4.

In Chapter 6, the optimal model of Chapter 5 is validated experimentally. Furthermore, an improved (more accurate) description of the measurement circuit has been added to the model. Electrical parameters of the measurement circuit have to be determined experimentally. Next, extensive experimental validation of the simulation model has been performed for MEMS resonators with two different thickness values. Most model parameters have been obtained directly from actual physical dimensions of the MEMS resonator and from physical properties of single-crystal silicon. However, the electrical parameters of the measurement circuit, the beam length l (to correct for under-etching), the dimensions of the electrode gaps d_1 and d_2 and the Q -factor related to anchor loss have to be determined experimentally. A straightforward validation approach has been proposed in order to determine these parameters from experiments. A good correspondence between experimental and numerical nonlinear dynamic responses has been obtained, already for a 1DOF simulation model. In this way, confidence has been gained in the derived model and the multiphysics modelling approach has been validated. Contrary to the results of the heuristic model of Section 3.2, subtle variations in the response have now been captured. A major advantage of the model is that it is based on first principles, which results in a model description in terms of parameters that have actual physical meaning and can be related directly to resonator dimensions and material properties.

From these results, it can be concluded that the 1DOF model is sufficiently accurate, when compared to experimental results, and captures essential nonlinear dynamic behaviour for both small-amplitude and large-amplitude excitations. Furthermore, the model is in functional representation, since its parameters have actual physical meaning and exhibit correct dependencies on the resonator dimensions and material properties. The model is suited for fast and accurate simulation and is in accordance with the first and second law of thermodynamics. In this way, all of the modelling requirements of Section 1.2.4 have been met, such that the main research objective is achieved.

Phase feedback (Chapter 7)

In Chapter 7, an approach called phase feedback has been proposed for oscillator circuits incorporating nonlinear MEMS resonators. The heuristic model for the electrostatically

actuated clamped-clamped beam MEMS resonator, derived in Section 3.2, has been included in a system level simulation model for an oscillator circuit. By means of an extensive simulation study with this model, phase feedback has been shown to be a powerful technique that allows for inclusion of a MEMS resonator in an oscillator circuit, while the resonator can operate in its nonlinear regime. Optimal operation points for the oscillator circuit can be selected by setting the amplifier phase and the saturation value in the system according to frequency-phase and power-phase curves. Additionally, the closed-loop system has been found to be more robust with respect to dynamic pull-in than the open-loop system. The control parameters of the amplifier provide a means for (fine-)tuning both the oscillation frequency and the output power of the oscillator circuit.

8.2 Recommendations

In this section, some aspects are discussed that may be focused on in future work.

Multiphysics modelling framework

The first and most important recommendation for the multiphysics modelling framework is that it should be applied to various MEMS resonators that have been modelled with heuristic models up to now. Especially for the cases where experimental results are available, further validation of the modelling framework can take place and insight can be gained in physical parameters that influence the dynamic behaviour and the performance of MEMS resonators. For those MEMS resonators that have a geometrically simple shape, the framework can be applied in a relatively straightforward way. Heuristic models for such MEMS resonators are documented in, for instance, Mattila et al. (2002b), who describes a longitudinal resonator, in Kaajakari et al. (2004c), who describe a square plate resonator or in Hao et al. (2004), Pourkamali et al. (2004) and Lin et al. (2004), in which bulk mode disk resonators are described. Application of the modelling framework will provide more insight in the physical parameters that determine the performance of these resonators.

In the second case study in Chapter 3 (Section 3.3), a partly heuristic modelling approach has been applied to a dog-bone MEMS resonator, see also van den Hoven (2008). This resonator is also described in van Beek et al. (2007). The model of Section 3.3 is found to be unable to describe experimentally observed behaviour. A new modelling effort, in line with the framework presented in Chapter 4 should be undertaken, such that the mode coupling phenomenon is correctly captured.

Furthermore, the obtained model description and structure according to the multiphysics modelling framework depends to a large extent on the shape and type of the spatial basis functions that are used for Galerkin discretisation. For a resonator with a simple geometric shape, such as the clamped-clamped beam resonator of Chapter 5, the choice of basis functions is straightforward. However, for geometrically more complex microstructures, such as the dog-bone resonator, the choice of spatial basis functions is far from trivial.

In order to cope with this issue, an analytical or numerical procedure for determining and selecting base functions for geometrically complex structures is needed. In order to retain the first-principles nature of the modelling framework, in which actual physical parameters are present, the procedure should determine base functions in a parameterised description. In this way, the applicability of the modelling framework can be increased to geometrically (more) complex structures.

The modelling framework described in Chapter 4 includes the mechanical, electrical and thermal domains. For the MEMS resonators considered in this thesis, the inclusion of these three domains is found to be adequate. As stated before in Section 8.1, the modelling framework can also be applied to other fields in which the dynamics of microstructures are of interest: MEMS resonant filters, sensors and switches, for instance. Often, these MEMS devices are not operated in vacuum. Therefore, fluidic effects like flow, radiation and squeeze film damping are likely to be relevant, see for instance Senturia (2001), Veijola and Turowski (2001), Veijola (2004) or Kaajakari (2009). A logical step in the multiphysics modelling framework is to extend it with the fluidic domain and its related (multi)physical effects. Either first-principles based descriptions (PDEs) for these effects have to be included such that they can be Galerkin discretised in a similar way as is done currently, or functional descriptions for these effects can be added to the modelling framework. Inclusion of the fluidic domain imposes quite a challenge for the modelling framework, since (multiphysical) effects in the fluidic domain are inherently dissipative of nature. Therefore, their explicit dependency on the motion of the microstructure has to be taken into account.

An additional multiphysical extension to the modelling framework, the description of the thermal domain and its couplings with the other domains may be expanded. Namely, temperature effects, other than thermoelastic damping may be described, in which, for instance, mechanical, electrical and fluidic parameters depend on temperature as well. Especially for application of resonators in time reference oscillators, in which high-performance operation over a large range of temperatures is required, the thermal behaviour of the resonator is very important (Vig and Ballato, 1999).

A final recommendation with respect to the multiphysics modelling framework is the following. The analytical derivation of anchor loss, based on Hao et al. (2003) and Hao and Xu (2009) is found to result in a Q -factor that is significantly lower than the experimentally determined one. A possible for this is that their derivations are based on a semi-infinite substrate, into which stress waves are radiated. In order to investigate this and in order to derive a better description of anchor loss in the presence of non-semi-infinite substrates, more insight has to be gained into how reflected waves influence the loss mechanism. Understanding of anchor loss is very relevant for MEMS resonators, since, together with thermoelastic damping, this is one of the principal loss mechanisms for MEMS resonators that operate in vacuum.

Phase feedback

Finally, the concept of phase feedback has been investigated and evaluated entirely by numerical simulations. On simulation level, phase feedback is found to be a promising technique for using nonlinear MEMS resonators in oscillator circuits and for tuning their frequency and output power. Therefore, the concept and its limitations should be further validated and understood by means of experiments. Experimental validation allows for addressing possible noise aliasing effects (Kaajakari et al., 2005a) as well as accuracy, long-term stability and temperature effects (Koskenvuori et al., 2004; Kaajakari et al., 2005b; Kim et al., 2005; Candler et al., 2006a; Kim et al., 2007).

Silicon as an engineering material

Abstract / In this appendix, the structural, mechanical and thermal properties of silicon are described. Additionally, some information on manufacturing techniques is included as well as the derivation of the nonlinear Young's modulus under uni-axial homogeneous loading.

A.1 Structural and mechanical properties

Single-crystal silicon is increasingly employed in microelectromechanical devices, not only because of its electronic properties, but also because of its excellent mechanical properties (Petersen, 1982; Stemme, 1991). General overviews of its properties are given in Hull (1999) and INSPEC (1988), and references cited therein.

A.1.1 Crystal structure

Pure single-crystal silicon (element symbol Si) has an FCC crystal structure, in which each silicon atom is covalently bonded to four neighbouring atoms in a tetrahedral three-dimensional stacking, see Figure A.1. The three main crystal directions $[100]$, $[010]$ and

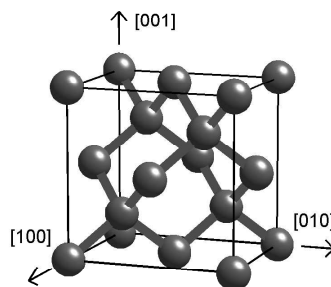


Figure A.1 / Silicon crystal unit cell.

[001] correspond with the edges of the unit cell. More background on crystal structures and crystallographic planes and directions can be found in Lovett (1989) and Callister (1999). The lattice parameter of the unit cell (edge dimension) equals $d = 0.54310644 \pm 0.00000008$ nm at a temperature of 22.5°C in vacuum (Hull, 1999). The density of silicon equals $\rho = 2329.00 \pm 0.08$ kg/m³ at 25°C (INSPEC, 1988).

A.1.2 Elastic properties

In contrary to polycrystalline silicon (poly-Si), the more or less isotropic equivalent of silicon, single-crystal silicon features anisotropic elastic properties. This means that its elastic behaviour depends on the orientation of the material. Due to the cubic crystal structure, special symmetry properties for the relevant elastic coefficients result. Additional background on theory on elasticity of solids and crystals can be found in, for instance, Nye (1985), Lovett (1989) and Sadd (2005).

Second-order elastic constants

The general form of Hooke's law for elasticity of three-dimensional solids can be given in index-notation as

$$\sigma_{ij} = C_{ijkl}\eta_{kl}, \quad (\text{A.1})$$

where σ_{ij} is the symmetric stress tensor, C_{ijkl} is the fourth-order elasticity tensor and η_{kl} is the symmetric Green-Lagrange strain tensor. For this notation, Einstein's summation convention is used, implying summation over all repeated indices. Relation (A.1) can also be written in terms of strain as a function of stress using the fourth-order compliance tensor S_{ijkl} :

$$\eta_{ij} = S_{ijkl}\sigma_{kl}. \quad (\text{A.2})$$

Because of symmetry considerations in the cubic crystal structure, the stress-strain relations (A.1) and (A.2) contain numerous superfluous terms. After taking symmetry into account, (A.1) can be written as:

$$\sigma_{ii} = C_{11}\eta_{ii} + C_{12}(\eta_{jj} + \eta_{kk}), \quad (\text{A.3a})$$

$$\tau_{ij} = C_{44}\gamma_{ij} \quad (i \neq j), \quad (\text{A.3b})$$

where σ_{ii} , τ_{ij} , η_{ii} and $\gamma_{ij} (= 2\eta_{ij})$, ($i, j = 1, 2, 3$) denote normal stress, shear stress, normal Green-Lagrange strain and shear Green-Lagrange strain, respectively. The indices 1, 2 and 3 correspond with the three principal directions, that is, they coincide with three orthogonal edges of the cubic unit cell, depicted in Figure A.1. Due to the cubic crystal structure, only three independent constants are present in (A.3): C_{11} , C_{12} and C_{44} . Similarly, (A.2) can be written as

$$\eta_{ii} = S_{11}\sigma_{ii} + S_{12}(\sigma_{jj} + \sigma_{kk}), \quad (\text{A.4a})$$

$$\gamma_{ij} = S_{44}\tau_{ij} \quad (i \neq j), \quad (\text{A.4b})$$

which contain three independent compliance coefficients. Contracted (or Voigt) notation¹ is used for the indices of the elastic constants C_{ij} and S_{ij} . The stiffness coefficients are related to the compliance coefficients by the following relations:

$$C_{11} = \frac{S_{11} + S_{12}}{(S_{11} - S_{12})(S_{11} + 2S_{12})}, \quad (\text{A.5})$$

$$C_{12} = \frac{-S_{12}}{(S_{11} - S_{12})(S_{11} + 2S_{12})}, \quad (\text{A.6})$$

$$C_{44} = \frac{1}{C_{44}}. \quad (\text{A.7})$$

Numerical values for the stiffness and compliance coefficients are listed in various references (McSkimin, 1953; McSkimin and Andreatch, 1964a,b; Hall, 1967; Goncharova et al., 1983). From an overview and comparison of these values, given in Hull (1999), the values of Hall (1967) are considered to be the most accurate. These are listed in Table A.1.

Table A.1 / Numerical values for stiffness and compliance coefficients at room temperature and atmospheric pressure (Hall, 1967). Errors are approximately $\pm 0.02\%$.

Stiffness	Value (Pa)	Compliance	Value (Pa^{-1})
C_{11}	$1.6564 \cdot 10^{11}$	S_{11}	$0.7691 \cdot 10^{-11}$
C_{12}	$0.6394 \cdot 10^{11}$	S_{12}	$-0.2142 \cdot 10^{-11}$
C_{44}	$0.7951 \cdot 10^{11}$	S_{44}	$1.2577 \cdot 10^{-11}$

The elastic properties vary with orientation of the cubic crystal (see for instance Date and Andrews, 1969; Turley and Sines, 1971; Brantley, 1973). Young's modulus E is defined as the ratio of stress to strain for a material that is stretched in a single direction, while it is free to move in the other directions. For instance, a stress σ_{11} , applied in direction 1, results in strain ε_{11} . Young's modulus is then $E = \frac{\sigma_{11}}{\varepsilon_{11}}$. Furthermore, due to stretching in this direction, contraction in other directions takes place. Poisson's ratio is defined as the ratio of side contraction to length extension $\nu_{12} = -\frac{\eta_{22}}{\eta_{11}}$ or $\nu_{13} = -\frac{\eta_{33}}{\eta_{11}}$.

To understand how Young's modulus and Poisson's ratio can be calculated, consider the following example, where the three principal directions of stress and strain are chosen along three orthogonal edges of the cubic unit cell. In this case, indices 1, 2 and 3 correspond with the [100], [010] and [001] directions, respectively. Assume that a stress σ_{11} is applied in [100] direction on the cubic unit cell and that all other applied stresses are zero. Either by solving (A.3a)–(A.3b) for η_{ii} or by using (A.4a)–(A.4b) directly, Young's modulus in [100] direction can be found:

$$E_{[100]} = \frac{\sigma_{11}}{\varepsilon_{11}} = \frac{1}{S_{11}} = C_{11} - 2C_{12} \frac{C_{12}}{C_{11} + C_{12}}. \quad (\text{A.8})$$

¹Contracted notation is a mapping for the indices: 11 \sim 1, 22 \sim 2, 33 \sim 3, 23 \sim 4, 13 \sim 5, 12 \sim 6.

In a similar way, Poisson's ratio becomes:

$$\nu_{[100]} = \nu_{12} = \nu_{13} = -\frac{S_{12}}{S_{11}} = \frac{C_{12}}{C_{11} + C_{12}}. \quad (\text{A.9})$$

Only in this specific case, it holds that $\nu_{12} = \nu_{13}$. However, in general, this is not the case and even $\nu_{ij} \neq \nu_{ji}$. If uniaxial stresses are applied in the 2 and 3 directions ([010] and [001] directions, respectively), similar expressions for Young's modulus and Poisson's ratio result. This is due to the cubic crystal symmetry.

Figure A.2 shows the dependence of Young's modulus E on the direction within the unit cell. Young's modulus is depicted as a surface and its value in an arbitrary direction is given by the distance from this surface to the origin (0,0,0). From the figure, it can be

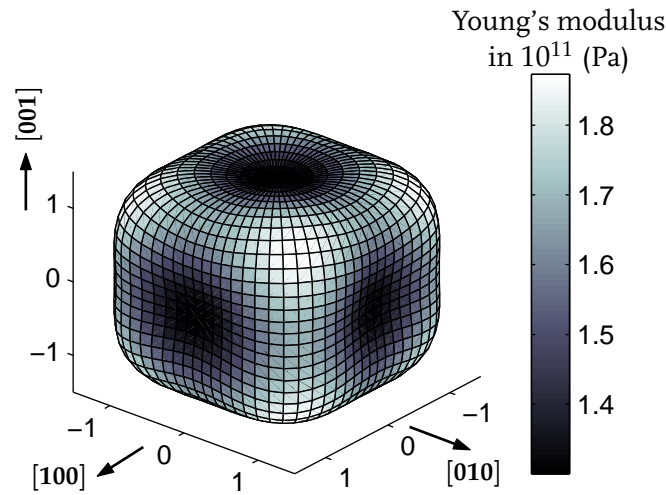


Figure A.2 / Young's modulus of single-crystal silicon as a function of the direction in the cubic crystal. The value of Young's modulus, indicated in grey scale, is given by the distance from the surface to the origin.

seen that Young's modulus varies from a minimum value of 130 GPa in $\langle 100 \rangle$ direction to approximately 188 GPa in $\langle 111 \rangle$ direction. Therefore, the elastic properties of a resonator, constructed from single-crystal silicon, depend on how the resonator is cut from the bulk material. Cut-directions are usually specified in terms of crystallographic planes, see, for instance, Lovett (1989) for more information.

In-plane elastic properties of the crystal may also be calculated. As an example, consider Figure A.3, in which Young's modulus and Poisson's ratio are depicted as a function of direction in the (100) plane, specified by an angle ranging from 0 to 90 degrees. This figure is constructed by defining a rotational transformation, such that the first coordinate axis (1) of the rotated coordinate system is perpendicular to the plane of interest (the [100] direction is normal to the (100) plane). Next, rotation about this axis is performed to obtain the directional dependence of the in-plane elastic properties. The other axes are chosen orthogonal to each other in the plane of interest. For the example considered

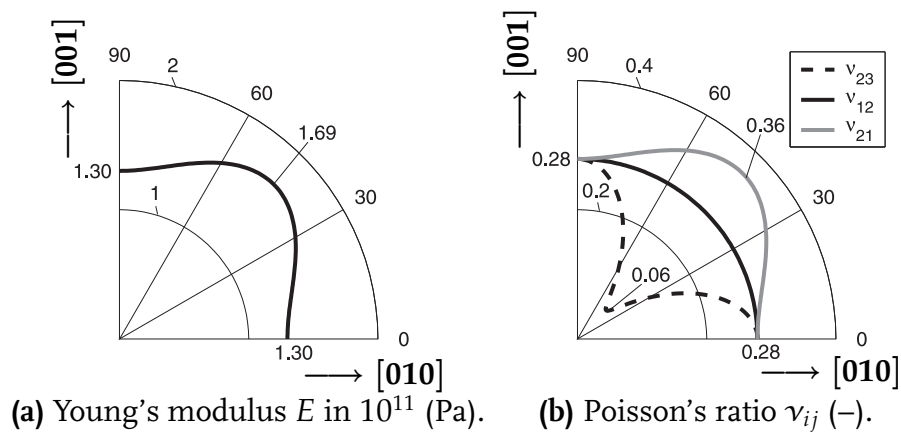


Figure A.3 / Variation of Young's modulus and Poisson's ratio with orientation in the (100) plane. Poisson's ratios are depicted for both in-plane and out-of-plane values.

here, for an angle of 0 degrees, the 1-axis corresponds with the [100] direction, the 2-axis with the [010] direction and the 3-axis with the [001] direction (see also Figure A.1). The radial direction in Figure A.3 specifies the magnitude of the quantity considered. Due to cubic crystal symmetry, only the first quadrant of each plane is depicted. Furthermore, the plot for Poisson's ratio (Figure A.3(b)) contains three different curves. The ν_{12} and ν_{21} curves show Poisson's ratio between one of the two in-plane directions and the direction normal to the plane and vice versa. For instance, in case of zero rotation angle, ν_{21} is the ratio of side contraction in [100] direction to length extension in [010] direction, whereas ν_{12} is the ratio of [010] contraction to [100] elongation. Here, it is seen that, in general, $\nu_{12} \neq \nu_{21}$. The curve for ν_{23} shows the in-plane dependence of Poisson's ratio. In case of zero rotation angle, this means, length extension in [010] direction versus side contraction in [001] direction.

Third-order elastic constants

In classical elasticity theory, strains and deformations are assumed to be infinitesimal. As a result, the strain energy function is a homogeneous quadratic function of the strains (Lovett, 1989; Hearmon, 1961), see also Section A.4. Non-linear elasticity theory describes the non-linear effects in the material behaviour for elastic deformations that are no longer finite (see Murnaghan, 1951; Hearmon, 1953; Zarembko and Krasil'nikov, 1971; Hiki, 1981). On the one hand, these non-linearities arise because the components of the strain tensor are no longer linearly related to the displacement gradients. This feature of finite strain does not depend on the physical properties of the material considered and is, therefore, usually termed a geometrical non-linearity. On the other hand, a physical non-linearity is present, which arises from the fact that the internal (or strain) energy of the deformed solid is not purely a quadratic function of the invariants of the strain tensor, but also a cubic one, etc. This physical non-linearity is determined by elastic moduli of third and higher order. The existence of both non-linearities results in a deviation of linear Hooke's law. In general, both the physical and geometrical non-linearity are present and, therefore, they are usually considered simultaneously, see for instance, Seeger and Buck

(1960) and Hiki (1981).

From literature (Hearmon, 1961; Every and McCurdy, 1992), it becomes clear, that crystals with cubic symmetry have 6 third-order elastic constants. Measurements of these constants have been performed by McSkimin and Andreatch (1964b) and Hall (1967) (see also Section A.1.5). The data of Hall (1967) for pure silicon are considered to be most accurate (Hull, 1999) and are listed in Table A.2. These third-order constants describe the

Table A.2 / Numerical values for the third-order stiffness coefficients of pure silicon at 298 K (Hall, 1967).

Constant	Value (Pa)	Accuracy (Pa)
C_{111}	$-7.95 \cdot 10^{11}$	$\pm 0.10 \cdot 10^{11}$
C_{112}	$-4.45 \cdot 10^{11}$	$\pm 0.10 \cdot 10^{11}$
C_{123}	$-0.75 \cdot 10^{11}$	$\pm 0.05 \cdot 10^{11}$
C_{144}	$0.15 \cdot 10^{11}$	$\pm 0.05 \cdot 10^{11}$
C_{166}	$-3.10 \cdot 10^{11}$	$\pm 0.05 \cdot 10^{11}$
C_{456}	$-0.86 \cdot 10^{11}$	$\pm 0.05 \cdot 10^{11}$

strain dependence of the second-order elastic constants. In generic form, stress component σ_{ij} can be expanded as $\sigma_{ij} \propto C_{ijkl}\eta_{kl} + \frac{1}{2}C_{ijklmn}\eta_{kl}\eta_{mn} + \dots$, but for more details see Appendix A.4 and equation (A.37). In lumped models for the material behaviour, the effect will show up as a non-linear stiffness (see for instance Kim and Sachse, 2000). The effect of third-order elastic constants for silicon under uni-axial homogeneous loading will be described in Section A.4.

A.1.3 Intrinsic losses

The Q -factor of a silicon microdevice depends on various dissipation mechanisms. Only internal material losses are related to the material directly. The intrinsic Q -factor depends on the purity (see also Section A.1.4), the amount of dislocations and the thermoelastic losses of the material (Stemme, 1991). Thermoelastic losses are due to irreversible heat conduction induced by, for instance, flexural motion of a mechanical component. Low-level impurity single-crystal silicon resonators can have Q -factors up to 10^6 . This value decreases with the amount of doping. Polycrystalline materials have lower Q -factors than single crystal materials. If a single-crystal material, such as silicon, is used, the contribution of the intrinsic material losses can often be considered negligible (Stemme, 1991), since other dissipation mechanisms dominate the response.

A.1.4 Effect of impurities

Impurities are always present to some extent in silicon in the form of atoms of different type than silicon. As these atoms have a smaller or larger atomic radius than the parent

lattice atoms, their presence results in contraction or expansion of the crystal unit cell in proportion to their concentration. The most frequent undesired impurities in silicon are carbon and oxygen. For large amounts of impurities, even the density of the material may change.

In addition to carbon and oxygen impurities, so-called dopant impurities are normally added intentionally to silicon. Namely, silicon is a semiconductor material (with 4 valence electrons), whose electric behaviour depends on the amount of electrons and holes (electron deficiencies) in the material. By adding impurities with a different number of valence electrons (dopants), the electric properties can be influenced. Atoms with 5 valence electrons produce *n*-type (negatively charged) semiconductors by providing additional electrons whereas atoms with 3 valence atoms result in *p*-type (positive) semiconductors containing additional electron deficiencies, or holes. As explained by Keyes (1976), elastic properties of semiconductors depend on the carrier concentration (amount of electrons). As a result, elastic constants may change significantly with electronic doping concentration. For instance, the influence of doping was investigated by Hall (1967) for *n*-type silicon and by Mason and Bateman (1964) for *p*-type silicon. It is difficult to precisely quantify the effect of doping. However, in general, it can be stated that the typical effect of heavy doping is to decrease the second-order constants C_{ij} by 1–3% and to modify the temperature dependencies. Third-order constants may change in much larger proportions.

A.1.5 Measurement techniques

As has become clear from the previous Sections, the elastic properties of silicon are very important since they characterise the material response. Furthermore, they depend on the direction within the crystal and they vary with both temperature and doping level.

Several different methods are available for measuring the elastic properties of silicon, allowing for determination of both second-order and third-order elastic constants (Every and McCurdy, 1992; Willardson et al., 1992). These will be described next.

Ultrasonic wave propagation

In this method, ultrasonic wave velocity is measured in small specimens of silicon with respect to various wave propagation directions. This method is based on the fact that a pulse of ultrasonic waves (either longitudinal or transverse), started in a material specimen, will reflect at the boundary interfaces of the specimen. By varying the frequency of the induced waves, in-phase and out-of-phase conditions take place, due to reflection of waves with a certain propagation velocity. If the density of the material is also known, elastic moduli or stiffnesses of the material can be calculated. Moreover, the variation of ultrasonic wave velocity with applied stress or strain reveals higher-order effects. Namely, third-order elastic constants translate to strain (or stress) dependence of the second-order coefficients.

Between 1950 and 1970, the mathematical framework for both second- and third-order elastic constants of materials has been established and numerous measurements of these parameters have been performed. The method has been used frequently, under a variety of conditions (both temperature and pressure dependency of elastic moduli has been investigated) and is described in detail in, for instance, McSkimin (1950), McSkimin (1953), Seeger and Buck (1960), McSkimin (1961), Mason and Bateman (1964), McSkimin and Andreatch (1964a), McSkimin and Andreatch (1964b), Thurston and Brugger (1964), Hiki (1981) and Goncharova et al. (1983). The method described in these references, has been the most important measurement method in the past, since it is a method by which a great majority of third-order stiffnesses have been measured (see Every and McCurdy, 1992), and it is the only one which, on its own, can yield a complete set of third-order constants.

Static tensile test

In static tensile tests, the deviation from linear Hooke's law can be determined by measuring the stress-strain relation of a specimen (Seeger and Buck, 1960; Hiki, 1981). This method requires careful preparation, since the elastic non-linearity can mainly be observed in tensile tests on very thin whiskers (thin single-crystal wires), having very high yield strength. If specimens of different orientation are available, orientation dependence can also be determined. However, this method does not yield a complete set of parameters, but is more suited to determine the elastic properties in a single direction of interest. Furthermore, very precise measurements of force and dimensional changes of the specimen are needed, since calculation of Young's modulus requires differentiation of stress with respect to strain, which, in turn, requires differentiation of displacement with respect to specimen dimension. As a result, the method has only a very limited accuracy.

Material parameter extraction

A third method for determining the elastic properties of silicon is by measuring resonant frequencies or pull-in voltages of dedicated and accurately defined microstructures. For instance, in Zhang et al. (1990), resonant microstructures are used and in Osterberg (1995) and Osterberg and Senturia (1997), the pull-in voltage is used for electrostatically actuated microstructures. The measured resonance frequencies or pull-in voltages can be compared to calculated theoretical ones, thereby providing an expression for extracting an approximation for relevant material parameters of the structure. Like the static tensile test method, discussed previously, this method does not yield a complete set of elastic constants, but can be used to determine an accurate representative non-linear stiffness relation for a certain vibration mode or structure of interest. Since the method makes use of actual devices, it is very suited for direct (on-wafer) measurements. Moreover, even some dedicated microstructures (with certain representative geometrical layouts) can be designed to serve as test structures for determining material parameters.

A.2 Thermal properties

A general overview of the thermal properties of silicon is presented in Hull (1999). Some properties that are relevant for the work in this thesis, mainly related to thermoelastic damping, will be described next. Values for the properties will be taken at a temperature around 25°C. Additionally, the influence of temperature on the elastic constants, described in Section A.1.2, will be discussed.

A.2.1 Specific heat

The specific heat c_p of single-crystal silicon at a constant pressure is tabulated in Hull (1999). For the work on thermoelastic damping, the value at 300 K (27°C) will be used:

$$c_p = 713 \text{ J kg}^{-1} \text{ K}^{-1}. \quad (\text{A.10})$$

A.2.2 Thermal expansion coefficient

The material parameters of silicon change with temperature. Thermal expansion/contraction takes place as well as change in elastic constants as a function of temperature. Experimental determination of the temperature dependence of the silicon lattice parameter (see Section A.1.1) has been described in Okada and Tokumaru (1984). Here, the following empirical relation for the linear thermal expansion coefficient has been determined, valid for temperatures between 120 K and 1500 K:

$$\alpha(T) = 3.725 \cdot 10^{-6} [1 - \exp(-5.88 \cdot 10^{-3}(T - 124))] + 5.548 \cdot 10^{-10} T \text{ K}^{-1}. \quad (\text{A.11})$$

The accuracy of this description is about $2 \cdot 10^{-7} \text{ K}^{-1}$. The value for the linear thermal expansion coefficient of silicon at a temperature of 300 K is given by Hull (1999) as

$$\alpha = 2.616 \cdot 10^{-6} \text{ K}^{-1}. \quad (\text{A.12})$$

The thermal expansion coefficient for the three principal directions in the crystal, see Figure A.1, is the same and equals the one given in (A.12). In shear direction, no thermal expansion occurs.

A.2.3 Thermal conductivity

In general, the thermal conductivity k of single-crystal silicon exhibits a temperature dependence characteristic of single-crystal dielectric materials (Hull, 1999). Furthermore, there is no directional dependence for this quantity. The value of k listed for a temperature of 300 K equals

$$k = 156 \text{ W m}^{-1} \text{ K}^{-1}. \quad (\text{A.13})$$

A.2.4 Temperature influence on elastic constants

The temperature effects on the second-order elastic constants C_{ij} of silicon have been investigated by McSkimin (1953) in the range of 77–300 K, by Hall (1967) in the range 4.2–310 K and by Burenkov and Nikanorov (1974) up to 1273 K. From these references, it is found that between 150 and 1000 K, the decrease of C_{ij} is fairly linear with increasing temperature. Rates reported in literature (Burenkov and Nikanorov, 1974) are:

$$\frac{1}{C_{11}} \frac{dC_{11}}{dT} = -9.3 \cdot 10^{-5} \text{ K}^{-1}, \quad (\text{A.14})$$

$$\frac{1}{C_{12}} \frac{dC_{12}}{dT} = -9.8 \cdot 10^{-5} \text{ K}^{-1}, \quad (\text{A.15})$$

$$\frac{1}{C_{44}} \frac{dC_{44}}{dT} = \begin{cases} -1.0 \cdot 10^{-4} \text{ K}^{-1}, \\ -7.3 \cdot 10^{-5} \text{ K}^{-1}. \end{cases} \quad (\text{A.16})$$

For constant C_{44} , two different measurements have been made, which is the reason that two values are listed in (A.16).

Information on the effect of temperature on third-order stiffness (see Table A.2) is fragmentary and not measured accurately. General trend is that the values increase (become less negative) for increasing temperature (Every and McCurdy, 1992). However, when considered in relation to the measurement errors, the effect is relatively small.

A.3 Manufacturing techniques

Manufacturing processes for microstructures bear a similarity to conventional machining in the sense that the objective is to precisely define arbitrary features in or on a block of material. However, some important differences are the following. Firstly, micromachining is a parallel or batch process in which dozens to tens of thousands of identical elements are fabricated simultaneously on the same wafer. Furthermore, in some processes, dozens of wafers are processed at the same time. Another key difference is the characteristic feature dimension, which is in the order of one micrometer for microstructures. This is one to two orders of magnitude smaller than what can be achieved by conventional machining techniques.

From the mechanical and thermal properties, discussed in the previous sections, it has become clear that high-quality single-crystal silicon, forms a promising material for microdevices. Although silicon is an intrinsically strong material, the actual properties of a particular mechanical component strongly depend on the crystallographic orientation and geometry, the number and size of surface, edge and bulk imperfections, and the stresses introduced and accumulated during growth, polishing and subsequent processing. Proper accounting for these conditions will result in high-quality mechanical components with accurately known mechanical properties.

Usually, a combination of deposition, patterning and etching steps is repeated until completion of the microstructure is achieved. For an overview of the wide variety of

manufacturing techniques, the reader is referred to Petersen (1982), Senturia (2001), Maluf and Williams (2004) and Allen (2005).

A.4 Effect of third-order elastic constants

As already indicated in Section A.1.2, nonlinear material effects in silicon are both physical and geometrical of nature. The material presented in this section is based on Kaplan (1931), Birch (1947), Hearmon (1953), Seeger and Buck (1960), Brugger (1964), Zarembko and Krasil'nikov (1971), Hiki (1981), Every and McCurdy (1992), and Kim and Sachse (2000). In Sections A.4.1 and A.4.2, the difference between linear and nonlinear elasticity theory will be explained. Finally, in Section A.4.3, the nonlinear Young's modulus will be derived for the case of homogeneous uni-axial loading.

A.4.1 Linear elasticity

As has become clear from Appendix A.1.2, the three-dimensional relation between stress and strain of an elastic body is given by the generalised Hooke's law (A.1), containing second-order tensors σ_{ij} and ε_{kl} . The strain tensor contains elements, related to the partial derivatives of displacements u_i , ($i = 1, 2, 3$) of material points with respect to their position vector x_i , ($i = 1, 2, 3$). In linear elasticity theory, the so-called infinitesimal linear strain tensor (see Hiki, 1981; Sadd, 2005) is used, which is the linear part of the Green-Lagrange strain tensor E (which will be discussed in the next section). Its components are given by

$$\varepsilon_{ij} = \frac{1}{2} \left(\frac{\partial u_i}{\partial x_j} + \frac{\partial u_j}{\partial x_i} \right). \quad (\text{A.17})$$

Only linear terms are present in (A.17), as displacement gradients are assumed to be infinitesimally small. Therefore, terms containing products of deformation gradients do not appear. When an elastic body is deformed, the work $d\mathcal{W}$ done per unit volume by the external forces and the energy \mathcal{U} stored per unit volume are given by

$$d\mathcal{W} = \sigma_{ij} d\varepsilon_{ij}, \quad (\text{A.18})$$

$$\mathcal{U} = \frac{1}{2} C_{ijkl} \varepsilon_{ij} \varepsilon_{kl}. \quad (\text{A.19})$$

A.4.2 Nonlinear elasticity

In non-linear elasticity, displacements are no longer assumed to be infinitesimally small. As a result, non-linear terms show up in the strain tensor, as can be seen in the components of the non-linear Green-Lagrange strain tensor E :

$$\eta_{ij} = \frac{1}{2} \left(\frac{\partial u_i}{\partial a_j} + \frac{\partial u_j}{\partial a_i} + \frac{\partial u_k}{\partial a_i} \frac{\partial u_k}{\partial a_j} \right), \quad (\text{A.20})$$

where a_i denotes the position before deformation (undeformed, or natural state). The Green-Lagrange strain is referred to the undeformed state, whereas the stress σ_{ij} , mentioned before, is defined as the force per unit area in the deformed body. As a result, (A.18) no longer holds when the higher-order effect is taken into account. Due to this difference, a different tensor quantity, the so-called thermodynamic tension, has to be introduced, which is related to the engineering stress σ_{ij} . Hence the work done per unit volume becomes

$$d\mathcal{W} = t_{ij}d\eta_{ij}, \quad (\text{A.21})$$

with the thermodynamic tension t_{ij} related to the engineering stress as follows

$$t_{ij} = J \frac{\partial a_i}{\partial x_k} \frac{\partial a_j}{\partial x_l} \sigma_{kl}, \quad (\text{A.22})$$

where x_i denotes the position after deformation and J is the dilatation factor or the determinant of a 3×3 matrix containing the elements

$$J_{ij} = \frac{\partial x_i}{\partial a_j} = \delta_{ij} \lambda_i \quad (i \text{ not summed}). \quad (\text{A.23})$$

In (A.23), λ_i is the principal stretch which can be related to the principal Lagrangian strains η_i ($\eta_i = \eta_{ij} \delta_{ij}$, $i = 1, 2, 3$) by

$$\eta_i = \frac{1}{2}(\lambda_i^2 - 1). \quad (\text{A.24})$$

Various thermodynamic functions can be defined by choosing either t_{ij} or η_{ij} and T (temperature) or S (entropy) as independent variables. For instance, the internal energy $\mathcal{U}(\eta_{ij}, S)$ and the Helmholtz free energy $\mathcal{F}(\eta_{ij}, T) = \mathcal{U} - TS$ are given in differential form as (see Brugger, 1964; Hiki, 1981)

$$d\mathcal{U} = \frac{1}{\rho_a} t_{ij} d\eta_{ij} + T dS, \quad (\text{A.25})$$

$$d\mathcal{F} = \frac{1}{\rho_a} t_{ij} d\eta_{ij} - S dT, \quad (\text{A.26})$$

where \mathcal{U} , \mathcal{F} and S are per unit mass of the material and ρ_a is the material density in natural state.

According to Brugger (1964), the formal thermodynamic definition of adiabatic ($S = \text{constant}$) and isothermal ($T = \text{constant}$) elastic constants of second order is

$$C_{ijkl}^S = \left(\frac{\partial t_{ij}}{\partial \eta_{kl}} \right)_S = \rho_a \left(\frac{\partial^2 \mathcal{U}}{\partial \eta_{ij} \partial \eta_{kl}} \right)_S, \quad (\text{A.27})$$

$$C_{ijkl}^T = \left(\frac{\partial t_{ij}}{\partial \eta_{kl}} \right)_T = \rho_a \left(\frac{\partial^2 \mathcal{F}}{\partial \eta_{ij} \partial \eta_{kl}} \right)_T. \quad (\text{A.28})$$

Upon ignoring the difference between adiabatic and isothermal conditions, these constants can be regarded as the same constants that appear in linear elasticity (A.1). The expressions (A.27) and (A.28) can be extended to define higher (n^{th}) order elastic constants:

$$C_{ijklmn\dots}^S = \rho_a \left(\frac{\partial^n \mathcal{U}}{\partial \eta_{ij} \partial \eta_{kl} \partial \eta_{mn} \dots} \right)_S, \quad (\text{A.29})$$

$$C_{ijklmn\dots}^T = \rho_a \left(\frac{\partial^n \mathcal{F}}{\partial \eta_{ij} \partial \eta_{kl} \partial \eta_{mn} \dots} \right)_T. \quad (\text{A.30})$$

By combining (A.27) and (A.29), the third-order adiabatic stiffness can also be written as

$$C_{ijklmn}^S = \rho_a \left(\frac{\partial^3 \mathcal{U}}{\partial \eta_{ij} \partial \eta_{kl} \partial \eta_{mn}} \right)_S = \left(\frac{\partial C_{ijkl}^S}{\partial \eta_{mn}} \right)_S, \quad (\text{A.31})$$

which means that the third-order elastic constant describes the strain dependence of the second order stiffness constant. By using the expressions (A.27)–(A.30), the internal energy \mathcal{U} and the free energy \mathcal{F} of an elastic body can be expanded in a Taylor series about the natural state:

$$\rho_a \mathcal{U}(\eta_{ij}, S) = \rho_a \mathcal{U}(0, S) + \frac{1}{2} C_{ijkl}^S \eta_{ij} \eta_{kl} + \frac{1}{6} C_{ijklmn}^S \eta_{ij} \eta_{kl} \eta_{mn} + \dots, \quad (\text{A.32})$$

$$\rho_a \mathcal{F}(\eta_{ij}, T) = \rho_a \mathcal{F}(0, T) + \frac{1}{2} C_{ijkl}^T \eta_{ij} \eta_{kl} + \frac{1}{6} C_{ijklmn}^T \eta_{ij} \eta_{kl} \eta_{mn} + \dots \quad (\text{A.33})$$

Furthermore, the thermodynamic stresses t_{ij}^a can be related to the natural state by (Kim and Sachse, 2000):

$$t_{ij}^a = \rho_a \left(\frac{\partial \mathcal{U}}{\partial \eta_{ij}} \right)_S = \rho_a \left(\frac{\partial \mathcal{F}}{\partial \eta_{ij}} \right)_T. \quad (\text{A.34})$$

In general, the fourth-order tensor, containing the second-order elastic constants C_{ijkl} , has 81 ($= 3^4$) components and the sixth-order tensor containing the third-order constants C_{ijklmn} has 729 ($= 3^6$) distinct components. However, due for materials with a cubic crystal structure, the number of constants reduces to 3 second-order constants C_{11} , C_{12} and C_{44} and 6 third-order constants C_{111} , C_{112} , C_{123} , C_{144} , C_{166} and C_{456} (see for instance Hearmon, 1961; Every and McCurdy, 1992). Furthermore, for cubic crystals, the constants obey the following symmetry relations for the second-order constants:

$$C_{11} = C_{22} = C_{33}, \quad (\text{A.35a})$$

$$C_{12} = C_{21} = C_{13} = C_{31} = C_{23} = C_{32}, \quad (\text{A.35b})$$

$$C_{44} = C_{55} = C_{66}, \quad (\text{A.35c})$$

and for the third-order constants:

$$C_{111} = C_{222} = C_{333}, \quad (\text{A.36a})$$

$$C_{112} = C_{113} = C_{122} = C_{133} = C_{223} = C_{233}, \quad (\text{A.36b})$$

$$C_{123} = C_{123}, \quad (\text{A.36c})$$

$$C_{144} = C_{255} = C_{366}, \quad (\text{A.36d})$$

$$C_{166} = C_{155} = C_{244} = C_{266} = C_{344} = C_{355}, \quad (\text{A.36e})$$

$$C_{456} = C_{456}. \quad (\text{A.36f})$$

A.4.3 Nonlinear Young's modulus for homogeneous uni-axial loading

For the case of homogeneous uni-axial loading, the nonlinear Young's modulus can be calculated using the theory from Section (A.4.2), see, for instance Kim and Sachse (2000).

Consider a specimen that is loaded in the 1-direction only. A principal strain $\eta_1 = \eta_{11}$ results, yielding a principal stretch λ_1 , see also (A.23)–(A.24). The principal strains in the other two directions equals $\eta_2 = \eta_{22} = \eta_{33} = \eta_3$, with corresponding principal stretch $\lambda_2 = \lambda_3$.

Rewrite (A.22) to find σ_{ij} in terms of t_{kl} . Next, use (A.23), substitute (A.32) into the expression for t_{ij} (A.34) and use this in the equation found for σ_{ij} to obtain the expression for stress σ_{ij}^x at a deformed point x in terms of the engineering strains:

$$\sigma_{ij}^x = \frac{1}{\lambda_1 \lambda_2^2} \lambda_i \lambda_j \left(C_{ijkl} \eta_{kl} + \frac{1}{2} C_{ijklmn} \eta_{kl} \eta_{mn} \right). \quad (\text{A.37})$$

For uni-axial loading, only the principal stress in 1-direction is nonzero: $\sigma_1 = \sigma_{11} = \sigma$ and $\sigma_{22} = \sigma_{33} = 0$. Using this in (A.37), the following is obtained:

$$\sigma_1 = \sigma = \frac{\lambda_1}{\lambda_2^2} \left(C_{1k} \eta_k + \frac{1}{2} C_{1kl} \eta_k \eta_l \right), \quad (\text{A.38a})$$

$$\sigma_2 = 0 = \frac{1}{\lambda_1} \left(C_{2k} \eta_k + \frac{1}{2} C_{2kl} \eta_k \eta_l \right), \quad (\text{A.38b})$$

$$\sigma_3 = 0 = \frac{1}{\lambda_1} \left(C_{3k} \eta_k + \frac{1}{2} C_{3kl} \eta_k \eta_l \right). \quad (\text{A.38c})$$

By using $\lambda_i = \sqrt{1 + 2\eta_i}$ (A.24) and $\eta_2 = \eta_3$, (A.38a)–(A.38c) can be rewritten to two nonlinear equations

$$\frac{\sqrt{1 + 2\eta_1}}{1 + 2\eta_2} \left\{ C_{11} \eta_1 + 2C_{12} \eta_2 + \frac{1}{2} [C_{111} \eta_1^2 + C_{112} (2\eta_2^2 + 4\eta_1 \eta_2) + 2C_{123} \eta_2^2] \right\} = \sigma, \quad (\text{A.39a})$$

$$C_{12} \eta_1 + (C_{11} + C_{12}) \eta_2 + \frac{1}{2} [C_{111} \eta_2^2 + C_{112} (\eta_1^2 + 3\eta_2^2 + 2\eta_1 \eta_2) + 2C_{123} \eta_1 \eta_2] = 0, \quad (\text{A.39b})$$

which have to be solved in order to obtain the relation between σ and η_1 :

$$\sigma = \eta_1 \underbrace{(E_0 + E_1 \eta_1 + E_2 \eta_1^2 + E_3 \eta_1^3 + \dots)}_{E(\eta_1)}. \quad (\text{A.40})$$

The term in brackets in (A.40) denotes the nonlinear Young's modulus $E(\eta_1)$. In Kim and Sachse (2000), a power series solution for (A.40), containing terms up to E_2 is obtained by solving (A.39) symbolically. The expressions are:

$$E_0 = C_{11} - 2\nu_0 C_{12}, \quad (\text{A.41a})$$

$$E_1 = E_0(1 + 2\nu_0) + C_{12}\left(\frac{h_3}{\nu_0} - 3h_1 - 6\nu_0 h_1 + 3\nu_0 h_2 - 2\nu_0^2 h_3\right), \quad (\text{A.41b})$$

$$E_2 = E_0(2\nu_0 + 4\nu_0^2 + 2\nu_0 g_1 - \frac{1}{2}) + C_{12}\left[\left(\frac{1}{\nu_0} + 2\right)(h_3 - 3\nu_0 h_1 - 6\nu_0^2 h_1 + 3\nu_0^2 h_2 - 2\nu_0^3 h_3) - 2\nu_0(2h_1 g_1 - h_2 g_1 + g_2)\right], \quad (\text{A.41c})$$

with help variables

$$\nu_0 = \frac{C_{12}}{C_{11} + C_{12}}, \quad (\text{A.42a})$$

$$h_1 = \frac{C_{112}}{2C_{12}}, \quad h_2 = \frac{C_{112} + C_{123}}{C_{11} + C_{12}}, \quad h_3 = \frac{C_{111} + 3C_{112}}{2(C_{11} + C_{12})}, \quad (\text{A.42b})$$

$$g_1 = h_1 - h_2 + \nu_0 h_3, \quad g_2 = h_2^2 - h_1 h_2 + \nu_0 h_3(2h_1 - 3h_2) + 2\nu_0^2 h_3^2. \quad (\text{A.42c})$$

The expression for E_0 in (A.41a) corresponds with the linear Young's modulus in [100] direction, see (A.8).

Alternatively, (A.39) can be solved numerically for η_1 and η_2 as a function of σ , using the second- and third-order constants for silicon from Tables A.1 and A.2. The result of this numerical calculation is depicted in Figure A.4.

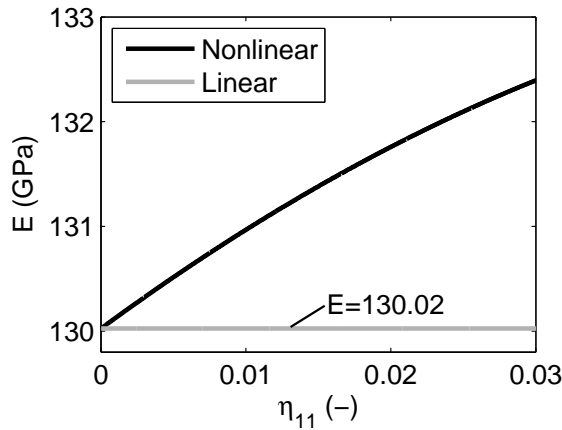


Figure A.4 / Nonlinear Young's modulus for uni-axial loading.

A numerical fit to the resulting curve gives the numerical values for the constants E_0 – E_3 in (A.40). These are listed in Table A.3, together with the values from Kim and Sachse (2000), using (A.41a)–(A.42c). Excellent agreement is found.

Table A.3 / Numerical values of the coefficients in (A.40) obtained from Kim and Sachse (2000) and by numerical calculation. Values are in GPa.

Coefficient	Kim and Sachse (2000)	Numerical fit
E_0	130.02	130.02
E_1	101.77	101.77
E_2	-738.18	-738.18
E_3	-	-647.45

Some aspects of the clamped-clamped beam MEMS resonator models

Abstract / In this appendix, various aspects of the models for the clamped-clamped beam MEMS resonator are described. Their derivation using Hamilton's principle is detailed and basis functions for the Galerkin discretisation are derived. Finally, expressions for the multi-mode Galerkin discretisations of models *II* and *III* are presented.

B.1 Beam theory

In Chapter 5, two different beam theories are used to represent the kinematics of deformation for the clamped-clamped beam MEMS resonator. These are the Euler-Bernoulli beam theory (Weaver et al., 1990; Rao, 1995; Meirovitch, 2001) and the Timoshenko beam theory (Timoshenko, 1921, 1922). In order to describe the kinematics according to these two theories, consider Figure B.1, in which a part of an undeformed beam is depicted. The coordinate system is the same as used in Figure 5.1. The x -coordinate is taken along the length of the beam. The y -direction is in the thickness direction and z is in transverse (width) direction. In general, in beam theory the displacements (u, v, w) along the directions (x, y, z) are only functions of x and z , see Wang et al. (2000) and the assumptions in Section 5.2.1. Furthermore, the displacement v equals zero.

For the Euler-Bernoulli beam theory, see Figure B.1, the displacement fields u and w are the following:

$$u(x, z, t) = u_0(x, t) - z \frac{\partial w_0(x, t)}{\partial x}, \quad (\text{B.1a})$$

$$w(x, z, t) = w_0(x, t), \quad (\text{B.1b})$$

where u_0 and w_0 denote the longitudinal and transverse displacement of a point $(x, 0)$ on the midplane ($z = 0$) of the beam, respectively. For the sake of convenience the

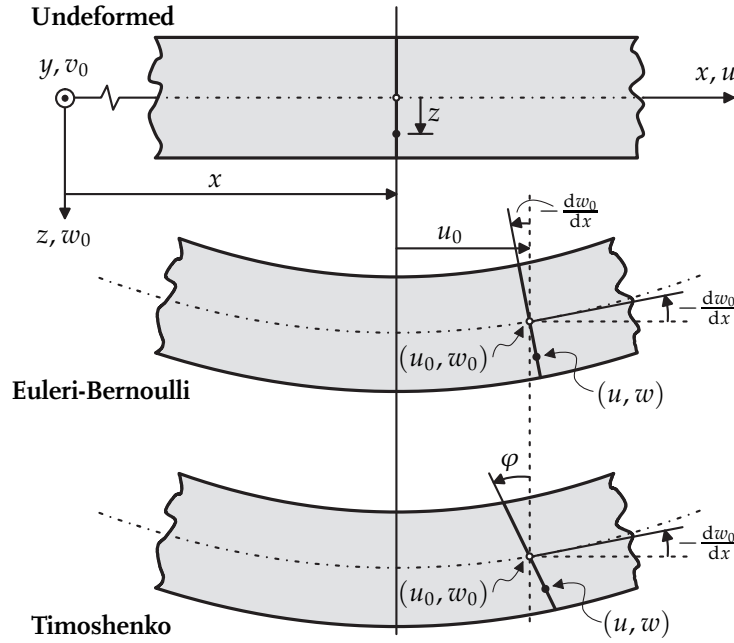


Figure B.1 / Kinematics according to Euler-Bernoulli and Timoshenko beam theory.

arguments of the fields u_0 and w_0 are omitted. The displacement field (B.1) implies that straight lines, normal to the midplane before deformation remain straight and normal to the midplane after deformation, see also Figure B.1.

According to Timoshenko beam theory, the displacement fields u and w are given by:

$$u(x, z, t) = u_0(x, t) + z\varphi(x, t), \quad (\text{B.2a})$$

$$w(x, z, t) = w_0(x, t), \quad (\text{B.2b})$$

where u_0 and w_0 denote the same as in the Euler-Bernoulli case, and where φ denotes the rotation of the cross section or the shear deformation field, see Figure B.1. In Timoshenko beam theory (B.2), the normality assumption for lines perpendicular to the midplane of the beam is relaxed. Instead, a constant state of transverse shear strain (and therefore constant shear stress) is assumed with respect to the width coordinate z . For this purpose, shear correction factors are needed in Timoshenko beam theory, in order to compensate for the error introduced by the constant shear stress assumption.

In the following section, the kinematics from the two beam theories will be used in the derivation of the models for the clamped-clamped beam MEMS resonator.

B.2 Models for the clamped-clamped beam MEMS resonator

In this section, a detailed derivation of the three different MEMS resonator models will be presented. The models contain different effects, as described in Table 5.2.

B.2.1 Strain-displacement relations

Models I and II

Models I and II are based on Euler-Bernoulli beam theory. The strain-displacement relations can be found by using the displacement fields (B.1) in the components of the Green-Lagrange strain tensor (4.1). Furthermore, in Euler-Bernoulli beam theory, only the axial strain component η_{xx} is assumed to be present. As a result, the strain-displacement relations, expressed in the coordinates (x, y, z) as shown in Figure B.1, are the following:

$$\eta_{xx} = \frac{\partial u_0}{\partial x} + \frac{1}{2} \left(\frac{\partial w_0}{\partial x} \right)^2 - z \frac{\partial^2 w_0}{\partial x^2}, \quad (\text{B.3a})$$

$$\eta_{yy} = \eta_{zz} = \gamma_{xy} = \gamma_{yz} = \gamma_{xz} = 0. \quad (\text{B.3b})$$

Model III

Model III is based on Timoshenko beam theory, which includes, next to axial strain η_{xx} , also transverse shear strain γ_{xz} . Using the displacement fields (B.2) for the components of the Green-Lagrange strain tensor yields:

$$\eta_{xx} = \frac{\partial u_0}{\partial x} + \frac{1}{2} \left(\frac{\partial w_0}{\partial x} \right)^2 + z \frac{\partial \varphi}{\partial x}, \quad (\text{B.4a})$$

$$\gamma_{xz} = \varphi + \frac{\partial w_0}{\partial x}, \quad (\text{B.4b})$$

$$\eta_{yy} = \eta_{zz} = \gamma_{xy} = \gamma_{yz} = 0. \quad (\text{B.4c})$$

B.2.2 Hamilton's principle

In order to apply Hamilton's principle (4.6) for deriving the partial differential equations in the different models, the expressions for the variation of the kinetic energy \mathcal{T} , the internal (or strain) energy \mathcal{U}_{in} and the external work \mathcal{W}_{ex} have to be evaluated, see (4.7)–(4.9). For all three models, the expression for the external work equals:

$$\delta \mathcal{W}_{\text{ex}} = - \int_0^l q_e(x, t) \delta w_0 \, dx, \quad (\text{B.5})$$

where $q_e(x, t)$ is the distributed electrostatic load, acting on the beam. An expression for $q_e(x, t)$ will be derived in Section B.2.5.

Models I and II

For models I and II, based on Euler-Bernoulli beam theory, the variation of the kinetic energy and the internal energy can be evaluated using (B.1) and (B.3). For the kinetic

energy, this yields:

$$\begin{aligned}\delta\mathcal{T} &= \int_{\mathcal{V}} \left(\rho \frac{\partial u_0}{\partial t} \delta \frac{\partial u_0}{\partial t} + \frac{\partial w_0}{\partial t} \delta \frac{\partial w_0}{\partial t} \right) d\mathcal{V} \\ &= \int_0^l \left(\rho A \frac{\partial u_0}{\partial t} \delta \frac{\partial u_0}{\partial t} + \rho I \frac{\partial^2 w_0}{\partial x \partial t} \delta \frac{\partial^2 w_0}{\partial x \partial t} + \rho A \frac{\partial w_0}{\partial t} \delta \frac{\partial w_0}{\partial t} \right) dx,\end{aligned}\quad (\text{B.6})$$

where the first and third term in on the right-hand side of (B.6) denote axial and transverse inertia, and the second term denotes rotary inertia. The internal energy becomes:

$$\begin{aligned}\delta\mathcal{U}_{\text{in}} &= \int_{\mathcal{V}} \sigma_{xx} \delta \eta_{xx} d\mathcal{V} \\ &= \int_0^l \left\{ N_{xx} \left(\delta \frac{\partial u_0}{\partial x} + \frac{\partial w_0}{\partial x} \delta \frac{\partial w_0}{\partial x} \right) + M_{xx} \delta \frac{\partial^2 w_0}{\partial x^2} \right\} dx,\end{aligned}\quad (\text{B.7})$$

where the axial force N_{xx} and the bending moment M_{xx} are given by

$$N_{xx} = \int_{\mathcal{A}} \sigma_{xx} d\mathcal{A}, \quad \text{and} \quad M_{xx} = - \int_{\mathcal{A}} \sigma_{xx} z d\mathcal{A}. \quad (\text{B.8})$$

By application of Hamilton's principle, using (B.5)–(B.8), the PDEs describing the beam, and the associated boundary conditions can be derived. Partial integration is applied to relieve any spatial or temporal derivative of u_0 or w_0 from variation, see for instance Reddy (2007). Furthermore, the fundamental lemma of variational calculus is applied to derive the following PDEs for variations in δu_0 and δw_0 , respectively:

$$\delta u_0 : \quad \frac{\partial N_{xx}}{\partial x} - \rho A \frac{\partial^2 u_0}{\partial t^2} = 0, \quad (\text{B.9a})$$

$$\delta w_0 : \quad - \frac{\partial^2 M_{xx}}{\partial x^2} + \frac{\partial}{\partial x} \left(N_{xx} \frac{\partial w_0}{\partial x} \right) + q_e + \rho I \frac{\partial^4 w_0}{\partial x^2 \partial t^2} - \rho A \frac{\partial^2 w_0}{\partial t^2} = 0. \quad (\text{B.9b})$$

The associated natural (force) and geometric boundary conditions for (B.9) also follow from the derivation. These equal, respectively:

$$\left. \begin{aligned} N_{xx} &= 0 \quad \text{or} \quad u_0 = 0 \\ \frac{\partial M_{xx}}{\partial x} - N_{xx} \frac{\partial w_0}{\partial x} &= 0 \quad \text{or} \quad w_0 = 0 \\ M_{xx} &= 0 \quad \text{or} \quad \frac{\partial w_0}{\partial x} = 0 \end{aligned} \right\} \quad \text{at} \quad x = 0, l. \quad (\text{B.10})$$

Since the clamped-clamped beam MEMS resonator has fixed ends, the geometric boundary conditions will be used, see (5.2).

Model III

For the model based on Timoshenko beam theory, the variation of the kinetic energy becomes:

$$\delta\mathcal{T} = \int_0^l \left(\rho A \frac{\partial u_0}{\partial t} \delta \frac{\partial u_0}{\partial t} + \rho I \frac{\partial \varphi}{\partial t} \delta \frac{\partial \varphi}{\partial t} + \rho A \frac{\partial w_0}{\partial t} \delta \frac{\partial w_0}{\partial t} \right) dx, \quad (\text{B.11})$$

where, similar to the Euler-Bernoulli case, the first and third term in on the right-hand side of (B.6) denote axial and transverse inertia, and the second term denotes rotary inertia. The internal energy becomes:

$$\begin{aligned}\delta\mathcal{U}_{\text{in}} &= \int_V (\sigma_{xx}\delta\eta_{xx} + \tau_{xz}\delta\gamma_{xz}) dV \\ &= \int_0^l \left\{ N_{xx} \left(\delta \frac{\partial u_0}{\partial x} + \frac{\partial w_0}{\partial x} \delta \frac{\partial w_0}{\partial x} \right) + M_{xx} \delta \frac{\partial \varphi}{\partial x} + Q_x \left(\delta \varphi + \delta \frac{\partial^2 w_0}{\partial x^2} \right) \right\} dx, \quad (\text{B.12})\end{aligned}$$

where the axial force N_{xx} , the bending moment M_{xx} and the transverse shear force Q_x are given by:

$$N_{xx} = \int_A \sigma_{xx} dA, \quad M_{xx} = \int_A \sigma_{xx} z dA, \quad \text{and} \quad Q_x = k_s \int_A \tau_{xz} dA. \quad (\text{B.13})$$

In the expression for Q_x in (B.13), k_s denotes the shear correction factor, given in (5.11).

Similar to the approach for the Euler-Bernoulli case (models *I* and *II*), Hamilton's principle is applied to derive the PDEs and the boundary conditions. The PDEs, for variations δu_0 , $\delta \varphi$ and δw_0 are given by, respectively:

$$\delta u_0 : \quad \frac{\partial N_{xx}}{\partial x} - \rho A \frac{\partial^2 u_0}{\partial t^2} = 0, \quad (\text{B.14a})$$

$$\delta \varphi : \quad \frac{\partial M_{xx}}{\partial x} - Q_x - \rho I \frac{\partial^2 \varphi}{\partial t^2} = 0 \quad (\text{B.14b})$$

$$\delta w_0 : \quad \frac{\partial Q_x}{\partial x} + \frac{\partial}{\partial x} \left(N_{xx} \frac{\partial w_0}{\partial x} \right) + q_e - \rho A \frac{\partial^2 w_0}{\partial t^2} = 0. \quad (\text{B.14c})$$

The associated natural (force) and geometric boundary conditions for (B.14) also follow from the derivation.

$$\left. \begin{aligned} N_{xx} = 0 & \quad \text{or} \quad u_0 = 0 \\ M_{xx} = 0 & \quad \text{or} \quad \varphi = 0 \\ Q_x + N_{xx} \frac{\partial w_0}{\partial x} = 0 & \quad \text{or} \quad w_0 = 0 \end{aligned} \right\} \quad \text{at} \quad x = 0, l. \quad (\text{B.15})$$

Since the clamped-clamped beam MEMS resonator has fixed ends, the geometric boundary conditions will be used, see (5.12). Other references, dealing on the derivation of the equations of motion for a Timoshenko beam are, for instance, Traill-Nash and Collar (1953), Kounadis (1980), Reddy and Singh (1981) and Abramovich and Elishakoff (1990).

B.2.3 Inclusion of the constitutive equations

Now that the general PDEs have been derived for all three models, the axial force N_{xx} , the bending moment M_{xx} and the shear force Q_x (for model *III*) have to be related to the displacement field through the expressions for the strain and the constitutive equations.

Furthermore, as indicated in the assumptions in Section 5.2.1, axial inertia is neglected for the models. This implies that the terms $\rho A \frac{\partial^2 u_0}{\partial t^2}$ vanish in (B.9a) and (B.14a), such that $\frac{\partial N_{xx}}{\partial x} = 0$ remains. This implies that $N_{xx} = \text{constant}$. By using this relation, N_{xx} can be solved explicitly by integrating over the length of the beam:

$$\int_0^l N_{xx} dx = \int_0^l \int_{\mathcal{A}} \sigma_{xx} d\mathcal{A} dx. \quad (\text{B.16})$$

Evaluation of (B.16) yields

$$N_{xx} = \frac{1}{l} \int_0^l \int_{\mathcal{A}} \sigma_{xx} d\mathcal{A} dx + N_0, \quad (\text{B.17})$$

where N_0 denotes the initial axial tension in the beam. In this way, by means of (B.17), the axial force is accounted for in each of the three models.

In the following, the inclusion of the constitutive equations in each of the three models will be described.

Model I

In the first model, nonlinear elasticity is taken into account. For this purpose, constitutive equation (4.13):

$$\sigma_{xx} = E(\eta_{xx})\eta_{xx} = (E_0 + E_1\eta_{xx} + E_2\eta_{xx}^2)\eta_{xx}, \quad (\text{B.18})$$

is used, together with (B.3). Upon evaluating η_{xx}^2 and η_{xx}^3 in (B.18), terms containing products with $\frac{\partial u_0}{\partial x}$ will be neglected, since the in-plane displacement u_0 is two to three orders of magnitude smaller than the transverse displacement w_0 , see Section 5.2.1. This assumption has been verified by finite element simulations using Comsol Multiphysics. The expressions for the axial force and bending moment (B.8) evaluate to:

$$N_{xx} = E_0 A \left[\frac{\partial u_0}{\partial x} + \frac{1}{2} \left(\frac{\partial w_0}{\partial x} \right)^2 \right] + \frac{E_1 A}{4} \left(\frac{\partial w_0}{\partial x} \right)^4 + E_1 I \left(\frac{\partial^2 w_0}{\partial x^2} \right)^2 + \frac{E_2 A}{8} \left(\frac{\partial w_0}{\partial x} \right)^6 + \frac{3E_2 I}{2} \left(\frac{\partial w_0}{\partial x} \right)^2 \left(\frac{\partial^2 w_0}{\partial x^2} \right)^2, \quad (\text{B.19a})$$

$$M_{xx} = \left[E_0 I + E_1 I \left(\frac{\partial w_0}{\partial x} \right)^2 + \frac{3E_2 I}{4} \left(\frac{\partial w_0}{\partial x} \right)^4 + \frac{9E_2 I h^2}{20} \left(\frac{\partial^2 w_0}{\partial x^2} \right)^2 \right] \frac{\partial^2 w_0}{\partial x^2}. \quad (\text{B.19b})$$

Using (B.19a) in (B.17) causes the term $E_0 A \frac{\partial u_0}{\partial x}$ in the right-hand side of (B.19a) to vanish, due to the boundary conditions $u_0 = 0$ at $x = 0, l$. This results in:

$$N_{xx} = \int_0^l \left\{ \frac{E_0 A}{2l} \left(\frac{\partial w_0}{\partial x} \right)^2 + \frac{E_1 A}{4l} \left(\frac{\partial w_0}{\partial x} \right)^4 + \frac{E_1 I}{l} \left(\frac{\partial^2 w_0}{\partial x^2} \right)^2 + \frac{E_2 A}{8l} \left(\frac{\partial w_0}{\partial x} \right)^6 + \frac{3E_2 I}{2l} \left(\frac{\partial w_0}{\partial x} \right)^2 \left(\frac{\partial^2 w_0}{\partial x^2} \right)^2 \right\} dx + N_0. \quad (\text{B.20})$$

Next, since $N_{xx} = \text{constant}$, (B.9b) evaluates to:

$$\rho A \frac{\partial^2 w_0}{\partial t^2} - \rho I \frac{\partial^4 w_0}{\partial x^2 \partial t^2} + \frac{\partial^2 M_{xx}}{\partial x^2} - N_{xx} \frac{\partial^2 w_0}{\partial x^2} = q_e. \quad (\text{B.21})$$

In order to arrive at the final PDE for model *I*, see (5.1) in Section 5.2.2, (B.19b) and (B.20) are used in (B.21). The boundary conditions are given by (5.2). The expression for the distributed electrostatic load will be derived in Appendix B.2.5.

Model II

Model *II* is based on linear elastic material behaviour, including the effects of thermal expansion. For this purpose, (4.21) can be written as:

$$\eta_{xx} = S_{11}\sigma_{xx} + \alpha\theta, \quad (\text{B.22a})$$

$$\eta_{yy} = \eta_{zz} = S_{12}\sigma_{xx} + \alpha\theta, \quad (\text{B.22b})$$

where θ denotes the temperature difference $\theta = T - T_0$ with respect to a reference temperature T_0 . Although η_{yy} and η_{zz} are assumed to be zero according to Euler-Bernoulli beam theory, their expressions will be taken into account for the derivation of the heat equation, see Appendix B.2.4. Next, (B.22a) is rewritten as:

$$\sigma_{xx} = \frac{1}{S_{11}}(\eta_{xx} - \alpha\theta), \quad (\text{B.23})$$

where $\frac{1}{S_{11}}$ equals the Young's modulus of silicon in [100]-direction, see (A.8). For the sake of convenience, $E = \frac{1}{S_{11}}$ will be used in the following. By using (B.23), N_{xx} and M_{xx} from (B.8) can be evaluated as:

$$N_{xx} = EA \left[\frac{\partial u_0}{\partial x} + \frac{1}{2} \left(\frac{\partial w_0}{\partial x} \right)^2 \right] - N_T, \quad (\text{B.24a})$$

$$M_{xx} = EI \frac{\partial^2 w_0}{\partial x^2} + M_T, \quad (\text{B.24b})$$

where the thermoelastic moment M_T and the thermoelastic axial force N_T have been given in (5.7) in Section 5.2.2. Substitution of (B.24a) into (B.17) leads to:

$$N_{xx} = \frac{EA}{2l} \int_0^l \left(\frac{\partial w_0}{\partial x} \right)^2 dx + N_0 - \frac{1}{l} \int_0^l N_T dx, \quad (\text{B.25})$$

which, together with (B.24b), is used in (B.21) (which is the same for models *I* and *II*), to arrive at the final PDE for model *II*. The resulting equation has already been given in (5.6). Corresponding boundary conditions are given in (5.2).

Model III

Similar to model II, model III is based on linear elastic material behaviour and includes the effects of thermal expansion. The constitutive equations can be written as:

$$\eta_{xx} = S_{11}\sigma_{xx} + \alpha\theta, \quad (\text{B.26a})$$

$$\eta_{yy} = \eta_{zz} = S_{12}\sigma_{xx} + \alpha\theta, \quad (\text{B.26b})$$

$$\gamma_{xz} = S_{44}\tau_{xz}. \quad (\text{B.26c})$$

Again, (B.26a) is rewritten to the form (B.23), where $E = \frac{1}{S_{11}}$ is used. Furthermore, (B.26c) is rewritten to

$$\tau_{xz} = \frac{1}{S_{44}}\gamma_{xz}, \quad (\text{B.27})$$

where $\frac{1}{S_{44}}$ denotes the shear modulus G , which will be used in the following. By using (B.23) and (B.27), N_{xx} , M_{xx} and Q_x from (B.13) can be evaluated as:

$$N_{xx} = EA \left[\frac{\partial u_0}{\partial x} + \frac{1}{2} \left(\frac{\partial w_0}{\partial x} \right)^2 \right] - N_T, \quad (\text{B.28a})$$

$$M_{xx} = EI \frac{\partial \varphi}{\partial x} - M_T, \quad (\text{B.28b})$$

$$Q_x = k_s GA \left(\varphi + \frac{\partial w_0}{\partial x} \right), \quad (\text{B.28c})$$

where the thermoelastic moment M_T and the thermoelastic axial force N_T are the same as for model II, see (5.7). Note that (B.28a) is the same as (B.24a). Therefore, substitution of (B.28a) into (B.17) yields also the same result, see (B.25). As a last step, substitution of (B.25), (B.28b) and (B.28c) into (B.14b) and (B.14c) yields the final PDEs as given in (5.10). The corresponding boundary conditions are given in (5.12).

B.2.4 The heat equation

In models II and III, thermoelastic damping is included. For this purpose, the heat equation, for which the general form is given in (4.23), is used. For the models considered, it is assumed that the heat conduction only takes place in z -direction. This gives:

$$\rho c_p \frac{\partial \theta}{\partial t} = k \frac{\partial^2 \theta}{\partial z^2} + T_0 \beta \frac{\partial e}{\partial t}, \quad (\text{B.29})$$

where e denotes the dilatation, given by (see also (4.24)):

$$e = \eta_{xx} + \eta_{yy} + \eta_{zz}. \quad (\text{B.30})$$

In the following, the effect of the shear strain γ_{xz} on the dilatation according to model III is neglected. Therefore, the expression for the dilatation according to models II and III is the same and can be derived by substituting (B.22) or (B.26) into (B.30):

$$e = (S_{11} + 2S_{12})\sigma_{xx} + 3\alpha\theta. \quad (\text{B.31})$$

Next, (B.23) is used in (B.31) to arrive at:

$$e = \frac{S_{11} + 2S_{12}}{S_{11}}(\eta_{xx} - \alpha\theta) + 3\alpha\theta. \quad (\text{B.32})$$

By using (B.32) and the relation between the thermal expansion coefficient α and the thermal modulus β , given in (4.22), the second term on the right-hand side of (B.29) can be evaluated as:

$$\begin{aligned} T_0\beta\frac{\partial e}{\partial t} &= -\frac{T_0\alpha}{S_{11} + 2S_{12}}\frac{\partial}{\partial t}\left(\frac{S_{11} + 2S_{12}}{S_{11}}(\eta_{xx} - \alpha\theta) + 3\alpha\theta\right) \\ &= -\frac{T_0\alpha}{S_{11}}\frac{\partial\eta_{xx}}{\partial t} - 2\frac{T_0\alpha^2}{S_{11}}\left(\frac{S_{11} - S_{12}}{S_{11} + 2S_{12}}\right)\frac{\partial\theta}{\partial t}. \end{aligned} \quad (\text{B.33})$$

Next, (A.8) and (A.9) are used to rewrite the terms with S_{11} and S_{12} to terms containing the Young's modulus E and Poisson's ratio ν in the $[100]$ -direction. Substitution of the resulting expression into (B.29) yields:

$$\left(\rho c_p + 2T_0\alpha^2\frac{E(1+\nu)}{1-2\nu}\right)\frac{\partial\theta}{\partial t} = k\frac{\partial^2\theta}{\partial z^2} - T_0\alpha E\frac{\partial\eta_{xx}}{\partial t}. \quad (\text{B.34})$$

For silicon, using the material parameters listed in Table 5.5, it can be observed that $\rho c_p \gg 2T_0\alpha^2\frac{E(1+\nu)}{1-2\nu}$. Therefore, the second term on the left-hand side of (B.34) is omitted. The resulting equation equals:

$$\rho c_p\frac{\partial\theta}{\partial t} = k\frac{\partial^2\theta}{\partial z^2} - T_0\alpha E\frac{\partial\eta_{xx}}{\partial t}. \quad (\text{B.35})$$

For model *II*, based on Euler-Bernoulli beam theory, (B.3a) is used in (B.35) to find the final form of the heat equation, see (5.8). Additionally, since the PDE for the axial field u_0 is assumed to be stationary, the term $\frac{\partial}{\partial t}\left(\frac{\partial u_0}{\partial x}\right)$ is omitted. The boundary conditions for this equation correspond to an insulated (zero heat flux) top and bottom boundary of the beam and are given in (5.9).

For model *III*, based on Timoshenko beam theory, a similar approach is utilised. In this case, (B.4a) is used in (B.35) to find the heat equation, see (5.13). Additionally, stationarity of the PDE for the axial field is used to omit the term $\frac{\partial}{\partial t}\left(\frac{\partial u_0}{\partial x}\right)$. The boundary conditions for the resulting equation are the same as for model *II* and are given in (5.9).

B.2.5 Distributed electrostatic load

The distributed electrostatic load q_e can be determined as the electrostatic force per unit length, using (4.27) and the total capacitance (including fringing fields, see Figure 4.4) between the beam and the electrodes. The effect of fringing fields is accounted for by including first-order correction terms to the parallel plate capacitance according to Osterberg (1995) and Osterberg and Senturia (1997). These authors base their derivation on the

classical conformal mapping theory presented in Palmer (1937). In this way, the capacitances per unit length between the two electrodes and the beam become (see also Figure 5.1):

$$C_1 = \frac{\epsilon_0 b}{d_1 - w_0} \left[1 + \frac{2(d_1 - w_0)}{\pi b} + \frac{2(d_1 - w_0)}{\pi b} \ln \left(\frac{\pi b}{d_1 - w_0} \right) \right], \quad (\text{B.36a})$$

$$C_2 = \frac{\epsilon_0 b}{d_2 + w_0} \left[1 + \frac{2(d_2 + w_0)}{\pi b} + \frac{2(d_2 + w_0)}{\pi b} \ln \left(\frac{\pi b}{d_2 + w_0} \right) \right]. \quad (\text{B.36b})$$

A voltage $V_1(t)$ is applied over electrode gap 1 and a voltage V_2 is applied over electrode gap 2, see Figure 5.1(a) and the expressions in (5.4). Therefore, by using (4.27), the distributed electrostatic load q_e can be evaluated as:

$$\begin{aligned} q_e &= \frac{1}{2} V_1^2(t) \frac{dC_1}{dw_0} + \frac{1}{2} V_2^2 \frac{dC_2}{dw_0} \\ &= \frac{\epsilon_0 b V_1^2(t)}{2(d_1 - w_0)^2} \left(1 + \frac{2}{\pi} \frac{d_1 - w_0}{b} \right) - \frac{\epsilon_0 b V_2^2}{2(d_2 + w_0)^2} \left(1 + \frac{2}{\pi} \frac{d_2 + w_0}{b} \right). \end{aligned} \quad (\text{B.37})$$

In literature (Osterberg and Senturia, 1997), often the approximation $\frac{2}{\pi} \approx 0.65$ is used. This has also been done for the expression for q_e used for the three models in Chapter 5, see (5.3).

B.3 Basis functions for Galerkin discretisation

The basis functions for Galerkin discretisation, described in Tables 5.3 and 5.4 in Section 5.2.4 are derived from the linear homogeneous versions of the respective PDEs. In the following sections, first the basis functions for the mechanical part of the Euler-Bernoulli and Timoshenko beam will be described. Finally, the derivation of the basis functions for the thermal field is presented.

B.3.1 Basis functions for Euler-Bernoulli beam

Basis functions $W_{E,i}(x)$ for the transverse displacement field for the Euler-Bernoulli beam are determined for the linear, undamped and uncoupled versions of (5.17) (model I) and (5.19) (model II). For this purpose, linear, undamped eigenmodes, found from Blevins (1979) are used. The non-dimensional modeshapes, which, a priori, satisfy the boundary conditions (5.18) are given by:

$$W_{E,i}(x) = \cosh \lambda_i x - \cos \lambda_i x - \sigma_i (\sinh \lambda_i x - \sin \lambda_i x), \quad (\text{B.38})$$

where the coefficient in (B.38) is given by

$$\sigma_i = \frac{\cosh \lambda_i - \cos \lambda_i}{\sinh \lambda_i - \sin \lambda_i} \quad (\text{B.39})$$

and where λ_i are the roots of the frequency equation:

$$\cos \lambda \cosh \lambda - 1 = 0. \quad (\text{B.40})$$

B.3.2 Basis functions for the Timoshenko beam

As basis functions for the displacement field of the Timoshenko beam (model *III*), eigenmode pairs $W_{T,i}(x)$, $\Phi_{T,i}(x)$ are used. These non-dimensional modeshapes are determined from the linear, undamped and homogeneous version (with $\sigma_0 = 0$) of (5.22) using a separation of variables method. The approach follows a derivation for dimensional modeshapes described in Han et al. (1999). The homogeneous, linear version of (5.22), without thermoelastic coupling and midplane stretching terms reads:

$$\frac{\partial^2 w_0}{\partial t^2} - k_s \left(\frac{1}{c_1} \frac{\partial \varphi}{\partial x} + \frac{\partial^2 w_0}{\partial x^2} \right) = 0 \quad (\text{B.41a})$$

$$c_r \frac{\partial^2 \varphi}{\partial t^2} - \frac{\partial^2 \varphi}{\partial x^2} + k_s c_s \left(\varphi + c_1 \frac{\partial w_0}{\partial x} \right) = 0, \quad (\text{B.41b})$$

Separation of variables, that is:

$$w_0(x, t) = W(x)T(t), \quad \text{and} \quad \varphi(x, t) = \Phi(x)T(t), \quad (\text{B.42})$$

is applied to (B.41) to arrive at:

$$W(x) \frac{d^2 T(t)}{dt^2} = k_s c_s \left(\frac{1}{c_1} \frac{d\Phi(x)}{dx} + \frac{d^2 W(x)}{dx^2} \right) T(t), \quad (\text{B.43a})$$

$$c_r \Phi(x) \frac{d^2 T(t)}{dt^2} = \left[\frac{d^2 \Phi(x)}{dx^2} - k_s c_s \left(\Phi(x) + c_1 \frac{dW(x)}{dx} \right) \right] T(t). \quad (\text{B.43b})$$

Here, $W(x)$ and $\Phi(x)$ denote the spatially dependent transverse deflection and shear deformation fields and $T(t)$ denotes the time-dependency. Both $w_0(x, t)$ and $\varphi(x, t)$ are assumed to have the same time-dependency. Separation of the temporal and spatial parts of leads to:

$$-\frac{\frac{d^2 T(t)}{dt^2}}{T(t)} = -\frac{k_s c_s \left(\frac{1}{c_1} \frac{d\Phi(x)}{dx} + \frac{d^2 W(x)}{dx^2} \right)}{W(x)}, \quad (\text{B.44a})$$

$$-\frac{\frac{d^2 T(t)}{dt^2}}{T(t)} = -\frac{\frac{d^2 \Phi(x)}{dx^2} - k_s c_s \left(\Phi(x) + c_1 \frac{dW(x)}{dx} \right)}{c_r \Phi(x)}. \quad (\text{B.44b})$$

The left-hand side of (B.44) is a function of time t , whereas the right-hand side is a function of x . This is only possible if both sides are equal the so-called separation constant, which will be indicated by ω^2 . Using this separation constant, (B.44) can be written as:

$$\frac{d^2 T(t)}{dt^2} + \omega^2 T(t) = 0, \quad (\text{B.45a})$$

$$\omega^2 W(x) + k_s c_s \left(\frac{1}{c_1} \frac{d\Phi(x)}{dx} + \frac{d^2 W(x)}{dx^2} \right) = 0, \quad (\text{B.45b})$$

$$c_r \omega^2 \Phi(x) + \frac{d^2 \Phi(x)}{dx^2} - k_s c_s \left(\Phi(x) + c_1 \frac{dW(x)}{dx} \right) = 0. \quad (\text{B.45c})$$

The spatial equations (B.45b)–(B.45c) can be written in matrix notation as

$$\begin{bmatrix} k_s c_s & 0 \\ 0 & 1 \end{bmatrix} \begin{bmatrix} \frac{d^2 W(x)}{dx^2} \\ \frac{d^2 \Phi(x)}{dx^2} \end{bmatrix} + \begin{bmatrix} 0 & \frac{k_s c_s}{c_l} \\ -k_s c_s c_l & 0 \end{bmatrix} \begin{bmatrix} \frac{dW(x)}{dx} \\ \frac{d\Phi(x)}{dx} \end{bmatrix} + \begin{bmatrix} \omega^2 & 0 \\ 0 & c_s \omega^2 - k_s c_s \end{bmatrix} \begin{bmatrix} W(x) \\ \Phi(x) \end{bmatrix} = \begin{bmatrix} 0 \\ 0 \end{bmatrix}. \quad (\text{B.46})$$

Furthermore, the equations for $W(x)$ and $\Phi(x)$ can be decoupled by writing (B.46) as:

$$\frac{d^4 W(x)}{dx^4} + \left(c_r + \frac{1}{k_s c_s} \right) \omega^2 \frac{d^2 W(x)}{dx^2} - \omega^2 W(x) + \frac{c_r}{k_s c_s} \omega^4 W(x) = 0, \quad (\text{B.47a})$$

$$\frac{d^4 \Phi(x)}{dx^4} + \left(c_r + \frac{1}{k_s c_s} \right) \omega^2 \frac{d^2 \Phi(x)}{dx^2} - \omega^2 \Phi(x) + \frac{c_r}{k_s c_s} \omega^4 \Phi(x) = 0. \quad (\text{B.47b})$$

Since these equations have the same form, solutions for $W(x)$ and $\Phi(x)$ will have the same form too, and will only differ by a constant:

$$\begin{bmatrix} W(x) \\ \Phi(x) \end{bmatrix} = d \mathbf{u} e^{rx}, \quad (\text{B.48})$$

where r and \mathbf{u} denote eigenvalues and eigenvectors that need to be determined, respectively. Substitution of (B.48) into (B.47) yields

$$\begin{bmatrix} k_s c_s r^2 + \omega^2 & \frac{k_s c_s}{c_l} r \\ -k_s c_s c_l r & r^2 + c_r \omega^2 - k_s c_s \end{bmatrix} \mathbf{u} = \mathbf{0}. \quad (\text{B.49})$$

In order to have non-trivial solutions to (B.49), the determinant of the matrix has to be zero. This gives the eigenvalues r_i and eigenvectors \mathbf{u}_i :

$$r_i = \pm \sqrt{-\left(c_r + \frac{1}{k_s c_s} \right) \frac{\omega^2}{2} \pm \frac{1}{2} \sqrt{\left(c_r + \frac{1}{k_s c_s} \right)^2 \omega^4 + 4 \left(\omega^2 - \frac{c_r}{k_s c_s} \omega^4 \right)}} \quad (\text{B.50})$$

$$\mathbf{u}_i = \begin{bmatrix} -\frac{k_s c_s}{c_l} r_i \\ k_s c_s r_i^2 + \omega^2 \end{bmatrix} \quad \text{and} \quad \mathbf{u}_i = \begin{bmatrix} r_i^2 + c_r \omega^2 - k_s c_s \\ k_s c_s c_l r_i \end{bmatrix}, \quad (\text{B.51})$$

From (B.50), it can be seen that two of the roots are always imaginary and that the other two are either real or imaginary, depending on the value of ω . Define the non-dimensional critical angular frequency $\omega_c = \sqrt{\frac{k_s c_s}{c_r}}$. Then, the roots are imaginary if $\omega > \omega_c$ and real if $\omega < \omega_c$. From the non-dimensional parameters of the beam (5.16), the nominal beam dimensions (see Table 5.1) and the beam parameters (see Table 5.5), it follows that $\omega_c = \mathcal{O}(10^3)$. Therefore, for the first eight natural frequencies of the resonator considered, it holds that $\omega < \omega_c$. In that case, the solution (B.48) can be written as

$$\begin{bmatrix} W(x) \\ \Phi(x) \end{bmatrix} = \sum_{i=1}^4 d_i \mathbf{u}_i e^{r_i x} = d_1 \mathbf{u}_1 e^{j a x} + d_2 \mathbf{u}_2 e^{-j a x} + d_3 \mathbf{u}_3 e^{b x} + d_4 \mathbf{u}_4 e^{-b x}, \quad (\text{B.52})$$

where

$$a = \sqrt{\left(c_r + \frac{1}{k_s c_s}\right) \frac{\omega^2}{2} + \frac{1}{2} \sqrt{\left(c_r + \frac{1}{k_s c_s}\right)^2 \omega^4 + 4\left(\omega^2 - \frac{c_r}{k_s c_s} \omega^4\right)}}, \quad (\text{B.53a})$$

$$b = \sqrt{-\left(c_r + \frac{1}{k_s c_s}\right) \frac{\omega^2}{2} + \frac{1}{2} \sqrt{\left(c_r + \frac{1}{k_s c_s}\right)^2 \omega^4 + 4\left(\omega^2 - \frac{c_r}{k_s c_s} \omega^4\right)}}. \quad (\text{B.53b})$$

Solution (B.52) can also be written as

$$\begin{bmatrix} W(x) \\ \Phi(x) \end{bmatrix} = \begin{bmatrix} C_1 \\ D_1 \end{bmatrix} \sin ax + \begin{bmatrix} C_2 \\ D_2 \end{bmatrix} \cos ax + \begin{bmatrix} C_3 \\ D_3 \end{bmatrix} \sinh bx + \begin{bmatrix} C_4 \\ D_4 \end{bmatrix} \cosh bx. \quad (\text{B.54})$$

Relations between coefficients C_i and D_i , $i = 1, 2, 3, 4$ can be established by substituting (B.54) into (B.46). This gives

$$D_1 = \alpha C_2, \quad D_2 = -\alpha C_1, \quad (\text{B.55a})$$

$$D_3 = \beta C_4, \quad D_4 = -\beta C_3, \quad (\text{B.55b})$$

where α and β are given by:

$$\alpha = \frac{(k_s c_s a^2 - \omega^2) c_1}{k_s c_s a}, \quad \beta = \frac{(k_s c_s b^2 + \omega^2) c_1}{k_s c_s b}. \quad (\text{B.56})$$

Next, the frequency equation can be derived by applying the boundary conditions (see also (5.23))

$$W(0) = W(1) = 0, \quad \Phi(0) = \Phi(1) = 0 \quad (\text{B.57})$$

to (B.54), using (B.55). This gives

$$\begin{bmatrix} 0 & 1 & 0 & 1 \\ \sin a & \cos a & \sinh b & \cosh b \\ -\alpha & 0 & -\beta & 0 \\ -\alpha \cos a & \alpha \sin a & -\beta \cosh b & -\beta \sinh b \end{bmatrix} \begin{bmatrix} C_1 \\ C_2 \\ C_3 \\ C_4 \end{bmatrix} = \begin{bmatrix} 0 \\ 0 \\ 0 \\ 0 \end{bmatrix}. \quad (\text{B.58})$$

In order to avoid trivial solutions, the determinant of the matrix in (B.58) has to be zero. This yields the frequency equation

$$\alpha^2 \sin a \sinh b + 2\alpha\beta \cos a \cosh b - \beta^2 \sin a \sinh b - 2\alpha\beta = 0, \quad (\text{B.59})$$

where (B.53) and (B.56) are used. Roots ω_i of the frequency equation (B.59) have to be calculated numerically. Furthermore, by establishing relations between the different coefficients C_i , $i = 1, 2, 3, 4$, the modeshapes can be found. For eigenmode i , these are denoted by $W_{T,i}(x)$ and $\Phi_{T,i}(x)$ for the transverse deflection and the shear deformation, respectively, and are given by:

$$W_{T,i}(x) = \cos a_i x - \cosh b_i x - \sigma_i \left(\sin a_i x - \frac{\alpha_i}{\beta_i} \sinh b_i x \right), \quad (\text{B.60a})$$

$$\Phi_{T,i}(x) = \alpha_i \sin a_i x + \beta_i \sinh b_i x + \alpha_i \sigma_i (\cos a_i x - \cosh b_i x), \quad (\text{B.60b})$$

where coefficient σ_i is given by:

$$\sigma_i = \frac{\cos a_i - \cosh b_i}{\sin a_i - \frac{\alpha_i}{\beta_i} \sinh b_i}. \quad (\text{B.61})$$

B.3.3 Basis functions for the heat equation

In this section, basis functions are derived for the non-dimensional heat equation for models *II* and *III*. For this purpose, linear (without the mid-plane stretching term) versions of the heat equations are considered. For model *II*, the linear, non-dimensional heat equation is given by (see also (5.20)):

$$\frac{\partial \theta}{\partial t} = c_k \frac{\partial^2 \theta}{\partial z^2} + c_{1,E} z \frac{\partial^3 w_0}{\partial x^2 \partial t}, \quad (\text{B.62})$$

and for model *III*, the non-dimensional linear heat equation reads (see also (5.24)):

$$\frac{\partial \theta}{\partial t} = c_k \frac{\partial^2 \theta}{\partial z^2} - c_{1,T} z \frac{\partial^2 \varphi}{\partial x \partial t}. \quad (\text{B.63})$$

Since both equations are very similar in form, the derivation of the basis function will only be presented for (B.62).

Similar to the approach used for deriving the basis functions for the Timoshenko beam, the principle of separation of variables is applied here. Therefore, write the temperature field $\theta(x, z, t)$ and beam deflection $w_0(x, t)$ as

$$\theta(x, z, t) = \Theta(x, z)T(t), \quad \text{and} \quad w_0(x, t) = W(x)T(t), \quad (\text{B.64})$$

where $\Theta(x, z)$ and $W(x)$ denote spatial fields and $T(t)$ denotes a function of time. Apply (B.64) to (B.62) to obtain

$$\Theta(x, z) \frac{dT(t)}{dt} = c_k \frac{d^2 \Theta(x, z)}{dz^2} T(t) + c_{1,E} z \frac{d^2 W(x)}{dx^2} \frac{dT(t)}{dt}, \quad (\text{B.65})$$

which can be separated as follows:

$$-\frac{\frac{dT(t)}{dt}}{T(t)} = -\frac{c_k \frac{d^2 \Theta(x, z)}{dz^2}}{\Theta(x, z) - c_{1,E} z \frac{d^2 W(x)}{dx^2}}. \quad (\text{B.66})$$

The left-hand side of (B.66) is a function of time and the right-hand side is a function of spatial coordinates. Therefore, (B.66) can only hold if both sides are equal to a constant, which will be called $\frac{1}{\tau}$. Using this separation constant, from (B.66) it follows that

$$\tau \frac{dT(t)}{dt} + T(t) = 0, \quad (\text{B.67a})$$

$$\tau c_k \frac{d^2 \Theta(x, z)}{dz^2} + \Theta(x, z) = z c_{1,E} \frac{d^2 W(x)}{dx^2}. \quad (\text{B.67b})$$

The solution to the spatial part (B.67b) consists of a homogeneous and a non-homogeneous part and can be written as

$$\Theta(x, z) = C_1 \sin az + C_2 \cos az + c_{1,E} z \frac{d^2 W(x)}{dx^2}, \quad (\text{B.68})$$

where

$$a = \frac{1}{\sqrt{\tau c_k}}. \quad (\text{B.69})$$

The constants C_1 and C_2 follow from the boundary conditions, which require that $\frac{d\Theta(x,z)}{dz} = 0$ at $z = \pm \frac{1}{2}$ (see (5.21)). This yields the following system of equations:

$$\begin{bmatrix} a \cos \frac{a}{2} & -a \sin \frac{a}{2} \\ a \cos \frac{a}{2} & a \sin \frac{a}{2} \end{bmatrix} \begin{bmatrix} C_1 \\ C_2 \end{bmatrix} = -c_{1,E} \frac{d^2 W(x)}{dx^2} \begin{bmatrix} 1 \\ 1 \end{bmatrix}. \quad (\text{B.70})$$

Direct solution of (B.70) yields

$$C_1 = -c_{1,E} \frac{d^2 W(x)}{dx^2} \frac{1}{a \cos \frac{a}{2}}, \quad C_2 = 0. \quad (\text{B.71})$$

Therefore, the temperature profile becomes (using (B.71) in (B.68)):

$$\Theta(x, z) = c_{1,E} \frac{d^2 W(x)}{dx^2} \left(z - \frac{\sin az}{a \cos \frac{a}{2}} \right). \quad (\text{B.72})$$

This solution is very similar to the one from Lifshitz and Roukes (2000). It can be seen that the temperature profile depends on the beam deformation $W(x)$ with respect to the x -direction. For a different vibration mode $W(x)$, a different temperature profile results. Furthermore, note that division by $a \cos \frac{a}{2}$ in the mode shape (B.72) is only allowed if

$$\begin{aligned} a \cos \frac{a}{2} &\neq 0 \quad \Leftrightarrow \\ a &\neq 0 \quad \wedge \quad a \neq (1 + 2k)\pi, \quad k = 0, \pm 1, \pm 2, \dots \end{aligned} \quad (\text{B.73})$$

In order to complete the solution, an expression for a has to be found, such that the time constant τ can be related to a , using (B.69). The characteristic constants from the system of equations for the boundary conditions can be obtained by avoiding trivial solutions, $C_1 = C_2 = 0$ in (B.70) by setting the determinant of the matrix in these equations to zero. This gives

$$2a^2 \cos \frac{a}{2} \sin \frac{a}{2} = 0 \quad \Leftrightarrow \quad (\text{B.74})$$

$$\sin a = 0 \quad \wedge \quad a \neq 0, \quad (\text{B.75})$$

whose solutions are $a = k\pi$, $k = 1, 2, \dots$ ($k = 0$ is no solution, since $a = 0$ is not allowed). By combining these characteristic solutions with the modeshape (B.72) and condition (B.73), the only solutions that are valid are

$$a = 2k\pi, \quad k = \pm 1, \pm 2, \dots \quad (\text{B.76})$$

Using the solution for $k = 1$ from (B.76) in (B.72) results in the following basis function for the thermal field of model II:

$$\Theta_{E,i}(x, z) = c_{1,E} \frac{d^2 W_{E,i}(x)}{dx^2} \left(z + \frac{1}{2\pi} \sin 2\pi z \right), \quad (\text{B.77})$$

where it can be seen that basis function $\Theta_{E,i}(x, z)$ depends on mechanical mode $W_{E,i}(x)$. Furthermore, by using (B.69), the time constant τ can be found to equal:

$$\tau = \frac{1}{4\pi^2 c_k}. \quad (\text{B.78})$$

The thermal time constant from the classical theory on thermoelastic damping, see Zener (1937) and Zener (1938), equals (see (4.17)):

$$\tau = \frac{h^2 \rho c_p}{\pi^2 k}. \quad (\text{B.79})$$

In order to compare this value with the approach for the basis functions used in this section, the thermal time constant has also been derived using the approach of (B.64)–(B.78) for the heat equation in dimensional form. This yields

$$\tau = \frac{h^2 \rho c_p}{4\pi^2 k}, \quad (\text{B.80})$$

which is a factor 4 different from (B.79). Where this difference stems from is still to be investigated.

In a similar way, a basis function for the thermal field of model *III*, based on Timoshenko beam theory, can be derived:

$$\Theta_{T,i}(x, z) = -c_{1,T} \frac{d\Phi_{T,i}(x)}{dx} \left(z + \frac{1}{2\pi} \sin 2\pi z \right). \quad (\text{B.81})$$

Similar to the $\Theta_{E,i}(x, z)$, also the basis function for the thermal field $\Theta_{T,i}(x, z)$ in model *III* depends on the mechanical part, through the shear deformation field $\Phi_{T,i}(x)$.

B.4 Multi-mode Galerkin discretisations

In this section, the multi-mode Galerkin discretisations for models *II* and *III* are elaborated. Only the 3-mode discretisations will be presented in the following. The 2-mode discretisations can be found by omitting the terms related to the third basis function. For model *II*, this means that the terms with q_5 and r_5 are set to zero and for model *III*, terms with p_5 , q_5 and r_5 are set to zero.

Model *II*

In the 3-mode discretisation, the flexural displacement field and the thermal field are approximated using three basis functions:

$$w_0 = q_1 W_{E,1} + q_3 W_{E,3} + q_5 W_{E,5}, \quad (\text{B.82a})$$

$$\theta = r_1 \Theta_{E,1} + r_3 \Theta_{E,3} + r_5 \Theta_{E,5}. \quad (\text{B.82b})$$

By using (B.82), the three-mode Galerkin discretisation of (5.19) and (5.20), has the following general form:

$$\mathbf{M}\ddot{\mathbf{q}} + \mathbf{f}_{\text{in}}(\mathbf{q}, \dot{\mathbf{q}}, \mathbf{r}) = \mathbf{f}_{\text{ex}}(\mathbf{q}, t), \quad (\text{B.83a})$$

$$\mathbf{T}\dot{\mathbf{r}} = \mathbf{f}_{\text{th}}(\mathbf{r}, \dot{\mathbf{q}}), \quad (\text{B.83b})$$

where (B.83a) corresponds to the 3-mode Galerkin discretised version of (5.19) and (B.83b) corresponds to (5.20).

The matrices and columns in (B.83) are given by:

$$\mathbf{q} = [q_1 \quad q_3 \quad q_5]^T, \quad (\text{B.84a})$$

$$\mathbf{r} = [r_1 \quad r_3 \quad r_5]^T, \quad (\text{B.84b})$$

$$\mathbf{M} = \mathbf{I} - c_r \mathbf{A}_{\text{ww}}, \quad (\text{B.84c})$$

$$\mathbf{f}_{\text{in}}(\mathbf{q}, \dot{\mathbf{q}}, \mathbf{r}) = \mathbf{\Lambda}\mathbf{q} + \mathbf{C}\dot{\mathbf{q}} + c_{\text{M,E}}\mathbf{A}_{\theta\text{w}}\mathbf{r} - k(\mathbf{q})\mathbf{A}_{\text{ww}}\mathbf{q}, \quad (\text{B.84d})$$

$$\mathbf{f}_{\text{ex}}(\mathbf{q}, t) = c_v \begin{bmatrix} \int_0^1 f_{\text{el}} W_{\text{E},1} dx \\ \int_0^1 f_{\text{el}} W_{\text{E},3} dx \\ \int_0^1 f_{\text{el}} W_{\text{E},5} dx \end{bmatrix}, \quad (\text{B.84e})$$

$$\mathbf{T} = \begin{bmatrix} \int_0^1 \int_{-\frac{1}{2}}^{\frac{1}{2}} \Theta_{\text{E},1}^2 dz dx & \int_0^1 \int_{-\frac{1}{2}}^{\frac{1}{2}} \Theta_{\text{E},3} \Theta_{\text{E},1} dz dx & \int_0^1 \int_{-\frac{1}{2}}^{\frac{1}{2}} \Theta_{\text{E},5} \Theta_{\text{E},1} dz dx \\ \int_0^1 \int_{-\frac{1}{2}}^{\frac{1}{2}} \Theta_{\text{E},1} \Theta_{\text{E},3} dz dx & \int_0^1 \int_{-\frac{1}{2}}^{\frac{1}{2}} \Theta_{\text{E},3}^2 dz dx & \int_0^1 \int_{-\frac{1}{2}}^{\frac{1}{2}} \Theta_{\text{E},5} \Theta_{\text{E},3} dz dx \\ \int_0^1 \int_{-\frac{1}{2}}^{\frac{1}{2}} \Theta_{\text{E},1} \Theta_{\text{E},5} dz dx & \int_0^1 \int_{-\frac{1}{2}}^{\frac{1}{2}} \Theta_{\text{E},3} \Theta_{\text{E},5} dz dx & \int_0^1 \int_{-\frac{1}{2}}^{\frac{1}{2}} \Theta_{\text{E},5}^2 dz dx \end{bmatrix}, \quad (\text{B.84f})$$

$$\mathbf{f}_{\text{th}}(\mathbf{r}, \dot{\mathbf{q}}) = c_k \mathbf{A}_{\theta\theta}\mathbf{r} + c_{1,\text{E}} \mathbf{A}_{\text{w}\theta}\dot{\mathbf{q}}, \quad (\text{B.84g})$$

where $\mathbf{I} \in \mathbb{R}^{3 \times 3}$ is the identity matrix and where:

$$\mathbf{A}_{\text{ww}} = \begin{bmatrix} \int_0^1 \frac{\partial^2 W_{\text{E},1}}{\partial x^2} W_{\text{E},1} dx & \int_0^1 \frac{\partial^2 W_{\text{E},3}}{\partial x^2} W_{\text{E},1} dx & \int_0^1 \frac{\partial^2 W_{\text{E},5}}{\partial x^2} W_{\text{E},1} dx \\ \int_0^1 \frac{\partial^2 W_{\text{E},1}}{\partial x^2} W_{\text{E},3} dx & \int_0^1 \frac{\partial^2 W_{\text{E},3}}{\partial x^2} W_{\text{E},3} dx & \int_0^1 \frac{\partial^2 W_{\text{E},5}}{\partial x^2} W_{\text{E},3} dx \\ \int_0^1 \frac{\partial^2 W_{\text{E},1}}{\partial x^2} W_{\text{E},5} dx & \int_0^1 \frac{\partial^2 W_{\text{E},3}}{\partial x^2} W_{\text{E},5} dx & \int_0^1 \frac{\partial^2 W_{\text{E},5}}{\partial x^2} W_{\text{E},5} dx \end{bmatrix}, \quad (\text{B.85a})$$

$$\mathbf{\Lambda} = \begin{bmatrix} \lambda_1^4 & 0 & 0 \\ 0 & \lambda_3^4 & 0 \\ 0 & 0 & \lambda_5^4 \end{bmatrix}, \quad \mathbf{C} = \begin{bmatrix} c_1 & 0 & 0 \\ 0 & c_3 & 0 \\ 0 & 0 & c_5 \end{bmatrix}, \quad (\text{B.85b})$$

$$\mathbf{A}_{\theta\text{w}} = \begin{bmatrix} \int_0^1 \int_{-\frac{1}{2}}^{\frac{1}{2}} \frac{\partial^2 \Theta_{\text{E},1}}{\partial x^2} W_{\text{E},1} z dz dx & \int_0^1 \int_{-\frac{1}{2}}^{\frac{1}{2}} \frac{\partial^2 \Theta_{\text{E},3}}{\partial x^2} W_{\text{E},1} z dz dx & \int_0^1 \int_{-\frac{1}{2}}^{\frac{1}{2}} \frac{\partial^2 \Theta_{\text{E},5}}{\partial x^2} W_{\text{E},1} z dz dx \\ \int_0^1 \int_{-\frac{1}{2}}^{\frac{1}{2}} \frac{\partial^2 \Theta_{\text{E},1}}{\partial x^2} W_{\text{E},3} z dz dx & \int_0^1 \int_{-\frac{1}{2}}^{\frac{1}{2}} \frac{\partial^2 \Theta_{\text{E},3}}{\partial x^2} W_{\text{E},3} z dz dx & \int_0^1 \int_{-\frac{1}{2}}^{\frac{1}{2}} \frac{\partial^2 \Theta_{\text{E},5}}{\partial x^2} W_{\text{E},3} z dz dx \\ \int_0^1 \int_{-\frac{1}{2}}^{\frac{1}{2}} \frac{\partial^2 \Theta_{\text{E},1}}{\partial x^2} W_{\text{E},5} z dz dx & \int_0^1 \int_{-\frac{1}{2}}^{\frac{1}{2}} \frac{\partial^2 \Theta_{\text{E},3}}{\partial x^2} W_{\text{E},5} z dz dx & \int_0^1 \int_{-\frac{1}{2}}^{\frac{1}{2}} \frac{\partial^2 \Theta_{\text{E},5}}{\partial x^2} W_{\text{E},5} z dz dx \end{bmatrix}, \quad (\text{B.85c})$$

$$k(\mathbf{q}) = c_m \left[q_1^2 \int_0^1 \left(\frac{\partial W_{\text{E},1}}{\partial x} \right)^2 dx + q_3^2 \int_0^1 \left(\frac{\partial W_{\text{E},3}}{\partial x} \right)^2 dx + q_5^2 \int_0^1 \left(\frac{\partial W_{\text{E},5}}{\partial x} \right)^2 dx + 2q_1 q_3 \int_0^1 \frac{\partial W_{\text{E},1}}{\partial x} \frac{\partial W_{\text{E},3}}{\partial x} dx \right. \\ \left. + 2q_1 q_5 \int_0^1 \frac{\partial W_{\text{E},1}}{\partial x} \frac{\partial W_{\text{E},5}}{\partial x} dx + 2q_3 q_5 \int_0^1 \frac{\partial W_{\text{E},3}}{\partial x} \frac{\partial W_{\text{E},5}}{\partial x} dx \right] + c_{\sigma} \sigma_0, \quad (\text{B.85d})$$

$$f_{\text{el}} = V_1^2 \frac{1 + 0.65c_b(1 - q_1 W_{\text{E},1} - q_3 W_{\text{E},3} - q_5 W_{\text{E},5})}{(1 - q_1 W_{\text{E},1} - q_3 W_{\text{E},3} - q_5 W_{\text{E},5})^2} \\ - V_2^2 \frac{1 + 0.65c_b(c_d + q_1 W_{\text{E},1} + q_3 W_{\text{E},3} + q_5 W_{\text{E},5})}{(c_d + q_1 W_{\text{E},1} + q_3 W_{\text{E},3} + q_5 W_{\text{E},5})^2}, \quad (\text{B.85e})$$

$$\mathbf{A}_{\theta\theta} = \begin{bmatrix} \int_0^1 \int_{-\frac{1}{2}}^{\frac{1}{2}} \frac{\partial^2 \Theta_{E,1}}{\partial z^2} \Theta_{E,1} dz dx & \int_0^1 \int_{-\frac{1}{2}}^{\frac{1}{2}} \frac{\partial^2 \Theta_{E,3}}{\partial z^2} \Theta_{E,1} dz dx & \int_0^1 \int_{-\frac{1}{2}}^{\frac{1}{2}} \frac{\partial^2 \Theta_{E,5}}{\partial z^2} \Theta_{E,1} dz dx \\ \int_0^1 \int_{-\frac{1}{2}}^{\frac{1}{2}} \frac{\partial^2 \Theta_{E,1}}{\partial z^2} \Theta_{E,3} dz dx & \int_0^1 \int_{-\frac{1}{2}}^{\frac{1}{2}} \frac{\partial^2 \Theta_{E,3}}{\partial z^2} \Theta_{E,3} dz dx & \int_0^1 \int_{-\frac{1}{2}}^{\frac{1}{2}} \frac{\partial^2 \Theta_{E,5}}{\partial z^2} \Theta_{E,3} dz dx \\ \int_0^1 \int_{-\frac{1}{2}}^{\frac{1}{2}} \frac{\partial^2 \Theta_{E,1}}{\partial z^2} \Theta_{E,5} dz dx & \int_0^1 \int_{-\frac{1}{2}}^{\frac{1}{2}} \frac{\partial^2 \Theta_{E,3}}{\partial z^2} \Theta_{E,5} dz dx & \int_0^1 \int_{-\frac{1}{2}}^{\frac{1}{2}} \frac{\partial^2 \Theta_{E,5}}{\partial z^2} \Theta_{E,5} dz dx \end{bmatrix}, \quad (\text{B.85f})$$

$$\mathbf{A}_{w\theta} = \begin{bmatrix} \int_0^1 \int_{-\frac{1}{2}}^{\frac{1}{2}} \frac{\partial^2 W_{E,1}}{\partial x^2} \Theta_{E,1} z dz dx & \int_0^1 \int_{-\frac{1}{2}}^{\frac{1}{2}} \frac{\partial^2 W_{E,3}}{\partial x^2} \Theta_{E,1} z dz dx & \int_0^1 \int_{-\frac{1}{2}}^{\frac{1}{2}} \frac{\partial^2 W_{E,5}}{\partial x^2} \Theta_{E,1} z dz dx \\ \int_0^1 \int_{-\frac{1}{2}}^{\frac{1}{2}} \frac{\partial^2 W_{E,1}}{\partial x^2} \Theta_{E,3} z dz dx & \int_0^1 \int_{-\frac{1}{2}}^{\frac{1}{2}} \frac{\partial^2 W_{E,3}}{\partial x^2} \Theta_{E,3} z dz dx & \int_0^1 \int_{-\frac{1}{2}}^{\frac{1}{2}} \frac{\partial^2 W_{E,5}}{\partial x^2} \Theta_{E,3} z dz dx \\ \int_0^1 \int_{-\frac{1}{2}}^{\frac{1}{2}} \frac{\partial^2 W_{E,1}}{\partial x^2} \Theta_{E,5} z dz dx & \int_0^1 \int_{-\frac{1}{2}}^{\frac{1}{2}} \frac{\partial^2 W_{E,3}}{\partial x^2} \Theta_{E,5} z dz dx & \int_0^1 \int_{-\frac{1}{2}}^{\frac{1}{2}} \frac{\partial^2 W_{E,5}}{\partial x^2} \Theta_{E,5} z dz dx \end{bmatrix}. \quad (\text{B.85g})$$

Model III

In the 3-mode discretisation, the flexural displacement field, the shear deformation field and the thermal field are approximated using three basis functions:

$$w_0 = q_1 W_{T,1} + q_3 W_{T,3} + q_5 W_{T,5}, \quad (\text{B.86a})$$

$$\varphi = p_1 \Phi_{T,1} + p_3 \Phi_{T,3} + p_5 \Phi_{T,5}, \quad (\text{B.86b})$$

$$\theta = r_1 \Theta_{T,1} + r_3 \Theta_{T,3} + r_5 \Theta_{T,5}. \quad (\text{B.86c})$$

Using (B.86) results in the following reduced-order model:

$$\mathbf{M}\ddot{\mathbf{q}} + \mathbf{f}_{\text{in}}(\mathbf{q}, \dot{\mathbf{q}}, \mathbf{r}) = \mathbf{f}_{\text{ex}}(\mathbf{q}, t), \quad (\text{B.87a})$$

$$\mathbf{T}\dot{\mathbf{r}} = \mathbf{f}_{\text{th}}(\mathbf{r}, \dot{\mathbf{q}}), \quad (\text{B.87b})$$

where (B.87a) contains the 3-mode Galerkin discretised versions of (5.22) and where (B.87b) contains the discretised version of (5.24).

The terms in (5.31) are given by:

$$\mathbf{q} = [p_1 \quad p_3 \quad p_5 \quad q_1 \quad q_3 \quad q_5]^T, \quad (\text{B.88a})$$

$$\mathbf{r} = [r_1 \quad r_3 \quad r_5]^T, \quad (\text{B.88b})$$

$$\mathbf{M} = \begin{bmatrix} c_r \mathbf{A}_{\varphi\varphi} & \mathbf{O} \\ \mathbf{O} & \mathbf{A}_{ww} \end{bmatrix}, \quad (\text{B.88c})$$

$$\mathbf{f}_{\text{in}}(\mathbf{q}, \dot{\mathbf{q}}, \mathbf{r}) = \begin{bmatrix} \mathbf{A}_{\varphi\varphi} \mathbf{C}_{\varphi} & \mathbf{O} \\ \mathbf{O} & \mathbf{A}_{ww} \mathbf{C}_w \end{bmatrix} \dot{\mathbf{q}} + \begin{bmatrix} c_{M,T} \mathbf{A}_{\theta\varphi} \\ \mathbf{O} \end{bmatrix} \mathbf{r} + \begin{bmatrix} k_s c_s \mathbf{A}_{\varphi\varphi} - \mathbf{K}_{\varphi\varphi} & k_s c_s c_1 \mathbf{K}_{w\varphi} \\ -\frac{k_s c_s}{c_1} \mathbf{K}_{\varphi w} & -(k_s c_s + k(\mathbf{q})) \mathbf{K}_{ww} \end{bmatrix} \mathbf{q}, \quad (\text{B.88d})$$

$$\mathbf{f}_{\text{ex}}(\mathbf{q}, t) = c_v \begin{bmatrix} 0 \\ 0 \\ 0 \\ \int_0^1 f_{\text{el}} W_{T,1} dx \\ \int_0^1 f_{\text{el}} W_{T,3} dx \\ \int_0^1 f_{\text{el}} W_{T,5} dx \end{bmatrix}, \quad (\text{B.88e})$$

$$\mathbf{T} = \begin{bmatrix} \int_0^1 \int_{-\frac{1}{2}}^{\frac{1}{2}} \Theta_{T,1}^2 dz dx & \int_0^1 \int_{-\frac{1}{2}}^{\frac{1}{2}} \Theta_{T,3} \Theta_{T,1} dz dx & \int_0^1 \int_{-\frac{1}{2}}^{\frac{1}{2}} \Theta_{T,5} \Theta_{T,1} dz dx \\ \int_0^1 \int_{-\frac{1}{2}}^{\frac{1}{2}} \Theta_{T,1} \Theta_{T,3} dz dx & \int_0^1 \int_{-\frac{1}{2}}^{\frac{1}{2}} \Theta_{T,3}^2 dz dx & \int_0^1 \int_{-\frac{1}{2}}^{\frac{1}{2}} \Theta_{T,5} \Theta_{T,3} dz dx \\ \int_0^1 \int_{-\frac{1}{2}}^{\frac{1}{2}} \Theta_{T,1} \Theta_{T,5} dz dx & \int_0^1 \int_{-\frac{1}{2}}^{\frac{1}{2}} \Theta_{T,3} \Theta_{T,5} dz dx & \int_0^1 \int_{-\frac{1}{2}}^{\frac{1}{2}} \Theta_{T,5}^2 dz dx \end{bmatrix}, \quad (\text{B.88f})$$

$$\mathbf{f}_{\text{th}}(\mathbf{r}, \dot{\mathbf{q}}) = c_k \mathbf{A}_{\theta\theta} \mathbf{r} - c_{1,T} \mathbf{A}_{\varphi\theta} \dot{\mathbf{q}}, \quad (\text{B.88g})$$

where $\mathbf{O} \in \mathbb{R}^{3 \times 3}$ denotes the zero matrix and where:

$$\mathbf{A}_{\varphi\varphi} = \begin{bmatrix} \int_0^1 \Phi_{T,1}^2 dx & \int_0^1 \Phi_{T,3} \Phi_{T,1} dx & \int_0^1 \Phi_{T,5} \Phi_{T,1} dx \\ \int_0^1 \Phi_{T,1} \Phi_{T,3} dx & \int_0^1 \Phi_{T,3}^2 dx & \int_0^1 \Phi_{T,5} \Phi_{T,3} dx \\ \int_0^1 \Phi_{T,1} \Phi_{T,5} dx & \int_0^1 \Phi_{T,3} \Phi_{T,5} dx & \int_0^1 \Phi_{T,5}^2 dx \end{bmatrix}, \quad (\text{B.89a})$$

$$\mathbf{A}_{ww} = \begin{bmatrix} \int_0^1 W_{T,1}^2 dx & \int_0^1 W_{T,3} W_{T,1} dx & \int_0^1 W_{T,5} W_{T,1} dx \\ \int_0^1 W_{T,1} W_{T,3} dx & \int_0^1 W_{T,3}^2 dx & \int_0^1 W_{T,5} W_{T,3} dx \\ \int_0^1 W_{T,1} W_{T,5} dx & \int_0^1 W_{T,3} W_{T,5} dx & \int_0^1 W_{T,5}^2 dx \end{bmatrix}, \quad (\text{B.89b})$$

$$\mathbf{C}_\varphi = \begin{bmatrix} c_{1,\varphi} & 0 & 0 \\ 0 & c_{3,\varphi} & 0 \\ 0 & 0 & c_{5,\varphi} \end{bmatrix}, \quad \mathbf{C}_w = \begin{bmatrix} c_{1,w} & 0 & 0 \\ 0 & c_{3,w} & 0 \\ 0 & 0 & c_{5,w} \end{bmatrix}, \quad (\text{B.89c})$$

$$\mathbf{A}_{\theta\varphi} = \begin{bmatrix} \int_0^1 \int_{-\frac{1}{2}}^{\frac{1}{2}} \frac{\partial \Theta_{T,1}}{\partial x} \Phi_{T,1} z dz dx & \int_0^1 \int_{-\frac{1}{2}}^{\frac{1}{2}} \frac{\partial \Theta_{T,3}}{\partial x} \Phi_{T,1} z dz dx & \int_0^1 \int_{-\frac{1}{2}}^{\frac{1}{2}} \frac{\partial \Theta_{T,5}}{\partial x} \Phi_{T,1} z dz dx \\ \int_0^1 \int_{-\frac{1}{2}}^{\frac{1}{2}} \frac{\partial \Theta_{T,1}}{\partial x} \Phi_{T,3} z dz dx & \int_0^1 \int_{-\frac{1}{2}}^{\frac{1}{2}} \frac{\partial \Theta_{T,3}}{\partial x} \Phi_{T,3} z dz dx & \int_0^1 \int_{-\frac{1}{2}}^{\frac{1}{2}} \frac{\partial \Theta_{T,5}}{\partial x} \Phi_{T,3} z dz dx \\ \int_0^1 \int_{-\frac{1}{2}}^{\frac{1}{2}} \frac{\partial \Theta_{T,1}}{\partial x} \Phi_{T,5} z dz dx & \int_0^1 \int_{-\frac{1}{2}}^{\frac{1}{2}} \frac{\partial \Theta_{T,3}}{\partial x} \Phi_{T,5} z dz dx & \int_0^1 \int_{-\frac{1}{2}}^{\frac{1}{2}} \frac{\partial \Theta_{T,5}}{\partial x} \Phi_{T,5} z dz dx \end{bmatrix}, \quad (\text{B.89d})$$

$$\mathbf{K}_{\varphi\varphi} = \begin{bmatrix} \int_0^1 \frac{\partial^2 \Phi_{T,1}}{\partial x^2} \Phi_{T,1} dx & \int_0^1 \frac{\partial^2 \Phi_{T,3}}{\partial x^2} \Phi_{T,1} dx & \int_0^1 \frac{\partial^2 \Phi_{T,5}}{\partial x^2} \Phi_{T,1} dx \\ \int_0^1 \frac{\partial^2 \Phi_{T,1}}{\partial x^2} \Phi_{T,3} dx & \int_0^1 \frac{\partial^2 \Phi_{T,3}}{\partial x^2} \Phi_{T,3} dx & \int_0^1 \frac{\partial^2 \Phi_{T,5}}{\partial x^2} \Phi_{T,3} dx \\ \int_0^1 \frac{\partial^2 \Phi_{T,1}}{\partial x^2} \Phi_{T,5} dx & \int_0^1 \frac{\partial^2 \Phi_{T,3}}{\partial x^2} \Phi_{T,5} dx & \int_0^1 \frac{\partial^2 \Phi_{T,5}}{\partial x^2} \Phi_{T,5} dx \end{bmatrix}, \quad (\text{B.89e})$$

$$\mathbf{K}_{w\varphi} = \begin{bmatrix} \int_0^1 \frac{\partial W_{T,1}}{\partial x} \Phi_{T,1} dx & \int_0^1 \frac{\partial W_{T,3}}{\partial x} \Phi_{T,1} dx & \int_0^1 \frac{\partial W_{T,5}}{\partial x} \Phi_{T,1} dx \\ \int_0^1 \frac{\partial W_{T,1}}{\partial x} \Phi_{T,3} dx & \int_0^1 \frac{\partial W_{T,3}}{\partial x} \Phi_{T,3} dx & \int_0^1 \frac{\partial W_{T,5}}{\partial x} \Phi_{T,3} dx \\ \int_0^1 \frac{\partial W_{T,1}}{\partial x} \Phi_{T,5} dx & \int_0^1 \frac{\partial W_{T,3}}{\partial x} \Phi_{T,5} dx & \int_0^1 \frac{\partial W_{T,5}}{\partial x} \Phi_{T,5} dx \end{bmatrix}, \quad (\text{B.89f})$$

$$\mathbf{K}_{\varphi w} = \begin{bmatrix} \int_0^1 \frac{\partial \Phi_{T,1}}{\partial x} W_{T,1} dx & \int_0^1 \frac{\partial \Phi_{T,3}}{\partial x} W_{T,1} dx & \int_0^1 \frac{\partial \Phi_{T,5}}{\partial x} W_{T,1} dx \\ \int_0^1 \frac{\partial \Phi_{T,1}}{\partial x} W_{T,3} dx & \int_0^1 \frac{\partial \Phi_{T,3}}{\partial x} W_{T,3} dx & \int_0^1 \frac{\partial \Phi_{T,5}}{\partial x} W_{T,3} dx \\ \int_0^1 \frac{\partial \Phi_{T,1}}{\partial x} W_{T,5} dx & \int_0^1 \frac{\partial \Phi_{T,3}}{\partial x} W_{T,5} dx & \int_0^1 \frac{\partial \Phi_{T,5}}{\partial x} W_{T,5} dx \end{bmatrix}, \quad (\text{B.89g})$$

$$\mathbf{K}_{ww} = \begin{bmatrix} \int_0^1 \frac{\partial^2 W_{T,1}}{\partial x^2} W_{T,1} dx & \int_0^1 \frac{\partial^2 W_{T,3}}{\partial x^2} W_{T,1} dx & \int_0^1 \frac{\partial^2 W_{T,5}}{\partial x^2} W_{T,1} dx \\ \int_0^1 \frac{\partial^2 W_{T,1}}{\partial x^2} W_{T,3} dx & \int_0^1 \frac{\partial^2 W_{T,3}}{\partial x^2} W_{T,3} dx & \int_0^1 \frac{\partial^2 W_{T,5}}{\partial x^2} W_{T,3} dx \\ \int_0^1 \frac{\partial^2 W_{T,1}}{\partial x^2} W_{T,5} dx & \int_0^1 \frac{\partial^2 W_{T,3}}{\partial x^2} W_{T,5} dx & \int_0^1 \frac{\partial^2 W_{T,5}}{\partial x^2} W_{T,5} dx \end{bmatrix}, \quad (\text{B.89h})$$

$$k(\mathbf{q}) = c_m \left[q_1^2 \int_0^1 \left(\frac{\partial W_{T,1}}{\partial x} \right)^2 dx + q_3^2 \int_0^1 \left(\frac{\partial W_{T,3}}{\partial x} \right)^2 dx + q_5^2 \int_0^1 \left(\frac{\partial W_{T,5}}{\partial x} \right)^2 dx + 2q_1 q_3 \int_0^1 \frac{\partial W_{T,1}}{\partial x} \frac{\partial W_{T,3}}{\partial x} dx \right. \\ \left. + 2q_1 q_5 \int_0^1 \frac{\partial W_{T,1}}{\partial x} \frac{\partial W_{T,5}}{\partial x} dx + 2q_3 q_5 \int_0^1 \frac{\partial W_{T,3}}{\partial x} \frac{\partial W_{T,5}}{\partial x} dx \right] + c_\sigma \sigma_0, \quad (\text{B.89i})$$

$$f_{el} = V_1^2 \frac{1 + 0.65c_b(1 - q_1 W_{T,1} + q_3 W_{T,3} + q_5 W_{T,5})}{(1 - q_1 W_{T,1} - q_3 W_{T,3} - q_5 W_{T,5})^2} \\ - V_2^2 \frac{1 + 0.65c_b(c_d + q_1 W_{T,1} + q_3 W_{T,3} + q_5 W_{T,5})}{(c_d + q_1 W_{T,1} + q_3 W_{T,3} + q_5 W_{T,5})^2}, \quad (\text{B.89j})$$

$$\mathbf{A}_{\theta\theta} = \begin{bmatrix} \int_0^1 \int_{-\frac{1}{2}}^{\frac{1}{2}} \frac{\partial^2 \Theta_{T,1}}{\partial z^2} \Theta_{T,1} dz dx & \int_0^1 \int_{-\frac{1}{2}}^{\frac{1}{2}} \frac{\partial^2 \Theta_{T,3}}{\partial z^2} \Theta_{T,1} dz dx & \int_0^1 \int_{-\frac{1}{2}}^{\frac{1}{2}} \frac{\partial^2 \Theta_{T,5}}{\partial z^2} \Theta_{T,1} dz dx \\ \int_0^1 \int_{-\frac{1}{2}}^{\frac{1}{2}} \frac{\partial^2 \Theta_{T,1}}{\partial z^2} \Theta_{T,3} dz dx & \int_0^1 \int_{-\frac{1}{2}}^{\frac{1}{2}} \frac{\partial^2 \Theta_{T,3}}{\partial z^2} \Theta_{T,3} dz dx & \int_0^1 \int_{-\frac{1}{2}}^{\frac{1}{2}} \frac{\partial^2 \Theta_{T,5}}{\partial z^2} \Theta_{T,3} dz dx \\ \int_0^1 \int_{-\frac{1}{2}}^{\frac{1}{2}} \frac{\partial^2 \Theta_{T,1}}{\partial z^2} \Theta_{T,5} dz dx & \int_0^1 \int_{-\frac{1}{2}}^{\frac{1}{2}} \frac{\partial^2 \Theta_{T,3}}{\partial z^2} \Theta_{T,5} dz dx & \int_0^1 \int_{-\frac{1}{2}}^{\frac{1}{2}} \frac{\partial^2 \Theta_{T,5}}{\partial z^2} \Theta_{T,5} dz dx \end{bmatrix}, \quad (\text{B.89k})$$

$$\mathbf{A}_{\varphi\theta} = \begin{bmatrix} \int_0^1 \int_{-\frac{1}{2}}^{\frac{1}{2}} \frac{\partial \Phi_{T,1}}{\partial x} \Theta_{T,1} z dz dx & \int_0^1 \int_{-\frac{1}{2}}^{\frac{1}{2}} \frac{\partial \Phi_{T,3}}{\partial x} \Theta_{T,1} z dz dx & \int_0^1 \int_{-\frac{1}{2}}^{\frac{1}{2}} \frac{\partial \Phi_{T,5}}{\partial x} \Theta_{T,1} z dz dx \\ \int_0^1 \int_{-\frac{1}{2}}^{\frac{1}{2}} \frac{\partial \Phi_{T,1}}{\partial x} \Theta_{T,3} z dz dx & \int_0^1 \int_{-\frac{1}{2}}^{\frac{1}{2}} \frac{\partial \Phi_{T,3}}{\partial x} \Theta_{T,3} z dz dx & \int_0^1 \int_{-\frac{1}{2}}^{\frac{1}{2}} \frac{\partial \Phi_{T,5}}{\partial x} \Theta_{T,3} z dz dx \\ \int_0^1 \int_{-\frac{1}{2}}^{\frac{1}{2}} \frac{\partial \Phi_{T,1}}{\partial x} \Theta_{T,5} z dz dx & \int_0^1 \int_{-\frac{1}{2}}^{\frac{1}{2}} \frac{\partial \Phi_{T,3}}{\partial x} \Theta_{T,5} z dz dx & \int_0^1 \int_{-\frac{1}{2}}^{\frac{1}{2}} \frac{\partial \Phi_{T,5}}{\partial x} \Theta_{T,5} z dz dx \end{bmatrix}. \quad (\text{B.89l})$$

Bibliography

- ABDEL-RAHMAN, E. M. and NAYFEH, A. H. (2003). Secondary resonances of electrically actuated resonant microsensors. *Journal of Micromechanics and Microengineering*, **13**(3), 491–501.
- ABDEL-RAHMAN, E. M., YOUNIS, M. I., and NAYFEH, A. H. (2002). Characterization of the mechanical behavior of an electrically actuated microbeam. *Journal of Micromechanics and Microengineering*, **12**(6), 759–766.
- ABRAMOVICH, H. and ELISHAKOFF, I. (1990). Influence of shear deformation and rotary inertia on vibration frequencies via Love's equations. *Journal of Sound and Vibration*, **137**(3), 516–522.
- ALBLAS, J. B. (1961). On the general theory of thermo-elastic friction. *Applied Scientific Research A*, **10**, 349–362.
- ALLEN, J. J. (2005). *Micro Electro Mechanical System Design*. Taylor and Francis, Boca Raton.
- ANDRES, M. V., FOULDS, K. W. H., and TUDOR, M. J. (1987). Nonlinear vibrations and hysteresis of micromachined silicon resonators designed as frequency-out sensors. *Electron Letters*, **23**(18), 952–954.
- ATAMAN, C. and UREY, H. (2006). Modeling and characterization of comb-actuated resonant microscanners. *Journal of Micromechanics and Microengineering*, **16**(1), 9–16.
- BANNON, F. D., CLARK, J. R., and NGUYEN, C. T.-C. (1996). High Frequency Microelectromechanical IF Filters. *Proceedings of the IEEE International Electron Devices Meeting (IEDM 1996)*, San Francisco, CA, USA, December 8–11, 773–776.
- BANNON, F. D., CLARK, J. R., and NGUYEN, C. T.-C. (2000). High-Q HF Microelectromechanical Filters. *IEEE Journal of Solid-State Circuits*, **35**(4), 512–526.
- BARKE, E. (1988). Line-to-Ground Capacitance Calculation for VLSI: A Comparison. *IEEE Transactions on Computer-Aided Design*, **7**(2), 295–298.
- BATRA, R. C., PORFIRI, M., and SPINELLO, D. (2006a). Capacitance estimate for electrostatically actuated narrow microbeams. *Micro & Nano Letters*, **1**(2), 71–73.
- BATRA, R. C., PORFIRI, M., and SPINELLO, D. (2006b). Electromechanical Model of Electrically Actuated Narrow Microbeams. *Journal of Microelectromechanical Systems*, **15**(5), 1175–1189.
- BATRA, R. C., PORFIRI, M., and SPINELLO, D. (2007). Review of modeling electrostatically actuated microelectromechanical systems. *Smart Material Structures*, **16**(6), R23–R31.
- BATRA, R. C., PORFIRI, M., and SPINELLO, D. (2008). Vibrations of narrow microbeams predeformed by an electric field. *Journal of Sound and Vibration*, **309**(3–5), 600–612.
- BEEBY, S. P. (2004). *MEMS Mechanical Sensors*. Artech House Publishers.
- BEEBY, S. P. and TUDOR, M. J. (1995). Modelling and optimization of micromachined silicon resonators. *Journal of Micromechanics and Microengineering*, **5**(2), 103–105.
- VAN BEEK, J. T. M., STEENEKEN, P. G., and GIESBERS, B. (2006). A 10MHz piezoresistive MEMS resonator with high Q. *Proceedings of the IEEE International Frequency Control Symposium*, Miami, USA, June 4–7, 475–480.

- VAN BEEK, J. T. M., PHAN, K. L., VERHEIJDEN, G. J. A., KOOPS, G. E. J., VAN DER AVOORT, C., VAN WINGERDEN, J., BADAROGLU, D. E., BONTEMPS, J. J. M., and PUERS, R. (2007). A piezo-resistive resonant MEMS amplifier. *Proceedings of the IEEE International Electron Devices Meeting (IEDM 2008)*, San Francisco, USA, December 15–17, 411–414.
- BELL, D. J., LU, T. J., FLECK, N. A., and SPEARING, S. M. (2005). MEMS Actuators and Sensors: Observations on Their Performance and Selection for Purpose. *Journal of Micromechanics and Microengineering*, 15(7), S153–S164.
- BEST, R. E. (2003). *Phase-locked loops: design, simulation and applications*. McGraw-Hill, London, 5th edition.
- BIRCH, F. (1947). Finite Elastic Strain of Cubic Crystals. *Physical Review*, 71(11), 809–824.
- BLEVINS, R. D. (1979). *Formulas for Natural Frequency and Mode Shape*. Van Nostrand Reinhold, London.
- BOLEY, B. A. and WEINER, J. H. (1960). *Theory of thermal stresses*. John Wiley & Sons, Inc.
- BONTEMPS, J. J. M. (2006). *MEMS resonator; research concept or market product?* PDEng. Thesis, Stan Ackermans Institute, Eindhoven, The Netherlands.
- BRANTLEY, W. A. (1973). Calculated Elastic Constants for Stress Problems Associated with Semiconductor Devices. *Journal of Applied Physics*, 44(1), 534–535.
- BRUGGER, K. (1964). Thermodynamic Definition of Higher Order Elastic Coefficients. *Physical Review*, 133(6), A1611–A1612.
- BURENKOV, Y. A. and NIKANOROV, S. P. (1974). Temperature Dependence of the Elastic Constants of Silicon. *Soviet Physics – Solid State*, 16(5), 963–964.
- BUSER, R. A. and DE ROOIJ, N. F. (1990). Very High Q-factor Resonators in Monocrystalline Silicon. *Sensors and Actuators A*, 21(1–3), 323–327.
- CALLISTER, W. D. (1999). *Materials Science and Engineering; an Introduction*. John Wiley & Sons, Inc., 5th edition.
- CANDLER, R. N., DUWEL, A., VARGHESE, M., CHANDORKAR, S. A., HOPCROFT, M. A., PARK, W.-T., KIM, B., YAMA, G., PARTRIDGE, A., LUTZ, M., and KENNY, W. (2006a). Impact of Geometry on Thermoelastic Dissipation in Micromechanical Resonant Beams. *Journal of Microelectromechanical Systems*, 15(4), 927–934.
- CANDLER, R. N., HOPCROFT, M. A., KIM, B., PARK, W.-T., MELAMUD, R., AGARWAL, M., YAMA, G., PARTRIDGE, A., LUTZ, M., and KENNY, T. W. (2006b). Long-Term and Accelerated Life Testing of a Novel Single-Wafer Vacuum Encapsulation for MEMS Resonators. *Journal of Microelectromechanical Systems*, 15(6), 1446–1456.
- CARTMELL, M. P. and ROBERTS, J. W. (1988). Simultaneous combination resonances in an autoparametrically resonant system. *Journal of sound and vibration*, 123(1), 81–101.
- CHANG, W. H. (1976). Analytical and Numerical Studies on Viscous Energy Dissipation in Laterally Driven Microcomb Structures. *IEEE Transactions on Microwave Theory and Techniques*, MTT-24(9), 608–611. also Vol. MTT-25(8), p. 712.
- DATE, E. H. F. and ANDREWS, K. W. (1969). Anisotropic and Composition Effects in the Elastic Properties of Polycrystalline Metals. *Journal of Physics D: Applied Physics*, 2(10), 1373–1381.
- DE, S. K. and ALURU, N. R. (2006). Complex Nonlinear Oscillations in Electrostatically Actuated Microstructures. *Journal of Microelectromechanical Systems*, 15(2), 355–369.
- DEVOE, D. L. (2001). Piezoelectric thin film micromechanical beam resonators. *Sensors and Actuators A*, 88(3), 263–272.
- DOEDEL, E., CHAMPNEYS, A. R., FAIRGRIEVE, T. F., KUZNETSOV, Y. A., SANDSTEDE, B., and WANG, X. (1998). *AUTO97: Continuation and Bifurcation Software for Ordinary Differential Equations (with Hom-Cont)*, Technical Report. Concordia University.
- DUWEL, A., CANDLER, R. N., KENNY, T. W., and VARGHESE, M. (2006). Engineering MEMS Resonators With Low Thermoelastic Damping. *Journal of Microelectromechanical Systems*, 15(6), 1437–1445.
- EVERY, A. G. and MCCURDY, A. K. (1992). Low Frequency Properties of Dielectric Crystals, Subvolume A; Second and Higher Order Elastic Constants. In D. F. NELSON (ed.), *Landolt-Börnstein; Numerical Data and Functional Relationships in Science and Technology, New Series*, 29. Springer-Verlag, Berlin.

- FEY, R. H. B. (1992). *Steady-State Behaviour of Reduced Dynamic Systems with Local Nonlinearities*. PhD Thesis, Technische Universiteit Eindhoven, The Netherlands.
- FEY, R. H. B., DE KRAKER, A., VAN CAMPEN, D. H., and MEIJER, G. J. (1990). Stable and unstable periodic solutions of reduced dynamic systems with local nonlinearities. In J. F. DIJKSMAN and F. T. M. NIEUWSTADT (eds.), *Integration of Theory and Applications in Applied Mechanics*, 247–254. Kluwer Academic Publishers, Dordrecht, the Netherlands.
- FEY, R. H. B., VAN CAMPEN, D. H., and DE KRAKER, A. (1996). Long term structural dynamics of mechanical systems with local nonlinearities. *Transactions of the ASME, Journal of Vibration and Acoustics*, **118**(2), 147–153.
- FEYNMAN, R. P. (1960). There's Plenty of Room at the Bottom; An Invitation to Enter a New Field of Physics. *Engineering and Science*, **23**(5), 22–36.
- FEYNMAN, R. P. (1992). There's Plenty of Room at the Bottom. *Journal of Microelectromechanical Systems*, **1**(1), 60–66.
- FEYNMAN, R. P. (1993). Infinitesimal Machinery. *Journal of Microelectromechanical Systems*, **2**(1), 4–14.
- GABBAY, L. D., MEHNER, J. E., and SENTURIA, S. D. (2000). Computer-Aided Generation of Nonlinear Reduced-Order Dynamic Macromodels – I: Non-Stress-Stiffened Case. *Journal of Microelectromechanical Systems*, **9**(2), 262–269.
- GAD-EL HAK, M. (2002). *The MEMS Handbook*. CRC Press.
- GAST, T. (1985). Sensors with oscillating elements. *Journal of Physics E: Scientific Instruments*, **18**(9), 783–789.
- GERBER, E. A. and BALLATO, A. (1985). *Precision Frequency Control; Volume 2: Oscillators and Standards*. Academic Press, London.
- GONCHAROVA, V. A., CHERNYSHEVA, E. V., and VORONOV, F. F. (1983). Elastic Properties of Silicon and Germanium Single Crystals at Pressures up to 8 GPa at Room Temperature. *Soviet Physics – Solid State*, **25**(12), 2118–2121.
- GONZALEZ, G. (1997). *Microwave Transistor Amplifiers; Analysis and Design*. Prentice-Hall, New Jersey, 2nd edition.
- GREYWALL, D. S. (2005). Sensitive magnetometer incorporating a high-Q nonlinear mechanical resonator. *Measurement Science and Technology*, **16**(12), 2473–2482.
- GREYWALL, D. S., YURKE, B., BUSCH, P. A., PARGELLIS, A. N., and WILLETT, R. L. (1994). Evading Amplifier Noise in Nonlinear Oscillators. *Physical Review Letters*, **72**(19), 2992–2995.
- GRIFFITHS, D. J. (1999). *Introduction to Electrodynamics*. Prentice-Hall, 3rd edition.
- GUCKENHEIMER, J. and HOLMES, P. (1983). *Nonlinear Oscillations, Dynamical Systems, and Bifurcations of Vector Fields*. *Applied Mathematical Sciences* 42. Springer-Verlag.
- GUI, C., LEGTENBERG, R., TILMANS, H. A. C., FLUITMAN, J. H. J., and ELWENSPOEK, M. (1998). Nonlinearity and Hysteresis of Resonant Strain Gauges. *Journal of Microelectromechanical Systems*, **7**(1), 122–127.
- HAJIMIRI, A. and LEE, T. H. (1999). *The Design of Low Noise Oscillators*. Kluwer Academic Publishers, Dordrecht.
- HALL, J. J. (1967). Electronic Effects in the Elastic Constants of *n*-Type Silicon. *Physical Review*, **161**(3), 756–761.
- HAM, D., ANDRESS, W., and RICKETTS, D. (2004). Phase Noise in Oscillators. *Proceedings of the Second International Symposium on Acoustic Wave Devices for Future Mobile Communication Systems, Japan*, 57–68.
- HAN, S. M., BENAROYA, H., and WEI, T. (1999). Dynamics of transversely vibrating beams using four engineering theories. *Journal of Sound and Vibration*, **225**(5), 935–988.
- HAO, Z. and AYAZI, F. (2007). Support loss in the radial bulk-mode vibrations of center-supported micro-mechanical disk resonators. *Sensors and Actuators A*, **134**(2), 582–593.

- HAO, Z. and XU, Y. (2009). Vibration displacement on substrate due to time-harmonic stress sources from a micromechanical resonator. *Journal of Sound and Vibration*, **322**(1–2), 196–215.
- HAO, Z., ERBIL, A., and AYAZI, F. (2003). An analytical model for support loss in micromachined beam resonators with in-plane flexural vibrations. *Sensors and Actuators A*, **109**(1–2), 156–164.
- HAO, Z., POURKAMALI, S., and AYAZI, F. (2004). VHF Single-Crystal Silicon Elliptic Bulk-Mode Capacitive Disk Resonators – Part I: Design and Modeling. *Journal of Microelectromechanical Systems*, **13**(6), 1043–1053.
- HAUPTMANN, P. (1991). Resonant Sensors and Applications. *Sensors and Actuators A*, **25–27**, 371–377.
- HEARMON, R. F. S. (1953). ‘Third-Order’ Elastic Coefficients. *Acta Crystallographica*, **6**(4), 331–340.
- HEARMON, R. F. S. (1961). *An Introduction to Applied Anisotropic Elasticity*. Oxford University Press.
- HEATH, M. T. (2002). *Scientific Computing: An Introductory Survey*. McGraw-Hill, 2nd edition.
- HEWLETT-PACKARD COMPANY (1997a). *Fundamentals of Quartz Crystal Oscillators*. Hewlett-Packard, Electronic Counters Series, Application Note 200-2.
- HEWLETT-PACKARD COMPANY (1997b). *S-Parameter Techniques for Faster, More Accurate Network Design, Test & Measurement*. Hewlett-Packard, Application Note 95-1.
- HIKI, Y. (1981). Higher Order Elastic Constants of Solids. *Annual Review of Materials Science*, **11**, 51–73.
- VAN DEN HOVEN, E. J. P. (2008). *Modeling the nonlinear dynamics of a silicon MEMS resonator; physical analysis, numerical simulation and experimental validation*. MSc. Thesis, Technische Universiteit Eindhoven, Department of Mechanical Engineering, Dynamics and Control Group, DCT 2008.100.
- HOWE, R. T. and MULLER, R. S. (1986). Resonant-Microbridge Vapor Sensor. *IEEE Transactions on Electron Devices*, **33**(4), 499–506.
- HULL, R. (1999). *Properties of Crystalline Silicon*. Institution of Electrical Engineers, London.
- HUNG, E. S. and SENTURIA, S. D. (1999). Generating Efficient Dynamical Models for Microelectromechanical Systems from a few Finite-Element Runs. *Journal of Microelectromechanical Systems*, **8**(3), 280–289.
- HUNG, E. S., YANG, Y.-J., and SENTURIA, S. D. (1997). Low-Order Models for Fast Dynamical Simulation of MEMS Microstructures. *Proceedings of the 1997 International Conference on Solid-State Sensors and Actuators (Transducers '97)*, Chicago, Illinois, USA, 1101–1104.
- INSPEC (1988). *EMIS Datareview Series No. 4; Properties of Silicon (Chapter 1)*. Institution of Electrical Engineers, London, UK.
- IWATSUBO, T. and SAIGO, M. (1973). Parametric instability of clamped-clamped and clamped-simply supported columns under periodic axial load. *Journal of sound and vibration*, **30**(1), 65–77.
- JOHNSON, J. B. (1928). Thermal agitation of electricity in conductors. *Physical Review*, **32**(1), 110–113.
- KAAJAKARI, V. (2009). *Practical MEMS*. Small Gear Publishing.
- KAAJAKARI, V., MATTILA, T., KIIHAMÄKI, J., KATTELUS, H., OJA, A., and SEPPÄ, H. (2003a). Nonlinearities in Single-Crystal Silicon Micromechanical Resonators. *Transducers '03, Proceedings of the 12th International Conference on Solid-State Sensors, Actuators and Microsystems*, June 8–12, Boston, 1574–1577.
- KAAJAKARI, V., MATTILA, T., OJA, A., KIIHAMÄKI, J., KATTELUS, H., KOSKENVUORI, M., RANTAKARI, P., TITTONEN, I., and SEPPÄ, H. (2003b). Square-Extensional Mode Single-Crystal Silicon Micromechanical RF-Resonator. *Transducers '03, Proceedings of the 12th International Conference on Solid-State Sensors, Actuators and Microsystems*, June 8–12, Boston, 951–954.
- KAAJAKARI, V., MATTILA, T., OJA, A., and SEPPÄ, H. (2004a). Nonlinear Limits for Single-Crystal Silicon Microresonators. *Journal of Microelectromechanical Systems*, **13**(5), 715–724.
- KAAJAKARI, V., MATTILA, T., LIPSANEN, A., and OJA, A. (2004b). Nonlinear mechanical effects in silicon longitudinal mode beam resonators. *Sens. Actuators A*, **120**(1), 64–70.
- KAAJAKARI, V., MATTILA, T., OJA, A., KIIHAMÄKI, J., and SEPPÄ, H. (2004c). Square-Extensional Mode Single-Crystal Silicon Micromechanical Resonator for Low-Phase-Noise Oscillator Applications. *IEEE Electron Device Letters*, **25**(4), 173–175.

- KAAJAKARI, V., KOSKINEN, J. K., and MATTILA, T. (2005a). Phase Noise in Capacitively Coupled Micromechanical Oscillators. *IEEE Transactions on Ultrasonics, Ferroelectrics, and Frequency Control*, **52**(12), 2322–2331.
- KAAJAKARI, V., KIIHAMÄKI, J., OJA, A., SEPPÄ, H., PIETIKÄINEN, S., KOKKALA, V., and KUISMA, H. (2005b). Stability of Wafer Level Vacuum Encapsulated Single-Crystal Silicon Resonators. *Transducers '05, Proceedings of the 13th International Conference on Solid-State Sensors, Actuators and Microsystems*, June 5–9, Seoul, Korea, 916–919.
- KANDA, Y. (1982). A Graphical Representation of the Piezoresistance Coefficients in Silicon. *IEEE Transactions on Electron Devices*, **ED-29**(1), 64–70.
- KANDA, Y. (1991). Piezoresistance effect of silicon. *Sensors and Actuators A*, **28**(2), 83–91.
- KANEKO, T. (1975). On Timoshenko's correction for shear in vibrating beams. *Journal of Physics D: Applied Physics*, **8**, 1927–1936.
- KAPLAN, C. (1931). On the Strain-Energy Function for Isotropic Bodies. *Physical Review*, **38**(5), 1020–1029.
- KEYES, R. W. (1976). Electronic Effects in the Elastic Properties of Semiconductors. In F. SEITZ, D. TURNBULL, and H. EHRENREICH (eds.), *Solid State Physics; Advances in Research and Applications*, **20**. Academic Press, Inc.
- KIM, B., CHANDLER, R. N., HOPCROFT, M., AGARWAL, M., PARK, W.-T., and KENNY, T. W. (2005). Frequency stability of wafer-scale film encapsulated silicon based MEMS resonators. *Transducers '05, Proceedings of the 13th International Conference on Solid-State Sensors, Actuators and Microsystems*, June 5–9, Seoul, Korea, 1965–1968.
- KIM, B., CANDLER, R. N., HOPCROFT, M. A., AGARWAL, M., PARK, W.-T., and KENNY, T. W. (2007). Frequency stability of wafer-scale film encapsulated silicon based MEMS resonators. *Sensors and Actuators A*, **136**(1), 125–131.
- KIM, K. Y. and SACHSE, W. (2000). Nonlinear Elastic Equation of State of Solids Subjected to Uniaxial Homogeneous Loading. *Journal of Materials Science*, **35**(13), 3197–3205.
- KOSKENVUORI, M., MATTILA, T., HÄÄRÄ, A., KIIHAMÄKI, J., TITTONEN, I., OJA, A., and SEPPÄ, H. (2004). Long-term stability of single-crystal silicon microresonators. *Sensors and Actuators A*, **115**(1), 23–27.
- KOUNADIS, A. N. (1980). On the derivation of equations of motion for a vibrating Timoshenko column. *Journal of Sound and Vibration*, **73**(2), 177–184.
- KREYSIG, E. (2006). *Advanced engineering mathematics*. Wiley, Chichester, 9th edition.
- KRYLOV, S. (2007). Lyapunov exponents as a criterion for the dynamic pull-in instability of electrostatically actuated microstructures. *International Journal of Non-Linear Mechanics*, **42**(4), 626–642.
- KRYLOV, S. and MAIMON, R. (2004). Pull-in Dynamics of an Elastic Beam Actuated by Continuously Distributed Electrostatic Force. *Transactions of the ASME, Journal of Vibration and Acoustics*, **126**(3), 332–342.
- KRYLOV, S. and SERETENSKY, S. (2006). Higher order correction of electrostatic pressure and its influence on the pull-in behavior of microstructures. *Journal of Micromechanics and Microengineering*, **6**(7), 1382–1396.
- KRYLOV, S., HARARI, I., and COHEN, Y. (2005). Stabilization of Electrostatically Actuated Microstructures Using Parametric Excitation. *Journal of Micromechanics and Microengineering*, **15**(6), 1188–1204.
- KRYLOV, S., ILIC, B. R., SCHREIBER, D., SERETENSKY, S., and CRAIGHEAD, H. (2008). Higher order correction of electrostatic pressure and its influence on the pull-in behavior of microstructures. *Journal of Micromechanics and Microengineering*, **18**(5), 055026 (20pp).
- LANGDON, R. M. (1985). Resonator sensors – a review. *Journal of Physics E: Scientific Instruments*, **18**(2), 103–115.
- LAU, S. L. and CHEUNG, Y. K. (1981). Amplitude incremental variational principle for nonlinear vibrations of elastic systems. *Journal of Applied Mechanics*, **48**(4), 959–964.

- LAU, S. L., CHEUNG, Y. K., and WU, S. Y. (1982). A variable parameter incrementation method for dynamic instability of linear and nonlinear elastic systems. *Journal of Applied Mechanics*, **49**(4), 849–853.
- LEE, S., DEMIRCI, M. U., and NGUYEN, C. T.-C. (2001). A 10-MHz Micromechanical Resonator Pierce Reference Oscillator for Communications. *Transducers '01, Eurosensors XV, Proceedings of the 11th International Conference on Solid-State Sensors and Actuators, June 10–14, Munich, Germany*, 1094–1097.
- LEE, T. H. and HAJIMIRI, A. (2000). Oscillator Phase Noise: A Tutorial. *IEEE Journal of Solid-State Circuits*, **35**(3), 326–336.
- LEESON, D. B. (1966). A Simple Model of Feedback Oscillator Noise Spectrum. *Proceedings of the IEEE*, **54**, 329–330.
- LEGTENBERG, R. and TILMANS, H. A. C. (1994). Electrostatically driven, vacuum-encapsulated polysilicon resonators; Part I: design and fabrication. *Sensors and Actuators A*, **45**(1), 57–66.
- LEUS, V. and ELATA, D. (2004). *Fringing field effect in electrostatic actuators*. Technion, Israel Institute of Technology, Faculty of Mechanical Engineering, Technical Report ETR-2004-2.
- LIFSHITZ, R. and CROSS, M. C. (2003). Response of parametrically driven nonlinear coupled oscillators with application to micromechanical and nanomechanical resonator arrays. *Physical Review B*, **66**(13), 134302–1–12.
- LIFSHITZ, R. and CROSS, M. C. (2008). Nonlinear dynamics of nanomechanical and micromechanical resonators. *Review of Nonlinear Dynamics and Complexity*, **1**, 1–52.
- LIFSHITZ, R. and ROUKES, M. L. (2000). Thermoelastic damping in micro- and nanomechanical systems. *Physical Review B*, **61**(8), 5600–5609.
- LIN, L., NGUYEN, C. T.-C., HOWE, R. T., and PISANO, A. P. (1992). Micro Electromechanical Filters for Signal Processing. *Proceedings of the IEEE Micro Electromechanical Systems Workshop, Travemünde, Germany, Feb. 4–7*, 226–231.
- LIN, R. M. and WANG, W. J. (2006). Structural dynamics of microsystems – current state of research and future directions. *Mechanical Systems and Signal Processing*, **20**(5), 1015–1043.
- LIN, Y.-W., LEE, S., LI, S.-S., XIE, Y., REN, Z., and NGUYEN, C. T.-C. (2004). Series-Resonant VHF Micromechanical Resonator Reference Oscillators. *IEEE Journal of Solid-State Circuits*, **39**(12), 2477–2491.
- LISHCHYNSKA, M., NORDERO, N., and SLATTERY, O. (2004). State of the Art in Prediction of Mechanical Behaviour of Microsystems. *Proceedings of the 5th International Conference on Thermal and Mechanical Simulation and Experiments in Micro-electronics and Micro-systems, Eurosime2004*, 287–294.
- LORD, H. W. and SHULMAN, Y. (1967). A generalized dynamical theory of thermoelasticity. *Journal of the Mechanics and Physics of Solids*, **15**(5), 299–309.
- LOVETT, D. R. (1989). *Tensor Properties of Crystals*. Adam Hilger.
- MALLON, N. J., FEY, R. H. B., NIJMEIJER, H., and ZHANG, G. Q. (2006). Dynamic buckling of a shallow arch under shock loading considering the effects of the arch shape. *International Journal of Non-linear Mechanics*, **41**(9), 1065–1075.
- MALLON, N. J., FEY, R. H. B., and NIJMEIJER, H. (2008). Dynamic stability of a thin cylindrical shell with top mass subjected to harmonic base-acceleration. *International Journal of Solids and Structures*, **45**(6), 1587–1613.
- MALUF, N. and WILLIAMS, K. (2004). *An Introduction to Microelectromechanical Systems Engineering*. Artech House Publishers.
- MASON, W. P. and BATEMAN, T. B. (1964). Ultrasonic Wave Propagation in Doped *n*-Germanium and *p*-Silicon. *Physical Review*, **134**(5), A1387–A1396.
- MATTILA, T., JAAKKOLA, O., KIIHAMÄKI, J., KARTTUNEN, J., LAMMINMÄKI, T., RANTAKARI, P., OJA, A., SEPPÄ, H., KATTELUS, H., and TITTONEN, I. (2002a). 14 MHz micromechanical oscillator. *Sensors and Actuators A*, **97–98**, 497–502.

- MATTILA, T., KIIHAMÄKI, J., LAMMINMÄKI, T., JAAKKOLA, O., RANTAKARI, P., OJA, A., SEPPÄ, H., KATTELUS, H., and TITTONEN, I. (2002b). A 12 MHz micromechanical bulk acoustic mode oscillator. *Sensors and Actuators A*, **101**(1–2), 1–9.
- MCSKIMIN, H. J. (1950). Ultrasonic Measurement Techniques Applicable to Small Solid Specimens. *Journal of the Acoustical Society of America*, **22**(4), 413–418.
- MCSKIMIN, H. J. (1953). Measurement of Elastic Constants at Low Temperatures by Means of Ultrasonic Waves – Data for Silicon and Germanium Single Crystals, and for Fused Silica. *Journal of Applied Physics*, **24**(8), 988–997.
- MCSKIMIN, H. J. (1961). Pulse Superposition Method for Measuring Ultrasonic Wave Velocities in Solids. *Journal of the Acoustical Society of America*, **33**(1), 12–16.
- MCSKIMIN, H. J. and ANDREATCH, P. (1964a). Elastic Moduli of Silicon vs Hydrostatic Pressure at 25.0°C and –195.8°C. *Journal of Applied Physics*, **35**(7), 2161–2165.
- MCSKIMIN, H. J. and ANDREATCH, P. (1964b). Measurement of Third-Order Moduli of Silicon and Germanium. *Journal of Applied Physics*, **35**(11), 3312–3319.
- MEHNER, J. E., GABBAY, L. D., and SENTURIA, S. D. (2000). Computer-Aided Generation of Nonlinear Reduced-Order Dynamic Macromodels – II: Stress-Stiffened Case. *Journal of Microelectromechanical Systems*, **9**(2), 270–278.
- MEHNER, J. E., DOETZEL, W., SHAUWECKER, B., and OSTERGAARD, D. (2003). Reduced Order Modeling of Fluid Structural Interactions in MEMS Based on Modal Projection Techniques. *Transducers '03, Proceedings of the 12th International Conference on Solid-State Sensors, Actuators and Microsystems*, June 8–12, Boston, 1574–1577.
- VAN DER MEIJS, N. P. and FOKKEMA, J. T. (1984). VLSI circuit reconstruction from mask topology. *Integration*, **2**, 85–119.
- MEIROVITCH, L. (2001). *Fundamentals of Vibrations*. McGraw-Hill, London.
- MESTROM, R. M. C., FEY, R. H. B., VAN BEEK, J. T. M., PHAN, K. L., and NIJMEIJER, H. (2006). Nonlinear oscillations in MEMS resonators. *Proceedings of the Eurosensors XX Conference*, September 17–20, Göteborg, Sweden, M2B–P26.
- MESTROM, R. M. C., FEY, R. H. B., and NIJMEIJER, H. (2007). On phase feedback for nonlinear MEM resonators. *Proceedings of IEEE Frequency Control Symposium, Timenav'07 Conference*, May 29 – June 1, Geneva, Switzerland, 765–770.
- MESTROM, R. M. C., FEY, R. H. B., VAN BEEK, J. T. M., PHAN, K. L., and NIJMEIJER, H. (2008a). Modelling the dynamics of a MEMS resonator: Simulations and experiments. *Sensors and Actuators A*, **142**(1), 306–315.
- MESTROM, R. M. C., FEY, R. H. B., and NIJMEIJER, H. (2008b). Theoretical and experimental nonlinear dynamics of a clamped-clamped beam MEMS resonator. *Proceedings of the EUROMECH Nonlinear Dynamics Conference (ENOC 2008)*, June 30 – July 4, Saint Petersburg, Russian Federation, c7p185r4415.
- MESTROM, R. M. C., FEY, R. H. B., PHAN, K. L., and NIJMEIJER, H. (2009a). Experimental validation of hardening and softening resonances in a clamped-clamped beam MEMS resonator. *Procedia Chemistry*, **1**(1), 812–815. *Proceedings of the Eurosensors XXIII Conference*, September 6–9, Lausanne, Switzerland.
- MESTROM, R. M. C., FEY, R. H. B., and NIJMEIJER, H. (2009b). Phase Feedback for Nonlinear MEM Resonators in Oscillator Circuits. *IEEE/ASME Transactions on Mechatronics*, **14**(4), 423–433.
- MIDDELHOEK, S., FRENCH, P. J., HUIJSING, J. H., and LIAN, W. J. (1988). Sensors with digital or frequency output. *Sensors and Actuators*, **15**(2), 119–133.
- MURNAGHAN, F. D. (1951). *Finite Deformation of an Elastic Solid*. John Wiley & Sons, Inc.
- NAPOLI, M., BASKARAN, R., TURNER, K., and BAMIEH, B. (2003). Validating Fast Simulation of Air Damping in Micromachined Devices. *Proceedings of the sixteenth international conference on Micro Electro Mechanical Systems, MEMS-03*, Jan. 19–23, Kyoto, Japan, 169–172.
- NAPOLI, M., ZHANG, W., TURNER, K., and BAMIEH, B. (2005). Characterization of Electrostatically Coupled Microcantilevers. *Journal of Microelectromechanical Systems*, **14**(2), 295–304.

- NATHANSON, H. C., NEWELL, W. E., WICKSTROM, R. A., and DAVIS JR., J. R. (1967). The Resonant Gate Transistor. *IEEE Transactions on Electron Devices*, **14**(3), 117–133.
- NAVID, R., CLARK, J. R., DEMIRCI, M., and NGUYEN, C. T.-C. (2001). Third-Order Intermodulation Distortion in Capacitively-Driven CC-Beam Micromechanical Resonators. *Proceedings of the fourteenth international conference on Micro Electro Mechanical Systems, MEMS-01, Jan. 21–25, Interlaken, Switzerland*, 228–231.
- NAYFEH, A. H. (1981). *Introduction to perturbation techniques*. Wiley-Interscience, Chichester.
- NAYFEH, A. H. and BALACHANDRAN, B. (1995). *Applied Nonlinear Dynamics: Analytical, Computational and Experimental Methods*. John Wiley & Sons, Inc.
- NAYFEH, A. H. and MOOK, D. T. (1977). Parametric excitations of linear systems having many degrees of freedom. *Journal of the Acoustical Society of America*, **62**(3), 375–381.
- NAYFEH, A. H. and YOUNIS, M. I. (2004). Modeling and simulations of thermoelastic damping in microplates. *Journal of Micromechanics and Microengineering*, **14**(12), 1711–1717.
- NAYFEH, A. H. and YOUNIS, M. I. (2005). Dynamics of MEMS resonators under superharmonic and subharmonic excitations. *Journal of Micromechanics and Microengineering*, **15**(10), 1840–1847.
- NAYFEH, A. H., YOUNIS, M. I., and ABDEL-RAHMAN, E. M. (2005). Reduced-Order Models for MEMS Applications. *Nonlinear Dynamics*, **41**(1–3), 211–236.
- NAYFEH, A. H., YOUNIS, M. I., and ABDEL-RAHMAN, E. M. (2007). Dynamic pull-in phenomenon in MEMS resonators. *Nonlinear Dynamics*, **48**(1–2), 153–163.
- NGUYEN, C. T.-C. (1995). Micromechanical Resonators for Oscillators and Filters. *Proceedings of the IEEE International Ultrasonics Symposium, Seattle, WA, USA, Nov. 7–10*, 489–499.
- NGUYEN, C. T.-C. (2005). Vibrating RF MEMS technology: fuel for an integrated micromechanical circuit revolution? *Transducers '05, Proceedings of the 13th International Conference on Solid-State Sensors, Actuators and Microsystems, June 5–9, Seoul, Korea*, 243–246.
- NGUYEN, C. T.-C. (2007). MEMS Technology for Timing and Frequency Control. *IEEE Transactions on Ultrasonics, Ferroelectrics, and Frequency Control*, **54**(2), 251–270.
- NGUYEN, C. T.-C. and HOWE, R. T. (1993a). CMOS Micromechanical Resonator Oscillator. *Proceedings of the IEEE International Electron Devices Meeting (IEDM 1993), Washington DC, USA, Dec. 5–7*, 199–202.
- NGUYEN, C. T.-C. and HOWE, R. T. (1993b). Low-Order Models for Fast Dynamical Simulation of MEMS Microstructures. *Proceedings of the 1993 International Conference on Solid-State Sensors and Actuators (Transducers '93), Yokohama, Japan, June 7–10*, 1040–1043.
- NGUYEN, C. T.-C. and HOWE, R. T. (1994). Polysilicon Microresonators for Signal Processing. *Proceedings of the Government Microcircuit and Application Conference, San Diego, CA, USA, Aug. 15*, 195–198.
- NGUYEN, C. T.-C. and HOWE, R. T. (1999). An Integrated CMOS Micromechanical Resonator High-Q Oscillator. *IEEE Journal of Solid-State Circuits*, **34**(4), 440–455.
- NILSSON, J. W. and RIEDEL, S. A. (2008). *Electric Circuits*. Prentice Hall, London, 8th edition.
- NOIJEN, S. P. M., MALLON, N. J., FEY, R. H. B., NIJMEIJER, H., and ZHANG, G. Q. (2007). Periodic excitation of a buckled beam using a higher order semi-analytical approach. *Nonlinear Dynamics*, **50**(1–2), 325–339.
- NOWINSKI, J. L. (1978). *Theory of thermoelasticity with applications*. Slijthof & Noordhoff International Publishers, Alphen aan den Rijn, the Netherlands.
- NYE, J. F. (1985). *Physical Properties of Crystals: Their Representation by Tensors and Matrices*. Oxford University Press.
- NYQUIST, H. (1928). Thermal agitation of electric charge in conductors. *Physical Review*, **32**(1), 97–109.
- OKADA, Y. and TOKUMARU, Y. (1984). Precise Determination of Lattice Parameter and Thermal Expansion Coefficient of Silicon Between 300 and 1500 K. *Journal of Applied Physics*, **56**(2), 314–320.
- OSTERBERG, P. M. (1995). *Electrostatically actuated microelectromechanical test structures for material property measurement*. PhD Thesis, Massachusetts Institute of Technology.

- OSTERBERG, P. M. and SENTURIA, S. D. (1997). M-TEST: A Test Chip for MEMS Material Property Measurement Using Electrostatically Actuated Test Structures. *Journal of Microelectromechanical Systems*, **6**(2), 107–118.
- PACI, D., STOFFELS, S., and TILMANS, H. A. C. (2006). Simulations of the Anchor Losses in MEM Disk Resonators. *Nanotech 2006, Proceedings of the NSTI Nanotechnology Conference and Trade Show, May 7–11, Boston, USA*, 558–561.
- PALMER, H. B. (March 1937). Capacitance of a Parallel-Plate Capacitor by the Schwartz-Christoffel Transformation. *Transactions of the AIEE*, **56**, 363–366.
- PAMIDIGHANTAM, S., PUERS, R., BAERT, K., and TILMANS, H. A. C. (2002). Pull-in voltage analysis of electrostatically actuated beam structures with fixed-fixed and fixed-free end conditions. *Journal of Micromechanics and Microengineering*, **12**(4), 458–464.
- PARK, Y.-H. and PARK, K. C. (2004a). High-Fidelity Modeling of MEMS Resonators – Part I: Anchor Loss Mechanisms Through Substrate. *Journal of Microelectromechanical Systems*, **13**(2), 238–247.
- PARK, Y.-H. and PARK, K. C. (2004b). High-Fidelity Modeling of MEMS Resonators – Part II: Coupled Beam-Substrate Dynamics and Validation. *Journal of Microelectromechanical Systems*, **13**(2), 248–257.
- PARKER, T. S. and CHUA, L. O. (1989). *Practical Numerical Algorithms for Chaotic Systems*. Springer-Verlag, New York.
- PETERSEN, K. E. (1982). Silicon as a Mechanical Material. *Proceedings of the IEEE*, **70**(5), 420–457.
- PHAN, K. L., VAN BEEK, J. T. M., and KOOPS, G. E. J. (2009). . *Transducers '09, Proceedings of the 15th International Conference on Solid-State Sensors, Actuators and Microsystems, June 21–25, Denver, USA*, 1413–1416.
- PIERRE, C. and DOWELL, E. H. (1985). A study of dynamic instability of plates by an extended incremental harmonic balance method. *Journal of Applied Mechanics*, **52**(3), 693–697.
- PIESSENS, R., DE DONCKER-KAPENGA, E., ÜBERHUBER, C. W., and KAHANER, D. K. (1983). *QUAD-PACK, A subroutine package for automatic integration*. Springer-Verlag.
- POURKAMALI, S. and AYAZI, F. (2003). SOI-based HF and VHF single-crystal silicon resonators with sub-100 nanometer vertical capacitive gaps. *Transducers '03, Proceedings of the 12th International Conference on Solid-State Sensors, Actuators and Microsystems, June 8–12, Boston, USA*, 837–840.
- POURKAMALI, S., HAO, Z., and AYAZI, F. (2004). VHF Single-Crystal Silicon Elliptic Bulk-Mode Capacitive Disk Resonators – Part II: Implementation and Characterization. *Journal of Microelectromechanical Systems*, **13**(6), 1054–1062.
- PRABHAKAR, S. and VENGALLATORE, S. (2008). Theory of Thermoelastic Damping in Micromechanical Resonators With Two-Dimensional Heat Conduction. *Journal of Microelectromechanical Systems*, **17**(2), 494–502.
- PRATT, R. I., JOHNSON, G. C., HOWE, R. T., and CHANG, J. C. (1991). Micromechanical structures for thin film characterization. *Transducers '91, Proceedings of the 6th International Conference on Solid-State Sensors, Actuators and Microsystems, June 24–27, San Francisco, USA*, 205–208.
- PRZEMIENIECKI, J. S. (1968). *Theory of matrix structural analysis*. McGraw-Hill, Inc., New York.
- RAO, S. S. (1995). *Mechanical Vibrations*. Addison-Wesley, Amsterdam, 3rd edition.
- REDDY, J. N. (2007). *Theory and Analysis of Elastic Plates and Shells*. CRC Press, Boca Raton, 2nd edition.
- REDDY, J. N. and RASMUSSEN, M. L. (1982). *Advanced engineering analysis*. John Wiley & Sons, New York.
- REDDY, J. N. and SINGH, I. R. (1981). Large deflections and large-amplitude free vibrations of straight and curved beams. *International Journal for Numerical Methods in Engineering*, **17**(6), 829–852.
- RHOADS, J. F., SHAW, S. W., TURNER, K. L., and BASKARAN, R. (2005). Tunable Microelectromechanical Filters that Exploit Parametric Resonance. *Transactions of the ASME, Journal of Vibration and Acoustics*, **127**(5), 423–430.
- RHOADS, J. F., SHAW, S. W., TURNER, K. L., MOEHLIS, J., DEMARTINI, B. E., and ZHANG, W. (2006). Generalized parametric resonance in electrostatically actuated microelectromechanical oscillators. *Journal of Sound and Vibration*, **296**(4–5), 797–829.

- ROBERTS, J. W. and CARTMELL, M. P. (August 1984). Forced vibration of a beam system with autoparametric coupling effects. *Strain*.
- ROCHA, L. A. (2005). *Dynamics and Nonlinearities of the Electro-Mechanical Coupling in Inertial MEMS*. PhD Thesis, Delft University of Technology, The Netherlands.
- ROCHUS, V., RIXEN, D. J., and GOLINVAL, J.-C. (2005). Electrostatic coupling of MEMS structures: transient simulations and pull-in. *Nonlinear Analysis*, **63**, e1619–e1633.
- ROCHUS, V., RIXEN, D. J., and GOLINVAL, J.-C. (2006). Monolithic modelling of electro-mechanical coupling in micro-structures. *International Journal for Numerical Methods in Engineering*, **65**(4), 461–493.
- ROESSIG, T. A., HOWE, R. T., and PISANO, A. P. (1997). Nonlinear mixing in surface-micromachined tuning fork oscillators. *Proceedings of the IEEE International Frequency Control Symposium, Orlando, FL, USA, May 28–30*.
- ROSZHART, T. V. (1990). The effect of thermoelastic friction on the Q of micromachined silicon Resonators. *Proceedings of the IEEE Solid-State Sensors and Actuators Workshop, Hilton Head Island, SC, USA, June 4–7*, 13–16.
- RUBY, R. and MERCHANT, P. (1994). Micromachined thin film bulk acoustic resonators. *Proceedings of the IEEE International Frequency Control Symposium, Boston, MA, USA, June 1–3*.
- SADD, M. H. (2005). *Elasticity: Theory, Applications, and Numerics*. Elsevier Inc.
- SALT, D. (1987). *Hy-Q Handbook of Quartz Crystal Devices*. Van Nostrand Reinhold (UK) Co. Ltd.
- SEEGER, A. and BUCK, O. (1960). Die experimentelle Ermittlung der elastischen Konstanten höherer Ordnung. *Zeitschrift für Naturforschung, Teil A*, **15**, 1056–1067.
- SENTURIA, S. D. (1998). Simulation and Design of Microsystems: a 10-Year Perspective. *Sensors and Actuators A*, **67**, 1–7.
- SENTURIA, S. D. (2001). *Microsystems Design*. Kluwer Academic Publishers.
- SENTURIA, S. D. (2003). Perspectives on MEMS, Past and Future: the Tortuous Pathway from Bright Ideas to Real Products. *Transducers '03, Proceedings of the 12th International Conference on Solid-State Sensors, Actuators and Microsystems, June 8–12, Boston*, 10–15.
- SENTURIA, S. D., ALURU, N., and WHITE, J. (1997). Simulating the Behavior of MEMS Devices: Computational Methods and Needs. *IEEE Computational Science & Engineering*, **4**(1), 30–43.
- SEYDEL, R. U. (1994). *Practical bifurcation and stability analysis: from equilibrium to chaos*. Springer, Berlin, 2nd edition.
- SHAO, L. C., WONG, C. L., and PALANIAPAN, M. (2008a). Study of the nonlinearities in micromechanical clamped-clamped beam resonators using stroboscopic SEM. *Journal of Micromechanics and Microengineering*, **18**(8), 085019 (11pp).
- SHAO, L. C., PALANIAPAN, M., and TAN, W. W. (2008b). The nonlinearity cancellation phenomenon in micromechanical resonators. *Journal of Micromechanics and Microengineering*, **18**(6), 065014 (9pp).
- SHIEH, R. C. (1975). Thermoelastic Vibration and Damping for Circular Timoshenko Beams. *Journal of Applied Mechanics*, **42**, Ser. E(2), 405–410.
- SHIEH, R. C. (1979). Eigensolutions for Coupled Thermoelastic Vibrations of Timoshenko Beams. *Journal of Applied Mechanics*, **46**(1), 169–174.
- STEMME, G. (1991). Resonant Silicon Sensors. *Journal of Micromechanics and Microengineering*, **1**(2), 113–125.
- STROGATZ, S. H. (2000). *Nonlinear Dynamics and Chaos: With Applications to Physics, Biology, Chemistry, and Engineering*. Westview Press.
- TANG, W. C., NGUYEN, T.-C. H., and HOWE, R. T. (1989). Laterally Driven Polysilicon Resonant Microstructures. *Sensors and Actuators*, **20**, 25–32.
- THOMPSON, J. M. T. and STEWART, H. B. (2002). *Nonlinear Dynamics and Chaos: Second Edition*. John Wiley & Sons, Ltd., Chichester.

- THOMSEN, J. J. (2003). *Vibrations and Stability; Advanced Theory, Analysis and Tools*. Springer Verlag, Berlin, 2nd edition.
- THURSTON, R. N. and BRUGGER, K. (1964). Third-Order Elastic Constants and the Velocity of Small Amplitude Elastic Waves in Homogeneously Stressed Media. *Physical Review*, **133**(6), A1604–A1610.
- TILMANS, H. A. C. and LEGTENBERG, R. (1994). Electrostatically driven, vacuum-encapsulated polysilicon resonators; Part II: theory and performance. *Sensors and Actuators A*, **45**(1), 67–84.
- TILMANS, H. A. C., ELWENPOEK, M., and FLUITMAN, J. H. J. (1992). Micro resonant force gauges. *Sensors and Actuators A*, **30**(1), 35–53.
- TIMOSHENKO, S. P. (1921). On the correction for shear of the differential equation for the transverse vibrations of prismatic bars. *Philosophical Magazine*, **41**, 744–746.
- TIMOSHENKO, S. P. (1922). On the transverse vibrations of bars of uniform cross-sections. *Philosophical Magazine*, **43**, 125–131.
- TRAILL-NASH, R. W. and COLLAR, A. R. (1953). The effects of shear flexibility and rotatory inertia on the bending vibrations of beams. *Quarterly Journal of Mechanics and Applied Mathematics*, **6**(2), 186–222.
- TUDOR, M. J., ANDRES, M. V., FOULDS, K. W. H., and NADEN, J. M. (1988). Silicon resonator sensors: interrogation techniques and characteristics. *IEE Proceedings Part D: Control Theory and Applications*, **135**(5), 364–368.
- TUFTE, O. N. and STELZER, E. L. (1963). Piezoresistive Properties of Silicon Diffused Layers. *Journal of Applied Physics*, **34**(2), 313–318.
- TURLEY, J. and SINES, G. (1971). The Anisotropy of Young's Modulus, Shear Modulus and Poisson's Ratio in Cubic Materials. *Journal of Physics D: Applied Physics*, **4**(2), 264–271.
- TURNER, K. L., MILLER, S. A., HARTWELL, P. G., MACDONALD, N. C., STROGATZ, S. H., and ADAMS, S. G. (1998). Five parametric resonances in a microelectromechanical system. *Nature*, **396**, 149–152.
- VANIER, J., GAGNEPAIN, J. J., RILEY, W. J., WALLS, F. L., and GRANVEAUD, M. (1992). Aging, warm-up time and retrace; important characteristics of standard frequency generations. *IEEE Frequency Control Symposium*, 807–815.
- VEIJOLA, T. (2004). Compact Models for Squeezed-Film Dampers with Inertial and Rarefied Gas Effects. *Journal of Micromechanics and Microengineering*, **14**(7), 1109–1118.
- VEIJOLA, T. and TUROWSKI, M. (2001). Compact Damping Models for Laterally Moving Microstructures with Gas-Rarefaction Effects. *Journal of Microelectromechanical Systems*, **10**(2), 263–273.
- VIG, J. R. and BALLATO, A. (1999). *Ultrasonic Instruments and Devices (Chapter 7: Frequency Control Devices)*. Academic Press, Inc.
- VAN DE VORST, E. L. B. (1996). *Long Term Dynamics and Stabilization of Nonlinear Mechanical Systems*. PhD Thesis, Technische Universiteit Eindhoven, The Netherlands.
- WANG, C. M., REDDY, J. N., and LEE, K. H. (2000). *Shear Deformable Beams and Plates: Relationships with Classical Solutions*. Elsevier, Amsterdam.
- WAUTELET, M. (2001). Scaling Laws in the Macro-, Micro- and Nanoworlds. *European Journal of Physics*, **22**, 601–611.
- WEAVER, JR., W., TIMOSHENKO, S. P., and YOUNG, D. H. (1990). *Vibration Problems in Engineering*. Wiley Interscience, New York, 5th edition.
- WILLARDSON, R. K., BEER, A. C., and WEBER, E. R. (1992). The Mechanical Properties of Semiconductors. In K. T. FABER and K. MALLOY (eds.), *Semiconductors and Semimetals*, **37**. Academic Press, Inc.
- WONG, A.-C. and NGUYEN, C. T.-C. (2004). Micromechanical Mixer-Filters ("Mixlers"). *Journal of Microelectromechanical Systems*, **13**(1), 100–112.
- YANG, J., ONO, T., and ESASHI, M. (2002). Energy Dissipation in Submicrometer Thick Single-Crystal Silicon Cantilevers. *Journal of Microelectromechanical Systems*, **11**(6), 775–783.
- YAO, J. J. and MACDONALD, N. C. (1996). A micromachined, single-crystal silicon, tunable resonator. *Journal of Micromechanics and Microengineering*, **6**(3), 257–264.

- YOUNIS, M. I. and NAYFEH, A. H. (2003). A Study of the Nonlinear Response of a Resonant Microbeam to an Electric Actuation. *Nonlinear Dynamics*, **31**(1), 91–117.
- YOUNIS, M. I., ABDEL-RAHMAN, E. M., and NAYFEH, A. H. (2003). A Reduced-Order Model for Electrically Actuated Microbeam-Based MEMS. *Journal of Microelectromechanical Systems*, **12**(5), 672–680.
- YOUNIS, M. I., ALSALEEM, F., and JORDY, D. (2007). The response of clamped-clamped microbeams under mechanical shock. *International Journal of Non-Linear Mechanics*, **42**(4), 643–657.
- YURKE, B., GREYWALL, D. S., PARGELLIS, A. N., and BUSCH, P. A. (1995). Theory of amplifier-noise evasion in an oscillator employing a nonlinear resonator. *Physical Review A*, **51**(5), 4211–4229.
- ZAREMBO, L. K. and KRASIL'NIKOV, V. A. (1971). Nonlinear Phenomena in the Propagation of Elastic Waves in Solids. *Soviet Physics USPEKHI*, **13**(6), 778–797.
- ZENER, C. (1937). Internal Friction in Solids; I. Theory of Internal Friction in Reeds. *Physical Review*, **52**(3), 230–235.
- ZENER, C. (1938). Internal Friction in Solids; II. General Theory of Thermoelastic Internal Friction. *Physical Review*, **53**(1), 90–99.
- ZENER, C. (1960). *Elasticity and anelasticity of metals*. The University of Chicago Press, Chicago, Illinois, 4th. edition.
- ZENER, C., OTIS, W., and NUCKOLLS, R. (1938). Internal Friction in Solids; III. Experimental Demonstration of Thermoelastic Internal Friction. *Physical Review*, **53**(1), 100–101.
- ZHANG, L. M., UTTAMCHANDANI, D., CULSHAW, B., and DOBSON, P. (1990). Measurement of Young's Modulus and Internal Stress in Silicon Microresonators Using a Resonant Frequency Technique. *Measurement Science and Technology*, **1**(12), 1343–1346.
- ZHAO, X., ABDEL-RAHMAN, E. M., and NAYFEH, A. H. (2004). A reduced-order model for electrically actuated microplates. *Journal of Micromechanics and Microengineering*, **14**(7), 900–906.
- ZOOK, J. D., BURNS, D. W., GUCKEL, H., SNIEGOWSKI, J. J., ENGELSTAD, R. L., and FENG, Z. (1991). Resonant microbeam strain transducers. *Transducers '91, Proceedings of the 6th International Conference on Solid-State Sensors, Actuators and Microsystems, June 24–27, San Francisco, USA*, 529–532.
- ZOOK, J. D., BURNS, D. W., GUCKEL, H., SNIEGOWSKI, J. J., ENGELSTAD, R. L., and FENG, Z. (1992). Characteristics of polysilicon resonant microbeams. *Sensors and Actuators A*, **35**(1), 51–59.

Dankwoord / Acknowledgements

*afgerond proefschrift
content met het resultaat
sta ik niet alleen*

(haiku door Rob Mestrom)

Startende vanuit de gedachte ‘we willen iets met micro en multiphysics’, ruim vier jaar terug, had ik niet gedacht dat er nu een proefschrift zou liggen over het modelleren van MEMS resonatoren. Dankzij de hulp van een aantal mensen is mijn werk tot dit eindresultaat gekomen.

Henk, jouw kritische blik als promotor en je gave om de grote lijnen te zien hebben veel aan dit werk bijgedragen en hebben mij veel geleerd.

Rob, een AIO mag zich gelukkig prijzen met een copromotor met een dergelijke nauwgezetheid en oog voor detail.

Furthermore, I would like to thank the members of the core committee, Steve Shaw, Peter Baltus and Kouchi Zhang, for their careful reading of the thesis and their useful comments.

Valuable discussions with the people from the NXP-TSMC Research Center, Joost van Beek, Kim Le Phan, Cas van der Avoort and Peter Vermeeren are gratefully acknowledged. Especially the discussions with Kim and his help with the experiments and the set-up have been of great value.

Ik wil tevens de studenten Arjan van Engelen en Hein van Beek bedanken voor hun bijdragen. Ook bedank ik student Eric van den Hoven die zich flink heeft vastgebeten in de ‘dog-bone’ resonator.

De aanwezigheid van fijne ‘roomies’ is mede van groot belang geweest bij het met plezier naar mijn werk gaan. Jan, Jan-Kees, Erik en Rob, bedankt! Ik wil verder al mijn collega’s van de sectie DCT bedanken voor de leuke tijd die ik met hen doorgebracht heb, zowel tijdens als na het werk.

Familie, schoonfamilie en vrienden wil ik danken voor de gezelligheid en hun interesse in mijn werk.

Pap en mam, dank jullie dat jullie in mij hebben geloofd en voor alle onvoorwaardelijke steun tijdens de 'ups' en 'downs' die ik doorgemaakt heb.

En ten slotte mijn lieve vriendin Petra. 'You're what makes me tick!' Zonder jouw liefde, steun en geduld had ik het in de laatste fase niet op deze manier afgerond gekregen. Dank je voor wie je bent.

Rob Mestrom
September 2009

Curriculum Vitae

Rob Mestrom was born on March 26, 1981 in Weert, the Netherlands. He completed his secondary education cum laude in 1999 at the Scholengemeenschap St. Ursula in Horn. He then started his academic education in Mechanical Engineering at the Eindhoven University of Technology in Eindhoven, the Netherlands. As a part of his study, he performed an international internship at the Technische Universität Hamburg-Harburg in Germany on the 'Design of a Dynamic Positioning System for a Floating Body'. He received his Master's degree cum laude in April 2005 on the thesis, entitled 'Stationary Resonances of Optical Discs; Geometry-Induced Excitation'. The work was performed in the Dynamics and Control Group and carried out at the Emerging Technologies and Systems Laboratory of Philips Optical Storage, Eindhoven, the Netherlands.

After completion of his Master's thesis, he started as a PhD student in the Dynamics and Control Group in May 2005. The topic of his PhD project was dynamics and multiphysics modelling of microelectromechanical resonators. For the experimental part, he cooperated with experts at the NXP-TSMC Research Center, NXP Semiconductors, Eindhoven, the Netherlands. The main results of his PhD research are presented in this thesis.